Investigating different aspects of stellar activity

– From elemental abundances in solar-like stars to giant flares on active M dwarfs –

Dissertation
zur Erlangung des Doktorgrades
des Department Physik
der Universität Hamburg

vorgelegt von

Carolin Liefke

aus Lübeck

Hamburg
2011

Gutachter der Dissertation:	Prof. Dr. Jürgen H. M. M. Schmitt Prof. Dr. Manuel Güdel
Gutachter der Disputation:	Prof. Dr. Peter H. Hauschildt Prof. Dr. Robi Banerjee
Datum der Disputation:	30. November 2011
Vorsitzender des Prüfungsausschusses:	Dr. Robert Baade
Vorsitzender des Promotionsausschusses:	Prof. Dr. Peter Hauschildt
Dekan der MIN-Fakultät:	Prof. Dr. Heinrich Graener
Leiterin des Fachbereichs Physik:	Prof. Dr. Daniela Pfannkuche

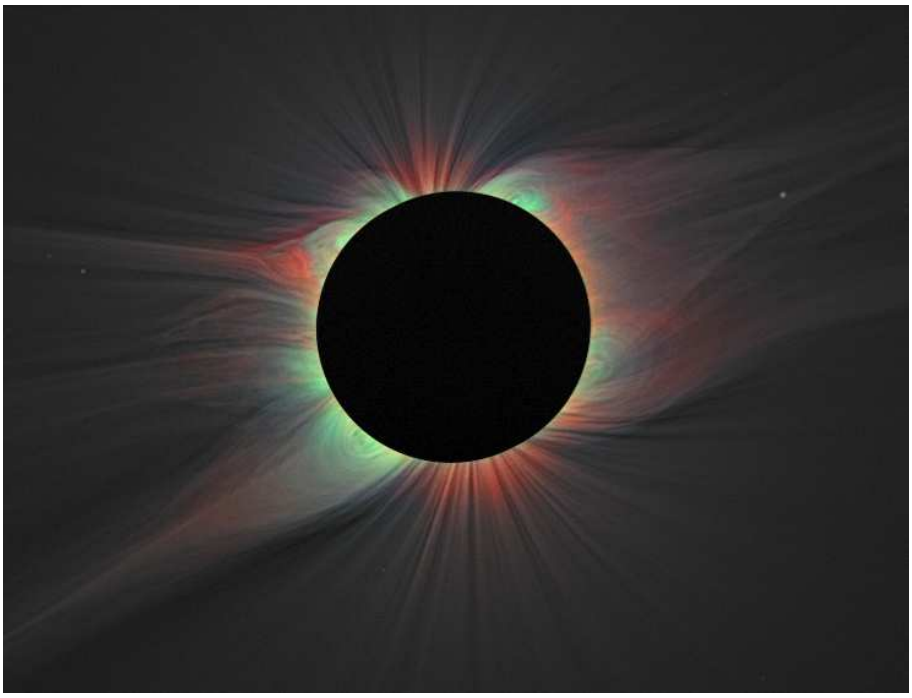

This image shows the corona during the total solar eclipse of 1 August 2008. It has been created from observations with narrowband filters centered on two optical coronal emission lines, Fe XI at 7892 Å colored in red and Fe XIV at 5303 Å shown in green. The fine structure information of the coronal plasma has been derived from optical white light exposures, which have been digitally processed with a sophisticated rotational gradient filter technique and added to the image. The spatial distribution of the cooler and hotter components of the coronal plasma, with Fe XIV primarily confined to closed-loop structures while Fe XI is predominantly found along open magnetic field lines such as in coronal holes or along streamers, beautifully illustrates a crucial part of the work I have done for stars, i. e. the determination of the amount of emitting plasma in stellar coronae as a function of temperature. From Habbal et al. (2010).

Zusammenfassung

Kühle Sterne der Spektraltypen A bis M zeigen häufig magnetische Aktivität, das Vorhandensein heißer Koronen ist einer der deutlichsten Hinweise darauf. Die Aktivität kann allerdings um mehrere Größenordnungen variieren. Für die aktivsten Sterne – frühe M-Sterne, RS CVn-Systeme oder junge Sterne – erreicht die Röntgenleuchtkraft einen Sättigungswert. Solche Sterne weisen oft starke Variabilität auf, insbesondere in Form von häufigen, unregelmäßigen Helligkeitsausbrüchen, den sogenannten Flares. Späte A-Sterne oder ältere Sterne wie die Sonne dagegen zeigen ein eher “gesetztes” Verhalten. Die vorliegende Arbeit beschäftigt sich mit verschiedenen Aspekten der stellaren Aktivität, unter anderem mit den Eigenschaften der Koronen sonnenähnlicher Sterne und aktiver M-Zwerge, sowie der detaillierten Untersuchung eines in mehreren Wellenlängenbereichen beobachteten, äußerst starken Flares auf einem M-Stern.

Die Untersuchungsmethoden, mit denen Beobachtungsdaten ausgewertet werden, sind die fundamentale Basis der erzielten Ergebnisse, sie müssen daher unbedingt zuverlässig sein. Bei den *Benchmark Exercises for stellar X-ray Spectroscopy Testing* wurden einmalig die verschiedenen Ansätze zur Ermittlung von Emissionsmaßverteilungen, Dichten und Elementhäufigkeiten stellarer Koronen, wie sie von verschiedenen Gruppen entwickelt und angewandt werden, miteinander verglichen. Zur Diskussion standen insbesondere die ermittelten Unsicherheiten und die Suche nach bislang unquantifizierten Fehlerquellen.

α Centauri ist eines der wenigen Beispiele für sonnennahe Sterne, deren Aktivitätsgrad ähnlich gering ist wie der der Sonne. Kürzlich an den Standardsatz photosphärischer Elementhäufigkeiten der Sonne angebrachte Änderungen führten zu einem Konflikt mit Modellen des Sonneninneren und helioseismologischen Messungen. Dieser hätte sich lösen lassen, wenn man stattdessen von einem erhöhten Verhältnis Neon zu Sauerstoff ausgegangen wäre, wie man es in den Koronen aktiver Sterne in Sonnenumgebung häufig beobachtet. Zieht man allerdings ein der Sonne sehr ähnliches Sternsystem wie α Cen zu Rate, läßt sich dieser Ansatz nicht untermauern.

Das Doppelsternsystem EQ Pegasi besteht aus zwei M-Sternen, die ihrem Spektraltyp nach nahe am Übergang von sonnenähnlichen Sternen mit einer äußeren Konvektionszone und daher einem klassischen $\alpha\Omega$-Dynamo zu voll konvektiven Sternen liegen, deren Magnetfelder mithilfe turbulenter Dynamomechanismen erzeugt werden. Ich habe daher die koronalen Eigenschaften der beiden Sterne bestimmt und mit denen anderer M-Sterne auf beiden Seiten der erwarteten Grenze verglichen. Dabei hat sich insbesondere herausgestellt, daß die Amplitude des sogenannten inversen FIP-Effektes, bei dem die Häufigkeiten chemischer Elemente mit hohem ersten Ionisationspotential systematisch höher sind während diejenigen mit niedrigem Ionisationspotential unterhäufig sind, hin zu späteren M-Sternen abnimmt.

CN Leonis ist ein mittlerer M-Stern mit gemäßigtem Aktivitätsgrad und abgesehen von der Sonne der einzige Stern, bei dem man bislang optische koronale Linienemission eindeutig nachweisen konnte. Bei der Untersuchung der Eigenschaften seiner Chromosphäre und Korona im Ruhezustand und während schwächerer Helligkeitsausbrüche ließ sich daher insbesondere auch diese optische koronale Emission mit der koronalen Röntgenstrahlung korrelieren.

Im Rahmen einer Beobachtungskampagne in mehreren Wellenlängenbereichen habe ich den Stern während eines extrem starken Flares untersucht, bei dem die Temperaturen und Dichten des Flareplasmas im Vergleich zur normalen koronalen Emission um Größenordnungen erhöht waren. Die zeitliche Entwicklung dieser beiden Parameter in der Korona läßt Rückschlüsse auf die Geometrie der koronalen Bögen in der aktiven Region zu, in der sich der Helligkeitsausbruch ereignet hat. Gleichzeitig kann man über das optische Kontinuum die Temperaturen bestimmen, zu der die Photosphärenregion aufgeheizt wird. Es stellte sich heraus, daß die Eisenhäufigkeit des koronalen Flareplasmas signifikant erhöht gegenüber der normalen Korona war. Dies deutet darauf hin, daß Chromosphäre und Photosphäre eine unterschiedliche Elementzusammensetzung haben, da große Teile des Flareplasmas aus diesen Schichten der Sternatmosphäre stammen. Das gesamte Flareereignis wurde offenbar durch einen extrem kurzen Ausbruch im Röntgenbereich ausgelöst, der zeitgleich mit dem optischen Maximum aufgetreten ist. Durch die kurze Zeitdauer läßt sich dieses Anfangsereignis in einer einzelnen magnetischen Flußröhre lokalisieren. Die detaillierten Beobachtungen ermöglichen die verschiedenen Aspekte der Auswirkungen des Ereignisses auf die einzelnen Atmosphärenschichten zu einem Gesamtbild des Ablaufs dieses Flares zusammenzufügen.

Abstract

Magnetic activity is widely observed among cool stars of spectral types A to M, with the existence of hot coronae as one of the most prominent indicators. The level of activity can however vary by orders of magnitude. For the most active stars – early M dwarfs, young stars, or RS CVn binaries – coronal X-ray emission reaches a saturation level. These stars additionally can exhibit strong variability and especially frequent flaring. Older stars like the Sun or late A stars show a different, more “sedate” behavior. The present thesis includes the work I have done on various aspects of stellar activity, ranging from the coronal properties of solar-like stars and active M dwarfs to the analysis of a giant stellar flare observed in a multiwavelength campaign.

The analysis methods applied to observed data are the fundamental basis of the results obtained. It is therefore crucial that their reliability is guaranteed. The *Benchmark Exercises for stellar X-ray Spectroscopy Testing* were a unique approach to compare different methods to determine the emission measure distributions, densities and abundances of stellar coronae as implemented by different groups, to check the specified uncertainties, and to spot additional error sources.

α Centauri is one of the rare examples of stars with an activity level similar to the Sun. Recent revisions of solar photospheric abundances resulted in a conflict with models of the solar interior and helioseismological observations that could be solved if an enhanced neon-to-oxygen abundance ratio is assumed as it is widely observed in the coronae of highliy active stars. A study of the coronae of the α Centauri system showed that this approach is not supported in the light of measurements from other stars with low activity levels.

The M dwarf binary EQ Pegasi consists of two components which are, based on their spectral types, expected to be located close to the transition from solar-like stars with outer convection zones and a classical $\alpha\Omega$-dynamo at work to fully convective stars whose activity must be driven by a turbulent dynamo. I investigated the coronal properties of these two stars and compared them with other M dwarfs. It turns out that the amplitude of the inverse first ionization potential (FIP) effect – an abundance anomaly where the coronal abundances of elements with high first ionization potential are enhanced while those with low first ionization potential are depleted – declines with later spectral type.

CN Leonis is a mid M dwarf with intermediate activity levels and – apart from the Sun – so far the only star where optical coronal line emission has been clearly detected. The properties of its chromosphere and corona during quiescent and flaring time intervals, and especially the correlation of coronal X-ray and optical emission have been investigated in a multiwavelength observing campaign.

The star was caught in a giant flare where the densities and temperatures of the flare plasma were orders of magnitude higher than the quiescent corona. The temporal evolution of temperature and emission measure allowed to characterize the geometry of the flaring loop. The slope of the flare continuum in the optical allows to determine the temperature and size of the heated photospheric area. The coronal iron abundance was clearly enhanced during the flare, indicating that the chemical compositions of the corona and the lower atmospheric layers – where major parts of the flare plasma evaporated from – differ. A very short X-ray burst is observed simultaneously to the optical flare peak. It can be ascribed to evaporated material confined in a single magnetic flux tube. This initial burst served as the trigger for the whole flare event. The final goal is putting together all the pieces of information obtained from the effects of the flare on the different layers of the stellar atmosphere to a comprehensive model of the flare process.

Contents

1 Introduction

What is stellar activity? For a layperson, the face of our very own star, the Sun, seems to be unchanging day after day, but solar observers can easily keep track of small dark spots on the solar surface already with small telescopes. These sunspots can unpredictably appear and vanish, grow and shrink, change their shape, or merge and fall apart within hours or days. Dedicated Hα telescopes show prominences, huge clouds of gas, rising and falling above the solar limb, while sudden brightenings, the so-called flares, may temporarily illuminate the regions where sunspots are visible in white light. On small scales, the Sun is changing all day long.

Spots, prominences, and flares are just a few examples from the wide variety of activity phenomena observed on the Sun; the sheer existence of the corona with its temperature of a few million degrees, which is primarily observed in X-rays, is another one. In the following, we will not only see that all activity-related features are coupled and have the same origin – magnetic fields – but that many stars can show the same effects, and sometimes orders of magnitude stronger than observed on the Sun.

1.1 Solar and stellar activity

1.1.1 The Structure of the Sun

When observed in continuous visible light, the Sun seems to have a strictly confined surface. This so-called photosphere (from Greek *phōs, phōtós*: "light") has a thickness of only a few hundred kilometers, which is very small compared to the solar radius of roughly 700 000 km. Radiation from layers below cannot pass directly because the material is optically thick. Our knowledge of the solar interior is based on theoretical models, which have in turn been refined by measurements of the neutrino fluxes generated as a byproduct of nuclear fusion in the central core and helioseismological data. The latter is illustrated in Fig. 1.1, where the inner solar layers are color-coded as deviations of the measured sound speed from "standard" model calculations. The boundaries between the core, the surrounding radiative zone, and the subsequent convection zone are marked with red and blue colors where the sound speed is faster or slower than expected.

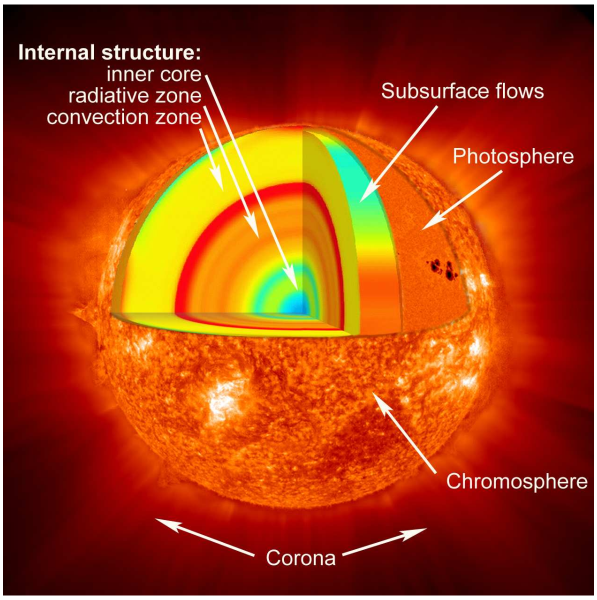

Figure 1.1: The structure of the Sun, visualized with data from the Solar and Heliospheric Observatory (SOHO). The solar interior is reconstructed from the deviations of the sound speed measured by the Michelson Doppler Imager/Solar Oscillations Investigation (MDI/SOI) and the Variability of Solar Irradiance and Gravity Oscillations (VIRGO) instruments from theory. Atmospheric layers are imaged by the MDI and Extreme Ultraviolet Imager (EIT) instruments. Image Credit: NASA

The uppermost part of the convection zone, where the hot material that rises from below is cooling down before it falls back, is imprinted on the photosphere as a grainy structure called granulation. Limb darkening, an optical depth effect that lets the light from the edges of the solar disk originate from the upper, cooler and thinner parts of the photosphere, lends a three-dimensional appearance to the glaring sphere of the Sun.

The physical properties of the solar photosphere are investigated in sophisticated spectral modeling approaches. Its overall spectrum easily reveals an effective temperature T_{eff} of roughly 5780 K and a wealth of Fraunhofer absorption lines, the "fingerprints" of many chemical elements. Optical depths, atmospheric pressures, surface gravities, and velocity fields can be inferred from the line profiles, and finally sets of elemental abundances can be determined (e. g. Asplund et al. 2009).

While the occurrence of sunspots is a phenomenon of the photosphere, prominences arising from the solar limb as shown in Fig. 1.1 belong to the layer above, the chromosphere. Above the photosphere, the solar atmosphere initially cools to a temperature minimum of ≈4500 K. While the density decreases exponentially, the temperature rises again, reaching values higher than 10 000 K. The ordinary chromosphere has a height of only a few thousand kilometers, however, prominences can rise as high as 150 000 km. Unlike the photosphere, the chromosphere shows a pronounced texture. The radiative properties of the thin chromospheric material differ considerably from those of the photosphere, resulting in line emission. The chromosphere is therefore best observed with narrowband filters centered on appropriate spectral lines, especially Hα; hence its name (from Greek *chrōma*: "color"). In white light, the photosphere outshines it by orders of magnitude.

The transition region from the chromosphere into the corona is characterized by a sudden drop in density, accompanied by an enormous increase in temperature of several 100 000 K within another few thousand kilometers. The corona itself is highly structured, as shown in Fig. 1.4, extends up to five solar radii, and merges smoothly with the solar wind and interplanetary space. Within the coronal plasma, temperatures of a few million degrees are easily reached. Compared to the photosphere, the particle density in the corona is eight orders of magnitude lower, at a level of 10^9–10^{10} cm^{-3}. The coronal plasma is often assumed to be optically thin and in an equilibrium state, with the ionization and excitation balance predominantly defined by collisions, and also recombination processes (see Sect. 1.2.2). Owing to these conditions, the modeling of the coronal plasma is much easier than for the lower atmospheric layers, where the complex framework of radiative transfer has to be taken into account (e. g. Gray 2005).

Due to the very different properties of the material in the individual layers of the solar atmosphere, multiwavelength observations have to be used to probe photosphere, chromosphere, and corona. The photosphere is best observed in broadband optical or infrared light. Candidates for chromospheric and transition region emission lines are found both in the ultraviolet and in the optical, but accumulate at shorter wavelengths. The corona shows line and continuum emission. The contribution of the continuum, and especially of its bremsstrahlung component, is increasing with temperature, but at typical coronal temperatures, the spectral energy distribution is dominated by the emission lines. Both are primarily observed in X-rays and in the far ultraviolet. The optical corona visible during solar eclipses is actually mainly scattered light from the photosphere (Golub & Pasachoff 2009).

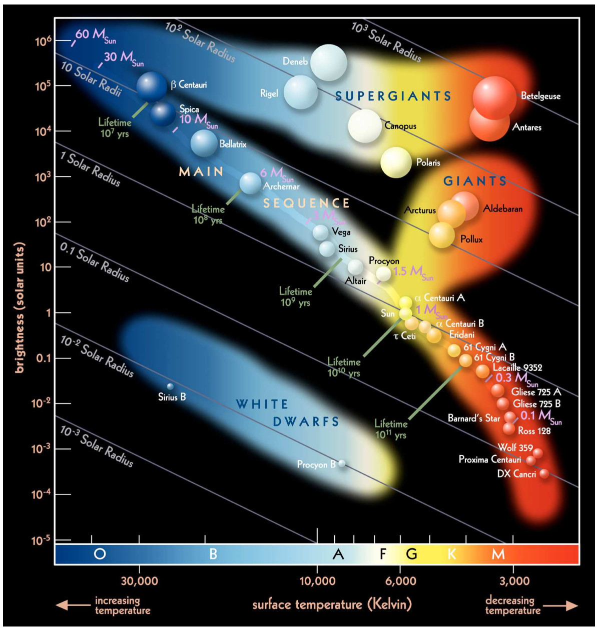

Figure 1.2: The Hertzsprung-Russell diagram of stars, with the position of some of the stars from the following chapters marked. In addition to the basic information spectral type / effective temperature and luminosity, the diagram shows the true colors of the stars, their radii, and the stellar masses and lifetimes on the main sequence. Image Copyright: Pearson Education 2008

1.1.2 Active Stars

Going from the Sun to other stars, both the internal structure and the stellar atmosphere change with properties like mass or effective temperature. Figure 1.2 sorts the stars according to their spectral type and luminosity in the so-called Hertzsprung-Russell (HR) diagram. The spectral sequence OBAFGKM corresponds to a downward sequence in effective temperature. For the biggest part of their lifetime, stars are located on the main sequence reaching from high temperatures and high luminosities to low temperatures and low luminosities. The main sequence is also a mass sequence as well as a radius sequence. Evolved stars can be found in the giant or supergiant regions at much higher luminosities and radii. The region of higher temperatures at low luminosities is occupied by white dwarfs, one of the final stages of stellar evolution.

In relation to the stellar radius, the size of the outer convection zone decreases with increasing stellar mass. Therefore main sequence stars with spectral types earlier than A7, i. e. with $T_{\mathrm{eff}} >$ 7800 K or $M > 1.7 M_\odot$ are no longer expected to have a convection zone at all, they become fully radiative. These stars do also no longer show chromospheres or coronae. Higher-mass stars with spectral type O and early B, which could have effective temperatures of several ten thousand Kelvins, develop convective cores. Additionally, strong stellar winds and high mass-loss rates are observed in this regime. In main sequence stars with spectral types later than the Sun on the other hand, the fraction the outer convection zone takes up grows. Mid M dwarfs with $T_{\rm eff} < 3000$ K are expected to become fully convective. Further details on the interior structure of stars can be found in e. g. Kippenhahn & Weigert (1994).

In the HR diagram, active stars concentrate on the cooler half of the main sequence, i. e. in general they are "normal" stars with outer convection zones. A large fraction of these late-type stars is well-known to show the same activity indicators as the Sun, often even at a much higher level: Doppler imaging reveals starspots that may cover large fractions of the stellar surface (see e. g. Strassmeier 2009a). For many stars, chromospheric emission as traced by the so-called calcium S-index exhibits a periodic behavior (Baliunas et al. 1995) analogously to the solar sunspot number, which follows an 11-year cycle. Finally, X-ray emission from stellar coronae turned out to be ubiquitous among late-type stars (Schmitt & Liefke 2004), with luminosities often orders of magnitude higher than observed for the Sun. Stellar activity does not start to decline before the regime of late M dwarfs is reached. But still, even brown dwarfs are found to show Hα emission and flares, indicating the existence of chromospheres and coronae.

1.1.3 The magnetic dynamo

The energy source of activity is buried deep in the stellar interior. Stars like the Sun should rotate differentially, both with a latitudinal pattern and, depending on their internal structure, also radially. For the Sun, it turns out that core and radiative zone rotate like a rigid body, and differential rotation sets in at the boundary to the convection zone. There, a shear layer, the tachocline, forms where magnetic fields are generated in a dynamo process based on differential rotation and convective motions, the so-called $\alpha\Omega$-dynamo.

Figure 1.3 illustrates the concept of the $\alpha\Omega$-cycle: In ideal magnetohydrodynamics, magnetic fields can be assumed to be coupled to the material, and thus they have to participate in plasma motions. Starting with a poloidal field, i. e. of dipolar and axisymmetric structure, differential rotation in the convection zone with a shorter rotation period further inside stretches the field lines and wraps them around the tachocline. Subsequently, first a helical and eventually an annular toroidal field forms perpendicularly to the rotation axis. This is called the Ω-effect. Convective motions lift the field lines up, and Coriolis forces twist the thus created loop-like structures. Finally, the loops merge to a dipolar field with reversed polarity, which is called the α-effect. For a detailed description see e. g. Jones et al. (2010).

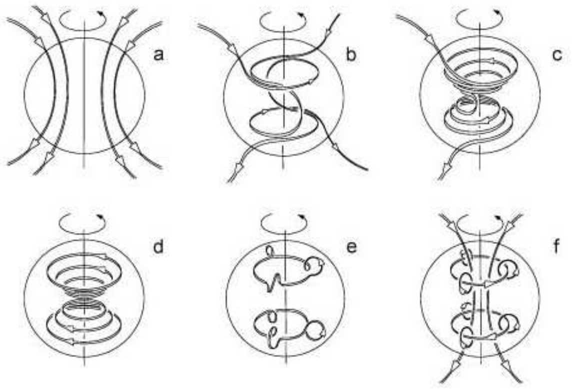

Figure 1.3: The principle of the $\alpha\Omega$-dynamo. Differential rotation (b and c) wraps the initially poloidal field (a) around the shear layer (Ω-effect) and a toroidal field emerges (d). Convective motions lift the field lines up (e) and Coriolis forces twist them (α-effect). The thus created loops merge into the original poloidal field (f). Note that the figure has actually been created for the Earth's geodynamo and is therefore missing the tachocline. From Love (1999).

The scenario of the $\alpha\Omega$-dynamo is in very good agreement with the sunspot cycle, which turns out to be actually a 22-year cycle of twice the 11-year cycle but with reversed polarity. Individual spots in larger sunspot groups agglomerate to a bipolar structure, and solar magnetograms show that they mark the two polarities of magnetic flux tubes from the solar interior, which are lifted by buoyancy forces until they break through the surface. This effect emerges more frequently during the later phases of the dynamo cycle when the solar magnetic field is in the more complex twisted toroidal configuration. Finally, this leads to periodically increasing and decreasing sunspot numbers in the course of the cycle. Both the occurrence of chromospheric prominences and coronal emission follow this behavior as well. Depending on the energy range, the solar coronal X-ray emission varies by a factor up to 100 from maximum to minimum sunspot numbers. Further observations that relate the solar activity cycle and the magnetic dynamo are summarized by Charbonneau (2010).

The origin of the $\alpha\Omega$-dynamo suggests a dependence of the overall level of activity on stellar rotation. Actually, Pallavicini et al. (1981) found a relationship between the projected surface rotational velocity $v \sin i$ and the X-ray luminosity $L_{\rm X}$, which however saturates at $L_{\rm X}/L_{\rm bol} \approx 10^{-3}$ for very fast rotators. Since young stars are well-known to rotate faster, the initial dependence between rotation and activity translates also into an age-activity relationship. Stellar rotation rates decrease due to angular momentum loss, e. g. in magnetized winds. This weakens the dynamo process so that finally stellar activity decreases with age.

The observation that stars with spectral types earlier than A7 do no longer show coronal X-ray emission is consistent with the absence of the tachocline in fully radiative stars, which prevents the generation and amplification of magnetic fields. However, the $\alpha\Omega$-dynamo must also fail in fully convective stars, but coronal X-ray emission is still at the saturation level at spectral types M3–M4. Turbulent dynamo mechanisms are expected to take over; however, this implicates weaker fields structured on smaller scales and a more uniform coverage of the stellar surface compared to the large-scale axisymmetric fields obtained for solar-like stars, which can concentrate in active regions with small filling factors. The different field strengths and geometries suggest a discontinuity in activity between solar-like and fully convective stars, which is not observed. The dynamo mechanism for fully convective stars must therefore be able to sustain the level of activity; probably the two mechanisms merge smoothly over several spectral subtypes. Recent models of fully convective stars confirmed that large-scale magnetic fields of the required strength can be actually be generated this way (Chabrier & Küker 2006; Dobler et al. 2006; Browning 2008).

1.2 Physics of stellar coronae

1.2.1 Coronal heating

Although the emission from chromosphere and corona comprises only a small fraction of the overall luminosity of active stars, a mechanism is needed that transports the energy from the interior to the outer atmospheric layers and heats them to the high temperatures observed. The magnetic fields generated by the dynamo mechanisms are essential in this context, it is however still a matter of debate what the relevant process for energy transfer and dissipation into the corona is. There are basically two different approaches to solve this issue, but both have their limitations.

Plasma waves are generated on the stellar surface by turbulent convective motions and propagate into the outer atmosphere. Such waves can be observed on the Sun using high time resolution. A variety of different wave modes exist, which may even transform into each other. Magneto-acoustic waves should be able to transport enough energy into the chromosphere but not into the corona. Alfvén waves can avoid this issue but should not be able to deposit enough energy in the coronal plasma.

Continuous reconnection in countless small magnetic loops emerging from the surface to the so-called magnetic carpet should lead to a constant level of so-called nanoflares, which release the magnetic energy stored in the carpet to heat the corona (Parker 1988; Cargill & Klimchuk 2004). Nanoflares are thought to be scaled-down versions of larger flares (see Sect.1.3 for details), their amplitude is so small that they cannot be individually resolved so far. From observations of the smallest microflares discernible on the Sun, it is however unclear if the expected rate of nanoflares will be sufficient to balance the energy output of the corona. It is thus possible that both plasma waves and nanoflares are needed to explain the overall level of heating in the corona. See Walsh & Ireland (2003) and Klimchuk (2006) for recent discussions.

1.2.2 X-ray emission from hot, thin plasmas

Solar and stellar coronae are characterized by extremely high temperatures in combination with very low densities. Hot plasmas cool efficiently by radiation, primarily in the form of emission lines of trace elements in higher ionization stages. Hydrogen and helium are completely ionized and can therefore no longer contribute. However, at the highest temperatures, continuum emission additionally starts to play a major role.

Ionization and excitation are induced by collisions, predominantly with free electrons, but also with protons and other nuclei. Photoionization and radiative excitation processes are usually neglected, the coronal plasma is typically assumed to be optically thin. Additionally, variations on short timescales are typically ignored so that equilibrium conditions can be assumed in order to describe the radiative properties. The ionization balance summarizes ionization and recombination processes for a certain element as a function of temperature. In order to obtain the level population of a certain ion, not only spontaneous emission but also further collisions have to be considered. See Mason & Fossi (1994) for a detailed discussion of the involved processes.

The line flux corresponding to the transition from the upper level j to the lower level i in a certain ion from element X can thus be predicted with

$$f_{ji} = \frac{1}{4\pi d^2}\, Ab(X) \int G(T)\, DEM(T)\, dT \qquad (1.1)$$

where $Ab(X)$ is the elemental abundance relative to solar photospheric values, $G(T)$ is the so-called line contribution function that includes the atomic physics, and $DEM(T)$ is the differential emission measure which describes the properties of the emitting plasma.

The line contribution function

$$G(T) = A_{ji}\, \frac{n_j(X^{Z+})}{n(X^{Z+})}\, \frac{n(X^{Z+})}{n(X)}\, \frac{n(X)}{n(H)}_{\odot}\, \frac{n(H)}{n_e}\, \frac{1}{n_e}$$

consists of several factors. $n_j(X^{Z+})/n(X^{Z+})$ is the level population, described by the fraction of the specific ion found in the excitation state j. It is determined from statistical equilibrium equations, taking into account the relevant excitation and de-excitation processes, ideally for all levels. $n(X^{Z+})/n(X)$ is the fraction of atoms from element X in the ionization stage $Z+$. $n(X)/n(H)$ is the abundance of element X relative to hydrogen. This can expressed as $n(X)/n(H) = Ab(X) \cdot n(X)/n(H)_{\odot}$, which allows to consider the predetermined solar value and the usually unknown factor $Ab(X)$ separately. $n(H)/n_e$ is the hydrogen abundance relative to the electron density, the so-called proton-to-electron ratio. Finally, A_{ji} is the Einstein coefficient for spontaneous emission of a photon from the transition $j \rightarrow i$. Further simplifications are often applied within the so-called coronal approximation: Since the bulk of electrons originates from hydrogen and helium which are completely ionized, $n(H)/n_e$ is usually set to a constant value of ≈ 0.83, but actually it has a weak dependence on temperature and abundances. Additionally, the radiative decay times as expressed by A_{ji} are approximated by collisional excitation rates from the ground state C_{gj}.

While $G(T)$ is unique for each spectral line, the differential emission measure

$$DEM(T) = n_e^2\, \frac{dV}{dT} \qquad (1.2)$$

is used to describe the temperature structure of the emitting material. The DEM itself has no descriptive physical meaning, but summarizes all relevant parameters like volumes and their shapes, density distributions, and filling factors in a single term. For the DEM, a large plasma volume with a low density and a smaller volume with a higher density are equal if both produce the same flux as function of temperature.

Integrating the DEM over a certain temperature range results in the volume emission measure

$$EM = \int DEM(T)\, dT = \int n_e^2\, dV \qquad (1.3)$$

In the isothermal approximation, the emission measure is averaged for a certain temperature, which reduces Eq. 1.1 to the contribution function integrated over temperature and constant coefficients.

Continuum emission from coronal plasmas consists of free-free emission, free-bound emission, and two-photon emission: Free-free emission, also called bremsstrahlung, results from the interaction of free electrons with protons or heavier ions, while free-bound emission arises from recombination processes. Two-photon emission is a process to depopulate metastable energy levels in low-density plasmas, which is otherwise accomplished by collisions. The contribution of these three processes varies considerably with temperature. At a plasma temperature of only a few MK, they are roughly equivalent, with each of them defining the shape of the continuum at certain wavelength ranges. At higher temperatures, bremsstrahlung starts to dominate the continuum emission. In analogy to Eq. 1.2.2, a continuum contribution function based on the three mechanisms can be defined which determines the continuum flux at a certain wavelength in combination with the DEM.

1.2.3 Loops and active regions

The left image of Fig. 1.4 shows typical views of the solar corona in two narrowband extreme ultraviolet filters centered on coronal emission lines from iron in different ionization stages. The image on the left uses Fe IX at a wavelength of 171 Å, which has a formation temperature ranging from 0.5 MK to 1 MK, to trace the upper transition region and cooler plasma in the quiescent corona, both of which show up as a diffusely glowing pattern relatively close to the solar surface. The major part of the emission is however concentrated in the so-called active regions. In a corresponding optical white light image, most of them would show up as photospheric sunspots, often surrounded by a bright, filamentary pattern of so-called faculae. In the corona, the dark spots turn into the bright footpoints of capillary loop-like structures that connect the two different parts of the sunspot group. Often such loops are also found to link different active regions or sunspot groups with each other. Like the sunspot groups, active regions are distributed inhomogeneously but within a preferred range of latitudes; their number varies strongly during the solar cycle.

Solar coronal loops can have very different configurations. They are observed in a broad range of different sizes, however, most of them have a height less than a quarter of the solar radius. Their composition seems to be randomly, but often they accumulate to bunches or form more complex structures like elongated arcades. The coronal plasma is

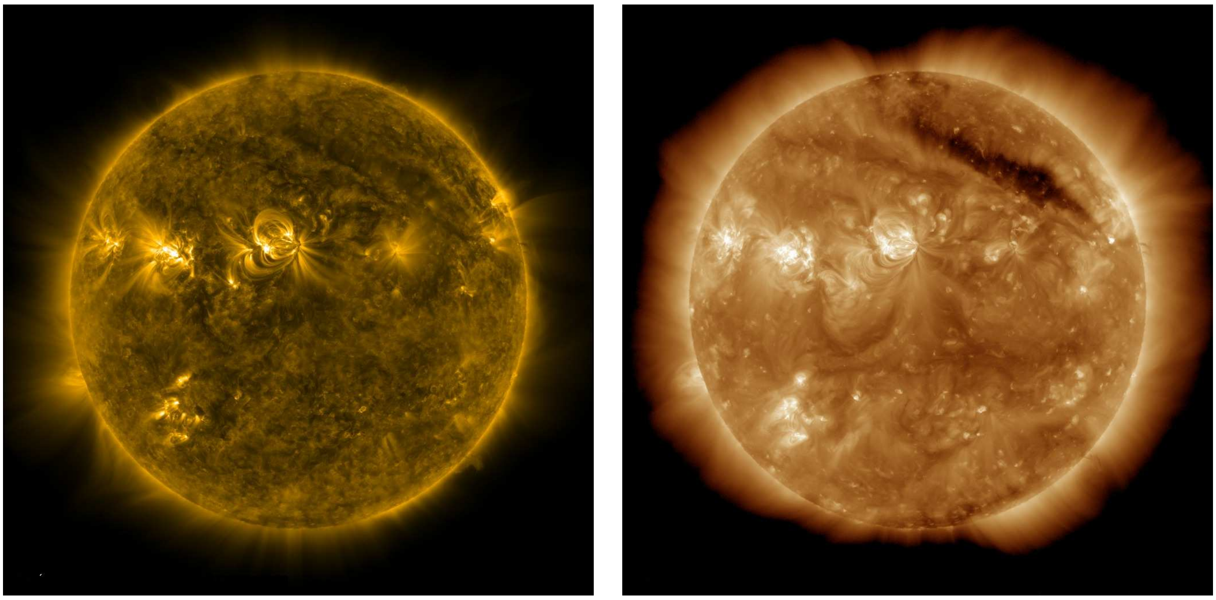

Figure 1.4: The solar corona on 30 July 2011 as observed by the Atmospheric Imaging Assembly (AIA) onboard the Solar Dynamics Observatory (SDO). Left: Active regions with loops and arcades observed at lower temperatures in Fe IX at 171 Å. Right: Streamers and coronal holes at higher temperatures in Fe XII and Fe XXIV around 193 Å. Image Credit: NASA/SDO and the AIA science teams

governed by this variety of closed-loop structures, which in turn visualize the magnetic flux tubes that break through the surface. Rosner et al. (1978) derived the basic parameters of a quasi-stationary loop model, assuming a hydrostatic equilibrium. They found that the temperature maximum within the loop is reached at the top, and that a simple relation exists between this loop top temperature, the pressure, and the loop length (see Eq. 8.12).

Long-term monitoring however easily shows that solar coronal loops can be very dynamic, even on timescales of only minutes or even seconds. Turbulent motions of the solar surface shift their footpoints, so that they have to rearrange their alignment. Obvious flows fill loops with fresh material, which later on may fall back to the surface. Changes in luminosity indicate effects of heating and cooling. See e. g. Aschwanden (2004) for a detailed discussion.

Refined versions of the scaling laws from Rosner et al. (1978) can be used to estimate the sizes of stellar coronal loops during flares (Reale et al. 1997; Reale 2007), and it turns out that they can be much larger than observed on the Sun, reaching up to several stellar radii. The large magnetosphere of a star can interact with other objects, so that e. g. in close binaries like RS CVn systems large coronal loops may form that connect the two stars with each other. In young stellar objects, similar loops may couple the star and its circumstellar disk (see also Fig. 1.5 f). Finally, even close-in planets may be influenced.

The right image of Fig. 1.4, taken almost simultaneously around 193 Å with the left one, covers both Fe XII and Fe XXIV with formation temperatures of ≈1.5 MK and ≈20 MK respectively, and therefore illustrates the normal corona and additionally hot flare plasma in the active regions. A halo of coronal plasma with a radial, but nonuniform structure emerges, very similar to the one observed in the optical during a solar eclipse. The plasma streams seem to be concentrated close to the loops and arcades of active regions, forming so-called helmet streamers. Their counterparts, the so-called coronal holes, are visible as X-ray dark patches. These open or large-dimensional magnetic field structures are the origin of the solar wind. The slow component of the solar wind emanates from the coronal streamers, while its fast component emerges from coronal holes.

1.3 Flares

X-ray and extreme ultraviolet images of the Sun as shown in Fig. 1.4 are available from space with very good spatial resolution; currently the Solar Dynamics Observatory (SDO) generates stunning views of the solar corona in a fast sequence. Active regions on the Sun are regularly caught during flares, coronal explosions that set free large amounts of energy. The resulting brightenings can not only be observed at high energies, but also in Hα and other chromospheric emission lines or in radio emission. White light flares on the Sun, which additionally affect the photosphere, are however very rare.

A comparison of images of a flaring region before and after the event shows that the loop geometry changes during the flare. The central element of a flare is therefore a process which rearranges the magnetic field, the so-called magnetic reconnection. The magnetic field changes to a lower-energy configuration, and the excess energy is deposited in the newly formed structures on the shortest timescales. This and the course of events that follow the reconnection itself demonstrates not only that flares are highly dynamic phenomena, but also that equilibrium conditions as they are assumed in Sect. 1.2.2 are not necessarily appropriate to calculate the emission of the cooling flare plasma.

The energy release of the magnetic reconnection event drives the acceleration of charged particles, mainly electrons, that radiate in radio gyrosynchrotron emission as they spiral down along the reconnecting field lines. Nonthermal hard X-rays are generated at the footpoints when the nonthermal electrons hit the thick, cool material of the lower atmospheric layers. The chromosphere and – depending on the size of the flare – also the photosphere is strongly heated by the impact of these particles. They immediately start cooling by radiation, both in the optical and UV continuum as well as in chromospheric and transition region emission lines. The newly formed coronal loops fill with evaporated hot material from the chromosphere, which subsequently cools down by soft X-ray emission. The strong X-ray and UV radiation field finally induces further chromospheric emission. The flare thus affects the whole stellar atmosphere, and the different aspects of its aftermath can be observed in various wavelength bands. See Benz & Güdel (2010) for a detailed discussion of the flare process.

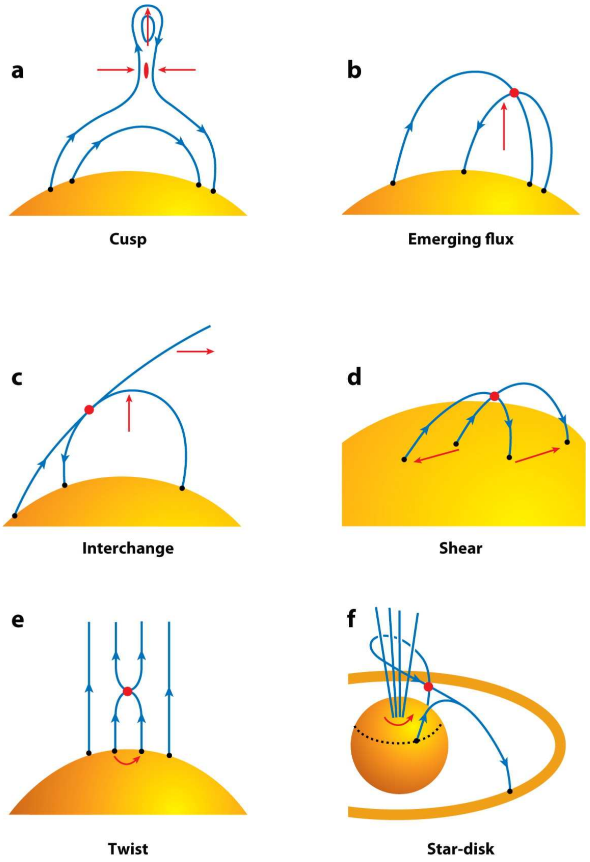

Figure 1.5: Different scenarios for magnetic reconnection events. (a) Reconnection below a rising loop, resulting in a cusp-shaped configuration. See Fig. 1.6 for details. An emerging flux tube can collide with another loop (b) or with open field lines (c). Footpoint motions shear two existing loops (d) or twists the field lines in open or large-scale structures (e). Different rotation rates wind up fields connecting a young star and its circumstellar disk (f). From Benz & Güdel (2010)

Magnetic reconnection can occur in various field configurations. The “standard model”, as it is illustrated in Figs. 1.5 a and 1.6 starts with an expanding loop or erupting prominence. The rising loop also takes surrounding field lines along upwards. A constriction forms below the loop, where finally reconnection takes place. This reduces the retention forces on the loop, which can expand further or erupt in a coronal mass ejection. The reconnected field lines form a cusp-like structure and finally the smaller flaring loops below the original loop. See also Hirayama (1974) for an illustration of the temporal evolution. Further scenarios involve e. g. emerging flux tubes that form new, expanding loops that clash into other, previously existing loops or open magnetic field lines, see Fig. 1.5 b and c. Relative footpoint motions as shown in Fig. 1.5 d and e can both accumulate large amounts of magnetic energy in sheared loops or twist adjacent field lines in larger loop structures or open field configurations leading to small flare events. Geometries involving star-disk interaction or multiple bodies are beyond the scope of this work.

Flaring loop structures can have very different sizes. The smallest nano and microflares do not only have small amplitudes but affect also only very small spatial scales and therefore easily go unnoticed within larger structures. However, even the dimensions of stronger flares can range from compact single loops to arcades that cover a large area. The emergence of flaring arcades, which are also called two-ribbon flares because of the two bright bands in Hα formed by their footpoints, is a chain reaction that can occur e. g. in the scenario of footpoint motions, when an already existing arcade-like

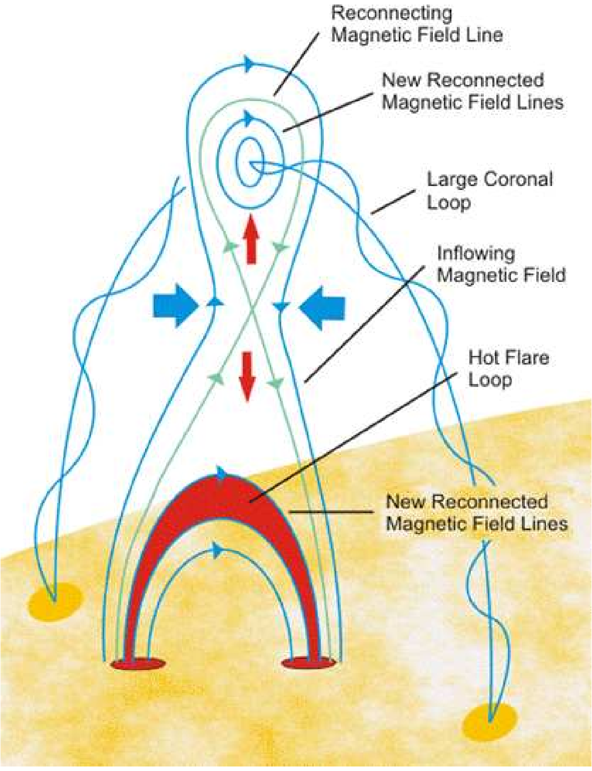

Figure 1.6: Schematic view of a reconnection event below a rising loop in two dimensions. Reconnection reduces the stress on the rising loop, which may result in a coronal mass ejection. Smaller flaring loops form below and perpendicular to the original loop. Image Credit: Gordon Holman (RHESSI Science Nuggets), after Shibata et al. (1995)

structure is distorted and starts to reconnect. Arcades can also be formed in a series of cusps along a larger eruptive prominence.

Flares on other stars can – with the exception of eclipse mapping techniques – not be spatially resolved. It can however be assumed that processes very similar to those observed on the Sun are responsible for them. Lightcurves and spectra provide information about the temporal evolution of the properties in the flare plasma, which indicate the same complex behavior with rapidly changing physical conditions in the stellar atmosphere. Nevertheless, the strongest stellar flares exceed those known from the Sun by orders of magnitude, so the question arises if these events can actually be described as scaled up versions of solar flares.

1.4 Outline

In this thesis, I present several projects in the field of stellar activity I have been working on during the last few years. Chapter 2 gives an account of the Benchmark Exercises for X-ray Spectroscopy Testing and presents the results I obtained in the course of this systematic cross-check of analysis methods for stellar coronal plasmas. Chapter 3 deals with the comparably inactive, solar-like binary system α Centauri, and in particular with its coronal neon-to-oxygen abundance ratio in the context of measurements from much more active stars. These studies have been continued by Robrade et al. (2008) later on. The analysis of the coronal properties of the M dwarf binary EQ Peg and other M dwarfs observed with *Chandra*'s High Energy Transmission Grating Spectrometer is contained in Chapter 4. Using these and other results, Wood & Linsky (2010) found a dependence of the so-called First Ionization Potential (FIP) effect on spectral type for moderately active stars.

The following chapters focus on multiwavelength observations of the intermediately active M dwarf CN Leo. Chapter 5 describes the first simultaneous X-ray and optical observations of this star with *XMM-Newton* and with the UVES spectrograph at the Very Large Telescope (VLT). Chapter 6 describes the analysis and modeling of the impulsive phase of a giant flare. While Chapter 7 discusses the impact of this flare on the lower atmospheric layers, Chapter 8 documents the evolution and properties of the coronal flare plasma. Finally, Chapter 9 gives a summary and an outlook.

Several of these projects have been conducted in close collaboration with others and with alternating leadership. I therefore explicitly point out my contribution or those of others to the work done at the beginning of each chapter. This thesis includes only those projects I contributed to in a major way. There are however also minor contributions to other projects which I list here in short: Günther et al. (2006) analyzed the *Chandra* HETGS spectrum of the classical T Tauri star V4046 Sagittarii with the focus on accretion signatures. I performed the data reduction and line flux measurements. Stelzer et al. (2006) observed a giant flare on the late M dwarf LP 412-31 with *XMM-Newton*. I performed the analysis of the corresponding Reflection Grating Spectrometer data, which however did not enter the final publication. Reiners et al. (2007) investigated the variability of the magnetic flux observed on CN Leo. I carried out the data reduction of the underlying optical spectra.

2 The BEXST challenge

The idea of the Benchmark Exercises for stellar X-ray Spectroscopy Testing, in short BEXST, was born during the splinter session on the future of stellar X-ray spectroscopy at the 13th Cool Star Workshop (Maggio et al. 2005a). Its concept has been worked out and presented at several occasions (e. g. Maggio et al. 2005b; Maggio 2006). Several groups, including David Huenemoerder, Jorge Sanz Forcada, Anton Raassen, Raanan Nordon, Jan-Uwe Ness, Costanza Argiroffi, Luigi Scelsi, and myself participated in the 1st and so far only exercise, worked out by Carole Jordan and Salvatore Orlando. Antonio Maggio collected and presented the results at the X-ray Grating Spectroscopy Workshop; the conclusions have not yet been published elsewhere.

Abstract

How reliable are reconstructions of emission measure distributions, or values of abundances and densities obtained for stellar coronae? A number of analysis methods with different approaches have been developed, based on different atomic databases and with varying levels of complexity. Given the fact that different methods often provide divergent results, the questions arise what limits the accuracy of the current approaches, to what level they are compatible and finally, how accurately they are actually able to reproduce the complex physical conditions in coronal plasmas. In order to address this issue, the BEXST challenge has been set up. Synthetic spectra, created from a predetermined but undisclosed set of input data and reduced to a certain level of spectral resolution and signal to noise, should be analyzed by the participants with the goal to recover the specified temperature structure, densities, and abundances. The results of the one and only such exercise that has been carried out were sobering to a certain degree, but did not come unexpectedly. None of the applied methods was able to reproduce the details of the shape of the input emission measure distribution, with each of the six approaches used leading to a different result. However, the resulting densities and abundances proved to be surprisingsly well-defined. The lesson to learn from the challenge is therefore that the reconstruction of emission measure distributions is easily affected not only by measurement uncertainties but also by the constraints and boundary conditions introduced by the analysis methods, and that it is therefore unlikely to recover the true detailed structure. Parameters like abundances and densities can be deduced, but the uncertainties are much larger than usually claimed, and the sources of systematic deviations have to be identified.

2.1 Introduction

The basic techniques to investigate the properties of stellar coronal plasmas have been developed for the Sun already decades ago when solar coronal physics was still in its infancy. With the launch of the first non-imaging X-ray spectrometers in the 1960s, the need for appropriate diagnostics of the coronal plasma arose when the overall structure of the corona and the mechanisms responsible for its X-ray emission were completely unknown.

With the lack of spatial resolution, Pottasch (1963) developed the concept of the emission measure to link the flux observed in individual emission lines that are known to form at a certain temperature with a model of the emitting plasma. In principle, the emission measure denotes the amount of material at different temperatures that can produce the measured fluxes, mathematically it is defined as the product of the electron and ion densities integrated over the emitting volume. The modeling therefore comprises on the one hand the atomic physics of a coronal plasma and on the other hand its inherent properties, see also Sect. 1.2.2. The latter also includes the elemental abundances, and already early estimates suggested that the composition of the solar corona differs considerably from that of the photosphere, with elements with a low first ionization potential (FIP) being strongly enhanced. This is the so-called FIP effect (see e. g. Feldman & Laming 2000). In addition to plasma temperatures and densities, abundance determinations thus became an additional objective of coronal diagnostics, which already suffered from many unknowns. At last, Gabriel & Jordan (1969) investigated the theory of line formation in He-like triplets and thus were able to introduce a method to determine the electron density of the emitting plasma from the ratio of the forbidden and intercombination lines.

Today, solar physicists are able to apply these methods to individual structures like active regions and coronal holes, and the solar corona has revealed an incredible level of complexity: Magnetic fields form inhomogeneous spatial structures like loops and arcades, which come in a wide range of sizes and are able to change their appearance on the shortest timescales. Different structures show not only different temperature and density distributions but also variable abundances. Large amounts of energy are set free during flares; such events disturb the sensitive equilibrium state of the plasma and require to expand the modeling to interaction with other atmospheric layers as well as more sophisticated modeling assumptions.

Meanwhile, stellar coronae have proved to be ubiquitous (Schmitt 1997; Schmitt & Liefke 2004), with the Sun typically at the moderate end of a broad distribution of properties. It seemed that diagnostics developed for the solar corona, e. g. loop models, could successfully be transferred to stellar coronae; nevertheless, the question is of course to what extend this practice is actually appropriate without further insight into the processes responsible for stellar coronal X-ray emission (Klimchuk 2002).

The high-resolution grating spectrometers onboard *Chandra* and *XMM-Newton* raised the hope that not only the properties of stellar coronal plasmas could be inferred with greater detail, like e. g. variations of elemental abundances with plasma temperature and therefore separate diagnostics of plasma contained in the quiescent corona and in active regions, but also that in-depth studies of the underlying physical processes, e. g. heating mechanisms, would become possible for stellar coronae. It seems however, that coronal diagnostics already get stuck when it comes to the definition of emission measure distributions over temperature or the specification of averaged sets of abundances and electron densities, as different groups applying different analysis methods continuously arrive at contradicting results.

Up to some point, this is however inherent in the nature of the modeling approaches and reconstruction techniques, which are, especially in the case of the emission measure, non-unique (Craig & Brown 1976; Craig 1977). Additionally, initial conditions are often needed to arrive at a final result, and the validity of these assumptions must not necessarily be given (Kashyap & Drake 1998; McIntosh et al. 2000). One of the main goals therefore must be to identify the intrinsic limitations of the available methods and to discuss their constraints and where simplifications are appropriate, e. g. when it comes to small-scale structures or inhomogeneities of the elemental abundances (Judge 2002). Additionally, further improvement may be achieved with more sophisticated theoretical models of coronal plasmas or with the implementation of more complex atomic physics.

These issues are well-known and therefore a matter of continuous discussion among the involved scientists. A lively discussion on where the current problems are and how they can be tackled has been held at the splinter session “What future for stellar X-ray spectroscopy?” at the 13th Cambridge Workshop on Cool Stars, Stellar Systems and the Sun in July 2004 (Maggio et al. 2005a). One of the main conclusions was that the community should face the challenge of a rigorous test of the analysis methods currently in use in order to compare their results, to determine their true uncertainties, and to spot and discuss their limitations. The testing should

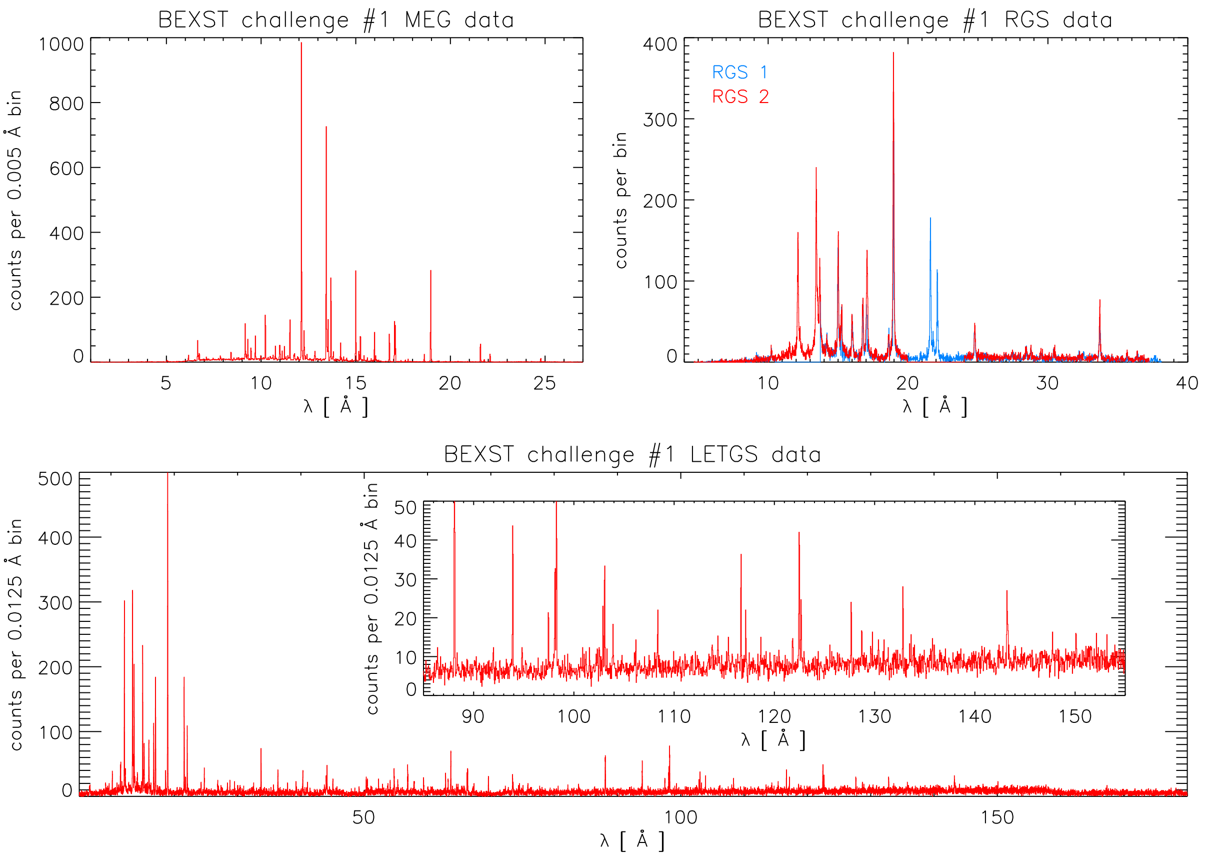

Figure 2.1: Non-background subtracted grating spectra created from the BEXST challenge #1 data sets. Top: *Chandra* HETGS MEG data (left) and *XMM-Newton* RGS1 and RGS2 data (right). Bottom: *Chandra* LETGS data; the inset shows a zoom into the wavelength range from 85 Å to 155 Å where the unusual lines from low ionization stages are located.

be realized as a “hare and hounds” exercise where the participants analyze synthetic spectra based on model parameters unknown to them but with the goal of recovering the properties of this underlying model.

In the following, Antonio Maggio, Savatore Orlando, Jeremy Drake, Fabio Favata, Manuel Güdel, and Carole Jordan joined forces to devise a reasonable physical model and create the resulting spectra. The test, termed Benchmark Exercises for stellar X-ray Spectroscopy Testing or BEXST, was officially announced at several occasions in 2005 and 2006, (e. g. Maggio et al. 2005b; Maggio 2006). A number of teams formed and agreed to take part, including David Huenemoerder, Jorge Sanz Forcada, Anton Raassen, Raanan Nordon, Jan-Uwe Ness, Costanza Argiroffi, Luigi Scelsi, and myself.

Further progress in the analysis of stellar coronae based on refined theoretical models of the physical processes in stellar coronae can only be made if the plausibility of the results and deductions is assured. BEXST is a systematical approach to assess the level of reliability of the analysis methods presently used in stellar X-ray spectroscopy. The involvement of the whole community and its general nature, but also its rigor and directness make it a unique effort.

2.2 The input data

By the end of November 2006, the final data sets for challenge #1 were available. The participants could choose among *XMM-Newton* RGS and *Chandra* HETGS and LETGS data. All data sets consisted of precompiled pulse height amplitude files for source and background as well as corresponding response matrices; spatial information and time stamps for individual photons have not been generated. Medium resolution CCD spectra that usually would accompany such data sets, i.e. originating from the *XMM-Newton* EPIC PN and MOS instruments or the *Chandra* ACIS-S 0th order image, were also not provided.

On inquiry, Antonio Maggio confirmed that all data sets are meant to be created from the same

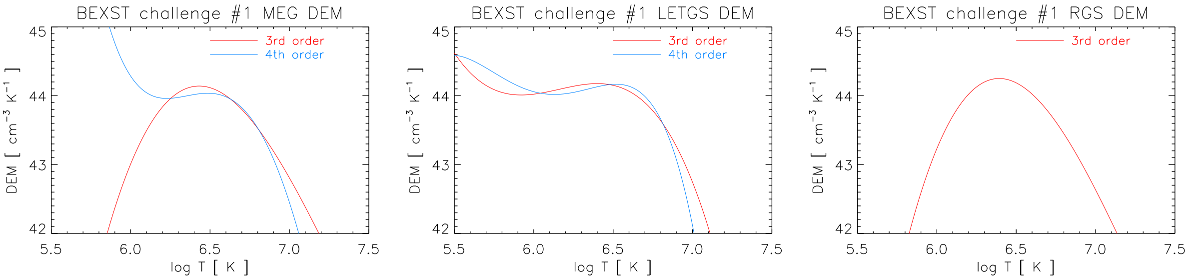

Figure 2.2: Differential emission measures obtained for the *Chandra* MEG (left) and LETGS (center) spectra, as well as for the RGS data (right). Note that the DEMs reconstructed from the MEG and RGS spectra are not constrained for temperatures less than 1.5 MK.

source, but that it should however be avoided to do a combined analysis. Apart from small modifications necessary to take into account deviations from regular file formatting, the data were processed using the same reduction routines and parameter sets I usually apply to real data. The resulting spectra (cf. Fig. 2.1) illustrate that the data sets have been generated with a very good data quality, i. e. with several tens of thousands of source counts and a low background level. The resulting signal-to-noise-ratios are comparable to those obtained from the very best real data sets available, and would therefore outstand the quality of a typical data set obtained from a coronal X-ray source by far.

The RGS data provide 1st order spectra from both RGS1 and RGS2 in the current setup; this includes the malfunctioning CCDs in each detector system, resulting in gaps between 10.50 Å to 13.73 Å and 19.98 Å to 24.03 Å in the RGS1 and RGS2 spectra respectively. The strongest lines originate from Ne IX, Ne X, O VII, and O VIII. The continuum level is rather low; the bulk of the continuum emission can be attributed to pseudo-continuum from weak, broadened emission lines. The simulated source therefore seems to be comparably cool.

In the *Chandra* HETGS data, the pseudo-continuum is largely resolved, although the data include only the first order spectra from the two grating arms of the MEG, but not of the HEG. The highly ionized iron lines in the wavelength range from 9 Å to 13 Å are rather weak, which is another indicator that the contribution of hot plasma to the source spectrum is small.

Additionally, a number of lines from elements in rather unusual ionisation stages show up in the long wavelength range of the *Chandra* LETGS spectrum. This includes O VI at 150.1 Å, Ne V at 143.2 Å, Ne VI at 122.5 Å, 122.8 Å and 147.8 Å, Ne VII at 97.5 Å, 116.7 Å and 127.7 Å as well as Ne VIII at 88.1 Å, 98.1 Å, 98.3 Å, 102.9 Å and 103.1 Å. Their formation temperatures are so low (with $T_{\rm Max}$ ranging from typically 300 000 K to 650 000 K, but their line contibution functions show extended wings up to a few MK) that they are not observed in the coronae of highly active stars, where the emission measure distribution is dominated by plasma in the temperature range of several MK and the ionization balance has shifted to higher ionization stages. The Fe IX line at 171.1 Å on the other hand, that is often prominent in the X-ray spectra of stars with contributions from low-temperature plasma and especially in the Sun, was not detected.

2.3 Analysis methods and results

I proceeded with the data sets as I would have done with any real X-ray spectra, i. e. I used the same software tools and applied the same analysis methods. Line fluxes have been measured with the CORA program (Ness & Wichmann 2002), using Moffat line profiles, i. e. modified Lorentzians given by

$$I(\lambda) = I_{max} \left(1 + \left(\frac{\lambda - \lambda_0}{\Delta\lambda/2}\right)^2\right)^{-\beta} \tag{2.1}$$

with $\beta = 2.5$ and a fixed FWHM of $\Delta\lambda = 0.02$Å and $\Delta\lambda = 0.055$Å for the MEG and the LETGS spectra respectively and a regular Lorentzian line profile ($\beta = 1$) for the RGS data. In order to reconstruct the emission measure distribution the synthesized spectra are based on, I used a procedure that first calculates the differential emission measure (Eq. 1.2) from temperature-sensitive line ratios and subsequently yields the elemental abundances of the plasma. To verify the results, and especially the abundance values, I used two additional approaches: I computed simple isothermal models and I applied a method that makes use of optimized linear combinations of line fluxes to calculate emission measure-independent abundance ratios. Densities have been determined for different temperatures from the ratios of forbidden and intercombination lines in helium-like triplets.

2.3.1 Fitting the differential emission measure

The DEM fitting procedure has originally been developed in the course of my diploma thesis (Liefke 2005). In its original implementation, it included two methods to approximate the shape of the differential emission measure in a certain temperature range with simple polynomials

$$\log DEM(\log T) = \sum_{i=0}^{N} a_i (\log T)^i \tag{2.2}$$

The first approach minimizes the difference between the measured ratios r_{mes} of H-like Lyman α and He-like resonance line fluxes (f_{H} and f_{He}) from the same element and their theoretical values

$$r_{\text{theo}} = \frac{\int G_{\text{H}}(\log T) \cdot T \cdot DEM(\log T)\, d\log T}{\int G_{\text{He}}(\log T) \cdot T \cdot DEM(\log T)\, d\log T}$$

based on the line contribution functions and the DEM in order to recover the latter as a function of temperature and independently from elemental abundances. This approach is very similar to the one elaborated by Schmitt & Ness (2004). Differing from Schmitt & Ness, I have abandoned the use of Chebyshev polynomials and thereby simplified the numerical implementation. The second approach uses line fluxes from a single element but many ionization stages and formation temeratures, and computes the DEM from their line contribution functions directly. Practically, this method can only be applied to iron, other elements do not provide enough strong lines from different ioniziation stages in the spectral range covered by the instruments available. The normalization of the DEM is obtained from continuum flux measurements in both cases.

In Liefke (2005), I found that the stability of the iron line approach depends strongly on the individual lines included, and due to the narrow shape of line contribution functions of lines in ionization stages that are neither hydrogen-like nor a noble gas configuration, also on the number of ionization stages covered. I therefore usually prefer the usage of the ratios of H-like Lyman α and He-like resonance lines. However, the fitting routine was later on expanded to include also other ratios of lines from two different ionization stages of the same element in order to cover the largest temperature range possible with the available line flux measurements. Additionally, the possibility to set artificial constraints on the shape of the DEM (zero points and gradients) has been included.

Depending on the quality of the data and on the number of line ratios available, it is appropriate to fit the DEM with polynomials of 3rd to 6th degree, and usually it is convenient to apply Occam's razor and choose a lower-order polynomial when the quality of the fit does not significantly improve for the higher-order one. Although the signal-to-noise ratio of all three data sets was excellent, the corresponding DEM fits were rather poor whatever polynomial degree was used. The best-fit χ^2_{red} values were 6.0 for the MEG and 12.9 for the LETGS spectrum, both obtained with a 4th order polynomial, as well as 4.1 for the RGS spectra with a 3rd order polynomial; their shapes are shown in Fig. 2.2. Note that the lines contained in the MEG and RGS spectra cover only the higher temperatures from about 1.5 MK to 10 MK, while the long-wavelength lines mentioned above could enter the analysis of the LETGS data, which enlarges the temperature range to temperatures lower than 1 MK.

All three datasets agree to show a maximum at $\approx$ 4 MK in the DEM. The contribution from temperatures up to 10 MK is low, and neglible for even higher temperatures. While both the MEG and RGS data are confined to higher temperatures, i. e. the reconstructed DEM is no longer constrained for temperatures below 1.5 MK, the LETGS data allow to go to temperatures as low as 500 000 K. For the lowest temperatures, the reconstructed DEM even exceeds the peak at higher temperatures, which would however require either a continuous transition from chromospheric to coronal temperatures in a large volume or a strongly enhanced density on smaller scales; both scenarios are inconsistent with transition region models.

The difficulty to obtain a good and realistic fit indicates systematic problems, such as incompatibilities of the atomic data. The fitting routine could at that time only adopt Chianti 5 (Dere et al. 1997; Landi et al. 2006), while it was known to the participants that APED (Smith et al. 2001b) was used to create the synthesized spectra.

2.3.2 Abundance determination from the reconstructed DEM

Both the shape of the DEM and its normalization have been calculated independently from the elemental abundances. Their values can therefore easily be inferred from the ratio of the line fluxes predicted by the DEM and the measured ones according to Eq. 1.1. Table 2.1 lists the obtained values for the three datasets and their best-fit polynomials. Note that the given uncertainties are 1σ errors based on the line flux measurements. Additional errors of $\approx$12%, 6%, and 5% have to be added to the MEG, LETGS, and RGS data respectively as a

Table 2.1: Elemental abundances of the BEXST challenge #1 test plasma relative to the solar photospheric values from Asplund et al. (2005) as determined from the 4th order polynomial fits of the DEM for the MEG and LETGS data and from the 3rd order polynomial for the RGS data.

	Absolute abundance values from		
Element	MEG	LETGS	RGS
C	—	0.37±0.05	0.40±0.03
N	0.65±0.07	0.41±0.04	0.47±0.02
O	0.65±0.02	0.45±0.06	0.46±0.01
Ne	4.03±0.17	1.33±0.25	2.46±0.08
Mg	0.47±0.04	0.41±0.06	0.17±0.03
Si	0.67±0.04	0.72±0.42	—
S	1.73±0.38	—	—
Fe	0.45±0.04	0.32±0.02	0.38±0.05

result of the continuum normalization. Uncertainties in the shape of the DEM have not been taken into account. The errors are therefore clearly underestimated.

Apart from neon which is clearly enhanced, the elemental abundances tend to lie in the range of 0.4–0.7 times the values in the solar photosphere according to Asplund et al. (2005). No trends, e. g. with first ionization potential, could be discerned.

2.3.3 Abundance ratios from emission measure-independent linear combinations of line fluxes

A very simple approach to derive abundance ratios independently from the emission measure distribution of the emitting plasma is to search for emission lines from two elements in different ionization stages where a linear combination of the line contribution functions from the first element equals another linear combination of contribution functions from the second element. The dependence on the plasma temperature therefore reduces to the temperature residuals of the ratio of the two linear combinations, and the abundance ratio can be determined from the linear combinations of the measured line fluxes. Due to the broad temperature range covered by their line contribution functions, the H-like Lyman α and He-like resonance lines of two elements with neighboring atomic numbers are perfectly suited for this approach, leading to the abundance ratios N/C, O/N, Ne/O, Mg/Ne, Si/Mg, and S/Si. Abundance ratios including iron can be determined with neon and magnesium. The method is described in detail in Sections 3.3.2 and 4.4.3.

The abundance ratios determined this way agree reasonably well with ratios that could be computed from Table 2.1. It is obvious that Ne/O is enhanced, while the ratios that do not include neon are close to 1.

Table 2.2: Emission measure-independent abundance ratios of the BEXST challenge #1 test plasma relative to the solar photospheric values from Asplund et al. (2005) as determined from linear combinations of measured line fluxes.

Ratio	MEG	LETGS	RGS
N/C	—	1.22±0.17	—
O/N	—	1.24±0.12	0.95±0.06
Ne/O	7.03±0.24	6.78±0.23	4.87±0.27
Mg/Ne	0.12±0.01	—	—
Si/Mg	1.59±0.15	—	—
Ne/Fe	11.63±0.25	11.99±0.34	10.46±0.44
Mg/Fe	1.02±0.05	—	—

2.3.4 Cross-check with isothermal models

In order to provide an additional cross-check also for the absolute values of the abundances, I used XSPEC (Arnaud 1996) to fit the spectra with isothermal models based on the APEC code (Smith et al. 2001a) with three temperature components. For these models, the abundances of helium, aluminium, calcium, and nickel have been fixed at solar photospheric values, while argon has been coupled to neon. All the other elements have been were free to vary, with the exception of carbon for the MEG fit. The three isothermal components converge to rather cool values compared to the coronae of typical active stars, with $kT_1 \approx 0.2$ keV, $kT_2 \approx 0.4$ keV, and $kT_3 \approx 1.0$ keV. The two cooler components dominated the plasma, with the emission measure of the third component an order of magnitude lower than the sum of first two. The abundance values were in good agreement to those obtained with with the DEM fitting technique.

2.3.5 Densities from He-like triplets

Emission-line based density diagnostics of a coronal plasma can be performed with the forbidden (f) and intercombination (i) lines of He-like triplets. Measured line fluxes from these lines can be converted to electron densities n_e using

$$\frac{f}{i} = \frac{R_0}{1 + n_e/N_c} \tag{2.3}$$

where R_0 is the low-density limit and N_c the critical density. These two parameters vary for each

Table 2.3: Electron densities $\log n_e$ for the BEXST challenge #1 test plasma determined from the f/i ratio of He-like triplets.

Ion	log T	MEG	LETGS	RGS 1	RGS 2
C V	6.0	—	$9.57^{+0.52}_{-0.28}$	—	—
N VI	6.15	—	$9.66^{+0.47}_{-0.52}$	9.72±0.41	low-density limit
O VII	6.3	$9.99^{+0.25}_{-0.36}$	< 9.77	low-density limit	—
Ne IX	6.6	$11.18^{+0.10}_{-0.11}$	low-density limit	—	$11.22^{+0.18}_{-0.24}$
Mg XI	6.8	low-density limit	—	—	—
Si XIII	6.95	$13.27^{+0.21}_{-0.25}$	—	—	—

triplet, the values used here have been taken from Ness et al. (2002a). Since the formation temperatures of the He-like triplet lines increase with atomic number, each triplet traces the density at a certain plasma temperature interval. Table 2.3 lists the He-like triplets covered by the three datasets, their peak formation temperatures, and the densities inferred from the measured line fluxes of the f and i lines.

Unfortunately, the determination of the densities is not straightforward. The silicon and magnesium triplets are only barely resolved in *Chandra* LETGS and *XMM-Newton* RGS data. Additionally, the effective area of all three instruments shows steep increases at the wavelenghts of the Si XIII triplet lines, which distorts their flux measurements. Furthermore, due to their high formation temperature, silicon lines are weak in general in the BEXST spectra with their relatively cool plasma distribution. Testa et al. (2004) showed that the lines of the Mg XI triplet are often blended with higher-order Ne X lines. Due to the high neon abundances obtained for the test plasma, this is a serious problem especially for the LETGS and RGS datasets, where the spectral resolution is too low to determine the flux contamination properly. Measurements for these two high-temperature triplets are therefore only possible in the MEG spectra. The Ne IX triplet on the other hand, which is often severely affected by highly ionized iron in the coronae of active stars (Ness et al. 2003b), is rather clean; the line fluxes can be measured directly in all three datasets. The oxygen and nitrogen triplets cover lower temperatures, they are not affected by blends. The LETGS is the only instrument that covers the C V triplet. Unfortunately, the C V lines are blended with the third order of the Ne IX triplet. The neon contribution could be scaled and subtracted in order to obtain carbon line fluxes that are more reliable.

Apart from neon and silicon, the f/i ratios yield densities $\log n_e$ close to 10, or within the low-density limit. As mentioned above, the Si XIII triplet is probably systematically biased.

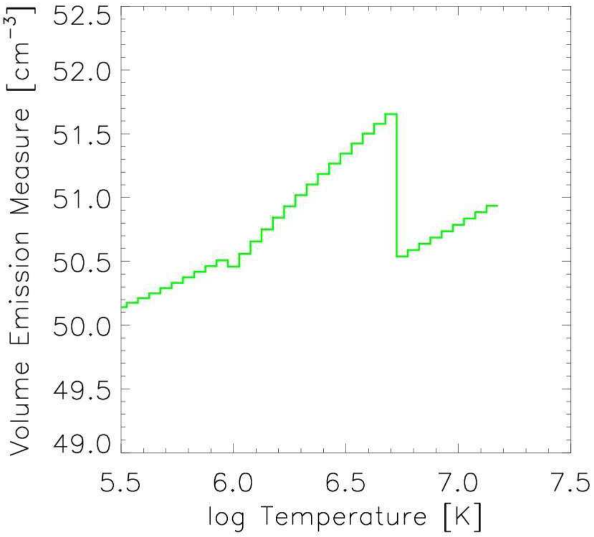

Figure 2.3: The emission measure distribution of the input model as constructed by Carole Jordan. Its two main components resemble the quiescent and flaring corona of a solar-like star, realized by two power laws with cutoffs. Figure courtesy of Antonio Maggio.

2.4 The solution

Antonio Maggio revealed the structure of the model emission measure distribution and the sets of abundances and densities used to create the synthetic spectra at the X-ray grating spectroscopy meeting in July 2007 and also presented the results of the challenge. Additionally, most of the participants of the challenge came together at this meeting and discussed its outcome and the resulting implications for their work.

The structure of the emission measure distribution is shown in Fig. 2.3. It is composed of three powerlaws, resulting in straight lines on the logarithmic scale. The first component with its slight increase in emission measure at low temperatures is responsible for the occurrence of the low-temperature lines, but it is only subsidiary to the

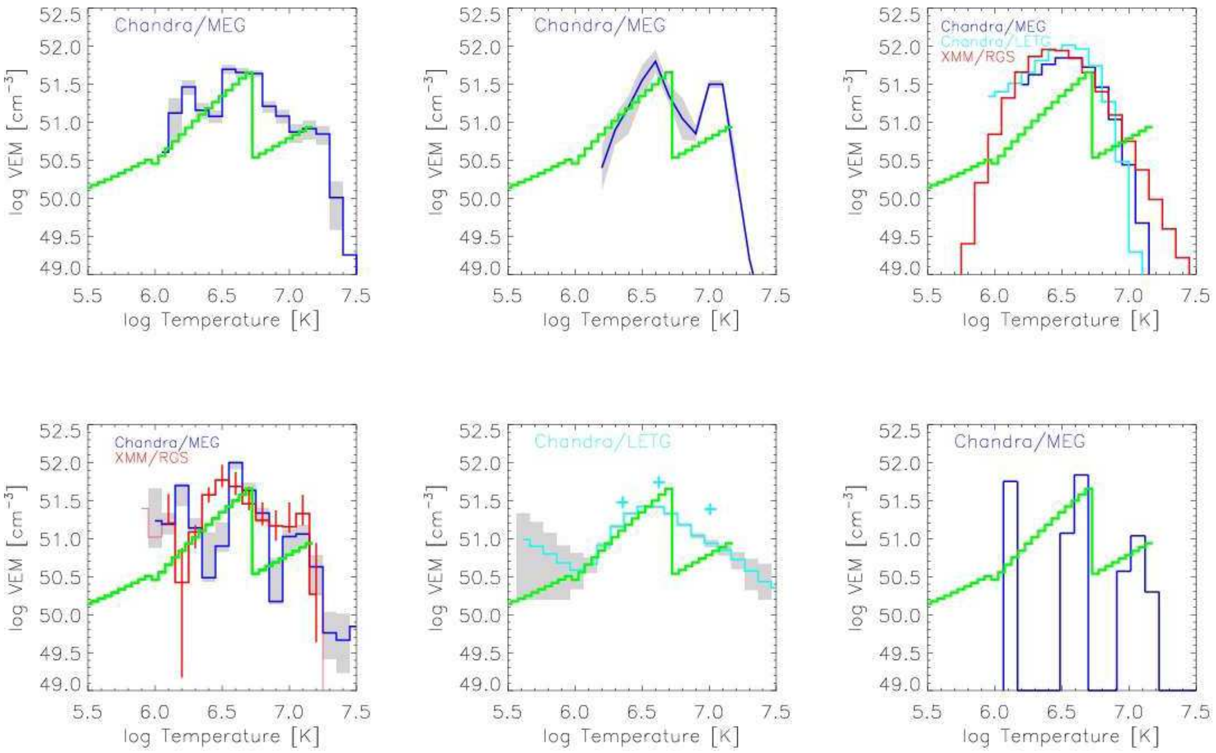

Figure 2.4: The best-fit emission measure distributions from the six groups participating in the BEXST challenge. My results are shown in the upper right panel. Figure courtesy of Antonio Maggio.

steeper second and third components, which are meant to depict the quiescent and flaring corona of a solar-like star. The powerlaws end in a cutoff, resulting in a sudden drop in the emission measure by more than an order of magnitude at $\log T = 6.7$ that divides the two main components, and a final cutoff at $\log T = 7.15$.

Albeit its simplicity, the emission measure distribution poses a serious problem for my DEM fitting routine. An approximation of its shape with any smooth continuous mathemathical function, especially with lower-grade polynomials, must fail to reproduce extreme discontinuities like the steep drop and the cutoff. Although the corona of a real star will probably be composed of several components representing different levels of activity, with coronal holes and active regions, and therefore show an emission measure distribution integrated over the complete surface with a smoother shape, emission measure distributions with such discontinuities can in principle occur in nature. My fitting routine will not be able to reconstruct their shapes until high-order polynomials are used, but this will usually exceed the number of available degrees of freedom. Lower-order polynomials on the other hand will erase smaller structures and distort discontinuities even on larger scales.

Figure 2.4 compares the fit results of the six participating groups with the model distribution. My own results are shown in the upper right panel. Note that the differential emission measures shown in Fig. 2.2 have been integrated with $\log \Delta T = 0.1$ steps, resulting a binned emission measure distribution. In summary, all approaches managed to recover general properties like the overall level and the location of the temperature maximum, but their detailed structure varies considerably. Nobody was able to reconstruct the shape of the model EMD within the formal uncertainties of the applied methods.

The abundance pattern chosen to create the line fluxes in the synthetic spectra is again rather simple: All elements have been set to half the solar photospheric value, apart from neon, where the solar value has been multiplied by 2.7. These abundances are likely meant to represent what the average finding in the coronae of active stars is, with most elements at sub-solar values but the neon abundance significantly enhanced.

Figure 2.5 shows the abundances obtained by the participating groups. Despite the discrepancies of the underlying emission measure distributions, all groups managed to deduce the rough abundance pattern. Coronal elemental abundances therefore seem to be strikingly robust, a finding I already confirmed in (Liefke 2005). A systematic analysis however shows that the distribution of the individual values is much broader than allowed by their for-

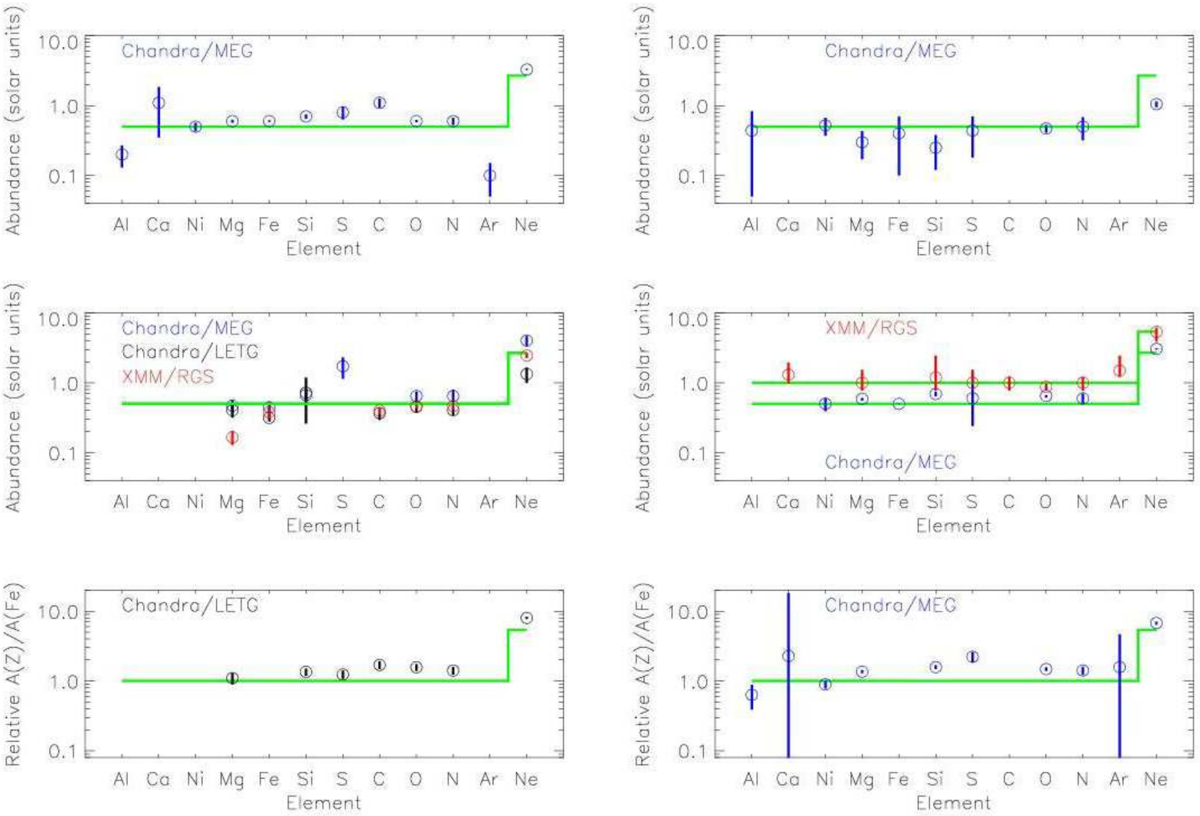

Figure 2.5: Abundances as obtained by the six participating groups. My results are shown in the left column, second row. Figure courtesy of Antonio Maggio.

mal 1σ errors, the uncertainties are therefore highly underestimated.

The line emissivities for the synthetic spectra have been calculated in the low-density limit. In Figure 2.6, the density measurements from different He-like triplets made by the participating groups have been merged into a single plot. The low density values have been recovered for most of the triplets but Ne IX and Si XIII are often overestimated. The well-known problems with the three higher-temperature ions Ne IX, Mg XI, and Si XIII as discussed in Sect. 2.3.5 seem to systematically affect the measured f/i ratios and the inferred densities.

2.5 Discussion and conclusions

Although it was well-known in advance that different analysis methods lead to deviating results in emission measure distribution, abundances and densities, the BEXST challenge showed that the situation is unsatisfactory. Sobering was not the fact that the discrepancies were found at all, but their magnitudes that were surprisingly high. Even with a simple model emisson measure distribution and synthetic spectra with very good signal-to-noise ratio, EMD reconstructions show large differences, the uncertainties of abundances are clearly underestimated, and inferred densities suffer from systematic influences.

The outcome of the challenge proved that both previous as well as future results published in this area should be questioned carefully, with the focus on the respective uncertainties. The techniques in use to reconstruct emission measure distributions may identify the basic structure of an EMD, but will probably fail to reconstruct the details. Conversely, any small-scale EMD feature predicted by these methods is dubious.

As a result of the higher uncertainty level of the emission measure distribution, error estimates for coronal abundances should be much larger. An interesting question is whether the error bars of the abundances would become large enough to explain the distribution of the discrepancies from the inherent values when the discrepancies of the recovered EMD from the model would be taken as the uncertainty of the EMD and propagated into the abundance determination. If this is not the case, other error sources must contribute at a similar level. Unfortunately, this has not been investigated in detail. The main goal concering this issue should be to identify the main error sources and to specify

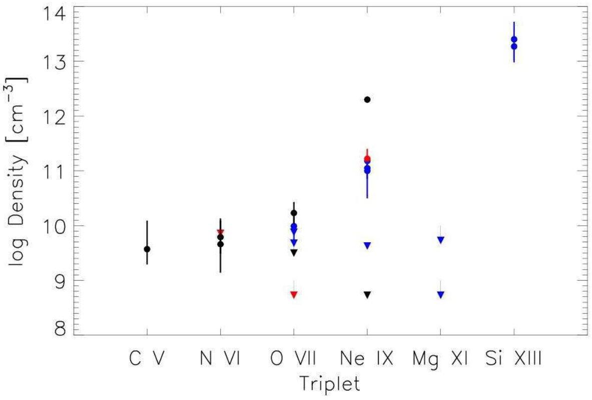

Figure 2.6: Electron densities obtained by the participating groups. Color coding of the different data points as in Figs. 2.4 and 2.5. Figure courtesy of Antonio Maggio.

their importance.

One of the major sources of additional errors remains the atomic physics underlying each conversion of measured line fluxes to the emission measure distribution. Although great progress has been made in recent years in this area, the rather large effects of e. g. dielectronic recombination on the ionization equilibrium or the recently improved calculations for H-like and He-like ions demonstrate that further adjustments could still be expected until the results finally settle down.

The example of density measurements from He-like triplets shows that line flux measurements can easily be affected by contamination which needs to be assessed, e. g. from satellite lines, and even the very details of detector sensitivity may play a role. The “human factor” could enter the process on several occasions, e. g. if line fluxes are measured individually and weak unresolved lines are not taken into account, or when the continuum level is adjusted by eye. This is actually a starting point to discuss the advantages and disadvantages of different analysis methods, which do not only include the usage of different atomic physics databases and codes or constraints set by the underlying reconstruction methods and their numerical implementation, but also the general difference between line-based methods and global fitting procedures.

The BEXST challenge was never meant to be a competition between the different techniques and procedures in use by the different groups in order to determine which one is “the best”, and fortunately it never turned into something like that. Nevertheless, I have not only learned a lot about the reliability of my own method and where its major pitfalls are located but also how its results compare to those of other approaches, and what its advantages and disadvantages are. Of course I knew well in advance that my DEM fitting routine with low-order polynomials can neither reproduce small-scale features nor discontinuities like sudden drops or cutoffs. Considering the finding that the detailed structure seems to be elusive anyway, I think it’s still the most appropriate approach to keep the reconstructed EMD as simple as possible.

Unfortunately, the most obvious conclusion of the challenge – that such benchmark tests should be continued and expanded to different levels of data quality and more complicated input data for the models in order to quantify the general uncertainties of published results for emission measure distributions, densities and abundances – has not been considered. The BEXST challenges ended with the first exercise.

3 The coronal Ne/O abundance of α Centauri

Motivated by the unsolved problem of the solar photospheric abundances and successively of the Ne/O ratio in the coronae of inactive stars like the Sun, I investigated the differential emission measure and the coronal abundances of α Cen. The content of this chapter has been presented at the 14th Cool Star Workshop and published by

C. Liefke and J. H. M. M. Schmitt
A&A, **458**, L1-L4 (2006)

Abstract

Recent improvements in the modeling of solar convection and line formation led to downward revisions of the solar photospheric abundances of the lighter elements, which in turn led to changes in the radiative opacity of the solar interior and hence to conflicts with the solar convection zone depth as inferred from helioseismic oscillation frequencies. An increase of the solar Ne/O abundance to values as observed for nearby stars has been proposed as a solution. Because of the absence of strong neon lines in the optical, neon abundances are difficult to measure and the correct solar and stellar Ne/O abundances are currently hotly debated. Based on X-ray spectra obtained with *XMM-Newton*, we determine a reference value of Ne/O for the inactive, solar-like star α Cen (primarily α Cen B, which is the dominant component in X-rays), with three independent, line-based methods, using differential emission measure reconstruction and an emission measure-independent method. Our results indicate a value of ≈ 0.28 for A_{Ne}/A_O in α Cen, approximately twice the value measured for the Sun, but still below the average value obtained for other stars. The low Ne/O abundance of the Sun is peculiar when compared to α Cen and other stars; our results emphasize the necessity to obtain more and accurate Ne/O abundance measurements of low activity stars.

3.1 Introduction

The canonical values of the solar photospheric elemental abundances have recently become far less canonical. Starting from the work of Anders & Grevesse (1989), a standard reference for many years, the absolute abundance values of the more abundant trace elements like carbon, nitrogen, oxygen, neon, or iron have been significantly reduced over the past decade, initially by Grevesse & Sauval (1998), and again more recently (Asplund et al. 2005, and references therein). These lighter elements considerably influence the physics of the solar interior since they provide a substantial contribution to its radiative opacity. A change in the elemental abundances usually changes the depth of the solar convection zone, which can be inferred from the measured helioseismological oscillation frequencies. With the "old" abundances by Grevesse & Sauval, good agreement could be found between the standard solar model of the appropriate age and the observed oscillation spectrum, while the "new" but rather controversial abundances proposed by Asplund et al. and collaborators turned out to be inconsistent with helioseismology (Bahcall et al. 2005a).

In order to rescue the agreement between the standard solar model and helioseismology the opacity reduction by the downward revision of the CNO abundances must be sufficiently compensated by increased abundances of other elements. The only suitable element is neon, since its (photospheric) abundance is not well determined due to the absence of strong photospheric lines; rather, the solar neon abundance is obtained either from solar energetic particles or from coronal measurements in the X-ray or EUV bands. The solar neon abundance is usually quoted relative to oxygen, and the solar Ne/O abundance ratio has remained more or less constant during the course of the revisions of the solar photospheric abundances, with values ranging from 0.14 from the compilation of Anders & Grevesse, 0.18 from Grevesse & Sauval, and 0.15 for the new set from Asplund et al.. An increase of the solar Ne/O abundance by a factor of 2.5–3.5 (Antia & Basu 2005; Bahcall et al. 2005b) would provide sufficient opacity to reconcile the low oxygen abundance with helioseismology. Evidence for an increased neon abundance has been proposed by Drake & Testa (2005) in their survey of the coronal Ne/O abundance in a sample of nearby stars, finding an average value of $A_{Ne}/A_O = 0.41$.

On the other hand, a re-analysis of *SOHO* CDS spectra and re-investigation of archival solar coronal X-ray spectra confirm the long-established, canonicallower A_{Ne}/A_O values (Young 2005; Schmelz et al. 2005). Also, a closer look at the sample of stars used by Drake & Testa reveals that most of these stars are RS CVn systems or well-known young and active stars, known to show the inverse FIP effect (Brinkman et al. 2001), i. e., an enhancement of elements with high first ionization potential. Since neon is (apart from helium) the element with the highest FIP and the occurrence of the inverse FIP effect is related to activity (Güdel 2004, and references therein), the sample may be biased to higher neon abundances and not be representative of the truecosmic neon abundance.

In order to settle the issue of a possible bias, a comparison to exclusively low-activity solar-like stars is needed. Due to their low X-ray luminosity, high-resolution X-ray spectra with reasonable signal-to-noise ratio of such inactive stars can be obtained only for very few objects, like ϵ Eri, Procyon, or α Cen. Additionally, their low coronal temperatures complicate the measurement of the otherwise prominent Ne IX and Ne X He-like and H-like lines that have peak formation temperatures of $\log T = 6.6$ and $\log T = 6.75$ respectively; for example, the *Chandra* LETGS spectra of α Cen A and B presented by Raassen et al. (2003)) do not show the Ne X Ly α line. Our new *XMM* RGS spectra of α Cen provide good sensitivity and signal-to-noise to detect and measure the relevant H- and He-like lines of O and Ne to allow an accurate determination of its neon-to-oxygen abundance.

3.2 Observations and data analysis

α Centauri is target of an *XMM-Newton* monitoring campaign of its long-term X-ray behavior. Since March 2003 X-ray observations have been performed regularly at intervals of approximately six months, lasting between 5 and 9 ks each. Results from the first five observations of the program focusing on variability and possible activity cycles of both components have been presented by Robrade et al. (2005). Two additional datasets (ObsIDs 0143630201 and 0202611201) are now available, resulting in 52 ks of accumulated observing time. All seven datasets were reduced with the *XMM-Newton* Science Analysis System (SAS) software, version 7.0, making use of standard selection and filtering criteria.

Robrade et al. showed that the K0 V star α Cen B is X-ray brighter than the solar twin α Cen A (spectral type G2 V) by factors ranging from 3.6 to 75; this applies also to the two latest observations. A spatially resolved spectral analysis of the α Cen system is not possible with *XMM-Newton*; the measured total X-ray flux refers essentially to α Cen B ($\approx$ 90–95%). The following analysis is based solely

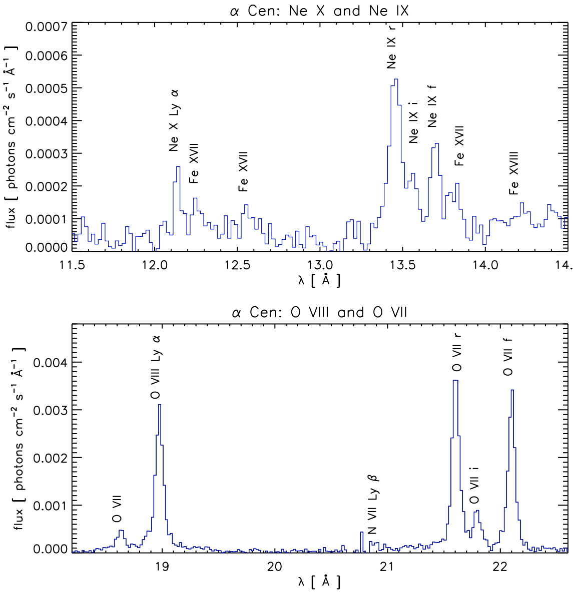

Figure 3.1: Segments of the merged RGS spectrum of α Cen, showing the spectral regions covering the neon (top) and oxygen (bottom) Ly α lines and He-like triplets. The spectra were created with the SAS task `rgsfluxer` from RGS 1 and 2 in 1st and 2nd order.

on the RGS data. We use the SAS task `rgscombine` to merge the individual RGS exposures to co-added spectra with corresponding response matrices. The resulting combined spectra thus constitute a mixture of α Cen A and B (with B by far dominating) and an average over the quiescent and flaring states of α Cen B and the long-term variability of α Cen A (Robrade et al. 2005). This is not critical for our purposes since we focus on the coronal abundances, which we do not expect to change during α Cen's different states of activity; also, Raassen et al. (2003) showed α Cen A and B to have similar abundances, thus we do not anticipate effects from the changing contributions of the two components. In Fig. 3.1 we plot the relevant portions of the RGS spectrum of α Cen that cover the He-like and H-like lines of neon and oxygen. While the O VII and O VIII lines are recorded with a very good signal-to-noise ratio, the signal is much lower for Ne IX and Ne X, but the lines are still easily detectable and the Ne IX resonance, intercombination and forbidden lines can be resolved. Using the CORA program (Ness & Wichmann 2002) we measured individual line fluxes in the RGS 1 and 2 spectra in 1st and 2nd order assuming Lorentzian line profiles. Error-weighted means were calculated for further analysis.

3.3 Abundance determination

3.3.1 Differential emission measure modeling

From our line flux measurements we proceed to determine the coronal Ne/O ratio of α Cen using three different methods. We reconstructed the differential emission measure (DEM) from abundance-independent ratios of the H-like Ly α and the He-like resonance lines from N, O, and Ne, analogous ratios of H-like Ly α and the lines originating from the $1s3p - 1s^2$ transition ("He-like Ly β") of C and O and the weakly temperature-dependent ratio of the Fe XVII lines at 15.01 Å and 16.78 Å. In addition we used continuum flux measurements at wavelengths around 20 Å where the spectrum is essentially line-free for normalization. Our DEM reconstruction method is similar to the one applied by Schmitt & Ness (2004) and makes use of CHIANTI 5.2 line and continuum emissivities (Landi et al. 2006). In a first approach, $\log DEM$ was modelled as a function of $\log T$ using polynomials of different orders without further constraints; the best-fit is obtained with a 3^{rd} order polynomial ($\chi^2_{red} = 0.6$). However, the available line ratios cover only temperatures $\log T > 6.0$ and abundance-independent line ratios with suitable signal-to-noise for lower temperatures are not available in the RGS spectral range. In a second approach, we model the linear DEM again with polynomials as a function of $\log T$. Additionally the DEM was forced to have two zeros defining the boundaries of the coronal DEM distribution. Here, the best fit is obtained with a 4^{th} order polynomial ($\chi^2_{red} = 2.2$). The resulting DEM distributions are shown in Fig. 3.2; they agree at higher temperatures, but differ significantly for $\log T < 6.2$, indicating the uncertainties due to the poor coverage of lower temperatures. The formation temperatures of the neon and oxygen He-like and H-like lines are however well-determined and there the DEM distributions look quite similar. In Table 3.1 we compare the observed line ratios with the line ratios "predicted" by the two methods; the two methods agree quite well except for the Ne X Ly α / Ne X r ratio, which is reproduced much better by method 1.

By forcing the DEM distributions obtained with both methods and the corresponding line contribution functions to reproduce the measured line fluxes, we determine the absolute (and relative) abundances of neon and oxygen. The results are listed in Table 3.2; the relative neon-to-oxygen abundance with method 1 is $A_{Ne}/A_O = 0.27 \pm 0.03$, while method 2 yields $A_{Ne}/A_O = 0.31 \pm 0.08$. Note that errors are based on count statistics alone, i. e. the smaller error for the first approach results in the

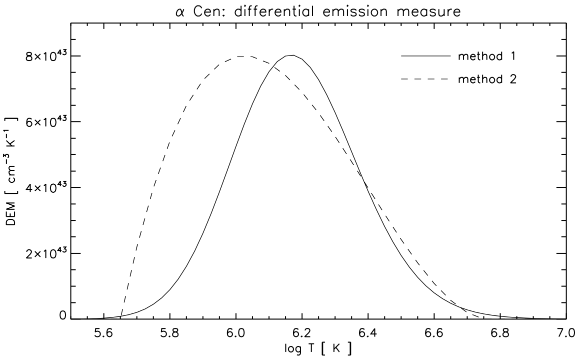

Figure 3.2: *DEM* distributions obtained by modeling a 3^{rd} order polynomial to $\log DEM(\log T)$ (method 1) and a 4^{th} order polynomial with two zeros to $DEM(\log T)$ (method 2). Note that the shape of the *DEM* is well-determined only for $\log T > 6.0$.

better quality of the fit, giving consistent individual abundances for the two neon lines, while they clearly deviate in the second approach.

3.3.2 Emission measure-independent linear combinations of line fluxes

Acton et al. (1975) proposed to determine the solar coronal Ne/O abundance ratio from the ratio of the measured line fluxes of the Ne IX resonance and O VIII Ly α lines since their contribution functions have similar peak formation temperatures and a similar temperature dependence. This approach thus avoids uncertainties in the abundance determination introduced by the initially unknown underlying temperature structure of the emitting plasma. Acton's method has been refined by Drake & Testa (2005) by adding a portion of the Ne X Ly α flux to reduce the temperature residuals. We further refined this approach by also taking the O VII resonance line into account and calculating optimal linear combinations of the measured fluxes. The coefficients for the linear combinations are obtained from a minimization procedure incorporating the corresponding ratios of the theoretical emissivities of the involved lines from the CHIANTI database. Relative to the Ne IX r line, we obtain scaling factors of 0.02, -0.17, and 0.69 for Ne X Ly α, O VII r, and O VIII Ly α respectively, for the line fluxes and line contribution functions in photon (not energy) units, see also Fig 3.3. These coefficients give $A_{Ne}/A_O = 0.28 \pm 0.05$, in very good agreement with the value obtained with the *DEM* reconstruction methods.

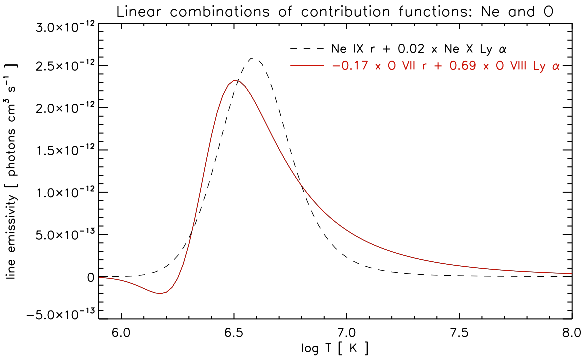

Figure 3.3: Linear combinations of contribution functions of H-like Ly α and He-like resonance lines of neon and oxygen.

3.4 Results and discussion

The results of our abundance modeling (cf., Table 3.2) are very robust and yield values of $A_{Ne}/A_O \approx 0.28$, independent of the applied method. This value is twice as large as the "canonical" A_{Ne}/A_O for the solar corona. α Cen is probably the most suitable star for a comparison with the Sun avoiding a possible FIP/I-FIP bias. Our *DEM* of α Cen resembles that of the quiet Sun (e. g. Brosius et al. 1996; Landi & Landini 1998), which typically peaks around $\log T \approx 6.0$–6.2. However our values refer to α Cen B, which is by far the more active component known to show flaring activity (Schmitt & Liefke 2004; Robrade et al. 2005).

Separate X-ray spectra of α Cen A and B are available from a 79 ks *Chandra* LETGS exposure. However, both spectra have extremely low signal in the wavelength range covering the Ne IX and Ne X lines. Values of $A_{Ne}/A_O = 0.18 \pm 0.07$ and 0.24 ± 0.09 for α Cen A and B respectively were derived from global fitting by Raassen et al. (2003) and are thus based primarily on Ne VII and Ne VIII lines located at longer wavelengths. Many of these lines suffer from significant blending as well as low signal and their atomic physics parameters should be considered as more uncertain than those of the H-like and He-like lines. Formally, the Ne/O abundances of α Cen A and B are consistent with each other, and the value for the B component is consistent with our XMM-Newton result.

Measurements of the solar Ne/O abundance ratio tend to show a broad scatter (cf. the compilation provided by Drake & Testa (2005) in the supplementary information, with values of A_{Ne}/A_O ranging from 0.08 to 0.47), but the majority of them, based on miscellaneous data like solar energetic particles, X-ray or EUV spectra, are in good agreement with the lowNe/O abundances. Additionally, the most recent analyses of Young (2005) and Schmelz

Table 3.1: Line ratios (photon fluxes) used in the fitting procedure.

line ratio	measured	method 1	method 2
N VII Ly α / N VI r	1.40 ± 0.16	1.36	1.30
O VIII Ly α / O VII r	0.79 ± 0.04	0.79	0.83
Ne X Ly α / Ne IX r	0.48 ± 0.10	0.47	0.28
C VI Ly α / C V β	24.17 ± 10.19	25.08	19.97
O VIII Ly α / O VII β	7.64 ± 0.67	7.85	8.22
Fe XVII 15.01 Å / 16.78 Å	1.70 ± 0.20	1.45	1.42

Table 3.2: Absolute abundances of neon and oxygen and the Ne/O abundance ratio of α Cen obtained with different methods.

	DEM modeling		linear	Asplund
	method 1	method 2	combinations	et al.
Ne	7.95 ± 0.04	8.01 ± 0.13	—	7.84
O	8.52 ± 0.01	8.51 ± 0.01	—	8.66
A_{Ne}/A_O	0.27 ± 0.03	0.31 ± 0.08	0.28 ± 0.05	0.15

et al. (2005), based on the most recent atomic data, clearly support values as low as 0.15.

All stars in the survey of Drake & Testa show higher values of A_{Ne}/A_O, incompatible with the kanonicallow solar value. The inference of the solar Ne/O abundance from other stars is, however, problematic. Apart from the fundamental question of why the Sun should implicitly show the same abundance pattern as other stars do (and many stellar photospheric measurements show that it does not), the most severe problem is to find truly solar-like stars, i. e. relatively old and inactive single stars of similar spectral type. These conditions and the basic requirement that the stars are observable in X-rays (or in the EUV) with a sufficient signal to obtain abundance measurements of neon and oxygen, are almost mutually exclusive since stars with an X-ray luminosity as low as that of the Sun can only be observed in the very solar vicinity with today's X-ray telescopes. Instead, the typical well-studied stellar coronal X-ray source is much brighter, usually consisting of an active young late-type star or even an RS CVn system. Such objects are not appropriate for a direct comparison with the Sun, especially if one accepts the reality of the inverse FIP effect, i. e. an enhancement of elements with high first ionization potential; while the physics of abundance anomalies like the inverse FIP effect and its counterpart, the FIP effect as observed on the Sun, are not fully understood, a framework to explain both effects has been provided by Laming (2004).

A correlation seems to exist in the sense that the FIP effect turns into the inverse FIP effect, with the inverse FIP effect becoming stronger with increasing activity. Clearly, the sample used by Drake & Testa is then strongly biased. The only star in their sample of truly solar-like activity is Procyon, where a value of 0.42 from Sanz-Forcada et al. (2004) was used, which was obtained from three combined *Chandra* LETGS spectra but still low signal at the wavelengths of the Ne IX and Ne X lines. For part of these data Raassen et al. (2002) obtained $A_{Ne}/A_O = 0.22$ with a global fitting approach, a value also found by the same authors from 91 ks of *XMM* RGS and MOS data; thus the correct Ne/O abundance ratio of Procyon remains an open issue.

Moderately active K dwarfs seem to have values of $A_{Ne}/A_O \sim 0.37$, i.e, slightly lower than the median obtained by Drake & Testa, but still at approximately twice the level of the Sun as shown by Wood & Linsky (2006), who investigated Ne/O abundance ratios of ϵ Eri, 36 Oph and 70 Oph. As pointed out above, our Ne/O value also refers to a K star, α Cen B, which is less active than any of the stars studied by Wood & Linsky. Therefore, none of the stars studied so far has a Ne/O abundance as low as observed for the Sun. Therefore, the question remains why the Sun is so special. Or do we first have to find a real solar-like star?

4 Coronal properties of the EQ Peg binary system

Stellar activity in mid to late M dwarfs is crucial for our understanding of the stellar interior in these stars. I analyzed the the coronal properties of the two components of the EQ peg binary system, which are expected to reside in the transition region where low-mass stars become fully convective, and compared them to five early to mid M dwarfs. I presented the results of this study at the X-ray Universe 2008. They have been published by

C. Liefke, J.-U. Ness, J. H. M. M. Schmitt and A. Maggio
A&A, **491**, 859-872 (2008)

Abstract

The activity indicators of M dwarfs are distinctly different for early and late types. The coronae of early M dwarfs display high X-ray luminosities and temperatures, a pronounced inverse FIP effect, and frequent flaring to the extent that no quiescent level can be defined in many cases. For late M dwarfs, fewer but more violent flares have been observed, and the quiescent X-ray luminosity is much lower. To probe the relationship between coronal properties with spectral type of active M dwarfs, we analyze the M3.5 and M4.5 components of the EQ Peg binary system in comparison with other active M dwarfs of spectral types M0.5 to M5.5. We investigate the timing behavior of both components of the EQ Peg system, reconstruct their differential emission measure, and investigate the coronal abundance ratios based on emission-measure independent line ratios from their *Chandra* HETGS spectra. Finally we test for density variations in different states of activity. The X-ray luminosity of EQ Peg A (M3.5) is by a factor of 6–10 brighter than that of EQ Peg B (M4.5). Like most other active M dwarfs, the EQ Peg system shows an inverse FIP effect. The abundances of both components are consistent within the errors; however, there seems to be a tendency toward the inverse FIP effect being less pronounced in the less active EQ Peg B when comparing the quiescent state of the two stars. This trend is supported by our comparison with other M dwarfs. As the X-ray luminosity decreases with later spectral type, so do coronal temperatures and flare rate. The amplitude of the observed abundance anomalies, i. e. the inverse FIP effect, declines; however, clear deviations from solar abundances remain.

4.1 Introduction

M dwarfs populate the low-mass and low-temperature end of the main sequence, with masses of approximately 0.6 $M_\odot$ and an effective temperature of about 3800 K at a spectral type of M0, down to 0.1 $M_\odot$ and 2200 K at spectral type M9. Conspicuous changes in the optical spectra become apparent in the later subclasses as more and more molecules form with decreasing photospheric temperature, and molecular bands start to dominate. Dust formation marks the transition from late M dwarfs to the brown dwarf regime of L and T dwarfs.

Somewhat surprisingly, all M dwarfs seem to show at least some activity phenomena, and in particular active M dwarfs of spectral types M0–M4 are strong coronal X-ray sources with X-ray luminosities often close to a saturation limit of $\log L_\mathrm{X}/L_\mathrm{bol} \sim -3.3$ (Fleming et al. 1993; Pizzolato et al. 2003). Frequent and strong flaring with increases in X-ray luminosity by more than two orders of magnitude (e. g. Favata et al. 2000; Güdel et al. 2002a; Schmitt et al. 2008) is widespread among these stars, with additional variability on all timescales and amplitude levels. Their emission measure distributions peak around 6–8 MK (Robrade & Schmitt 2005), thus their average coronal temperatures are much higher than solar (peak temperature 1–2 MK, see e. g. Brosius et al. 1996). Temperatures in excess of several 10 MK are typically measured during larger flare events (Robrade & Schmitt 2005).

On the other hand, late M dwarfs with spectral types M6–M9 are difficult to detect in X-rays at least during quiescence, yet their ability to produce transient X-ray luminosity enhancements by orders of magnitude during flares (Rutledge et al. 2000; Schmitt & Liefke 2002; Stelzer et al. 2006) remains. Intermediate objects with a spectral type of ≈ M5 have lower coronal temperatures than the more active early M dwarfs, the permanent state of variability is replaced by periods of quiescence interrupted by individual flares, and the overall X-ray luminosity starts to decrease by more than an order of magnitude at around spectral type M5 (Güdel et al. 2002a; Fuhrmeister et al. 2007).

The abundance patterns observed in stellar coronae also appear to be related to changes in the coronal activity level. On the one hand, there is the so-called FIP effect observed in (comparably) inactive stars like the Sun (Feldman & Laming 2000) or e. g. α Cen (Raassen et al. 2003), with the coronal abundances of elements with low first ionization potential (FIP) enhanced with respect to solar photospheric values. On the other hand, very active stars tend to show the inverse effect, i. e. elements with low FIP depleted and elements with a high FIP enhanced. Güdel et al. (2002b) and Telleschi et al. (2005) found that the solar-like FIP effect to first disappear and then reverse with increasing activity for solar analogs at different ages. This correlation can be expected to also apply to the sequence of M dwarfs: While the active early M dwarfs are well-known to show the inverse FIP effect (see e. g. Robrade & Schmitt 2005), Fuhrmeister et al. (2007) found the M5.5 star CN Leo to show much less pronounced abundance anomalies. Unfortunately, high-resolution X-ray spectra for intermediate objects are rare; and due to their low X-ray luminosity, it is in most cases impossible to obtain spectra suitable for a reasonable abundance analysis for late M dwarfs to confirm this trend.

Stellar coronal X-ray emission is associated with the production of magnetic fields driven by a dynamo mechanism (Parker 1955; Moffatt 1978), which is thought to be located in the transition layers between the rigidly rotating radiative core and the outer convection zone that rotates differentially for solar-like stars. However, models of the stellar interior predict that M dwarfs of spectral types later than ≈ M3 become fully convective (Chabrier & Baraffe 1997), leaving no shear layers between a radiative core and the convection zone behind. The solar-like $\alpha\omega$-dynamo thus does not work for these stars, and no dynamo-induced X-ray emission would be expected. Yet, the observed decline in X-ray luminosity around spectral type M5–M6 fits the finding of Mullan & MacDonald (2001) that the influence of magnetic fields can shift the fully convective cut-off towards later spectral types. Fully convective stars produce less quiescent X-ray emission, but other activity indicators like Hα emission even increase in strength towards the low-mass L dwarfs. Alternative dynamo mechanisms, driving the required magnetic fields, have been proposed for these objects (e. g. Durney et al. 1993). In these scenarios with α^2 or turbulent dynamos, the magnetic fields are sustained by small-scale velocity fields, while large-scale rotation plays only a minor role. As a consequence, no activity cycles and magnetic structures of small size and with a more uniform surface distribution are expected. However, most recent non-linear 3D simulations of dynamo action in fully convective stars (e. g. Chabrier & Küker 2006; Dobler et al. 2006; Browning 2008) have shown that also large-scale fields could be produced in fast-rotating late M dwarfs, but these models disagree about whether or not the magnetic fields have axisymmetric components and/or a cyclic behavior.

With the required change of the dominating dynamo mechanism operating in early and late M dwarfs in mind, changes in the abundance patterns between these objects are of particular interest to characterize the coronae induced by the different dynamos. The above considerations concerning luminosity demand investigations of coronal properties of M dwarfs located close to the expected transition. The binary system EQ Peg consists of an M3.5 and M4.5 star and thus provides the rare opportunity to compare two such stars, which should otherwise be very similar since they are co-eval.

In the following, we present our *Chandra* HETGS observations of EQ Peg, that allows us to perform a separate spectral analysis of the two components. We also compare our observations of EQ Peg A and B to HETGS spectra of other M dwarfs covering a range of spectral types. We propose a classification of the coronal properties of active M dwarfs based on their spectral type.

4.2 The EQ Peg binary system

The visual binary system EQ Peg consists of two M dwarfs at a distance of 6.25 pc with an angular separation of $\approx 6''$, i.e. EQ Peg A with spectral type M3.5 and an apparent magnitude $V_A = 10.35$ and EQ Peg B with spectral type M4.5 and magnitude $V_B = 12.4$. Both components are well-known (optical) flare stars (Pettersen 1976; Lacy et al. 1976). Jackson et al. (1989) observed microwave emission during quiescence, which they attributed to the brighter A component. Norton et al. (2007) find a photometric period of 1.0664 days for the EQ Peg system from data of the SuperWASP transit survey, however, due to the large aperture size of SuperWASP, this period cannot be clearly assigned to one of the two components of EQ Peg, nor to two other stars in the field of view. However, Zboril & Byrne (1998) find a rotational velocity of 14 km/s for EQ Peg A, while Delfosse et al. (1998) analyze only the B component and find 24.2±1.4 km/s; both $v \sin i$ values are rather high and thus consistent with a short rotation period.

The EQ Peg system is a strong X-ray and EUV source with a number of flares recorded, but previous missions were not able to angularly resolve the two stars. Pallavicini et al. (1990) discuss two flares observed with *EXOSAT*. The first one, with an atypically shaped lightcurve, was observed by Haisch et al. (1987) in the context of a simultaneous *EXOSAT* and *IUE* campaign. A second large amplitude flare was observed by Pallavicini et al. (1986). Katsova et al. (2002) observed another large flare with *ROSAT* with simultaneous optical photometry. All of these flares were attributed to the A component. Monsignori Fossi et al. (1995) observed another set of flares on EQ Peg with *EUVE* and derived a differential emission measure distribution, based on line flux measurements, with a peak at about 10 MK, which is, however, not well constrained. A first approach to separate the two components in X-rays was undertaken with *XMM-Newton* (Robrade et al. 2004). Although the two stars show considerable overlap owing to the instrumental point spread function, it was possible to attribute about three quarters of the overall X-ray flux to the A component. A subsequent detailed spectral analysis without resolving the binary has been performed by Robrade & Schmitt (2005). Our *Chandra* HETGS observations are the first X-ray observations that allow an unambiguous spectral separation of the two binary components.

4.3 Chandra HETGS observations of EQ Peg A and B

4.3.1 Observations and data analysis

EQ Peg was observed on four occasions between 2006 November 28th and December 3rd with a total exposure time of 100 ks with the *Chandra* High Energy Transmission Grating Spectrometer (HETGS); a journal of the observations is presented in Table 4.1. The HETGS consists of two grating arms, the Medium Energy Grating (MEG) and the High Energy Grating (HEG), which provide X-ray spectra in the wavelength range between ≈ 1.5 and 30 Å with medium (MEG: 0.023 Å FWHM) and high (HEG: 0.012 Å FWHM) resolution.[1] For data reduction we used the CIAO software version 3.4.

The separation of the 0th order images of EQ Peg A and B is $5.8''$ in the ACIS-S image, and therefore the dispersed spectra of the two stars can be easily separated with only a small overlap of the HEG and MEG grating arms at the shortest wavelengths (< 1.5 Å). We extracted 1st order HEG and MEG spectra for each component from each of the four datasets using the standard CIAO tools to obtain grating spectra for multiple sources.

For our final analysis we created separate HEG and MEG spectra for EQ Peg A and B, where we combined all four observations and the plus- and minus dispersion orders. Only for EQ Peg A have we also inspected the spectra from the individual observations.

For our final analysis, we created separate HEG and MEG spectra for EQ Peg A and B, where we combined all four observations and the plus and minus dispersion orders. Only for EQ Peg A we have also inspected the spectra from the individual ob-

---

[1] For a detailed description of the *Chandra* HETGS see the Chandra Proposers' Observatory Guide at http://asc.harvard.edu/proposer/POG/html/

Table 4.1: Observation log for EQ Peg.

ObsID	observation time	exp. time [ks]
8453	2006-11-28T01:51–2006-11-28T22:48	29.95
8484	2006-11-29T16:33–2006-11-29T08:59	10.95
8485	2006-11-30T16:59–2006-12-01T08:54	30.94
8486	2006-12-03T07:55–2006-12-03T09:02	27.95

servations. All line fluxes were measured with our CORA program (Ness & Wichmann 2002), fitting the lines with Moffat line profiles, i. e., modified Lorentzians, as given by Eq.2.1 with an exponent $\beta = 2.4$ and a fixed line width of 0.02 Å for MEG and 0.01 Å for HEG spectra.

4.3.2 Lightcurves

We first extracted background-subtracted lightcurves for EQ Peg A and B from the dispersed and non-dispersed (0th order) photons. In order to obtain equivalent lightcurves of the two stars with maximized signal-to-noise, we use total (i. e. 0th order + dispersed) photons of EQ Peg B and the dispersed photons of EQ Peg A, scaled by the ratio of total and dispersed photons from EQ Peg B (assuming a similar spectral energy distribution for the two stars), as the the 0th order of EQ Peg A is strongly affected by pileup. The resulting lightcurves are shown in Fig. 4.1 for the four observation intervals.

EQ Peg A shows several flares. The most conspicuous event started at 0:00 UT on December 1st with a relatively slow rise and lasted about 2 hours. Unfortunately, the flare decay phase was not observed completely, since the observation ended before quiescence was reached again. At flare peak, the flux increases by a factor of six, and the flare is strong enough to allow the extraction of separate MEG spectra. Additional smaller flares occurred on November 28th at 5:00 UT, with a flux increase of about a factor of four, lasting about half an hour, and on December 3rd at about 9:00 UT, with an increase by a factor of 2, and a longer decay of more than 2 hours. The underlying quiescent level is difficult to determine owing to a large number of small-scale variations and apparently different quiescent emission levels during the four individual observations, with the base level for the A component at $\sim$ 0.3–0.4 cts/s. Apart from pure statistical noise, such low-level amplitude variations can be caused either by small-scale flares or the evolution of active regions on the stellar surface. On November 29th the emission level was much higher than this quiescent level despite a lack of clear flare-like signatures, which might be explained by active regions newly emerged or rotated into the field of view, while on November 30th a slow decrease in count rate is observed that might be attributed to a long-duration flare. The B component at $\sim$ 0.05 cts/s is much fainter and does not show conspicuous short duration flares, except on Dec 3rd. On November 30th the count rate of EQ Peg B slowly decreased during the whole 8 hours of the observation and again we may have witnessed the decay of a flare.

We computed median and mean count rates in order to compare the flux levels of the two components outside obvious flaring periods, and find the quiescence level of EQ Peg B lower than that of A by factors of about 6 to 10. Both stars show a decay in count rate on November 30th, however, a direct connection of flare activity on the two components is difficult to envisage considering the distance of $\sim$ 36 AU between A and B, although a similar correlated behavior of the system with simultaneous quiescent and flaring states has been observed by Robrade et al. (2004) with *XMM-Newton*. These authors also found a lower flux ratio of 4–5 during quiescence and 2.5–3 during flaring states. However, due to the limited spatial resolution of *XMM*'s EPIC detectors, the exact brightness ratios are less certain.

We also extracted the lightcurves in different energy bands to obtain time-resolved hardness ratios. These give us the temperature evolution of the plasma. While there is no unique temperature that describes the spectrum (see Sect. 4.4.2), the temperature distribution cannot be mapped as a function of time, and the differential emission measure distribution can only by determined as an average over the entire observation. Because of pileup in the 0th order of the A component, we extracted the hardness ratios only from the dispersed photons for both stars. With the hard and soft bands chosen to range from 1.0–10.0 keV and 0.3–1.0 keV respectively, the two components show consistent hardness ratios during quiescence, with values ranging from 0.25 to 0.5, indicating a similar spectral energy distribution. Averaged over the total observing time, the hardness ratio for both stars is 0.43; a spectral hardening to values up to 0.8 is apparent during the major flares on the A component. For our spectral analysis, we considered only the

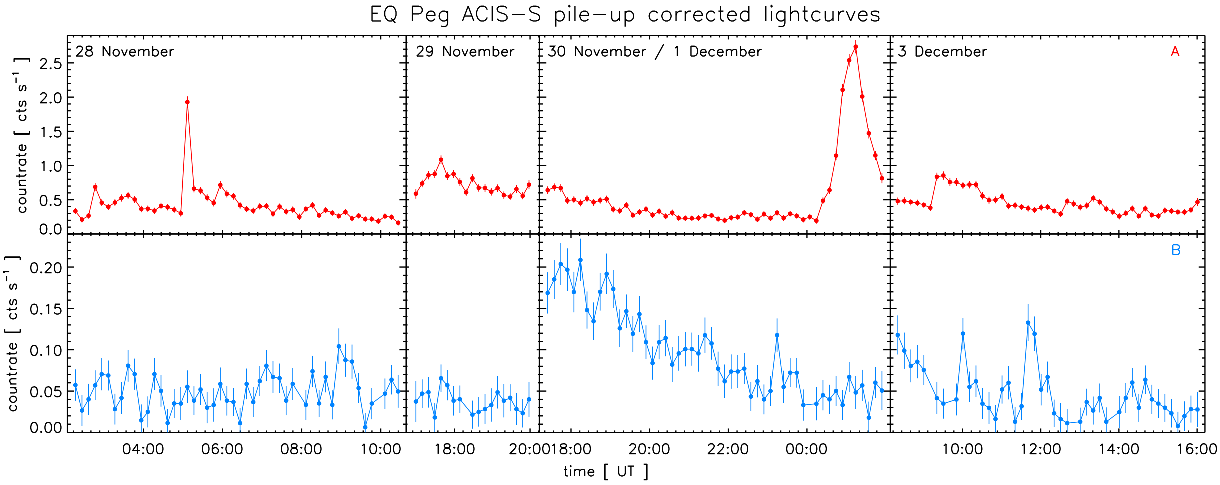

Figure 4.1: Background-subtracted and pileup-corrected lightcurves for EQ Peg A (top) and B (bottom). Binsize for both sources is 600 s.

total spectrum of EQ Peg B, while for EQ Peg A we considered the total spectrum and a "quiescent" spectrum, where we excluded the two larger flares on November 28th and December 1st.

We computed overall X-ray luminosities $\log L_{\mathrm{X}}$ of 28.71 for EQ Peg A (28.67 for the quiescent state only) and 27.89 for EQ Peg B from the integrated dispersed photons in the MEG spectra over a wavelength range from 2 to 25 Å, i. e. in this spectral range, the A component is by a factor of 6–7 more luminous than the B component. However, following Kenyon & Hartmann (1995), the bolometric luminosities of the two stars are $\log L_{\mathrm{bol}} \approx 31.90$ and 31.28. This results in $\log L_{\mathrm{X}}/L_{\mathrm{bol}}$ values of -3.19 (-3.23 during quiescence) and -3.39 for EQ Peg A and B respectively, i. e. both stars are located in the saturation regime of X-ray emission (Pizzolato et al. 2003).

4.3.3 Grating spectra

In Fig. 4.2 we show the *Chandra* MEG spectra of EQ Peg A (top) and B (bottom). Both stars show well-pronounced continua between 5 Å and 15 Å, indicating larger amounts of high-temperature plasma in their coronae. The strongest lines in the total MEG count spectra are Ne X and O VIII Ly α, other prominent lines originate from Si XIV and XIII, Ne IX, and Fe XVII. The iron lines tend to be somewhat stronger in EQ Peg B. The O VII triplet lines are clearly detected but suffer from the low effective area of the MEG at long wavelengths. The weak O VII 1s-3p line at 18.63 Å is also detected in both stars. After conversion of counts to photon fluxes, the O VIII Ly α line is the strongest line in the spectra, and also the O VII flux is quite high, indicating the presence of considerable amounts of low-temperature plasma.

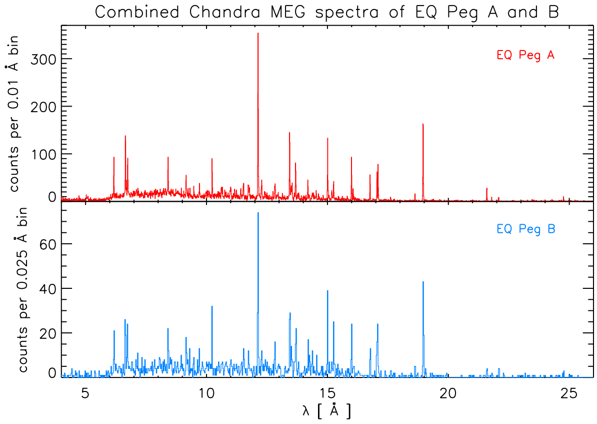

Figure 4.2: *Chandra* MEG spectra of EQ Peg A (top, red) and B (bottom, blue). Both spectra have been rebinned.

In order to probe the shape of the continua and to directly compare the two binary components, we computed the cumulative count spectra from 4 Å to 26 Å from the combined count spectra of EQ Peg A and B (top panel of Figure 4.3). A steep rise of the cumulative spectrum indicates a harder spectrum and thus higher temperatures, as observed for EQ Peg A compared to EQ Peg B. Since this may reflect the strong flares observed on the A component, we considered also the quiescent spectrum for EQ Peg A. As can be seen from Figure 4.3 (top), this spectrum is indeed closer to the B component, however, EQ Peg A still appears somewhat harder. When comparing the total spectra of A and B, these differences are relatively small, and a KS test returns probabilities of around 3% that the two stars are different in their spectral shape. We note that

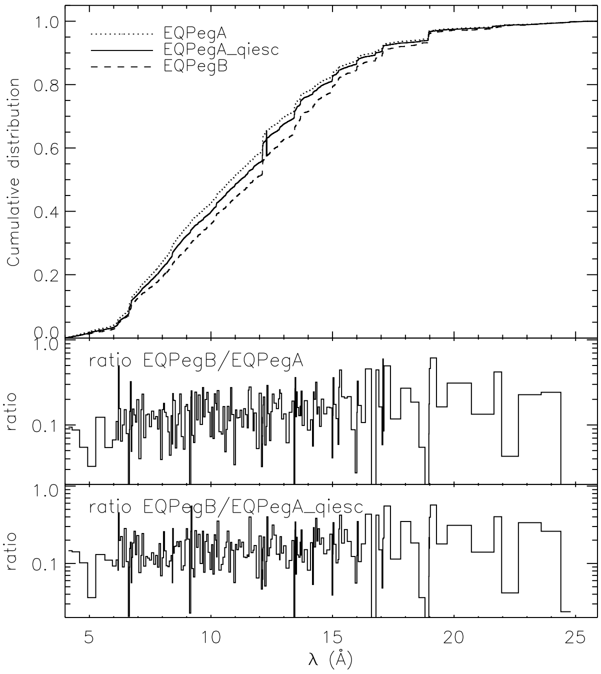

Figure 4.3: Cumulative distribution (top) of counts in the MEG spectra of EQ Peg A (dotted line: all data, solid line: with the large flare on December 1^{st} excluded) and B (dashed line); and ratio B / A (middle panel: all data, bottom: with the two larger flares on EQ Peg A excluded).

the presence of strong emission lines, e. g., Ne X at 12.12 Å, leads to steps in the cumulative spectrum. However, the depths of these steps seem similar for EQ Peg A and B, and the major differences in the cumulative distribution can be attributed to the continuum.

In Tables 4.2 and 4.3 we provide lists of the measured line counts and resulting photon fluxes for the combined spectra of EQ¯Peg A and B, and for the quiescent state of EQ Peg A, which we used in our subsequent analysis; note that a sophisticated procedure has been applied to deconvolve the blending of the Ne IX triplet and its contamination with iron lines, mainly from Fe XVII and Fe XIX (Ness et al. 2003b). In addition to the line fluxes of the three triplet constituents, we fitted global scaling factors to the line fluxes of the contamining ions observed by Ness et al. (2003b) in the well-exposed HETGS spectrum of Capella where the contamination is very strong. Additionally, the Ne X line at 12.13 Å has been corrected to account for a blend by Fe XVII at 12.12 Å. According to CHIANTI 5.2 (Landi et al. 2006), using the ionization balance from Mazzotta et al. (1998), the line emissivity of the contaminating line is comparable to the line at 12.26 Å, and the ratio of these two lines shows no dependence on electron density and only a mild dependence on electron temperature. Additionally, both transitions go to the ground state and share the same electron configuration in their excited states. We thus subtracted the line counts measured in the line at 12.26 Å from the Ne X line as a proxy for the unresolved blending line at 12.12 Å. Fig. 4.4 illustrates the fit for the total HEG and MEG spectra of EQ Peg A.

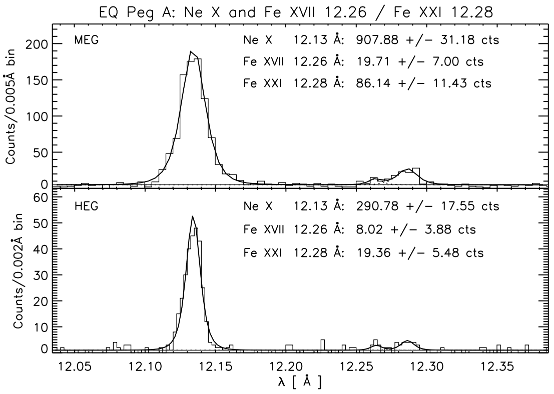

Figure 4.4: Spectral region around the Ne X line at 12.13 Å and the Fe XVII and Fe XXI lines at 12.26 and 12.28 Å in the total spectrum of EQ Peg A.

4.4 Results

4.4.1 Coronal densities

Using the forbidden and intercombination lines of the helium-like triplets of silicon, magnesium, neon, and oxygen, we computed the density-sensitive f/i-ratios of these ions for EQ Peg A and B. In Table 4.4 we list these ratios with the respective peak formation temperatures of the ion and the derived electron densities n_e for EQ Peg A and B. For the conversion of the measured f/i ratios to densities, we used Eq. 2.3 with values from Table 5 in Ness et al. (2002a) for the low-density limit R_0 and the critical density N_c. Theoretical modeling of the f/i ratios still suffers from the incompleteness of current atomic databases, as contributions from satellite lines and effects from dielectronic recombination have to be taken into account.

The uncertainty in the density derived from O VII is large, as a result of the low effective area at long wavelengths. While the Ne IX triplet around 13.5Å is well exposed, severe contamination complicates the line flux measurements, especially of the Ne IX i line at 13.54 Å (Ness et al. 2003b), see also Sect. 4.3.3. The density value derived for EQ Peg A is higher than the one derived from O VII. Since Ne IX traces higher coronal temperatures, this may indicate a higher pressure in the hotter plasma

Table 4.2: Measured line counts and photon fluxes (in 10^{-5} photons cm^{-2} s^{-1}) in the combined *Chandra* MEG spectra. Flux predictions from the reconstructed DEMs (see Setc. 4.4.2) are also listed.

λ	ion	EQ Peg A				EQ Peg B			
[Å]		counts	photon fluxes	method 1	method 2	counts	photon fluxes	method 1	method 2
4.73	S XVI	22.3±5.6	0.61±0.15	0.42	0.32	—	—	—	—
5.04	S XV	28.7±6.3	0.84±0.18	0.92	0.94	—	—	—	—
6.18	Si XIV	176.6±14.6	1.78±0.15	1.92	1.86	30.4±5.9	0.31±0.06	0.21	0.13
6.65	Si XIII	321.6±19.7	2.74±0.17	2.71	2.75	40.4±6.8	0.34±0.06	0.36	0.37
6.69	Si XIII	61.7±10.6	0.53±0.09	0.72	0.73	5.0±3.4	0.04±0.03	0.10	0.10
6.74	Si XIII	202.5±16.2	1.58±0.13	1.31	1.33	25.7±6.0	0.20±0.05	0.19	0.19
8.42	Mg XII	178.9±15.9	1.45±0.13	1.58	1.60	30.2±6.0	0.24±0.05	0.25	0.23
9.17	Mg XI	107.7±12.4	1.58±0.18	1.54	1.50	26.0±5.6	0.38±0.08	0.32	0.34
9.23	Mg XI	33.9±8.2	0.51±0.12	0.36	0.35	6.7±3.4	0.10±0.05	0.08	0.08
9.31	Mg XI	34.6±8.4	0.55±0.13	0.81	0.78	11.2±3.9	0.18±0.07	0.17	0.18
10.24	Ne X	160.8±14.4	2.42±0.22	3.05	3.07	29.4±5.91	0.44±0.09	0.34	0.36
11.17	Fe XXIV	47.2±9.7	0.95±0.19	0.48	0.44	—	—	0.02	0.01
11.55	Ne IX	101.3±12.3	2.13±0.26	1.80	1.84	19.5±5.12	0.41±0.11	0.28	0.28
11.74	Fe XXIII	65.1±10.5	1.50±0.24	0.91	1.00	—	—	0.13	0.09
11.78	Fe XXII	44.9±9.6	1.11±0.24	1.12	1.29	—	—	0.11	0.17
12.13	Ne X	891.8±29.9	24.47±0.82	24.00	24.06	104.8±10.6	2.88±0.29	2.75	2.92
13.45	Ne IX	320.2±17.9	15.89±0.88	17.02	16.58	51.4±7.5	2.26±0.33	2.66	2.56
13.55	Ne IX	77.2±8.8	3.28±0.37	3.67	3.57	9.1±3.0	0.39±0.13	0.56	0.56
13.69	Ne IX	184.0±13.6	8.90±0.66	9.53	9.28	32.0±5.7	1.55±0.28	1.45	1.46
14.21	Fe XVIII	92.2±11.1	5.80±0.70	4.77	4.86	18.7±4.6	1.18±0.29	0.70	0.76
15.01	Fe XVII	270.1±17.3	15.72±1.01	18.74	18.51	43.2±7.0	2.51±0.40	3.29	3.31
15.26	Fe XVII	102.2±9.3	6.60±0.60	5.36	5.29	26.5±5.7	1.71±0.36	0.95	0.95
16.01	O VIII	193.1±14.5	13.71±1.03	8.40	8.33	27.2±5.7	1.93±0.40	0.89	1.03
16.78	Fe XVII	116.4±11.3	10.36±1.00	11.41	11.25	18.3±4.6	1.63±0.41	2.05	2.04
17.05	Fe XVII	144.7±12.7	14.36±1.26	14.51	14.30	24.8±5.2	2.46±0.52	2.60	2.59
17.10	Fe XVII	139.3±12.4	14.07±1.25	12.10	11.93	26.2±5.4	2.65±0.55	2.15	2.16
18.63	O VII	33.9±6.2	4.78±0.87	3.37	3.43	7.3±3.1	1.03±0.43	0.51	0.48
18.97	O VIII	435.8±21.1	71.90±3.48	70.50	69.90	63.4±8.2	10.46±1.36	7.77	8.82
21.60	O VII	69.6±8.6	24.21±2.98	30.53	31.30	7.6±2.8	1.56±0.91	4.78	4.40
21.81	O VII	14.2±4.0	5.64±1.59	6.83	7.07	3.7±2.0	1.47±0.79	1.45	0.99
22.10	O VII	24.0±5.1	10.95±2.33	18.08	18.70	10.3±3.5	4.70±1.6	3.71	2.62
24.79	N VII	19.3±4.5	7.84±1.85	7.84	7.84	2.0±1.7	0.80±0.72	0.80	0.80

Table 4.3: Measured line counts and photon fluxes in the *Chandra* MEG spectra of the quiescent state of EQ Peg A.

λ [Å]	ion	counts	fluxes
4.73	S XVI	8.6±4.1	0.25±0.12
5.04	S XV	22.6±5.8	0.70±0.18
6.18	Si XIV	143.7±13.2	1.54±0.14
6.65	Si XIII	317.7±19.1	2.87±0.17
6.69	Si XIII	57.0±10.1	0.52±0.09
6.74	Si XIII	193.6±15.6	1.60±0.13
8.42	Mg XII	175.4±15.3	1.51±0.13
9.17	Mg XI	98.7±11.8	1.54±0.18
9.23	Mg XI	27.5±8.1	0.44±0.13
9.31	Mg XI	31.9±8.4	0.54±0.14
10.24	Ne X	155.6±14.0	2.49±0.22
11.17	Fe XXIV	20.6±7.6	0.44±0.16
11.55	Ne IX	90.3±11.5	2.02±0.26
11.74	Fe XXIII	45.9±9.0	1.12±0.22
11.78	Fe XXII	42.4±9.0	1.11±0.24
12.13	Ne X	813.8±28.5	23.75±0.83
13.45	Ne IX	293.4±17.1	13.67±0.80
13.55	Ne IX	61.1±7.8	2.76±0.35
13.69	Ne IX	169.1±13.0	8.69±0.67
14.21	Fe XVIII	82.7±10.6	5.53±0.71
15.01	Fe XVII	266.3±16.9	16.45±1.05
15.26	Fe XVII	92.8±10.7	7.39±0.77
16.01	O VIII	184.8±14.0	13.69±1.05
16.78	Fe XVII	114.3±11.0	10.80±1.04
17.05	Fe XVII	139.9±12.6	14.73±1.33
17.10	Fe XVII	137.2±12.4	14.70±1.33
18.63	O VII	30.3±5.6	4.55±0.87
18.97	O VIII	414.0±20.5	72.49±3.60
21.60	O VII	64.5±8.3	23.76±3.06
21.81	O VII	14.0±4.0	5.91±1.69
22.10	O VII	24.0±5.1	11.62±2.47
24.79	N VII	15.0±4.3	6.47±1.85

regions, however, the uncertainties do not include uncertainties from the deblending procedure. The f/i-ratio derived for the B component is – nominally – in the low-density limit region, however, the error is so large that the same density derived for the A component is also consistent with the data. The Mg and Si triplets are much stronger affected by satellite lines. Additionally, the Mg XI triplet is blended with higher-order lines from the Lyman series of Ne X as discussed by Testa et al. (2004). The flux in the magnesium triplet lines is too low in both components of the EQ Peg binary for a deblending procedure to yield any useful refinements. Since neon turns out to be far more abundant than magnesium (see Sect. 4.4.2), the blending contributions from neon amounts to a significant fraction of the line fluxes, and we consider the high densities derived from magnesium not reliable. Consistent with that interpretation, the Si XIII triplet lines are consistent with being in the low-density limit, which is not surprising since the density-sensitive range for this ion is higher than the densities normally encountered in stellar coronae. However, the Si triplet is also problematic because of a steep increase of the effective area in both the HEG and MEG that occurs exactly at the wavelength of the forbidden line.

The flux in the Ne IX triplet of EQ Peg A is large enough to investigate not only the density in the combined spectrum, but also in the individual datasets. In Fig. 4.5 we show the corresponding spectral region for each of our four data sets. While differences in the strength of the intercombination line at 13.55 Å are apparent in the individual datasets, no changes in density can be established at a statistically significant level. In addition to the complete dataset 8485, we show also the spectrum extracted for the large flare (shaded in gray in the bottom left panel of Fig. 4.5). Dividing this observation in flare and non-flaring states gives f/i-ratios of 1.13±0.59 and 2.24±0.61, or density values log n_e of $12.07^{+0.43}_{-0.31}$ and $11.49^{+0.32}_{-0.43}$, respectively. For the combined quiescent spectrum, we find $f/i = 2.77 \pm 0.42$, corresponding to log $n_e = 11.13^{+0.29}_{-0.09}$, which is lower but still consistent with the total spectrum (see Table 4.4) and clearly lower than during the large flare. This indicates activity-related density variations as observed by Maggio & Ness (2005) on the active M dwarf AD Leo. Unambiguous measurements of coronal density variations have so far only been observed during very large flares on the active M dwarfs Proxima Centauri and CN Leo (Güdel et al. 2002a; Liefke et al. 2007). The two density values derived here for flare and quiescence are consistent with each other at the 2σ level, however, the density values observed during flares on active stars in general – although consistent with the quiescent state – tend to result in higher densities (see e. g. Mitra-Kraev & Ness 2006).

We also note the different levels of contamination of the neon triplet by Fe XVII (13.8 Å) and Fe XIX (13.51 Å) in the different datasets. During the large flare, this can be attributed on the one hand to the higher coronal temperatures increasing the amount of Fe XIX compared to other ionization stages of iron, and on the other hand possibly also to an increased Fe/Ne abundance ratio during the flare, as discussed below.

4.4.2 Differential emission measure

In order to derive absolute abundances we investigated the differential emission measure (DEM) of the two stars from the line fluxes of the strongest

Table 4.4: f/i ratios (in photon units) and coronal densities for EQ Peg A and B from total *Chandra* MEG spectra.

		EQ Peg A		EQ Peg B	
ion	$\log T$	f/i	$\log n_e$	f/i	$\log n_e$
O VII	6.3	1.69 ± 0.60	$10.62^{+0.29}_{-0.27}$	2.81 ± 0.87	< 10.98
Ne IX	6.6	2.38 ± 0.32	$11.40^{+0.18}_{-0.22}$	3.53 ± 1.33	< 11.51
Mg XI	6.8	1.01 ± 0.35	$12.99^{+0.27}_{-0.23}$	1.68 ± 1.04	< 13.28
Si XIII	6.95	3.28 ± 0.62	< 11.17	5.08 ± 3.64	< 13.52

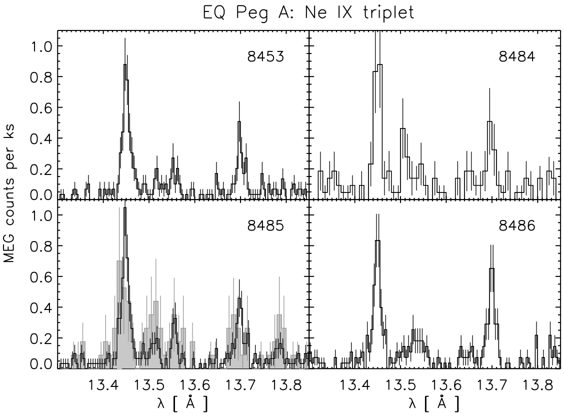

Figure 4.5: The Ne IX triplet in the MEG spectra of EQ Peg A during the four observations. On observation No. 8485 the flare spectrum only is overlaid in gray.

density-insensitive lines listed in Table 4.2. For EQ Peg A, the HEG spectrum can also be used in addition to the MEG spectrum, while for EQ Peg B only the MEG spectrum provides data with a reasonable signal-to-noise ratio. In a two-step procedure we first reconstructed the DEM utilizing an abundance-independent approach similar to the one proposed by Schmitt & Ness (2004). In a second step we then determined the abundances from the ratios of measured line fluxes to those predicted by the DEM.

We used a volume differential emission measure defined as

$$DEM(T) = n_e^2 \, \frac{dV}{dT} \tag{4.1}$$

in units cm^{-3} K^{-1}. The DEM is related to the theoretical photon flux f_{ji} (in photons cm^{-2} s^{-1}) of a spectral line originating from an atomic transition from the upper level j to the lower level i in the ion X^{Z+} by

$$f_{ji} = \frac{A_X}{4\pi d^2} \int G(T) \, DEM(T) \, dT \tag{4.2}$$

where A_X is the abundance of element X relative to solar photospheric values and the line contribution function $G(T)$ with

$$G(T) = A_{ji} \, \frac{n_j(X^{Z+})}{n(X^{Z+})} \frac{n(X^{Z+})}{n(X)} \frac{n(X)}{n(H)}_{\odot} \frac{n(H)}{n_e} \frac{1}{n_e} \tag{4.3}$$

A_{ji} being the Einstein coefficient for spontaneous emission of the transition, $n_j(X^{Z+})/n(X^{Z+})$ the level population of the upper level, $n(X^{Z+})/n(X)$ the ionization balance, $n(X)/n(H)_{\odot}$ the solar photospheric abundance, and $n(H)/n_e$ the proton-to-electron ratio, which is ≈ 0.83 for coronal plasmas where hydrogen and helium are usually fully ionized. While the DEM describes the properties of the emitting plasma, the line contribution function summarizes constants and the underlying atomic physics. We used CHIANTI 5.2 (Landi et al. 2006) and the ionization balance of Mazzotta et al. (1998) to calculate $G(T)$ for each line.

Our abundance-independent reconstruction of the DEM is based on line ratios, and we used the ratios of the H-like Lyα and the He-like resonance lines of oxygen, neon, magnesium, and silicon, plus several ratios of adjacent ionization stages of iron from Fe XVII to Fe XXIV. Since these line ratios involve only lines of the same element, the elemental abundances cancel out, and each ratio poses a constraint on the shape of the DEM. The choice of these lines yields a temperature coverage from ≈ 2 to 20 MK, however, the low effective area at longer wavelengths with low-temperature lines like O VII and O VIII results in relatively large uncertainties at temperatures below 5 MK. For EQ Peg A, a total of 13 ratios have been used, while some of the ratios consisting of higher ionization stages of iron could not be used for the B component because of low signal, leaving only 9 usable ratios. In order to fix the absolute level of the DEM in addition to constraining the shape by the ratios, but still independently of a reference element like iron, we force the DEM and the theoretical continuum emissivity as implemented in CHIANTI to reproduce the observed continuum flux. For both components of EQ Peg, we used the wavelength region around 7.5 Å, where the effective area of the MEG reaches its maximum, and the spectrum is, according to the CHIANTI database, essentially line-free, exept for a few weak aluminum and magnesium lines. We assume that any remaining emission at these wavelengths originates from the continuum and neglect the contribution of any further weak transitions. As a result of merging the four datasets, the determined DEMs constitute an average over these observations with the different states of activity and quiescent and flaring periods of the two stars.

We used two slightly different approaches to model the DEM, that we parameterize by polynomials of different orders. In our first method (method 1) we fitted the polynomial parameters as $\log DEM$, and with our second method (method 2) we model the linear DEM, both as a function of $\log T$. While for method 1 no boundary conditions are needed, for method 2 we forced the value of DEM to be zero at two variable temperatures, and positive between these temperatures. For a more detailed description we refer to Liefke & Schmitt (in preparation).

For EQ Peg A, both methods give acceptable best-fits to the selected line ratios assuming 3rd and 5th order polynomials, yielding values of reduced χ^2 of 2.06 and 2.36 for methods 1 and 2, respectively. These DEMs are shown in the top panel of Fig. 4.6. The polynomials are an analytical representation of the shape of the DEM, which is only valid for certain temperature range which is at first restricted by the temperature range covered by the emissivities of the lines implemented in the fit. In Fig. 4.6 we additionally plot the polynomials with solid lines in the temperature range we consider as well-constrained from the available lines, and with dashed or dotted lines outside this range. Since the high-temperature regime is better represented by the available ratios than the low-temperature range (see above), the two methods yield best agreement at high temperatures. However, the peaks in the DEM disagree from the two methods, and the poor constraints from temperatures $\log T$ below 6.5 lines make it difficult to quantify the exact amount of cool material; this may even falsely hint at a DEM peak at a lower temperature.

For EQ Peg B, this becomes even more apparent, see the bottom panel of Fig. 4.6. The best-fit results are obtained with 4th order polynomials with both methods, with reduced χ^2 values of 1.67 and 1.85; however, the two approaches give consistent results only in the range of $6.8 < \log T < 7.2$. The DEM reconstructed from method 2 shows an unphysical increase towards lower temperatures due to the fact that no ratios are available to adequately constrain the low-temperature slope.

When introducing higher-order polynomials (orders > 5), the DEMs of both stars start to develop two-peaked structures with maxima at $\log T \approx 6.2$–6.4 and 6.8–7.2. This would correspond to a low- and a high temperature component, where the first one causes the strong oxygen line fluxes, and the hotter component is related to the typical active M dwarf corona and the observed flares. However, the DEMs constructed with higher-order polynomials are often unstable, and the location and strength of certain structures often depends only on a single line flux measurement. Thus we cannot be certain about the reality of these structures, and we prefer the "simpler" DEMs with fewer free parameters.

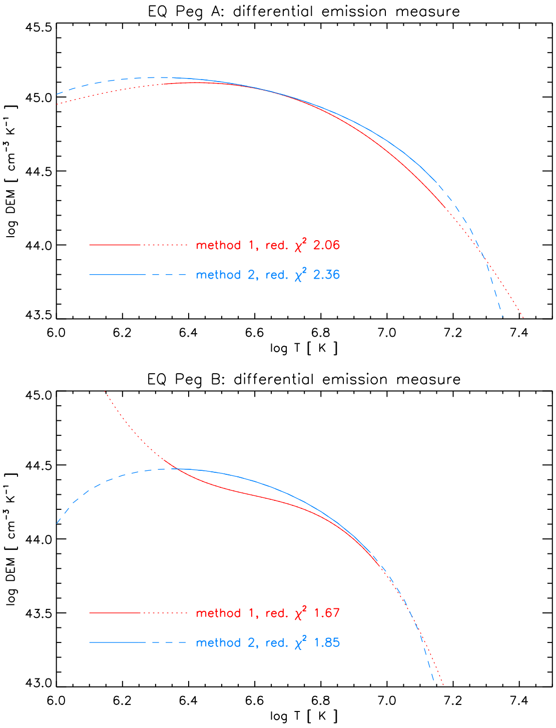

Figure 4.6: Differential emission measures of EQ Peg A (top) and B (bottom) for the total observation time (i. e. flare and quiescence).

Next, we used the DEMs from these two approaches for the two stars to predict line fluxes. Since the DEMs are determined independently of the abundances and are normalized to the continuum, any discrepancies between predictions and measurements of line fluxes must be due to different abundances than those assumed in predicting the line fluxes from a given DEM (here Asplund et al. 2005).

In Table 4.5 we list our results for the abundances with statistical uncertainties derived from the measurement uncertainties of the line fluxes; note that the quoted errors only reflect the statistical precision of the line flux measurements, but not the accuracy of the DEM nor the uncertainties from the continuum flux nor any errors arising from the atomic physics parameters used. The errors in the continuum amount to 2.5% and 8.2% for EQ Peg A and B, respectively, and affect only the absolute abundance level. While we experience great uncertainties in determining the exact shape of the DEM, the determination of abundances seems to be only relatively little affected. Polynomials of different orders always give abundances consistent within the errors and the abundances derived with method 1 are always consistent with those obtained from method 2. Similarly, Ness & Jordan (2008) performed a detailed emission measure analysis of ϵ Eridani, including ionization stages from many different ions. Close to the peak, their emission measure distribution agrees with that by Sanz-Forcada et al. (2004), but is more accurate at low temperatures. In spite of the differences, both find similar abundances. In general, the derived abundances turn out to be quite insensitive to changes in the shape of the DEM, polynomials of different orders always give abundance value consistent within the errors. Additionally, the abundances derived with method 1 are always consistent with those obtained from method 2. Liefke & Schmitt (in preparation) assess that the uncertainties on the abundances introduced by uncertainties on the shape of the DEM do not exceed 5%.

In Table 4.5 we show that the absolute abundances relative to Asplund et al. (2005) of EQ Peg A and B are roughly consistent for all elements, yielding a low metallicity compared to solar. This is typical for active M dwarfs (compare e. g. with the values derived by Robrade & Schmitt 2005, from global fitting approaches to CCD X-ray spectra). Nitrogen, oxygen, and neon may be somewhat more abundant in the A component, however, not at a statistically significant level; also note that the uncertainties for N and O are quite large. While the high-FIP element neon is about solar, the low-FIP element iron shows the lowest abundance value, and the other elements also follow the typical inverse FIP effect.

The computed abundances and DEMs can now be used to model the spectra of EQ Peg A and B. We list the calculated theoretical line fluxes together with the measured fluxes in Table 4.2.

4.4.3 Emission measure-independent abundances

Given the ill-posed nature of the DEM determinations and the resulting uncertainties in the DEM distributions, we also investigated emission measure-independent abundance determinations. The strongest lines in stellar coronal X-ray spectra (and thus easy to measure even in spectra with low signal) originate from the H-like and He-like lines of carbon, nitrogen, oxygen, neon, magnesium, and silicon, as well as Ne-like Fe XVII. In Fig. 4.7 we show the line emissivities for these ions as a function of temperature. While these lines are formed over a broad temperature range, their emissivity peaks are relatively narrow. Those lines for which the line contribution functions have similar peak formation temperatures yield a similar temperature dependence. Ratios of their line fluxes depend only weakly on temperature, but strongly on the abundance ratio of the respective elements. Already Acton et al. (1975) proposed to determine the solar coronal Ne/O abundance ratio from the ratio of the measured fluxes of the Ne IX resonance and O VIII Ly α lines. This method yields a comparably high precision (because of smaller measurement uncertainties), and also a higher accuracy (because no systematic uncertainties from the DEM are introduced). Recent examples of such approaches were presented by Schmitt & Ness (2002) and Drake & Testa (2005).

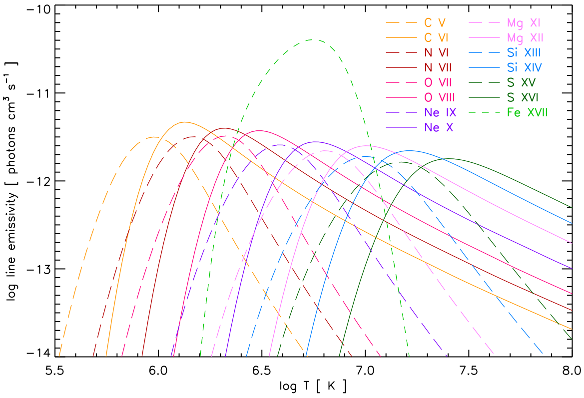

Figure 4.7: Line emissivity curves for different H-like and He-like ions, and Fe XVII at 15.01 Å from CHIANTI 5.2 (Landi et al. 2006) with the ionization balance from Mazzotta et al. (1998).

While for a given element, the peak formation temperature of the H-like ion always exceeds that of the corresponding He-like ion, the peak formation temperatures of the H-like and He-like ions shift to higher temperature with increasing atomic mass. Therefore, pairs of H-like and He-like ions of elements with different atomic mass yield similar peak formation temperatures, and their contribution functions have similar shapes. Further examples for such pairs are the H-like lines and He-like lines of carbon and nitrogen, nitrogen and oxygen, neon and magnesium, and magnesium and silicon respectively (Parkinson 1977). However, these ratios are not perfectly temperature-independent, and Drake & Testa (2005) have refined Acton's method by computing a linear combination of Ne X Ly α and the Ne IX r line in order to construct a new contri-

Table 4.5: Absolute coronal abundances (relative to Asplund et al. 2005) of EQ Peg A and B for the total observation time, determined with the DEM methods.

	EQ Peg A		EQ Peg B	
element	method 1	method 2	method 1	method 2
N	0.42±0.10	0.39±0.09	0.16±0.15	0.20 ±0.18
O	0.42±0.04	0.40±0.04	0.15±0.09	0.26 ±0.08
Ne	1.14±0.07	1.07±0.07	0.93±0.07	0.83 ±0.07
Mg	0.22±0.01	0.20±0.02	0.28±0.04	0.27 ±0.04
Si	0.51±0.02	0.46±0.02	0.54±0.07	0.52 ±0.07
S	0.64±0.16	0.58±0.21	—	—
Fe	0.19±0.02	0.18±0.01	0.20±0.02	0.17 ±0.02

bution function of Ne lines that is more similar in shape to the O VIII Ly α line.

This suggests to ask in general, which linear combinations of strong lines without significant blends (i. e. hydrogen- and helium-like lines and the strongest lines of Fe XVII as mentioned above) of two certain elements yield the smallest temperature residuals in their normalized contribution functions. We thus write for the abundance ratio of two elements with respective abundances A_1 and A_2

$$\frac{\mathrm{A}_1}{\mathrm{A}_2} = \frac{f(\mathrm{A}_1^{\mathrm{Z}-1}) + C_1 \cdot f(\mathrm{A}_1^{\mathrm{Z}})}{C_2 \cdot f(\mathrm{A}_2^{\mathrm{Z}-1}) + C_3 \cdot f(\mathrm{A}_2^{\mathrm{Z}})}, \tag{4.4}$$

with $f(\mathrm{A}_1^{\mathrm{Z}-1})$ and $f(\mathrm{A}_2^{\mathrm{Z}-1})$ denoting the measured line fluxes f of the He-like resonance lines and $f(\mathrm{A}_1^{\mathrm{Z}})$, and $f(\mathrm{A}_2^{\mathrm{Z}})$ the corresponding H-like Lyα lines of two elements A_1 and A_2, respectively, and

$$\frac{\mathrm{A}}{\mathrm{A}_{\mathrm{Fe}}} = \frac{C_4 \cdot (f(\mathrm{A}^{\mathrm{Z}-1}) + C_5 \cdot f(\mathrm{A}^{\mathrm{Z}}))}{\sum f(\mathrm{Fe\,XVII})} \tag{4.5}$$

where $\sum f(Fe\,\mathrm{XVII})$ corresponds to $f(Fe\,\mathrm{XVII}$ 15.01 Å) + $f(Fe\,\mathrm{XVII}$ 16.78 Å) + $f(Fe\,\mathrm{XVII}$ 17.05 Å) + $f(Fe\,\mathrm{XVII}$ 17.09 Å), to determine relative abundance ratios.

To obtain the coefficients C_1, C_2, C_3, C_4, and C_5, we performed a minimization of the temperature residuals of the corresponding linear combination of the theoretical emissivities ϵ for the involved lines over a given temperature range:

$$\chi^2 = \sum_i \Big(\epsilon_i(\mathrm{A}_1^{\mathrm{Z}-1}, T_i) + C_1 \cdot \epsilon_i(\mathrm{A}_1^{\mathrm{Z}}, T_i) - C_2 \cdot \epsilon_i(\mathrm{A}_2^{\mathrm{Z}-1}, T_i) - C_3 \cdot \epsilon_i(\mathrm{A}_2^{\mathrm{Z}}, T_i) \Big)^2 \tag{4.6}$$

for the coefficients in Eqn 4.4, and

$$\chi^2 = \sum_i \Big(\epsilon_i(\mathrm{A}^{\mathrm{Z}-1}, T_i) + C_5 \cdot \epsilon_i(\mathrm{A}^{\mathrm{Z}}, T_i) - \frac{1}{C_4} \cdot \sum \epsilon_i(\mathrm{Fe\,XVII}, T_i) \Big)^2 \tag{4.7}$$

for the coefficients in Eqn 4.5.

In Table 4.6 we list these coefficients for the temperature range where the line emissivities of all involved lines exceed 1% of their peak emissivity. In the given form, the coefficients convert the measured line fluxes in photon flux units to absolute abundance ratios, i. e. independent from any set of solar photospheric abundances; we used line emissivities from CHIANTI 5.2 (Landi et al. 2006).

There are still residuals in temperature for these linear combinations, and their amplitudes differ for each ratio. We found the lowest residuals for the Si/Mg ratio and the largest ones for the Ne/O ratio. In Fig. 4.8 we illustrate the best-fit linear combination of emissivities that yield the Si/Mg abundance ratio, and for the Ne/O ratio we refer to Fig. 3 of Liefke & Schmitt (2006), who had used the same coefficients as listed here to calculate the Ne/O abundance ratio of α Centauri. The first six ratios involve only H-like Ly α and He-like resonance lines. However, the S/Si ratio should only be used when the sulfur lines can be measured with reasonable signal-to-noise in *Chandra* HETGS spectra. Fe XVII can be matched with linear combinations of hydrogen- and helium-like lines of neon or magnesium. The residuals are much smaller for Mg, however, the Mg lines are often weak, introducing large measurement uncertainties. Especially the weak Mg XI line carries a large weight, and for the determination of Fe abundances we prefer the Ne/Fe ratio despite its larger residuals.

The coefficients of the linear combinations as listed in Table 4.6 can be adjusted in some cases where certain line fluxes are not available (e. g. the C V lines can only be measured with the *Chandra* LETGS), or are extremely weak (e. g. Mg XI or N VI, depending on temperature). The line fluxes $f(\mathrm{A}_1^{\mathrm{Z}-1})$ and $f(\mathrm{A}_2^{\mathrm{Z}})$ with $\mathrm{Z(A_1)} > \mathrm{Z(A_2)}$ provide the major constituents of the linear combinations for the ratios not involving Fe.

For example, the N VI resonance line is often weak in stars with hot coronae and is difficult to mea-

Table 4.6: Coefficients for Eqns 4.4 and 4.5 to obtain temperature-independent abundance ratios.

ratio	C_1	C_2	C_3	C_4	C_5
N / C	+0.13	−0.07	+0.73	—	—
O / N	+0.30	+0.01	+0.93	—	—
Ne / O	+0.02	−0.17	+0.69	—	—
Mg / Ne	+0.18	−0.08	+0.87	—	—
Si / Mg	+0.32	+0.05	+0.86	—	—
S / Si	+0.42	+0.15	+0.85	—	—
Ne / Fe	—	—	—	+34.71	+0.46
Mg / Fe	—	—	—	+67.73	−0.30

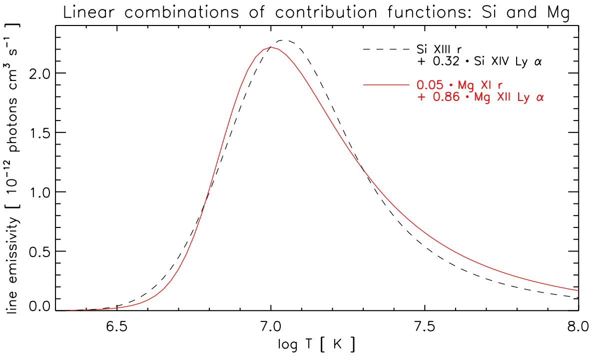

Figure 4.8: Best-fit linear combination of the contribution functions of the H-like Ly α and He-like resonance lines of silicon and magnesium.

sure in *Chandra* MEG spectra, however, this line contributes much less to the nitrogen linear combination in the O/N ratio than the N VII Ly α line (i. e. C_2 is much smaller than C_3). We readjusted C_1, and C_3 assuming the fixed value $C_2 = 0$ and found only marginal changes for the values of the other coefficients listed in Table 4.6. Although the value of C_1 is also quite low for the Ne X Ly α line in the Ne/O ratio, the situation is somewhat different. If we readjust the other coefficient after setting $C_1 = 0$, the residuals are much larger, especially at high temperatures where the emission measure distributions of active stars usually have their maximum.

Finally, the coefficients can be re-computed for the sum of the He-like resonance, intercombination, and forbidden lines for cases where these lines can not be resolved (e. g. Si XIII with the *Chandra* LETGS).

We applied Eqns 4.4 and 4.5, with the coefficients from Table 4.6 multiplied by the solar photospheric abundances of Asplund et al. (2005), to the line fluxes measured from the spectra of EQ Peg A (including and excluding periods of flare activity) and of EQ Peg B and list the resulting abundance ratios in Table 4.7.

Within the uncertainties, the derived abundance ratios are consistent for all three datasets. Only the Ne/Fe ratio is conspicuously lower in the quiescent spectrum of EQ Peg A compared to the total spectrum, and again lower for the more inactive EQ Peg B. Flare- or activity-related changes in the abundance ratios cannot be determined from count statistics; however, if real, the differences may be caused by a decreased iron abundance level or a higher neon abundance on the more active A component, especially during flares.

In Table 4.8 we list the abundance ratios formed from the absolute values listed in Table 4.5 for comparison. They are consistent within the errors with the values in Table 4.7, but the ratios obtained from the emission measure-independent method are more robust and have lower uncertainties.

4.5 EQ Peg in the context of active M dwarfs

In order to put EQ Peg into the context of other similar late-type stars, we extracted five additional *Chandra* HETGS spectra of active M dwarfs for comparison with our results; our sample thus contains YY Gem, AU Mic, EV Lac, AD Leo, and Proxima Cen in addition to EQ Peg A and B. Most of these archival observations have been included in many studies (e. g. Ness et al. 2003c, 2004; Testa et al. 2007), the X-ray lightcurves and spectra of AU Mic, EV Lac, and Proxima Cen are shown by Testa et al. (2004). While the two stars in the binary EQ Peg are co-eval, we are now dealing with a range of different ages, rotation periods, and metallicity. In Table 4.9 we summarize for each star their spectral type, distance (from the SIMBAD database), age estimates and rotation periods from the literature together with observation ID, exposure time, and X-ray luminosity obtained from integration of the dispersed photons over the range 2–25 Å. The bolometric luminosity for L_X/L_{bol} has

Table 4.7: Abundance ratios (relative to Asplund et al. 2005) applying temperature structure-independent linear combinations of coronal emission lines. Values given in brackets for EQ Peg A correspond to the quiescent state.

ratio	EQ Peg A		EQ Peg B
O / N	0.83±0.20	(1.00±0.29)	0.81±0.72
Ne / O	2.48±0.31	(2.02±0.16)	2.18±0.41
Mg / Ne	0.20±0.02	(0.19±0.02)	0.32±0.07
Si / Mg	2.52±0.21	(2.56±0.25)	2.05±0.44
S / Si	1.26±0.20	—	—
Ne / Fe	7.30± 0.64	(5.99± 0.34)	5.45 ± 0.78
Mg / Fe	1.27± 0.17	(1.09± 0.19)	1.63± 0.43

Table 4.8: Abundance ratios relative to Asplund et al. (2005) of EQ Peg A and B, determined from the absolute abundances listed in Table 4.5.

	EQ Peg A		EQ Peg B	
ratio	method 1	method 2	method 1	method 2
O / N	1.00±0.25	1.03±0.26	0.94±0.94	1.30 ±1.24
Ne / O	2.71±0.31	2.68±0.32	6.20±3.75	3.19 ±0.94
Mg / Ne	0.19±0.01	0.19±0.02	0.30±0.05	0.33 ±0.06
Si / Mg	2.32±0.14	2.30±0.25	1.93±0.37	1.93 ±0.39
S / Si	1.25±0.32	1.26±0.46	—	—
Ne / Fe	6.00±0.73	5.94±0.51	4.65±0.58	4.88 ±0.71
Mg / Fe	1.15±0.13	1.11±0.13	1.40±0.24	1.59 ±0.30

been calculated according to Kenyon & Hartmann (1995). While the X-ray luminosity decreases along the sequence of spectral types, $L_X/L_{\rm bol}$ is in the saturation regime of ≈ -3.3 for all stars except Proxima Cen.

YY Gem is an M0.5 companion of the Castor AB system. YY Gem itself is an eclipsing binary consisting of two almost identical early M dwarfs with an orbital period of 0.814 days at an inclination of 86.2, separated by 3.88 $R_\odot$. From eclipse mapping techniques based on an *XMM-Newton* observation, Güdel et al. (2001) found similar activity levels on both components, but concentrated in compact active regions at small scale heights, i. e. inter-binary loops as discussed for RS CVn systems are rather unlikely. This is confirmed by Stelzer et al. (2002), who modelled a flare in a simultaneous *XMM-Newton* and *Chandra* LETGS observation. Several strong flares occur also in the two HETGS observations discussed here. The young ($\approx$ 10 Myrs) star AU Mic, spectral type M1, has the highest X-ray luminosity within 10 pc to the Sun and has thus been extensively observed in X-rays and in the EUV. AU Mic shows a strong level of variability on all time scales and a high flare rate. From the HETGS dataset used here, Linsky et al. (2002) computed an emission measure distribution with a peak temperature of $\log T \approx 6.8$ and subsolar abundances with a pronounced inverse FIP effect. Magee et al. (2003) found similar values for the abundances based on an *XMM-Newton* observation. The *Chandra* HETGS observation of the M3.5 star EV Lac is part of a multiwavelength campaign and has been discussed in detail by Osten et al. (2005, 2006). Several flares occurred towards the end of the observation, and Osten et al. (2005) compared line ratios with different FIP dependencies during flares and quiescence and find a slight increase for low FIP/high FIP ratios during flares. Osten et al. (2006) derive a subsolar abundance level and an inverse FIP effect from an emission measure distribution of the quiescent state, with values consistent with an *XMM* observation analyzed by Robrade & Schmitt (2005). Both EV Lac and the M4.5 star AD Leo are young stars from the galactic disk population. AD Leo is another a well-known flare star (e. g. Hawley et al. 2003), however, no larger flares have occurred during the *Chandra* HETGS observation discussed here. This dataset was analyzed by Maggio & Ness (2005), with the focus on density diagnostics. Maggio et al. (2004) found a mild inverse FIP bias based on two *Chandra* LETGS observations, which is roughly consistent with the results obtained by Robrade & Schmitt (2005) and from an *XMM-Newton* observation. van den Besselaar et al. (2003) analyzed the same data. While Robrade &

Table 4.10: Abundance ratios of other M dwarfs observed with the *Chandra* HETGS. Values obtained for the quiescent state are given in brackets.

ratio	YY Gem		AU Mic		EV Lac		AD Leo	Proxima Cen	
O / N	0.62±0.12	(0.57±0.14)	0.48±0.09	(0.48±0.11)	0.53±0.10	(0.76±0.15)	0.60±0.13	0.30±0.09	(0.34±0.14)
Ne / O	1.97±0.12	(2.10±0.18)	2.36±0.19	(2.31±0.20)	2.07±0.50	(1.71±0.12)	2.33±0.19	1.72±0.31	(2.06±0.54)
Mg / Ne	0.18±0.02	(0.16±0.02)	0.11±0.01	(0.12±0.02)	0.24±0.02	(0.22±0.02)	0.21±0.02	0.31±0.06	(0.35±0.10)
Si / Mg	2.31±0.18	(2.59±0.31)	2.33±0.26	(1.84±0.26)	2.47±0.22	(2.25±0.25)	2.46±0.30	2.48±0.28	(2.50±1.28)
S / Si	1.27±0.18	(1.46±0.33)	—	—	1.82±0.33	—	—	—	—
Ne / Fe	7.08±0.33	(7.34±0.46)	8.85±0.57	(9.03±0.59)	5.73±0.29	(5.17±0.26)	6.78±0.41	4.44± 0.59	(4.45± 0.82)
Mg / Fe	1.23±0.19	(1.24±0.24)	0.84±0.18	(1.03±0.26)	1.28±0.15	(1.28±0.15)	1.13±0.19	1.44± 0.35	(1.60± 0.49)

Table 4.9: Properties of active M dwarfs observed with *Chandra* HETGS. X-ray luminosities are computed from the total background-subtracted counts contained in the MEG spectra from 2–25 Å. Values given in brackets correspond to the quiescent state.

star	spectral type	distance [pc]	age [Myrs]	$\mathrm{P_{rot}}$ [d]	ObsID	exposure time [ks]		log L_X		log $L_\mathrm{X}/L_\mathrm{bol}$	
YY Gem	M 0.5	15.27	370^1	0.814^5	8504/8509	136.0	(81.5)	29.63	(29.43)	−3.17	(−3.37)
AU Mic	M 1	9.94	12^2	4.865^6	17	58.8	(47.4)	29.19	(29.13)	−3.48	(−3.54)
EQ Peg A	M 3.5	6.25	950^3	(1.066^7)	8453/8484/8485/8486	98.5	(92.8)	28.71	(28.67)	−3.19	(−3.23)
EV Lac	M 3.5	5.05	45^3	4.376^8	1885	100.0	(87.3)	28.63	(28.51)	−3.10	(−3.22)
AD Leo	M 4.5	4.69	470^3	$2.7/14^{9,10}$	2570	45.2	—	28.54	—	−3.36	—
EQ Peg B	M 4.5	6.25	950^3	(1.066^7)	8453/8484/8485/8486	98.5	—	27.89	—	−3.39	—
Proxima Cen	M 5.5	1.30	5800^4	83.5^{10}	2388	42.4	(35.7)	26.85	(26.60)	−3.96	(−4.21)

[1] Torres & Ribas (2002), [2] Zuckerman et al. (2001), [3] Parsamyan (1995), [4] Yıldız (2007) , [5] Kron (1952), [6] Torres et al. (1972), [7] Norton et al. (2007), [8] Pettersen et al. (1992), [9] Spiesman & Hawley (1986), [10] Mahmoud (1993), [11] Benedict et al. (1998)

Schmitt and van den Besselaar et al. determined an overall subsolar abundance level, Maggio et al. found values much higher than for the solar photosphere, however with a large uncertainty in the overall normalization. EQ Peg A, EV Lac, and AD Leo have comparable X-ray luminosities. On the basis of a common origin with the α Centauri system, Proxima Cen can be considered older than the Sun. With a spectral type of M5.5, it is also the latest star in our sample. Its X-ray luminosity is comparable to the Sun, more than two orders of magnitude lower than that of AU Mic. Nevertheless, Proxima Cen is also a well-known flare star. Güdel et al. (2002a) and Güdel et al. (2004) discussed a large-amplitude long-duration flare observed with *XMM-Newton.* Güdel et al. (2004) and Nordon & Behar (2008) derived emission measure distributions for the different phases of the flare and found abundance ratios relative to iron to stay roughly constant, but with an overall tendency to an inverse FIP effect in the absolute level. Two flares are also included in the HETGS observation analyzed here.

In order to obtain self-consistent results, we applied the same data reduction and analysis techniques as described above to the spectra of the other four sample stars. However, even with typical flare rates and amplitudes for active M dwarfs known, the occurrence of individual flares is randomly distributed, and each X-ray observation is a snapshot that is not necessarily representative of the typical flaring behavior of the observed star. We filtered the observation for quiescent-only emission and include the quiescent luminosities in brackets in the last column of Tables 4.9.

We also computed the cumulative count spectra for the other five spectra as that shown in Fig. 4.3 for EQ Peg. In Fig. 4.9 we show these spectra for the quiescent states of the five stars as labeled in the legends, together with the well-exposed reference spectrum of Capella. For comparison, we included the cumulative spectra of EQ Peg A and B, bracketing the gray-shaded areas. In these plots, YY Gem, AU Mic and EV Lac are similar to the EQ Peg system, with YY Gem very similar to EQ Peg A, while AU Mic has stronger neon lines than EQ Peg, leading to larger steps in the cumulative distribution. AD Leo is more similar to EQ Peg B, and Proxima Cen is even softer. All seven M dwarfs differ considerably from Capella.

We applied our DEM-independent abundance determination using Eq. 4.4 with the coefficients listed in Table 4.6 to the total and quiescent-only spectra of AU Mic, EV Lac, AD Leo, and Proxima Cen and list the results in Table 4.10. These numbers have to be compared to the relative abundances for EQ Peg A and B listed in Table 4.7. For comparison of our results with other abundance determinations for our sample stars, we transformed the values determined by Robrade & Schmitt (2005), Güdel et al. (2001), Linsky et al. (2002), Magee et al. (2003), Osten et al. (2006), Maggio et al. (2004), and Güdel et al. (2004) to the reference set of solar photospheric abundances from Asplund et al. (2005) and found good agreement within the errors. Only for neon we found a slight tendency of overestimating the abundance, as the blends to the neon lines may not always have been taken properly into account.

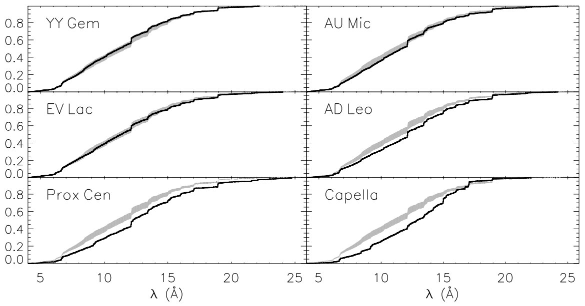

Figure 4.9: Cumulative distribution of counts in the quiescent spectra of the reference star Capella and other M dwarfs observed with the *Chandra* HETGS. The area between the curves for EQ Peg A and B is indicated in shades of gray for comparison.

For all seven stars, the Ne/O ratio is enhanced by about a factor of 2, which is well-consistent with what Drake & Testa (2005) found for their sample of active stars. Si/Mg is also enhanced by a factor of about 2, while Mg/Ne is depleted by factors from 3 (EQ Peg B and Proxima Cen) up to 10 (AU Mic). The values for O/N range from 0.3–1.0 times the solar level, partly with large uncertainties. The Ne/Fe ratio is clearly increased, by factors ranging from 4.5 (Proxima Cen) to 9 (AU Mic), while the Mg/Fe ratio is about solar. In Fig. 4.10 we give a graphical representation of the numbers listed in Tables 4.7 and 4.10 from the quiescent data.

O/N and Ne/O can be considered as high FIP/high FIP ratios, and within the errors, these ratios do not change with spectral type. No trends can also be identified for the low FIP/low FIP ratios Mg/Fe and Si/Mg. The low FIP/high FIP ratio Mg/Ne on the other hand clearly increases towards later spectral type, while the high FIP/low FIP ratio Ne/Fe decreases.

Mg/Ne and Ne/Fe are sensitive to a possible FIP bias, and both are anomalously low and high, respectively, for all stars in our sample, pointing towards an inverse FIP effect. This result holds for both total and quiescent-only spectra. Since we only have relative abundances, it is unclear whether high-FIP elements are overabundant or low-FIP elements are underabundant. A low Mg/Ne ratio may

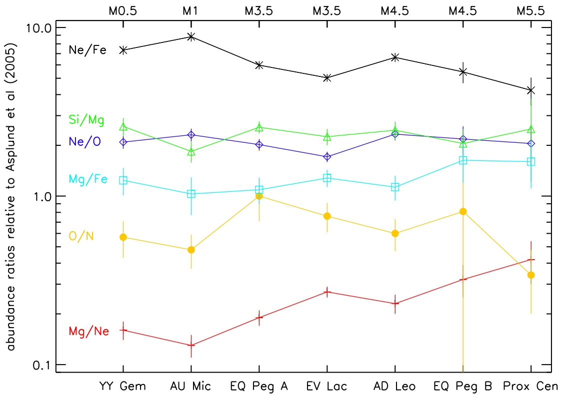

Figure 4.10: Relative abundances as a function of spectral type derived from the seven M dwarfs as listed in Tables 4.7 and 4.10.

be caused by an enhancement of neon, as supported by the increased Ne/O ratios, but also by a low Mg abundance, which would match the enhanced Si/Mg ratios, and so on.

The trends observed for Ne/Fe and Mg/Ne are roughly independent of the occurrence of flares. This confirms previous findings that strength of the inverse FIP effect scales with the general activity level of a star (Güdel et al. 2002b; Telleschi et al. 2005), as activity (in terms of X-ray luminosity) decreases with increasing spectral type. While the behavior of the Ne/Fe and Mg/Ne ratios in our M dwarf sample implies an absolute decrease of neon with later spectral type, the constant Ne/O ratio does not fit that picture. This indicates that not only a single element like neon causes this effect, but that the inverse FIP effect in general diminishes for later M dwarfs.

4.6 Discussion

The behavior of M dwarf coronae shows striking changes with spectral type. The early M dwarfs up to a spectral type of ≈ M3–M4 observed so far are strong X-ray emitters, showing permanent flaring, high coronal temperatures and a pronounced inverse FIP effect (Robrade & Schmitt 2005). X-ray luminosity, the level and peak temperature of the emission measure, and the flaring rate decrease for later M dwarfs. While for earlier M subclasses, it is difficult – if not impossible – to distinguish between weak flaring and quiescence, M dwarfs of spectral type M5 or later show periods of quiescence interrupted by discrete flares, and their coronal temperatures decrease (Fuhrmeister et al. 2007). Very late M dwarfs (>M7) become more and more difficult to detect as quiescent X-ray sources, yet they can still produce enormous X-ray luminosities during flares. Abundance determinations are difficult for these objects, but Güdel et al. (2004) and Fuhrmeister et al. (2007) found the inverse FIP effect to be less pronounced in the M5.5 stars Proxima Cen and CN Leo. With our systematic line ratio survey, we can consolidate the trend of the inverse FIP effect in M dwarf coronae weakening with later spectral subclass. This is coupled to the decrease of the activity observed with later subclass in general, while $L_{\mathrm{X}}/L_{\mathrm{bol}}$ is similar and dominated by saturation effects for all our sample stars except for the latest object Proxima Cen. Apart from the precise strength of single emission lines that are mostly determined by individual abundances, high resolution X-ray spectra of M dwarfs have a very similar overall shape. Only the continuum level decreases with later spectral type, as lower coronal temperatures reduce the amount of true continuum emission as well as the pseudo-continuum dominated by lines of highly ionized iron located at approximately 9–17 Å. The reduction of the continuum level can easily be quantified from the cumulative spectra and serves as an indicator for the average coronal temperature.

Both methods we used for our analysis, the cumulative spectra as well as the emission measure independent line ratios, can be applied to spectra with lower signal where only the strongest lines can be discerned. They are thus also suitable to determine coronal properties from the spectra of the fainter mid and late M dwarfs. Only very few grating spectra of such objects are available so far, and especially spectra of stars later than M6 would help to confirm the trend that the difference of the Ne/Fe and Mg/Ne ratios to solar photospheric values decreases with later spectral type. However, since the Ne/O and Si/Mg ratios stay enhanced by about a factor of two, there is no indication of all abundance anomalies to diminish. So at least in comparison to the saturated coronae of active M dwarfs, it is the solar photosphere which appears anomalous; and the abundances of M dwarfs seem to “converge” with later spectral subclass, but to values differing from the solar photospheric level.

The determination of reference sets of photospheric abundances of active M dwarfs is rather difficult, since reliable models of the stellar atmosphere including radiative transfer are required. The parameters involved in the modeling procedure, i. e. the stellar mass, effective temperature, $\log g$, and for M dwarfs, the influence of the stellar chromosphere and possibly the formation of dust, introduce large uncertainties in the derived abundances (Zboril & Byrne 1998). Additionally, only the abundances of heavier elements, often only that of iron, can be determined in the photosphere, while light elements like carbon, nitrogen and oxygen or noble gases like neon that dominate the coronal spectrum leave only weak or no signatures in the photospheric spectrum.

It may be questionable to line up active M dwarfs exclusively based on spectral type, since other parameters, especially the age, certainly have a non-negligible influence, and age-activity relations are well-established over all wavelengths and in particular for coronal X-ray emission (Vaiana et al. 1992; Favata et al. 1994). Our ultraluminous sample star AU Mic forms a proper motion pair with the M4/M4.5 binary AT Mic, both stars are members of the β Pictoris moving group and only about 10–12 Myrs old (Zuckerman et al. 2001). Robrade & Schmitt (2005) found AT Mic half an order of magnitude brighter in X-rays than our sample stars AD Leo, EV Lac and EQ Peg, which have similar spectral types. Stars with a common origin, like the two ZAMS stars AU Mic and AT Mic, or the coeval components of the binary EQ Peg thus provide a testbed independent of such biases. The M3.5 and M4.5 components of EQ Peg differ by one spectral subclass, but the X-ray luminosity of the M4.5 secondary is considerably lower, which we can attribute to a fairly reduced amount of coronal emission measure, but at temperatures similar to those found on the primary. Yet, in terms of $L_{\mathrm{X}}/L_{\mathrm{bol}}$, both stars are in the saturation regime, and thus again comparable. Similar considerations apply to a larger sample of different ages, ranging from a few Myrs (AU Mic) to almost one Gyr (EQ Peg); the cumulative spectra of very young stars like AU Mic or EV Lac are very similar to the much older EQ Peg system. Proxima Cen is also by far the oldest object, and the one with the longest rotation period. It is the only star from our sample where $L_{\mathrm{X}}/L_{\mathrm{bol}}$ deviates from the saturation level, yet it still fits the picture of the other saturated stars in terms of abundance trends. Here we probably see the well-established relationships between X-ray luminosity and age or, related via spin-down with age, rotation period/rotational velocity and X-ray luminosity (Pizzolato et al. 2003; Reiners 2007) or other activity indicators like Hα or Ca II emission at work. The age of the other sample stars is less than 1 Gyr and their rotation periods are typically only a few days. The sample of M dwarfs observed with high spectral resolution in X-rays is – by necessity – biased towards the more luminous younger objects, and it would be crucial to examine how further old and inactive objects like e. g. Barnard's star fit into that picture.

During quiescence, coronal densities on active stars typically range between 10^{10}–10^{11} cm^{-3} for the low-temperature plasma ($\approx$ 2 MK) traced by the O VII triplet (Ness et al. 2003a), and between 10^{11}–10^{12} cm^{-3} for Ne IX ($\approx$ 4 MK). Significantly higher values have so far only been observed during huge flares (Güdel et al. 2002a; Liefke et al. 2010), but in general, coronal densities tend to increase during periods of increased activity and lower amplitude flaring (e. g. Maggio & Ness 2005; Fuhrmeister et al. 2007). Mitra-Kraev & Ness (2006) thus developed a statistical approach that showed that the different f/i-ratios observed during flares and quiescence on EV Lac are actually highly significant.

Flares can considerably change the X-ray properties of active M dwarf stars. The flare plasma often dominates the coronal emission, although the dimensions of the flaring loops seldomly reach the size of the star itself, and the flaring region typically covers only a small fraction of the stellar surface. The plasma temperature and emission measure can increase by more than an order of magnitude during the strongest flares, which subsequently results in an enhanced level of continuum emission. The bulk of line emission is dominated by high-temperature ions. Based on current flare models, the flare plasma is largely composed of evaporated chromospheric or photospheric material filling the loop. In this context, abundance gradients between the different layers of the atmosphere, like the FIP effect observed on the Sun, become important. Nordon & Behar (2007) and Nordon & Behar (2008) investigated changes in the FIP bias during several larger flares on a sample of different active stars. For the very active stars that show an inverse FIP effect during quiescence, they found abundance ratios of the scheme high FIP/low FIP like Ne/Fe to decrease during flares, i. e. the inverse FIP effect turns into a solar-like pattern or even a FIP effect. This is in good agreement with the trends we find in our M dwarf sample. Thus abundance gradients, resulting in a different composition of the evaporated flare plasma, seem to be a common feature, and in contradiction to the corona, the underlying abundances of the lower atmospheric layers in active M dwarfs approach a more solar photospheric like pattern. This finding is also supported by Liefke et al. (2010), who found the coronal iron abundance of the M5.5 dwarf CN Leo to increase by a factor of two to the solar photospheric level during a large flare.

To what extent flares do have to be considered as the "usual" behavior of a stellar corona? Early M dwarfs are in a state of permanent flaring, and even during phases of apparent quiescence, the underlying basal coronal flux is difficult to disentangle from unresolved weaker flares. While larger flares can be separated, the characteristic flickering of early M dwarfs has to be taken as their typical "quasi-quiescent" behavior. The average coronal temperatures and densities of active stars will lower when the data is restricted to this quiescent state. However, we do not find that the flares included in the total datasets of our seven sample stars introduce large changes in the observed abundance ratios. Since the data do not include huge flares, this indicates a smooth transition between the quasi-quiescent state and intermediate flares, which supports the assumption that the unresolved flickering is indeed composed of smaller flares. When switching to intermediate and late M dwarfs and their single, discrete flares, it may on the other hand be possible to pin down the true basal coronal flux as observed on the Sun during quiescence, which seems to approach solar coronal conditions for these less active stars. The smooth transition in X-ray luminosity, flare rate, coronal temperatures and abundances we observe in our sequence of very active early M dwarfs towards intermediate and late M dwarfs, i. e., from stars with radiative interiors to fully convective interiors, suggests that the different dynamo mechanisms thought to operate in these stars to not lead to easily observable consequences in their coronal properties.

4.7 Summary and conclusions

We have investigated the coronal properties of the M3.5/M4.5 EQ Peg binary system from their *Chandra* HETGS spectra. No large flares occur during our observations, and we find coronal densities ranging from $4\cdot10^{10}$ cm^{-3} to $3\cdot10^{11}$ cm^{-3} or consistent with the low-density limit from the O VII and Ne IX triplets, i. e. values typical for active stars. The ratio of X-ray luminosities is 6:1 for EQ Peg A and B, but in terms of $L_\mathrm{X}/L_\mathrm{bol}$, both stars are saturated. The differential emission measures of both components peak around 3 MK, and their abundances are similar and follow the inverse FIP effect.

We compared all seven M dwarfs observed so far with the *Chandra* HETGS with two methods also suitable for spectra with low signal. The slope of the cumulative spectrum, which traces the continuum level and therefore the average coronal temperature, is very similar for spectral types M0.5 to M4 and then decreases. Emission measure-independent abundance ratios based on the line fluxes of strong lines with a similar temperature dependence confirm the existence of abundance anomalies compared to the solar photosphere for all M dwarfs in our sample. The ratios sensitive to a FIP bias, i. e. Mg/Ne and Ne/Fe, show a clear trend with increasing spectral type to approach the solar photospheric level, while ratios insensitive to a FIP bias like Si/Mg and Ne/O stay at a constant level. These trends seem to be independent of the age of the stars.

5 Simultaneous XMM-Newton and VLT/UVES observations of the flare star CN Leonis

The discovery of coronal Fe XIII line emission in the optical spectra of the M dwarf CN Leo by Schmitt & Wichmann (2001) led to a multiwavelength campaign on this star, performed over a period of two years. For this work, which covers the first three of six observations, I provided the analysis of the X-ray data as well as major parts of the writing. It has been published under

B. Fuhrmeister, C. Liefke, and J. H. M. M. Schmitt
A&A, **468**, 221-231 (2007)

Abstract

We present simultaneous observations with VLT/UVES and *XMM-Newton* of the active M5.5 dwarf CN Leo (Gl 406). The data were gathered during three half nights in May 2004 and December 2005, and they cover quiescent states, as well as flaring activity. Our main aim is to derive coronal properties from X-ray data and to compare these to results from the optical Fe XIII line. We studied simultaneously-measured coronal and chromospheric parameters of CN Leo as determined from the *XMM-Newton* X-ray data, the forbidden optical coronal Fe XIII line at 3388 Å, and various optical chromospheric emission lines. We find that different activity levels of CN Leo can be traced as well in X-rays as with the Fe XIII line. Moreover, the Fe XIII line flux is in good agreement with a prediction using the differential emission measure as determined from the X-ray spectrum and Fe atomic data. We also present coronal X-ray properties for the quiescent and flaring states of CN Leo. During a flare two He II transition region lines are also detected in the optical data.

5.1 Introduction

CN Leo (Gl 406) is a well-known nearby flare star with a spectral type of M5.5 (Reid et al. 1995) or M6.0 (Kirkpatrick et al. 1991) at a distance of 2.39 pc (Henry et al. 2004). Using a fixed $\log g$ of 5.0 and solar metallicity, Pavlenko et al. (2006) find a $T_{\rm eff}$ of 2800±100 K, while Fuhrmeister et al. (2005b) have fitted $\log g$ and $T_{\rm eff}$ simultaneously and determined $T_{\rm eff}$=2900 K and $\log g = 5.5$ using a grid with $\Delta T_{\rm eff} = 100$ K and $\Delta \log g = 0.5$. Pavlenko et al. (2006) also determined $M_{\rm bol} = 12.13 \pm 0.1$, yielding an age of 0.1–0.35 Gyr and a mass of 0.07-0.1 $M_\odot$ for CN Leo. This relatively young age corresponds well with CN Leo's high activity level. Surprisingly, CN Leo has been kinematically classified as an old disk star by Mohanty & Basri (2003), which would (statistically) imply a higher age. Therefore, Pavlenko et al. conclude that CN Leo is a young disk star, falling outside the kinematic dispersion of the young disk population. Interestingly, despite its high activity level, a rather low rotational velocity of $v \sin i < 3.0$ km s^{-1} has been found by Mohanty & Basri (2003).

CN Leo's high activity levels manifest themselves in its high relative Hα luminosity of $\log L_{\rm H\alpha}/L_{\rm bol} = -3.89$, (Mohanty & Basri 2003), the multitude of chromospheric emission lines in its near ultraviolet spectrum (Fuhrmeister et al. 2004), and its high X-ray flux. The X-ray luminosity of CN Leo observed during the *ROSAT* All-Sky survey was $\log L_{\rm X} = 26.97$, while two pointed observations with the *ROSAT* PSPC yielded higher values of $\log L_{\rm X} = 27.01$ and 27.64 (Schmitt & Liefke 2004). Also, CN Leo is the only M dwarf for which persistent but variable emission of the forbidden coronal Fe XIII line at 3388 Å could be established (Schmitt & Wichmann 2001; Fuhrmeister et al. 2004), although several surveys among M dwarfs with high and low activity levels have been carried out. Fuhrmeister et al. report one additional clear detection for LHS 2076 during a major flare for a sample of 15 very active M3–M6.5 dwarfs, while Wallerstein & Tyagi (2004) find no Fe XIII emission in a sample of 8 M dwarfs with rather low activity levels. This apparent rarity of M dwarfs exhibiting the Fe XIII forbidden coronal line may be due to the different coronal temperature structure of active M dwarfs as compared to the Sun. Typical emission measure distributions of the coronae of M3–M4 dwarfs peak around 7–8 MK as determined with XMM-Newton (Robrade & Schmitt 2005), i. e., a temperature too hot for significant amounts of Fe XIII.

However, the X-ray luminosity decreases rapidly for stars of spectral type M5 or later, with the values of $L_{\rm X}$ measured for CN Leo more than an order of magnitude lower than those found for the sample of Robrade & Schmitt (2005). Thus there are only a few late-type M dwarfs for which X-ray spectra of reasonable quality are available. The binary UV Cet (M5.5) has been spatially resolved by *Chandra* (Audard et al. 2003b) with $\log L_{\rm X} \sim 27.0$ for both components and a temperature of 3–6 MK. UV Cet was also searched for Fe XIII by Fuhrmeister et al. (2004), but due to its high rotational velocity only indirect evidence of the line could be found; therefore the question of whether UV Cet shows the forbidden Fe XIII line is still not settled at the moment. Another case is Proxima Centauri, where also no definitive statement could be made concerning Fe XIII line emission. A 65 ks observation with *XMM* showed quasi-quiescent emission at a level of $\log L_{\rm X} \sim 26.8$, as well as a huge long-duration flare with a peak luminosity of $\log L_{\rm X} = 28.5$ (Güdel et al. 2002a, 2004).

The lack of good X-ray data for very late-type M dwarfs and the uniqueness of CN Leo with respect to the persistent emission of the Fe XIII line suggests strictly simultaneous X-ray observations of CN Leo with a modern X-ray telescope such as *XMM-Newton* to determine coronal temperatures and densities and high-spectral optical/UV observations, allowing studies of the chromospheric emission and the coronal Fe XIII line from the ground. In this paper we report on a multi-wavelength campaign designed to cover the coronal and chromospheric properties of CN Leo by simultaneous observations in the optical and in the X-ray regime. In the subsequent sections we first describe our observations obtained with *XMM-Newton* and VLT/UVES in Sect. 5.2. In Sect. 5.3 we analyse the timing behaviour of CN Leo during the observations. The derived X-ray properties are presented in Sect. 5.4, while the analysis of the behaviour of the chromospheric lines is found in Sect. 5.5. A discussion and our conclusions are found in Sects. 5.6 and 5.7.

5.2 Observations and data analysis

The multi-wavelength observations reported in this paper were obtained strictly simultaneously with *XMM-Newton* and ESO's Kueyen telescope equipped with the Ultraviolet-Visual Echelle Spectrograph (UVES) on one night in May 2004 ($19^{th}/20^{th}$), and on two nights in December 2005 ($11^{th}/12^{th}$ and $13^{th}/14^{th}$); an overview of the observational parameters can be found in Table 5.1. Similar observations with, however, somewhat different instrumental setups both in the optical and in the X-ray band were performed in May 2006 and will be discussed in forthcoming papers.

UVES is an cross-dispersed echelle spectrograph mounted on the Nasmyth B focus of the Kueyen telescope (UT2). It can be operated in different wavelength intervals in the range from about 3000 to 11 000 Å. The light is dispersed onto two arms, each of which can be used either alone or in parallel using a dichroic beam splitter. Thus a large part of the optical wavelength range can be observed in a single exposure with an average resolution of ∼ 40 000. The blue spectrum is recorded with a single CCD detector, while the red arm is covered by a mosaic of two CCD chips, leading to a small gap in the red spectrum. While the chips for the blue arm and the bluer part of the red arm are identical (type EEV CCD-44), the CCD chip used for the redder part of the red arm is of type MIT/LL CCD-20, leading to reduced fringing.[1] In our specific setup used for the CN Leo observations presented here, the spectral coverage was between 3200 Å to 3860 Å in the blue arm and 4590 Å to 6620 Å in the red arm with a small gap from 5640 Å to 5660 Å due to the CCD mosaic.

All of the optical data analysed here were taken in service mode. Unfortunately, because of poor weather at Paranal, the optical observations for the 2004 campaign were almost totally lost. Only one red arm spectrum could be obtained at 22:45 UT with an exposure time of 260 s. The signal in the corresponding exposure in the blue arm is too low, leaving only the red arm spectrum with useful data. We used the UVES pipeline products that provide an absolute flux calibrated spectrum for this single exposure. The optical observations in December 2005 yielded a total of 36 spectra. For this run we used exposure times of 975 s and 450 s for the blue and the red parts of the spectrum, respectively. The optical spectra from this run were reduced using the IDL-based `REDUCE` reduction package (Piskunov & Valenti 2002). The wavelength calibration was carried out using Thorium-Argon spectra and resulted in an accuracy of ∼ 0.03 Å in the blue arm and ∼ 0.05 Å in the red arm. Absolute flux calibration was carried out using the UVES master response curve and extinction files provided by ESO. In addition to the high-resolution spectra, there are photometric data with a time resolution of approx. 1 sec from the UVES exposuremeter, which are, however, not flux-calibrated.

On board *XMM-Newton* there are three co-aligned X-ray telescopes, accompanied by the OM (Optical Monitor), an optical/UV telescope. Each of the three X-ray telescopes is equipped with one of the EPIC (European Photon Imaging Camera) instruments, CCD detectors providing medium-resolution imaging spectroscopy with $E/\Delta E \approx 20$–50 and timing analysis with a time resolution at the subsecond level. Two of the EPIC instruments are the identical MOS1 and MOS2 detectors operating in the energy range of 0.2–12.0 keV. The third EPIC instrument, the PN detector, covers the energy range of 0.2–15.0 keV with higher sensitivity, while the MOS detectors provide a better angular and spectral resolution; several filters and operating modes are available for these instruments. The X-ray telescopes with the MOS detectors also are equipped with reflective gratings and their corresponding CCD detectors. These Reflection Grating Spectrometers (RGS1 and RGS2) provide high-resolution spectroscopy in the energy range of 0.35–2.5 keV (5–38 Å) with $E/\Delta E$ of 200 to 800 and a spectral resolution of ≈ 0.06 Å FWHM so that the individual X-ray emission lines can be resolved. All instruments can be operated simultaneously and provide multiple measurements of the same target.[2]

Our *XMM-Newton* X-ray observations have durations of 20 ks (ObsID 0200530201) in May 2004 and 18 ks each (ObsIDs 0200530301 and 0200530401) in December 2005, and thus fully cover the time spanned by the optical observations (see also Figs. 5.1 and 5.2). The PN and MOS detectors were operated in Full Frame and Large Window mode with the medium filter. All X-ray data were reduced with the *XMM-Newton* Science Analysis System (SAS) software, version 7.0. EPIC lightcurves and spectra were obtained using standard filtering criteria. Spectral analysis was carried out with XSPEC V12.2 (Arnaud 1996), making use of two- and three-temperature component models with coupled abundances for each component. The plasma models assume a collisionally-ionised, low-density optically-thin plasma as calculated with the APEC code (Smith et al. 2001b). Abundances are calculated relative to the solar photospheric values from Anders & Grevesse (1989). Due to the proximity of CN Leo, interstellar absorption is negligible for the optical as well as for the X-ray data. Additionally we made use of the CORA program (Ness & Wichmann 2002) to measure individual line fluxes in the RGS and UVES spectra.

5.3 Spectra and timing behaviour

5.3.1 X-ray and optical light curves

In Fig. 5.1 we plot the X-ray light curve (taken with EPIC-PN) of our May 2004 run, while the X-ray

---

[1] A detailed description of the UVES spectrograph is available under http://www.eso.org/instruments/uves/doc/

[2] More details on the instruments onboard *XMM-Newton* can be found in the *XMM-Newton* Users' Handbook, available at http://xmm.vilspa.esa.es/external/xmm_user_support/documentation/uhb/index.html

Table 5.1: Observation log for CN Leo.

Instrument	Mode	Observation Time	Duration [s]
UVES	Dichroic 1 (346 / 564 nm)	2004-05-19T22:45–22:48	1 × 260 / 1 × 260
MOS 1&2	Full Frame / Medium filter	2004-05-19T20:46–20T03:13	22500
PN	Large Window / Medium filter	2004-05-19T22:43–20T03:08	15900
RGS 1&2		2004-05-19T20:46–20T03:16	20600
UVES	Dichroic 1 (346 / 564 nm)	2005-12-11T06:46–09:01	8 × 975 / 16 × 450
MOS 1&2	Full Frame / Medium filter	2005-12-11T05:38–10:46	18500
PN	Large Window / Medium filter	2005-12-11T06:07–10:41	16500
RGS 1&2		2005-12-11T05:37–10:50	18700
UVES	Dichroic 1 (346 / 564 nm)	2005-12-13T08:00–09:06	4 × 975 / 8 × 450
MOS 1&2	Full Frame / Medium filter	2005-12-13T03:59–08:59	18000
PN	Large Window / Medium filter	2005-12-13T04:28–08:54	15600
RGS 1&2		2005-12-13T03:59–09:02	17700

light curves (taken with EPIC-PN) for the two observation runs from December 2005 are shown in Fig. 5.2, also indicating the time overlap between the UVES and *XMM-Newton* data sets; the X-ray light curves were binned in 100 s bins. The individual blue-arm exposures are also indicated and numbered for easy reference. The exact start times for each blue exposure are listed in Table 5.4. Two red exposures cover one blue exposure and will be referenced with numbers using step size 0.5.

In the X-ray data from December 11^{th} 2005 (cf., Fig. 5.2, left panel), a shallow slope is apparent in the light curve, which we tentatively interpret as part of the decay phase of a very long-duration flare, the onset of which is not covered by our observations. The enhanced level of activity during this state is shown by the X-ray fluxes and the chromospheric emission lines, which will be discussed later.

There is also relatively weak X-ray flickering with two small flares at about 07:30 and 10:00 UT and a larger one at about 09:00 UT with an increase in count rate of about a factor of two. The flare at 07:30 UT, lasting about three minutes, is covered by UVES and also seen in the photometric data. In the blue arm it is covered in spectrum number 3 and in the red arm in spectrum number 3.5. The flare lasted for about three minutes and there was no detectable delay between the optical and the X-ray data at variance with a possible Neupert effect.

The X-ray light curve from December 13^{th} (cf., Fig. 5.2, right panel) shows the onset of another strong flare at its end; unfortunately the flare peak is not covered by our data. It is preceded by a short duration flare, which is also found in the optical photometer data; the corresponding UVES spectrum is spectrum number 11 (for the blue and the red arms). The short duration flare lasts about four minutes. With a binning of 10 seconds for the X-ray and optical data, we found that the optical peak precedes the X-ray peak by about one minute. Such delays are expected if the Neupert effect is at work, however, count statistics prevent us from verifying that the time derivative of the soft X-ray light curve does indeed approximate the shape of the optical light curve. Note that the increasing optical flux at the end of both observation runs is partly due to scattered sunlight indicating daybreak.

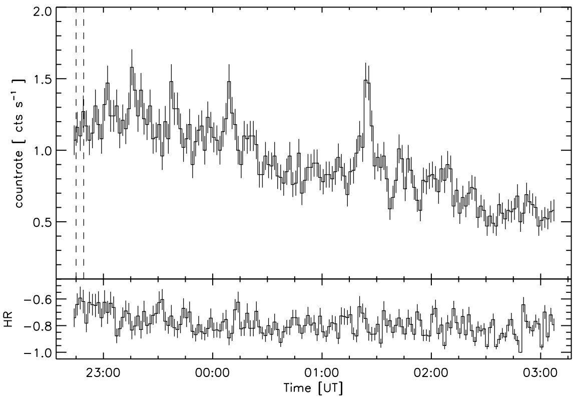

Figure 5.1: X-ray light curve and hardness ratio of CN Leo from May 19/20, 2004 taken with the PN instrument with a bin size of 100 s. The vertical lines show the time interval of the simultaneous UVES observation.

The X-ray count rate for the May 2004 run is again somewhat lower than on December 13^{th}. Besides some X-ray flickering, a small flare is observed at 1:30 UT. The X-ray light curve shows a similar but even stronger downward trend than the December 2005 data. Without the exposuremeter light curve and UVES spectra covering a longer period of time, especially the flare, we cannot make a statement about the simultaneous chromospheric activity.

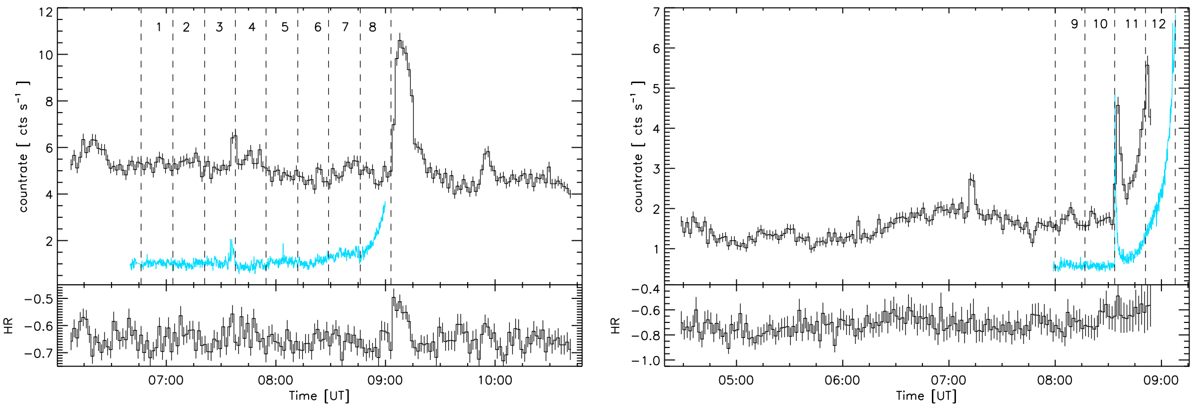

Figure 5.2: Light curves in the optical and in X-rays plus an X-ray hardness ratio for 11 (left) and 13 (right) December 2005. The black curves denotes the *XMM* EPIC PN detector and the grey / light blue curves the blue UVES exposuremeter, which is scaled down in intensity by a factor of 30. The vertical dashed lines mark the beginning of the UVES exposures of the blue arm. Note that the steep rise of the exposuremeter data at the end of each UVES run is partly due to scattered light of the beginning dawn. The time bin size of the X-ray data is 100 s.

In Figs. 5.1 and 5.2 we also show the time-dependent hardness ratios (HR); to derive HR, the source counts from the EPIC PN data are divided into "soft" and "hard" bands ranging from 0.15–1.0 keV (S) and 1.0 to 10.0 keV (H), respectively, and we define $HR = \frac{H-S}{H+S}$. The significance of the observed HR variations is difficult to assess; however, there seems to be a slight decrease from ≈ -0.65 to -0.8 and thus a softening in the first quarter of the May 2004 observations. No clear indications of spectral changes related to the small flare are observed. Apart from a clear hardening to ≈ -0.5 during the large flare at 9:00 UT, the hardness ratio of the December 11^{th} 2005 observation seems to be more or less constant at a level of ≈ -0.65 without a significant increase related to the two smaller flares, since other variations apparently unrelated to variations in the lightcurve are within the same order of magnitude. On December 13^{th}, the hardness ratio slowly increases from ≈ -0.75 to -0.6 at approximately 6:30 UT, then decreases back to -0.75, with a new increase obviously coupled to the two flares towards the end of the observation.

5.3.2 X-ray spectra and fluxes

We analysed the overall X-ray flux using the PN spectra from the individual runs in May 2004 and December 2005. The X-ray flux levels change significantly for the three exposures, as can be seen in Fig. 5.3; the X-ray flux was determined using the XSPEC best-fit spectral models (see Sect. 5.4) in the energy range 0.2 to 2.0 keV. Specifically, the 2004 EPIC PN exposure results in an X-ray flux of $2.1 \cdot 10^{-12}$ erg cm^{-2} s^{-1} ($L_X = 1.4 \cdot 10^{27}$ erg s^{-1}), the December 13^{th} exposure gives $4.3 \cdot 10^{-12}$ erg cm^{-2} s^{-1} ($L_X = 3.0 \cdot 10^{27}$ erg s^{-1}), and the data from December 11^{th} give $7.6 \cdot 10^{-12}$ erg cm^{-2} s^{-1} ($L_X = 5.2 \cdot 10^{27}$ erg s^{-1}). Since the X-ray luminosity of the 2004 run roughly agrees with the *ROSAT* X-ray luminosity, CN Leo seems to have been in a quiescent state at that time, while both runs in December 2005 show higher X-ray flux, the second one even with the flaring period at the end of the observation excluded. The X-ray flux enhancement of the first night (December 11^{th}) fits into the picture of CN Leo being in the decay phase of a long duration flare. Since even during the second night (December 13^{th}) the X-ray flux is not as low as in May 2004, the star must have still (or again) been in a state of increased activity.

In Fig. 5.4 we show the co-added and fluxed RGS spectrum of CN Leo obtained from all three observations. It resembles the RGS spectra of other M-dwarfs (cf. Robrade & Schmitt 2005), with O VIII Ly α being the strongest line and other prominent lines originating from Ne IX and X, Fe XVII, O VII, and C VI. While the true source continuum is not very pronounced, a pseudo-continuum between $\approx$ 10–17 Å resulting from the broad wings of brighter Ne and Fe lines, plus additional weak and unresolved lines, is clearly visible.

5.3.3 The optical spectra

The typical spectral resolution of our UVES spectra is $\sim 40\,000$. Unfortunately, the Hα line is saturated in our spectra; however, various members of the Balmer series are well-covered, i.e, Hβ in the

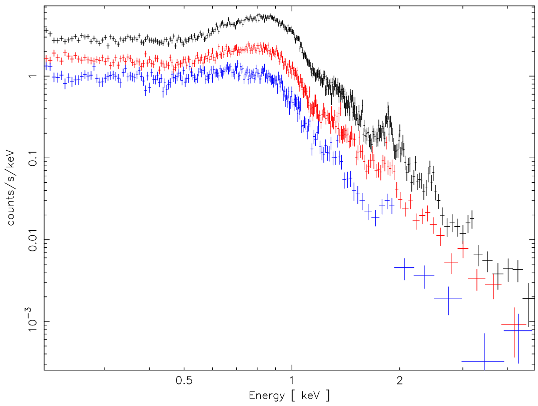

Figure 5.3: PN spectra from the December 11th 2005 run (top/black), the December 13th run (middle/red), and the May 19th 2004 run (bottom/blue).

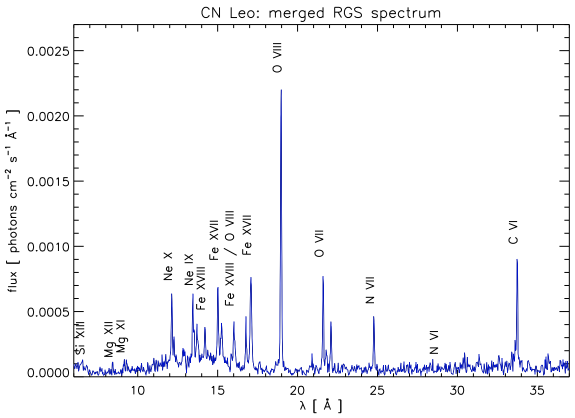

Figure 5.4: RGS spectrum of CN Leo constructed from RGS 1 and 2 in 1st order with the SAS task `rgsfluxer` from all three observations. Prominent emission features are labelled.

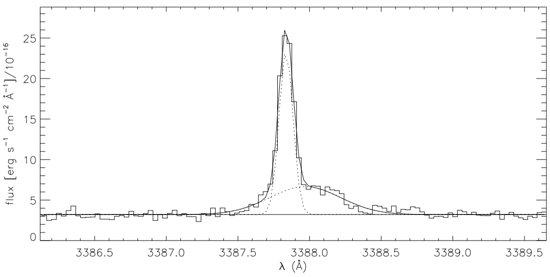

Figure 5.5: The (broad) forbidden coronal Fe XIII line at 3388 Å blended with the narrow chromospheric Ti II line; this spectrum is averaged from spectra 1 to 6 to increase the signal-to-noise ratio.

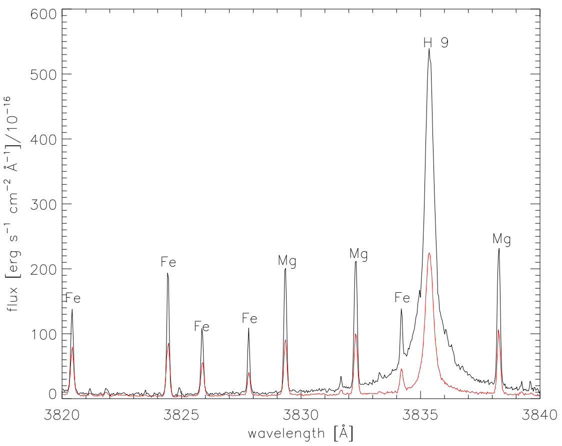

Figure 5.6: Spectral range around the H_9 line; various metal lines of Fe I and Mg I are indicated. The black spectrum is number 12 taken during the flare, the red/grey spectrum is number 1 from the December 11th 2005 run.

red arm and H_9 and higher Balmer lines up to H_{24} in the blue arm. In contrast to earlier M dwarfs, CN Leo shows an almost pure chromospheric emission line spectrum in the blue without hardly any photospheric absorption lines. The quality of the optical spectra for the spectral range around the forbidden Fe XIII line can be assessed from Fig. 5.5. Since the signal-to-noise ratio in this very blue region is low, the spectrum around the Fe XIII line was averaged from spectra 1 to 6 from the first night, where little variation in the Fe XIII line is seen and variations in the blending Ti II line are also small.

A much higher signal-to-noise ratio is obtained at the red end of the blue spectral arm, where most of the lines used for the chromospheric analysis are located. The spectral wavelength range around the H_9 line is shown in Fig. 5.6 for the quiescent and the flaring case; note the broad wings of the H_9 line, especially during the flare. These broad wings can be fitted using a linear combination of two Gaussians. For $H\beta$, a fit with a Voigt function resulted in worse fits, while for H_9 a Voigt profile resulted in similar good fits compared with two Gaussian components. For consistency we decided to also fit H_9 and higher Balmer lines with two Gaussian profiles.

5.4 Coronal properties of CN Leo

5.4.1 Coronal abundances and temperatures

We determined plasma temperatures and abundances relative to solar values (Anders & Grevesse 1989) with an iterative procedure of global fits to the EPIC and RGS spectra with APEC plasma models. As a starting point, we used the merged RGS and EPIC spectra of all three observations. First we fitted a two-temperature component model to the RGS data to establish an initial set of abundances. Al, C,a and Ni as elements with low first ionisation potentials (FIP) were coupled to Fe, and Ar as an element with a high first ionisation potential was coupled to Ne. Independent fits to these elements are not feasible due to the absence of pronounced lines in the RGS wavelength range. The thus determined abundances were fixed and used to determine the temperatures of a three-temperature component model fitting the EPIC data. The final abundances were then determined from a parallel fit to the RGS data with spectral bins below 6 Å excluded, and to the EPIC spectra restricted to the energy range from 1.2 to 5.0 keV (Table 5.2). Besides this global fit we also used two slightly different methods based on individual line fluxes from the RGS for comparison, as described in more detail in Sect. 5.4.2. The elemental abundances as determined from these line-based DEM methods are also listed in Table 5.2. An inspection of Table 5.2 shows that the abundances determined by the different methods are consistent within the errors, so we are confident that our abundances do not depend on the chosen analysis methods or models, while obviously the dependence on the atomic physics parameters remains.

While the Sun or stars with a low activity level often show an abundance pattern varying with the first ionisation potential (FIP), where the low FIP elements are enhanced in the corona, a reversed pattern – the inverse FIP effect – with depleted low-FIP elements and enhanced high-FIP elements is frequently found in stars of higher activity (e. g. Brinkman et al. 2001; Audard et al. 2003a). Although the abundance errors are relatively large, elements with low FIP like Mg, Fe, and Si seem to be less abundant in general than high FIP elements like C, O, N and Ne, indicating an inverse FIP effect.

We implicitly assume that our abundances do not change between the three observations and the changing states of activity, and therefore we fix the abundances at the values determined above. We then fitted temperatures and emission measures (EM) to the EPIC PN and MOS data in the energy range from 0.3–5.0 keV. We grouped the data for the first night into quiescent and flaring states, with the quiescent state representative of the state during the UVES exposures. The same procedure was applied to the second night, where the flaring state approximately corresponded to UVES exposures No. 11 and 12. The resulting fit parameters are listed in Table 5.3. We also binned the PN spectra into time intervals corresponding to the UVES exposures, where the exposures 9/10 and 11/12 had to be grouped to obtain higher signal. For these ten datasets, we fitted three overall temperature components with best-fit values of 0.26 keV, 0.64 keV, and 1.44 keV and with independent emission measures. The variation in the emission measures is shown in Fig. 5.9. Moreover we measured the broad band X-ray flux between 0.2 and 2.0 keV of these PN spectra as listed in Table 5.4.

Our spectral fits indicate two stable temperature components at about 2 MK (1 keV $\equiv$ 11.6 MK) and a stronger one at about 7 MK. On December 11^{th} and during the flare on December 13^{th} 2005, there is also a strong high-temperature component at about 18 MK. During the flares, the emission measure of the 2 MK and 7 MK temperature components is enhanced, which is also the case for the first night compared to the second night and for the whole 2005 run compared to the 2004 run. This again shows the higher state of activity of CN Leo in December 2005 and especially on December 11^{th}. The quiescent state of the observation from December 13^{th} may also be fitted with two temperature components, and the corresponding fit parameters are also listed in Table 5.3. The three temperature component fit, however, provides a better fit result, while a three temperature component model does not further improve the fit for the May 2004 observation.

5.4.2 Differential emission measure

In addition to the global fits we used other approaches to assess the coronal abundances of CN Leo. These methods make use of individual line fluxes measured from the *XMM-Newton* RGS. In order to achieve better signal-to-noise, we co-added the RGS spectra of all three observations with the SAS task `rgscombine`, here also assuming that the abundances did not change.

We reconstructed the shape of the differential emission measure (DEM) from abundance-independent ratios of the H-like Lyα and the He-like resonance lines from N, O, Ne, and Mg and from additional ratios of Fe XVII and Fe XVIII lines. The high-temperature slope of the DEM was also constrained by the ratio of continuum flux measurements at wavelengths around 7.5 Å and 20 Å, where the spectrum is essentially free of any clear lines; the latter continuum interval is also used for normalisation. As a result of the merging of the three RGS datasets, the determined DEM constitutes an average of these observations with their different states of activity and quiescent and flaring periods.

We used two slightly different approaches to model the DEM. First we fit $\log DEM$ as a func-

Table 5.2: Absolute coronal abundances of CN Leo. Abundances are derived from the RGS and EPIC data as fitted with a three component temperature model as described in Sect. 5.4.1. Methods 1 and 2 use a differential emission measure method as described in Sect. 5.4.2. The given errors are the statistical 1σ standard deviations.

	C	N	O	Ne	Mg	Si	S	Fe
XSPEC	1.49 ± 0.24	1.28 ± 0.21	0.62 ± 0.08	1.20 ± 0.16	0.85 ± 0.17	0.78 ± 0.33	1.41 ± 0.27	0.59 ± 0.07
DEM method 1	1.27 ± 0.13	1.03 ± 0.13	0.66 ± 0.03	1.22 ± 0.11	0.92 ± 0.16	n.a.	n.a	0.56 ± 0.04
DEM method 2	1.18 ± 0.12	0.97 ± 0.12	0.63 ± 0.03	1.17 ± 0.11	0.85 ± 0.15	n.a.	n.a	0.55 ± 0.04

Table 5.3: Best fit temperatures and emission measures for two and three component APEC models using the PN and MOS data.

date	state	kT_1 (keV)	EM_1 (10^{50} cm^{-3})	kT_2 (keV)	EM_2 (10^{50} cm^{-3})	kT_3 (keV)	EM_3 (10^{50} cm^{-3})	red. χ^2	DOF
2004-05-19	quiescence	0.20 ± 0.01	0.21 ± 0.01	0.61 ± 0.01	0.23 ± 0.01			1.91	334
2005-12-11	quiescence	0.26 ± 0.01	0.79 ± 0.03	0.64 ± 0.01	1.49 ± 0.03	1.29 ± 0.02	0.64 ± 0.02	1.50	541
2005-12-11	flare	0.24 ± 0.02	0.90 ± 0.09	0.67 ± 0.01	1.94 ± 0.09	1.50 ± 0.09	1.04 ± 0.07	0.93	267
2005-12-13	quiescence	0.20 ± 0.01	0.30 ± 0.01	0.62 ± 0.01	0.48 ± 0.01			1.83	382
2005-12-13	quiescence	0.24 ± 0.01	0.33 ± 0.01	0.61 ± 0.01	0.40 ± 0.01	1.82 ± 0.20	0.09 ± 0.01	1.50	380
2005-12-13	flare	0.19 ± 0.01	0.40 ± 0.03	0.65 ± 0.01	0.97 ± 0.04	1.59 ± 0.07	0.83 ± 0.05	1.21	187

tion of $\log T$ with polynomials of different orders with no further constraints (method 1), while in a second approach we model the linear DEM again with polynomials and as a function of $\log T$. In this second approach, the fit polynomial is then forced to have two zeros at variable temperatures, thereby defining the boundaries of the coronal emission measure distribution (method 2). Both methods give acceptable fit results already with 3^{rd} (method 1) and 4^{th} (method 2) order polynomials, with values of reduced χ^2 of 1.29 and 1.14, respectively. The resulting differential emission measure distributions are shown in Fig. 5.7, and they peak at temperatures of $\log T \approx 6.4$ ($T = 2.5$ MK). When introducing higher-order polynomials (orders 5 and 6), the DEM develops a two-peaked structure with maxima at $\log T \approx 6.3$ and 6.8–6.9, probably associated with the low-temperature component of the quiescent phases and the hotter component related to the flares and the higher level of activity during the whole December 11^{th} observation. Since we cannot be sure about the reality of these structures in the DEM, we prefer the "simpler" $DEMs$ with fewer free parameters according to Occam's razor.

With the differential emission measure from both methods, we then determined abundances as shown in Table 5.2 by forcing the DEM, abundance and line emissivities to reproduce the measured line fluxes according to $f = \frac{Ab(X)}{4\pi d^2} \int G(T) DEM(T)\, dT$, with the line flux f, the line contribution function $G(T)$, and the abundance $Ab(X)$ of element X generating the line. Note that the quoted errors result exclusively from count statistics of the flux measurements and assume (admittedly somewhat unrealistically) that the reconstructed DEM is free of errors. Especially the errors do not include the uncertainties of 12% on the continuum flux (originating from count statistics) propagating into the overall normalisation of the DEM and thus also into the absolute level of the abundances. Compared to the normalisation uncertainties due to low signal-to-noise of the continuum flux measurements, Liefke & Schmitt (in preparation) assess that uncertainties in the shape of the DEM have a smaller influence on the abundances, typically less than 5%.

To demonstrate the goodness of fit for our DEM fitting techniques, we used the determined DEMs and corresponding deduced sets of abundances to calculate synthetic spectra with CHIANTI (Landi et al. 2006). These synthetic spectra are in very good agreement with the RGS spectra, and the EPIC spectra are also reproduced quite well. Figure 5.8 shows the fit of the model spectrum determined from the DEM and abundances from method 2 to the combined MOS spectra of the three observations. Some slight systematic deviations related to individual emission features seem to be present, e. g. near 1 keV, indicating an overprediction of Ne X, while the discrepancies at low energies are probably due to RGS-EPIC cross-calibration problems.

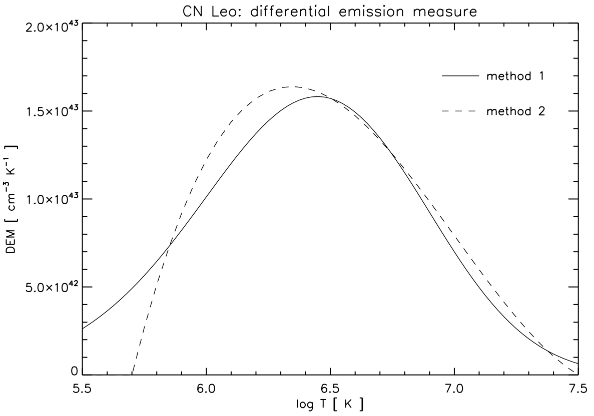

Figure 5.7: Differential emission measure for CN Leo as determined by a 3^{rd}-order polynomial fit (method 1) and a 4^{th}-order polynomial fit (method 2) of line ratios from the combined RGS observations. Note that the shape of the DEM at temperatures $\log T < 6$ cannot be determined from the available line ratios.

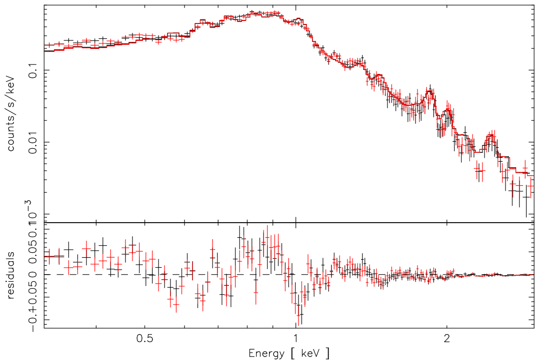

Figure 5.8: Comparison of a synthetic spectrum based on the DEM model and abundances from method 2 to the MOS1 (black) and MOS2 (red) spectra. The agreement is remarkably good, considering that the model has been determined independently from the EPIC data.

5.4.3 Coronal densities

We estimated coronal plasma densities using the density-sensitive ratio of the forbidden and intercombination lines of the O VII triplet from the three *XMM* observations. This method is described in

Gabriel & Jordan (1969) and was extensively used by Ness et al. (e. g. 2002b, 2003a). The measured f/i ratios are 2.63 ± 1.28 in May 2004, 1.60 ± 0.46 (2.03 ± 0.67 with the flare excluded) for the December 11^{th} 2005 observation, and 1.91 ± 0.74 (2.58 ± 1.28 with the flare excluded) for the December 13^{th} 2005 observation run. Given the large errors of these line ratios (caused by the weak intercombination line), it is difficult to claim significant changes during the individual data runs.

For the conversion of the measured f/i ratios to densities, we used the relation $f/i = R_0/(1+n_e/N_c)$ with the low-density limit R_0 and the critical density N_c where we adopted the values from Pradhan & Shull (1981) of 3.95 and $3.1 \cdot 10^{10}$ cm^{-3}, respectively. The average O VII f/i-ratio of 1.72 ± 0.35 is well below the low-density limit and corresponds to $n_\mathrm{e} = 4.0^{+1.9}_{-1.2} \cdot 10^{10}$ cm^{-3}. Concerning the individual observations, we find electron densities of $n_\mathrm{e} = 4.5^{+3.1}_{-1.7} \cdot 10^{10}$ cm^{-3} for December 11^{th} 2005 and $n_\mathrm{e} = 3.3^{+4.1}_{-1.8} \cdot 10^{10}$ cm^{-3} for December 13^{th} using the whole data sets. When excluding the flaring periods, we find a slightly lower density of $n_\mathrm{e} = 2.9^{+3.0}_{-1.5} \cdot 10^{10}$ cm^{-3} for the first night. During the second night, the f/i ratio yields $n_\mathrm{e} = 1.6^{+4.7}_{-1.6} \cdot 10^{10}$ cm^{-3}, consistent with the low-density limit. The same applies to the complete May 2004 observation. Thus the data suggest an increase in plasma density during the flares and for the first night. However, if the uncertainties are accounted for all the deduced densities are consistent within the errors. The corresponding f/i ratios of the Ne IX triplet always point to the low-density limit.

5.4.4 The forbidden coronal Fe XIII line

In addition to the X-ray data obtained with *XMM-Newton*, the coronal properties of CN Leo can be assessed using the forbidden coronal Fe XIII line at 3388 Å. As is well known, this line is blended with a Ti II chromospheric line (see Fig 5.5), but can be "deblended" with a suitable fit procedure. The results from a simultaneous fit of the two lines with CORA are presented in Table 5.4. The central reference wavelengths of both lines are provided through NIST (http://physics.nist.gov/PhysRefData/ASD/index.html) as 3387.84 Å for the Ti II line and 3388.1 Å for the Fe XIII line, which agrees with the central wavelength found in the fit for both lines. While the amplitude of the Ti II line reacts to the flare onsets in spectrum number 7/8 and 11/12, the Fe XIII line stays more or less constant for both nights albeit at different flux levels. The mean Fe XIII flux ratio between the first and the second night is 1.5 ± 0.3, in agreement with the X-ray flux ratio of 2.2 ± 0.4 measured from the RGS data of O VII resonance lines that have about the same peak formation temperature 1.6 and 2 MK for Fe XIII and O VII respectively, while the hotter 5 MK X-ray Fe XVII lines show a flux ratio of 3.5 to 4. Exclusion of flare time intervals leads to ratios of 2 to 3 depending on the Fe XVII lines used. Also the Fe XIII flux ratio is in agreement with the ratio of 1.8 for the EM of the cool 2 MK component.

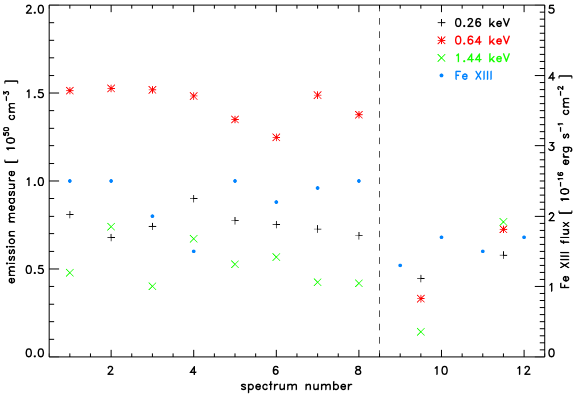

Figure 5.9: Variations in the line flux of the Fe XIII line and the corresponding emission measures of the cool, intermediate, and hot temperature component of the X-ray spectra. The vertical dashed line divides the two nights of the December 2005 observations. Note that flux variations within individual nights are not statistically significant.

The measured broad-band X-ray flux of the PN spectra corresponding to the UVES exposure time intervals also reflects the general behaviour of the forbidden Fe XIII line (see Table 5.4) in general, with the flux being lower on December 13^{th} than on December 11^{th}. However, the X-ray flux of course reacts strongly to the flare occurring during exposures No. 11 and 12. The Fe XIII line strength should be traced better by the emission measure of the low temperature component that approximately corresponds to the formation temperature of Fe XIII. Figure 5.9 shows the two flux different levels of the Fe XIII line on the two days. The low temperature component also has slightly lower emission measures on the second day, but it is difficult to confirm this trend with only two data points (and one of them affected by flares). On the contrary, the two hotter components are lower by factors greater than 2 during exposures No. 9 and 10 compared to the first night, increasing again (especially the very hot component) during the flare.

In order to assess the absolute flux variations, we computed the expected flux of the Fe XIII line from its emissivity as incorporated in the CHIANTI database, the differential emission measures reconstructed from the RGS data (see Sect. 5.4.2) and the corresponding iron abundances (see Table 5.2), resulting in predictions of $6.3 \cdot 10^{-16}$ erg s^{-1} cm^{-2} and $6.9 \cdot 10^{-16}$ erg s^{-1} cm^{-2} with method 1 and 2, respectively. These values must be compared to a mean of $(2.5 \pm 0.6) \cdot 10^{-16}\,\mathrm{erg\,s^{-1}\,cm^{-2}}$, measured directly from our UVES spectra. Various sources of error contribute to the overall uncertainties of both values, and it is difficult to assess which one dominates here. The main uncertainties of the X-ray prediction arise from the underlying atomic physics of the iron lines: On the one hand, there are systematic outliers among the strong Fe XVII and Fe XVIII lines defining the mean iron abundance; we found discrepancies of up to 25% from the error-weighted mean for CN Leo, as well as for other stars. On the other hand, systematic errors in the theoretical line emissivity of the Fe XIII line itself are difficult to evaluate. Uncertainties in the shape of the reconstructed *DEM* should only contribute to a lesser extent to the overall error estimate as mentioned above; and the uncertainties in the overall normalisation of the *DEM* and the corresponding global abundance level cancel out. Regarding the optical flux measurements, the errors of ≈ 20% are purely statistical, and it is a little hard to assess systematic errors like the quality of the absolute flux calibration of our optical spectra. Nevertheless, we consider the agreement between the simultaneously measured, but independently derived, flux values as satisfactory.

5.5 Chromospheric and transition region properties of CN Leo

In the following we address the chromosphere and transition region of CN Leo. We specifically considered the He I D_3 line, the Na I D line, four Ti II lines in the wavelength range 3370 to 3390 Å, and the Balmer lines (Hβ, H_9 to H_{15}), together with several blending metal lines. We refrained from fitting the higher Balmer lines up to H_{24}, since the background determination is difficult for these higher-order lines, and some of them are severely blended with metal lines. All line fluxes were fitted with CORA, the line fluxes of the Balmer lines, and the Balmer decrements with respect to the Hβ line (given in parenthesis) are listed in Table 5.5. The flux in the Hβ line, in the Na D lines, and in the He D_3 line is the mean from the two red spectra taken during each blue exposure. We estimate the measurement errors especially for the higher lines to be about 10 percent mainly due to uncertainties in the background determination.

The downward trend in the X-ray light curve on December 11^{th} is also reflected in the line fluxes of various chromospheric lines, e. g. in the four Ti II lines in the vicinity of the Fe XIII line, in the He D_3 line, and somewhat less clearly in the Balmer lines as well as in metal lines originating in the mid-to-lower chromosphere. Interestingly, this trend is not found in the line fluxes of the Na I D lines, but a stronger flux is visible in the first night than in the second night as for all other chromospheric emission lines as well as in X-rays. Also the ratio of the line fluxes for many chromospheric lines (for example the Mg I line at 3832.28 Å and the Fe I line at 3824.42 Å, but also the four Ti II lines) compared to the Balmer lines (here H_9) is higher for the first night. This may indicate that these lines evolve more slowly than the Balmer lines. Due to the coarse time resolution of the UVES spectra, the small flare at 07:30 UT is not found in a line flux increase for any measured chromospheric line, but it can be noticed as a broadening of the base of all the Balmer lines and an increase of the flux in the broad component compared to the narrow component.

A flare-like feature preceding the X-ray flare starting at 09:03 UT was also found in the chromospheric lines, starting at 08:20 UT and ending at 08:45 UT. This feature was indicated by a line flux increase in all chromospheric emission lines and a line broadening of the Balmer lines. Both started to decrease again in the blue spectrum number 8 and in the red spectra number 8.0 and 8.5, respectively. There was no corresponding feature either in the X-ray light curve or in the UVES photometer data. This brightening and broadening of the chromospheric lines preceded the X-ray flare peak by about 20 minutes. This is slightly more than the 10 minutes offset Mitra-Kraev et al. (2005) found between UV and X-ray lightcurves for active M dwarfs.

On December 13^{th}, the chromospheric lines reacted strongly to both the short duration flare and to the onset of the large flare. In this case there was no time lag between the X-ray data and the chromospheric lines. With the higher time resolution of the red spectra, a decline in the line broadening for Hβ after the short duration flare could be noticed before an extreme broadening set in. The variation of the line fluxes for various chromospheric emission lines for both nights are shown in Fig. 5.10. Broad components in the Balmer and other chromospheric and transition region lines were found for several M dwarfs, either as symmetric or asymmetric (blue or red wing enhanced) profiles. Asymmetric line wings are usually interpreted as due to downward or upward mass motions (see Fuhrmeister et al. 2005a; Crespo-Chacón et al. 2006, and references therein). Symmetric broadenings, which can be described by two Gaussian line components, have been described e. g. by Hawley et al. (2003). The symmetric broad-

Table 5.4: Line-fit parameters of the Fe XIII and the Ti II line. Both lines have been fitted using Gaussians with the central wavelength, amplitude, and halfwidth as free parameters. The broad band X-ray flux is given between 0.2 and 2.0 keV.

No.	date and UT	λ (Å)	Fe line flux (10^{-16} erg s^{-1} cm^{-2})	half width (Å)	λ (Å)	Ti line flux (10^{-16} erg s^{-1} cm^{-2})	half width (Å)	X-ray flux (10^{-12} erg s^{-1} cm^{-2})
1	2005-12-11T06:46	3387.95 ± 0.26	2.5 ± 0.6	0.29	3387.82 ± 0.04	3.2 ± 0.4	0.05	7.29
2	2005-12-11T07:03	3387.94 ± 0.20	2.5 ± 0.5	0.23 ± 0.01	3387.81 ± 0.04	3.0 ± 0.4	0.05	7.42
3	2005-12-11T07:20	3388.05 ± 0.31	2.0 ± 0.5	0.28	3387.82 ± 0.05	2.9 ± 0.4	0.06	7.01
4	2005-12-11T07:37	3387.93 ± 0.25	1.5 ± 0.5	0.26 ± 0.03	3387.82 ± 0.04	2.2 ± 0.4	0.05	7.81
5	2005-12-11T07:54	3387.94 ± 0.21	2.5 ± 0.5	0.23 ± 0.01	3387.82 ± 0.04	2.1 ± 0.4	0.05	6.83
6	2005-12-11T08:11	3387.96 ± 0.21	2.2 ± 0.5	0.23 ± 0.01	3387.82 ± 0.03	2.2 ± 0.4	0.04	6.43
7	2005-12-11T08:29	3387.98 ± 0.24	2.4 ± 0.6	0.25 ± 0.02	3387.82 ± 0.04	3.4 ± 0.4	0.05	6.84
8	2005-12-11T08:46	3387.95 ± 0.22	2.5 ± 0.6	0.24 ± 0.02	3387.83 ± 0.03	3.5 ± 0.4	0.04	6.77
9	2005-12-13T07:59	3387.98 ± 0.23	1.3 ± 0.4	0.21	3387.81 ± 0.05	1.1 ± 0.3	0.04	2.38
10	2005-12-13T08:16	3388.01 ± 0.29	1.7 ± 0.4	0.29	3387.83 ± 0.07	0.6 ± 0.2	0.04	
11	2005-12-13T08:33	3387.99 ± 0.45	1.5 ± 0.7	0.29	3387.82 ± 0.03	2.8 ± 0.4	0.04	5.08
12	2005-12-13T08:50	3387.88 ± 0.30	1.7 ± 0.7	0.25 ± 0.03	3387.81 ± 0.03	6.0 ± 0.5	0.04	

Table 5.5: Measured fluxes for the Balmer lines and other chromospheric emission lines in 10^{-16}erg s^{-1} cm^{-2} (narrow and broad components).

No.	Hβ	H_9	H_{10}	H_{11}	H_{12}	H_{13}	H_{14}	H_{15}	Na D 5889 Å	Na D 5895 Å	He D_3	Ti II 3372 Å
1	2193	132 (-1.22)	108 (-1.31)	88 (-1.40)	59 (-1.57)	34 (-1.81)	24 (-1.96)	16 (-2.09)	274	194	161	3.7
2	2082	124 (-1.23)	99 (-1.32)	83 (-1.40)	50 (-1.62)	31 (-1.83)	19 (-2.04)	13 (-2.14)	273	193	154	3.5
3	2052	129 (-1.20)	101 (-1.31)	80 (-1.41)	58 (-1.55)	32 (-1.81)	22 (-1.97)	13 (-2.12)	265	186	156	3.4
4	1856	103 (-1.26)	82 (-1.35)	66 (-1.45)	47 (-1.60)	27 (-1.84)	19 (-1.99)	13 (-2.11)	270	195	143	2.6
5	2032	117 (-1.24)	92 (-1.34)	77 (-1.42)	53 (-1.58)	31 (-1.82)	21 (-1.99)	14 (-2.11)	282	201	152	2.4
6	1946	121 (-1.21)	86 (-1.35)	71 (-1.44)	45 (-1.64)	26 (-1.87)	18 (-2.03)	11 (-2.18)	254	178	147	2.1
7	2605	144 (-1.26)	112 (-1.37)	90 (-1.46)	56 (-1.67)	33 (-1.90)	22 (-2.07)	14 (-2.20)	329	235	196	4.0
8	2261	138 (-1.21)	97 (-1.37)	74 (-1.49)	61 (-1.57)	35 (-1.81)	24 (-1.97)	17 (-2.08)	307	267	177	4.0
9	1252	74 (-1.23)	57 (-1.34)	47 (-1.43)	34 (-1.57)	19 (-1.82)	12 (-2.02)	9 (-2.09)	186	129	99	1.4
10	1130	67 (-1.23)	47 (-1.38)	31 (-1.56)	29 (-1.59)	16 (-1.85)	10 (-2.05)	8 (-2.13)	169	113	79	1.1
11	2228	221 (-1.00)	147 (-1.18)	113 (-1.29)	81 (-1.44)	44 (-1.70)	24 (-1.96)	16 (-2.05)	230	163	215	3.4
12	3769	480 (-0.89)	302 (-1.10)	220 (-1.23)	179 (-1.32)	97 (-1.59)	65 (-1.76)	41 (-1.89)	352	272	407	7.0

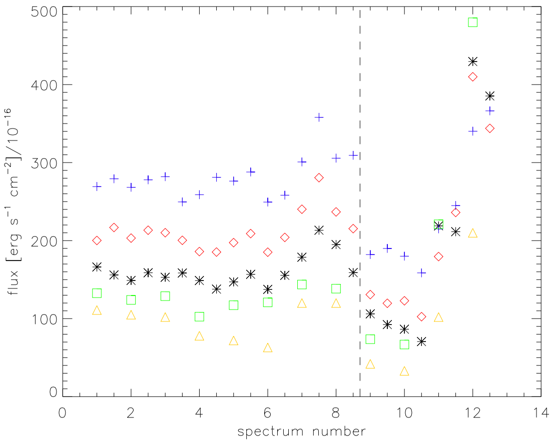

Figure 5.10: Line fluxes of various chromospheric emission lines. The black asterisks denote the He I D$_3$ line, the red diamonds the Hβ line scaled down by a factor of 10, the blue crosses the Na I D line at 5889 Å, the green squares the H$_9$ line, and the yellow triangles the Ti II line at 3372 Å scaled up by a factor of 30. The vertical dashed line marks the onset of the second night.

ening observed here can be due to either high turbulent velocities or Stark broadening caused by high electron densities. Since the broad component is also found outside the detected flares, Stark broadening seems to be an unlikely explanation, since the required electron densities are expected to be reached only during flares. On the other hand mass motions outside the obvious flares may be caused by microflares, therefore we favour an interpretation via turbulent mass motions.

In addition to the chromospheric emission lines, we find two He II lines at 3203.1 Å and 4685.7 Å originating in the transition region during the flare on December 13th. According to CHIANTI, the line at 3203.1 Å consists of 10 components from which only the 6 components between 3203.12 Å and 3203.19 Å are seen. The line at 4685.7 Å shows a double peak in the data, out of which we associate two CHIANTI components out of four to the first peak (4685.38 Å and 4685.41 Å) and all nine CHIANTI components (from 4685.71 Å to 4685.93 Å) to the second peak. Two additional components at 4685.54 Å and 4685.58 Å do not seem to be present in the data. We fitted the 3203.1 Å line using a single Gaussian profile and the 4685.7 Å using two Gaussian profiles. For the red line we also applied a non-constant background since there are many molecular lines present in the considered wavelength range, but used the first spectrum of the series as a background spectrum, assuming that there is no He II emission present outside the flare. Applying this procedure, we fitted the 4685 Å He II line in the spectra 11, 11.5, 12, and 12.5. The amplitude of the line in spectrum 11.5 is very low, therefore we excluded the fit from further analysis. Also we excluded the fit of the 12.5 spectrum because the first component of the 4685.7 Å could not be fitted well in this spectrum. The fit for spectrum 12 is shown in Fig. 5.11. The line fluxes, as well as their ratios, can be found in Table 5.6. Using the line flux ratios and CHIANTI, we also obtained rough estimates of the chromospheric electron density and temperature. We also verified that no consistent result can be found, if the missing components of the two lines are included, assuming that the same components are seen in both spectra. For spectrum 11 (which includes the short duration flare) we find a temperature of about $\log T = 4.7$ and an electron density of about $\log n_{\mathrm{e}} \gtrsim 10.0\,\mathrm{cm}^{-3}$ and for spectrum 12 $\log T \approx 5.0$ and $\log n_{\mathrm{e}} \approx 10.0\,\mathrm{cm}^{-3}$. The temperatures correspond approximately to the peak formation temperature of He II of $\log T = 4.7$.

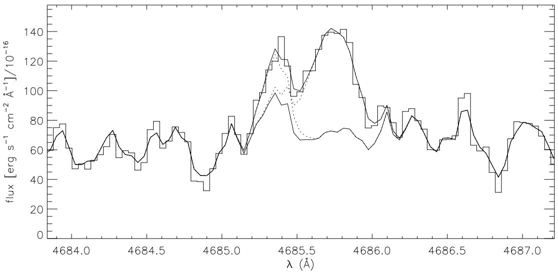

Figure 5.11: Fit of the He II line in spectrum number 12. The histogram-like curve is the data from spectrum 12, the lower black curve the background as taken from spectrum 1. The upper black curve is the fit to the data and the dotted lines are the two Gaussians (with respect to the background).

5.6 Discussion

Stars of spectral type M5–M6 are located at the boundary between early M dwarfs and late M dwarfs. Among the former, very strong X-ray emitters exhibiting more or less permanent flaring (Robrade & Schmitt 2005) are found, while the latter are often – in quiescence – hardly detectable as X-ray sources, yet these stars somehow have the ability to produce enormous enhancements in X-ray luminosity (as well as chromospheric and transition region radiation) during flares (Rutledge et al. 2000; Schmitt & Liefke 2002; Stelzer et al. 2006). In this context, CN Leo behaves according to expectations.

Table 5.6: Best-fit line fluxes for the two He II lines in 10^{-16} erg s^{-1} cm^{-2}.

No.	3203 Å	4685 Å 1^{st}	4685 Å 2^{nd}	ratio 1^1	ratio 2^2
11	2.4 ± 0.4	1.6 ± 0.7	15.8 ± 1.6	0.10 ± 0.04	0.14 ± 0.03
12	4.3 ± 0.5	5.6 ± 1.2	25.1 ± 1.6	0.22 ± 0.05	0.14 ± 0.02

[1] flux ratio between the two components of the line at 4685 Å

[2] flux ratio between both components of the 4685 Å line and the 3203 Å line

Its X-ray luminosity is lower than what is observed for late-type stars with spectral type M3/M4 or earlier; the more or less continuous flaring observed for these stars is replaced by either quiescent periods or well-identified individual flares, while only some low-amplitude flickering is left of the continuous variability of earlier M dwarfs. The example of Proxima Cen (Güdel et al. 2002a, 2004), however, shows that the flares observed for such "intermediate" objects can also reach very large amplitudes.

CN Leo's coronal temperature is lower than the coronal temperatures typically found for earlier M-type dwarfs (Robrade & Schmitt 2005). A temperature component in excess of 20 MK as found in the more active, earlier M dwarfs (Stelzer et al. 2002; Robrade & Schmitt 2005) could not be detected in CN Leo; instead a persistent 2 MK cool component was found in addition to a dominant 7 MK temperature component. The coronal densities obtained for CN Leo are low and hardly distinguishable from the low-density limit, consistently fitting the picture of typical stellar coronae as investigated by Ness et al. (2003a). Density variations related to different states of activity, as found by Maggio & Ness (2005), are consistent with the data, but remain speculative due to large measurement errors; clearly, much higher signal-to-noise is required for a definite measurement.

Stellar coronae often exhibit distinct abundance anomaly patterns. Only a few comparably inactive stars show a solar (photospheric) like coronal abundance pattern or even a FIP effect as observed on the Sun, with low first ionisation potential elements like iron enhanced by factors greater than two. Instead, especially very active stars exhibit the reverse pattern with the low-FIP elements being depleted and high-FIP elements enhanced. As a result, the metallicity in active stellar coronae is often low in general. These findings apply to active M dwarfs in particular and clear evidence for an inverse FIP effect has been found among early M dwarfs with respect to solar photospheric abundances (e. g. Maggio et al. 2004; Robrade & Schmitt 2005). The occurrence of FIP and IFIP effects seems to be correlated with activity (Güdel et al. 2002b; Telleschi et al. 2005): the FIP effect turns into the inverse FIP effect and the inverse FIP effect becomes stronger with increasing activity. Thus one would only expect a moderate IFIP effect for stars with decreasing activity like CN Leo, which is precisely what is observed. We find the overall abundance level to be about solar, also fitting the picture of an increased metallicity contrary to the sub-solar level often observed for very active stars. However, since coronal abundance determinations are difficult for very late M dwarfs, it is not clear if and how these trends proceed for such objects.

Our simultaneous VLT/UVES and *XMM-Newton* measurements have shown that the evolution of the lower-temperature X-ray component can be traced well from the ground using the Fe XIII 3388 Å flux. The different X-ray activity levels observed on December 11th and 13th are also found in the Fe XIII data. Unfortunately the signal-to-noise of these data is such that short-term variations within a given night can be detected only with great difficulty. However, long-term variability with possibly larger amplitudes should be easily detectable. The accuracy of the cross-calibration between the ground-based Fe XIII 3388 Å and predictions based on X-ray measurements is at the moment roughly a factor of ∼ 2. A possible repetition of such simultaneous observations should provide a more careful flux calibration of the optical data. The uncertainty arising from incorrectly assumed atomic physics parameters is difficult to assess, so more measurements are needed to ascertain which errors actually dominate the error budget.

Simultaneous multiwavelength campaigns of late-type stars allow the behaviour of different layers of the stellar atmosphere and their interactions to be directly evaluated. In this context correlated variations in different spectral bands or line fluxes are of specific interest. Many previous multiwavelength observations of active M dwarfs cover radio and X-ray observations with a focus on flares and on coronal properties (e. g. Güdel et al. 1996; Smith et al. 2005) with the intent of testing for relations like the Neupert effect or coronal heating models in the chromospheric evaporation scenario. Only a few recent studies (Hawley et al. 2003; Osten et al. 2005, 2006) also include UV or optical spectroscopy to monitor chromospheric emission lines. However, there does not seem to be a definite universal correlation between the fluxes in the different spectral bands. Nor is there any correlation between individual line fluxes, line broadening or velocity shifts. For example, Hawley et al. (2003) confirm the occurrence of the Neupert effect from their observations of individual flares on AD Leo and also discuss chromospheric evaporation and coronal backwarming. On the other hand, Osten et al. (2005) find a lack of correlation between different spectral bands and reject the Neupert effect as “the only” explanation of the mutual observed variations. Similarly, Smith et al. (2005) observed flares in X-rays on five active M dwarfs with missing counterparts in the radio, and vice versa, and discuss possible explanations.

Comparing our CN Leo observations to these studies, our target CN Leo has the advantage of showing discrete flares and periods of quiescence instead of permanent flaring, which makes it easier to clearly correlate variations observed in the different bandpasses and individual emission lines.

We covered two small flares with our simultaneous X-ray and optical observations. However, an in-depth discussion of the timing data to verify or falsify the presence of the Neupert effect would require far higher count rates to reduce statistical uncertainties. The time resolution of the blue optical spectra, covering most of the chromospheric emission lines, is low considering the time scales of the flare variations themselves. It is thus difficult to determine the exact onset of line variations from these spectra. The red spectra provide a better-resolved time coverage but lack the multitude of chromospheric lines seen in the blue range. Chromospheric line emission is clearly correlated with X-ray emission, at least concerning the two flares on December 13^{th}, if we consider the flux increase and line broadening observed towards the end of the December 11^{th} observations as connected to the strong flare about 20 minutes later and not covered by the optical data anymore.

5.7 Summary and conclusion

Our simultaneous optical/X-ray observations verify CN Leo’s status as a star of intermediate activity. Compared to earlier M dwarfs, its X-ray luminosity is lower, its coronal temperatures is dominated by cooler components, and the abundances lack a pronounced inverse FIP effect. CN Leo exhibits three different “quasi-quiescent” levels in X-rays during the observations, which are also clearly observed in the chromospheric lines in the optical. While the highest of these states on December 11^{th} 2005 may be due to the tail of the decay phase of a long duration flare, there is no such obvious explanation for the higher activity state on December 13^{th} compared to the May 2004 observation. Since the X-ray flux in the 2004 observation is comparable to the lowest X-ray luminosity measured by $ROSAT$, we regard this state as the true quasi-quiescent level of CN Leo.

We find coronal densities from the O VII triplets $n_e \sim 10^{10}$ cm^{-3}, while the Ne IX measurements are consistent with the low-density limit. During the flare on the second night, we also measured transition region densities from two He II lines that also give $n_e \sim 10^{10}$ cm^{-3}.

The line flux of the forbidden ultraviolet Fe XIII line at 3388 Å varied only a little during our observations, and the observed flux level is slightly lower on the second night compared to the first night. Variations in both the X-ray lines produced at similar coronal temperatures and in the emission measure of the cool 2 MK component agree well with the Fe XIII line flux, all turn out to be quite stable and did not vary at all, even during the onset of a flare in the second night. A line shift towards bluer wavelengths is indicated by the line fit (but within the errors the wavelength is in agreement with the rest wavelength). Such a line shift for the forbidden Fe XIII line during a short duration flare has been noticed before (Fuhrmeister et al. 2004) and would also be expected, as hot material is often shifted upwards or even ejected during flares. In general our observations show that the Fe XIII line is a good indicator of the behaviour of the cool coronal temperature component of CN Leo, whose status and whose variations can thus be diagnosed from ground-based observations alone from the relative variations in the Fe XIII 3388 Å line fluxes. The agreement between the “predictedänd observed absolute Fe XIII 3388 Å line fluxes is currently about a factor of 2, and it is unclear which errors dominate the error budget.

6 A coronal explosion on the flare star CN Leonis

A giant flare occurred during the first of the remaining three multiwavelength observations of CN Leo, whose high countrates allowed a detailed investigation of the early phases of the flare with a time resolution of one second. I presented preliminary results of this study at the 14th Cool Star Workshop and the conference on Coronae of Stars and Accretion Disks (Liefke et al. 2007). For the final publication, I performed the data reduction of both the X-ray and optical data, the analysis of the lightcurves, and the fitting of the X-ray and optical spectra.

J. H. M. M. Schmitt, F. Reale, C. Liefke, U. Wolter, B. Fuhrmeister, A. Reiners, and G. Peres
A&A, **481**, 799-805 (2008)

Abstract

We present simultaneous high-temporal and high-spectral resolution observations at optical and soft X-ray wavelengths of the nearby flare star CN Leo. During our observing campaign a major flare occurred, raising the star's instantaneous energy output by almost three orders of magnitude. The flare shows the often observed *impulsive behavior*, with a rapid rise and slow decay in the optical and a broad soft X-ray maximum about 200 seconds after the optical flare peak. However, in addition to this usually encountered flare phenomenology we find an extremely short ($\tau_{dec} \approx 2$ s) soft X-ray peak, which is very likely of thermal, rather than non-thermal nature and temporally coincides with the optical flare peak. While at hard X-ray energies non-thermal bursts are routinely observed on the Sun at flare onset, thermal soft X-ray bursts on time scales of seconds have never been observed in a solar nor stellar context. Time-dependent, one-dimensional hydrodynamic modeling of this event requires an extremely short energy deposition time scale τ_{dep} of a few seconds to reconcile theory with observations, thus suggesting that we are witnessing the results of a coronal explosion on CN Leo. Thus the flare on CN Leo provides the opportunity to observationally study the physics of the long-sought "micro-flares" thought to be responsible for coronal heating.

6.1 Introduction

The basic energy release in solar and stellar flares is thought to occur in the coronal regions of the underlying star, by conversion of non-potential magnetic energy through magnetic reconnection (Priest & Forbes 2002). Particle acceleration takes place and the accelerated particles and/or plasma waves move along the magnetic field lines and reach and heat cooler atmospheric layers (Syrovat-Skii & Shmeleva 1972; Brown 1973). Because of their small cooling times the heated photospheric layers start radiating immediately, serving as a proxy indicator for non-thermal particles, while the heated dense chromospheric layers "evaporate" leading to a soft X-ray flare (Brown 1973; Neupert 1968; Peres 2000). The heating and cooling time scales and the dynamic response of the various atmospheric layers are important for our understanding of solar and stellar flares and of coronal heating (Kostiuk & Pikelner 1975; Somov et al. 1981; Tamres et al. 1986; Fisher 1987); a popular hypothesis (Klimchuk 2006; Parker 1988) even attributes all of the required energy input to the quiescent solar corona to (nano)flare input.

Solar and stellar flares are observed to occur over vastly different time scales ranging from a few seconds (Vilmer et al. 1994; Schmitt et al. 1993) to more than a week (Kürster & Schmitt 1996), and the response of the heated plasma sensitively depends on the mode of energy input. Since the flare process involves plasma differing in temperature and density by more than four orders of magnitude, varying on short spatial and temporal scales, simultaneous multiwavelength data with sufficient spectral coverage and sufficient spectral and temporal resolution are required for any sensible observational diagnostics. Since the primary energy release and energy loss process of a flare is coronal, space-based X-ray observations are required. Using ESA's *XMM-Newton* X-ray observatory and ESO's Ultraviolet and Visual Echelle Spectrograph (UVES) on Kueyen on May 19^{th} 2006 we observed a spectacular flare on the nearby ($d = 2.39$ pc) flare star CN Leo (spectral type: M5.5–M6.0, $T_{\rm eff} = 2800$–2900 K). Despite its low apparent rotational velocity of $v \sin i < 3.0$ km s^{-1} (Fuhrmeister et al. 2004), CN Leo shows all the attributes of a magnetically active star, including chromospheric and coronal emission as well as flaring in the optical and in the X-ray bands (Fuhrmeister et al. 2007).

6.2 Observations and data reduction

The XMM-Newton observatory carries three co-aligned X-ray telescopes and a co-aligned smaller optical telescope equipped with the Optical Monitor (OM); this satellite and its instruments are described in detail in a Special Issue of Astronomy & Astrophysics Vol. 365 (Jan. 2001). For the CN Leo observations we used the medium filter in Full Frame and Large Window mode for all EPIC observations. The OM was operated in fast window mode, allowing U band flux measurements with a time resolution of 1 sec, limited by the chosen read-out sequence. The X-ray data were reduced with the XMM-Newton Science Analysis System (SAS) software, version 7.0. The basic XMM-Newton data consist of individual photons with known arrival time, position and energy; using standard filtering criteria these data are further processed into EPIC lightcurves and spectra.

UVES is an cross-dispersed echelle spectrograph mounted on the Nasmyth B focus of the Kueyen telescope (UT2) covering the wavelength range from about 3000 Å to 11 000 Å with a typical spectral resolution of ∼40 000. The temporal resolution of the high-resolution spectra is determined by the sum of exposure and read-out times (a few minutes in our case), a small fraction of the optical light is directed into an exposuremeter for each of the two spectral bands ("blue" and "red"), thus providing broad-band photometry with a time resolution of one second. These data are, however, taken mostly for engineering purposes, and are not corrected for background or airmass. For our analysis we used the UVES pipeline products with the wavelength calibration carried out using Thorium-Argon spectra resulting in an accuracy of ∼0.03 Å in the blue arm and ∼0.05 Å in the red arm. Absolute flux calibration is based on the UVES master response curve and extinction files provided by ESO.

6.3 Results

6.3.1 X-ray and optical light curves

In Fig. 6.1 we plot – from bottom to top – the recorded *XMM-Newton* X-ray light curve (i.e., the sum of the PN, MOS1, and MOS2 detectors), the *XMM-Newton* Optical Monitor (OM) U band light curve, and the UVES blue and red light curves for part of our observing run. In each panel we show a linear light curve covering 30 seconds around the flare onset, while the respective inserts show the logarithmic light curves of the whole flare event including some quiescence. The most notable feature in

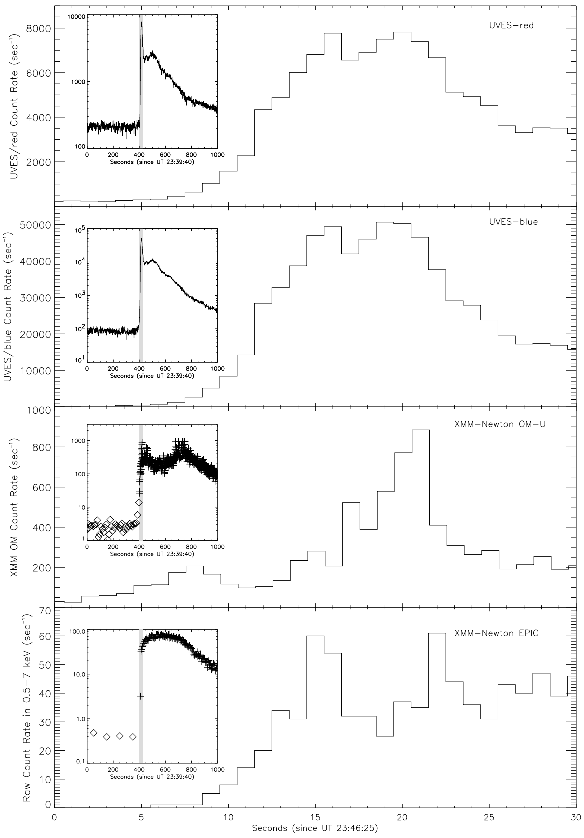

Figure 6.1: *XMM-Newton* EPIC raw X-ray (sum of PN,MOS1, and MOS2 detectors) and OM U band light curves (bottom panels), UVES blue and red channel (upper panels) during the first 30 seconds of the impulsive flare on CN Leo; all times are in UT seconds relative to May 19^{th} 2006, 23:46:25; the inserts show the same light curves covering 1000 seconds relative to May 19^{th} 2006, 23:39:40 in logarithmic scale including some quiescent emission and the full flare light curve; the light curve portions displayed enlarged are gray shaded. The X-ray light curves exclude events recorded in the center of the point response function to avoid pile-up effects; the total X-ray count rate is almost twice as large. The binning of all data is 1 s, except that of the X-ray data in the insert, which is set to 100 sec prior to the flare onset and to 10 sec afterwards. The OM light curve is dead time corrected; for rates above 500 cts/sec these corrections and the lightcurve become unreliable.

these light curves is the enormous, simultaneously occurring intensity increase in all considered energy bands starting at around UT = 23:46:20. The relative increase in terms of flare peak to pre-flare flux is >100 in X-rays and ≈750 in as shown in Fig. 6.1 are quite rare, and we are actually not aware of any examples in the literature sampled with the time resolution and spectral coverage of our data. The temporal alignment of the light curves in different bands ought to be accurate to at least 0.5 seconds and hence below the bin width. Fig. 6.1 shows four remarkable properties of our multiwavelength light curves: First, the flare onset appears to be earlier in the optical wavebands, in particular, there is no evidence for any significant soft X-ray "precursor" activity, while there is some "pre-flash" visible in the U band; second, the rise from quiescence to flare peak in the optical is 750 fold and occurs within ≈10 seconds; third, both the "red" and "blue" UVES light curves show two peaks separated by 5 seconds; and fourth, the first optical peak is accompanied by a soft X-ray peak. Note that this first soft X-ray peak is very sharp, lasting at most ∼2 seconds, and does not coincide with the main soft X-ray flare peak, which in fact is quite flat and occurs about 200 seconds later (cf., insert in bottom panel of Fig.6.1).

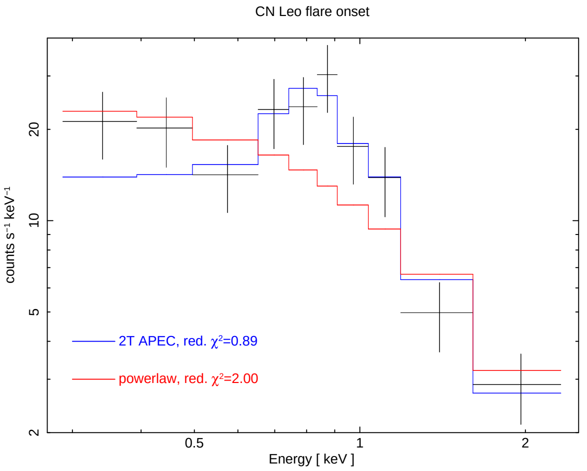

Figure 6.2: EPIC pn spectrum of burst between UT 23:46:36 to UT 23:46:44 (black data points) together with model fit assuming a thermal spectrum (blue curve) and a power law (red curve).

6.3.2 The spectral nature of the X-ray burst

The crucial question concerning the X-ray light curve is the nature of the soft X-ray peak at time T = 15 sec in Fig.6.1. We emphasize that this peak is statistically highly significant. We find a total of 105 counts in the two adjacent 1 sec bins around the optical flare maximum. A smooth interpolation of the flare rise light curve leads us to a "background" estimate of ≈55 counts in those two bins, implying an extremely high statistical significance of the 2 second flare peak. Accepting then the X-ray and optical peak and their close temporal as-

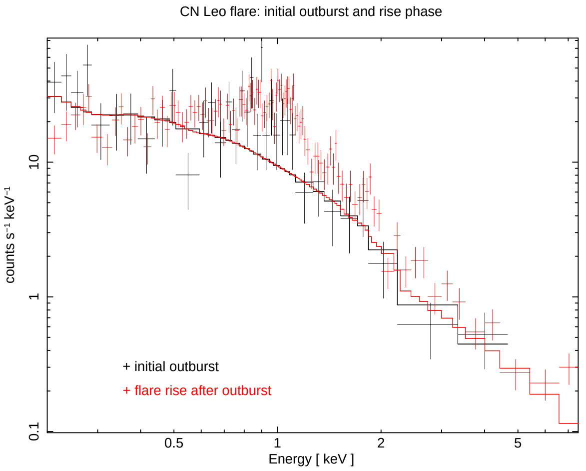

Figure 6.3: Comparison of burst spectrum between UT 23:46:36 to UT 23:46:44 (black data points) with postburst spectrum (red data points) between UT 23:46:44 to UT 23:47:44; a power law fit with photon index $\gamma = 2$ is also shown.

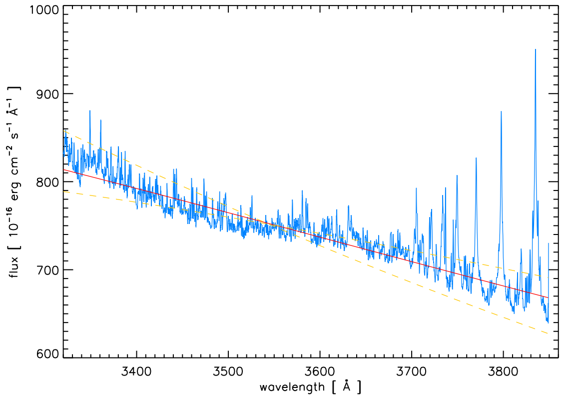

Figure 6.4: VLT/UVES spectrum (between UT 23:30:35 to 23:47:15) covering the wavelength range between 3300–3850 Å. Data points are shown as blue histogram, black body fits with temperatures of 11318 K in red and for 10 000 K and 15 000 K as dashed lines. Balmer line emission is visible at longer wavelengths, but at shorter wavelengths most of the flux resides in continuum.

sociation as real, on the one hand would suggest a non-thermal origin of the observed X-ray emission, while on the other hand, non-thermal X-ray emission has never been conclusively demonstrated from stars (Osten et al. 2007). Also, impulsive **soft** X-ray radiation is known from the Sun only on much longer time scales (Hudson et al. 1994). For the Sun, non-thermal, often impulsive X-ray emission is routinely observed, but below ∼25 keV the discrimination between thermal and non-thermal emission becomes exceedingly difficult (Kahler 1975). On the other hand, assuming a thermal origin of the first X-ray peak makes the observed fast decay time of ∼2 s difficult to reconcile with the usually invoked conductive or radiative cooling time scales.

Unfortunately the spectral analysis of the EPIC pulse height data in the respective time interval from UT 23:46:36 to UT 23:46:44 is plagued by the low SNR in this short stretch of data. The rebinned EPIC-pn spectrum of this time interval is shown in Fig. 6.2, together with a best fit assuming a thermal (blue curve) and a power law (red curve) spectral shape. For the thermal fit we assumed a two-temperature model with solar abundance, incidentally, a one-temperature component model with variable abundance also yields fits of comparable statistical quality. The fit quality of a power law fit ($\chi^2_{red} = 2.0$) is clearly far inferior to that of the thermal models ($\chi^2_{red} = 0.9$) , and a an improvement in quality of a power law fit can only be brought about by the introduction of substantial amounts of cold absorption ($N_H \sim 4{\cdot}10^{21}$ cm^{-2}), which we regard as utterly unphysical in the context of CN Leo. Therefore we clearly prefer a thermal interpretation of the “burst” spectrum purely on observational grounds. This thermal interpretation is supported by the X-ray spectrum between UT 23:46:44 to UT 23:47:44, immediately after the burst, displayed in Fig. 6.3, together with the power fit producing an acceptable fit to the burst spectrum in Fig. 6.2. Clearly, this spectrum cannot possibly be fit with a power law spectrum, the iron L complex and Ne lines in the energy range 0.7–1.2 keV prevent a power law description; formally, a power law fit with variable slope results in ($\chi^2_{red} = 3.32$), while a thermal spectrum yields ($\chi^2_{red} = 1.01$) and thus we conclude that the spectrum between between UT 23:46:44 to UT 23:47:44 is definitely thermal. Going back to Fig. 6.2 we realize that the largest power law fit residuals are found near 1 keV, precisely in that spectral range where the thermal nature of the post-burst spectrum becomes most apparent. If we assumed the burst spectrum to be non-thermal, the best fit power law slope of $\gamma = 2$ of the burst spectrum (cf., Fig. 6.2) would have to agree only coincidentally with the “slope” of the thermal spectrum in the post burst spectrum (cf., Fig. 6.3). Therefore we conclude that the EPIC pulse height spectra provide no proof for a non-thermal character of the observed X-ray emission during any time in the flare.

6.3.3 Optical burst spectrum

A high-resolution UVES spectrum covering the time interval UT 23:30:35 to UT 23:47:15 covering the wavelength range between 3200–3850 Å has been taken (see Fig. 6.4). While this spectrum covers also periods of quiescence, it is clearly dominated by the flare and can be taken as a representative mean spectrum of the first minute of flare emission. Over this wavelength range the emission is almost linearly decreasing with wavelength without any major emission lines except the Balmer lines at the long wavelength end; the bulk of the chromospheric emission lines appears only in later spectra. The slope of the best fit blackbody spectrum spectrum corresponds to an effective temperature of $\sim$11 320 K; other fits with temperatures fixed at 10 000 K and 15 000 K are also shown. Converting then the observed spectral normalization to an emission area (using the known distance towards CN Leo) results in an area estimate of $\approx 4.4 \cdot 10^{18}$ cm^2, while the other temperatures lead to values between 1.7–7.1 $\cdot\, 10^{18}$ cm^2. Some caution is warranted in this estimate: As is evident from Fig.6.1, significant photospheric temperature changes take place during the first 60 seconds, which cannot be resolved in the UVES spectrum. The derived temperature is therefore a mean and probably lower than the achieved maximum temperature. Further, no calibration spectra of standard stars were taken during the same night and using the spectra of different standard stars taken during different nights leads to errors in the absolute calibration of up to 50%. We therefore conclude that the emission area responsible for the observed blue optical emission was in the range 1–10 $\cdot\, 10^{18}$ cm^2. An independent estimate of the size of this emission area can be derived from the UVES photometer data. Using the mean temperature derived from the spectrum and the count rate during the spectral exposure, we can convert the observed count rate into an energy flux (from a comparison with other stars) and derive in this fashion an emission area of $\approx 8 \cdot 10^{18}$ cm^2, in good agreement with the estimate from the spectrum. We thus conclude that the photospheric flare peak temperature was in excess of 11 000 K and covered a flare area A_{fl} of 1–10 $\cdot\, 10^{18}$ cm^2 and obviously one expects the X-ray emission to arise from a similarly-sized region. Using the pile-up corrected PN light curve we can use the observed flare count rate in the energy band 0.5–8 keV to compute an (isotropic) radiative loss of $\approx 3.8 \cdot 10^{31}$ erg; we estimate that about two thirds of the overall radiative losses are contained in this energy band. During the first X-ray peak, the recorded X-ray luminosity is estimated to be $\sim 5 \cdot 10^{28}$ erg s^{-1} (Fig. 6.6).

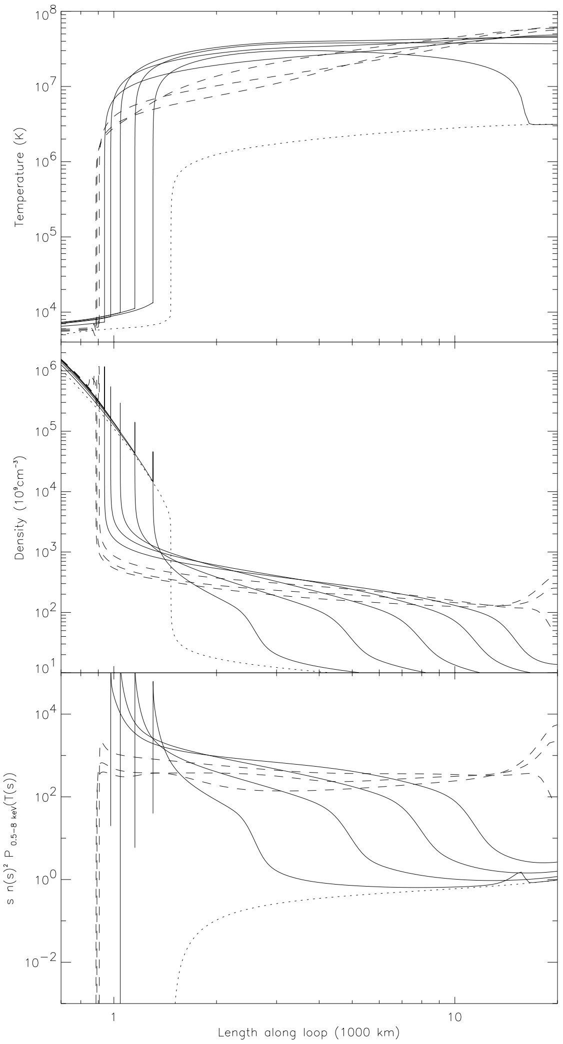

Figure 6.5: Calculated run of temperature (upper panel), density (in units of 10^9 cm^{-3}; medium panel) and emission measure weighted cooling function (bottom panel) for the first 20 seconds of a coronal explosion. The initial state (a quiescent loop with $T_{\max} = 3 \cdot 10^6$ K) is shown as dotted line, the evolution at times t = 2s, 4s, 8s and 10s, during which heating takes place, is shown as solid lines, that at times t = 13s, 16s, and 19s as long-dashed lines.

6.4 Modeling and Interpretation

6.4.1 Model ansatz

To address the question whether our observations and the above derived physical parameters are consistent with the expected hydrodynamic response of coronal plasma to a fast transient heat flux we performed a hydrodynamical simulation of an initially hydrostatic loop with prescribed length $L = 4 \cdot 10^9$ cm and apex temperature $T_{\max} = 2 \cdot 10^6$ K subjected to impulsive heating. For our hydrodynamical simulations we use the Palermo-Harvard (PH) code (Peres et al. 1982; Betta et al. 1997), which solves the time-dependent 1-D hydrodynamic equations on an Eulerian grid. The energy equation includes the effects of optically thin radiative losses, heating and thermal conduction, treated in the Spitzer form, which should apply in a high-density medium, where the heat pulse is deposited, The heating term Q consists of two contributions, a spatially and temporally constant term to produce a quiescent corona, and a spatially and temporally varying term to describe a flare. Since the microphysics of the heating is not well understood, we use an *ad hoc* parameterization of the form $Q_{fl} = H_0 f(t) g(s)$. For $g(s)$ we use a Gaussian $g(s) = \frac{1}{\sqrt{(2\pi\sigma)^2}} exp(\frac{-(s-s_0)^2}{2\sigma^2})$, centered at $s_0 = 2 \cdot 10^8$ cm (as measured from the loop footpoint) and $\sigma = 10^8$ cm, for $f(t)$ we use a symmetric triangular profile such that f(t) differs from 0 for a time interval t_{heat} and assumes a maximal value of unity and $H_0 = 7200$ erg cm^{-3} s^{-1}. The main difficulty for a numerical solution of the corona problem is the treatment of the transition region, where temperature and density gradients are extremely large. These numerical difficulties are aggravated by the fact that during the flare evolution the position of the transition region changes its spatial location. The PH code uses a re-adaptive grid, which insures a maximal relative change of 10% in all physical variables on adjacent grid points, provides a smoothly varying grid size over the whole computational domain and samples the whole region of interest with typically 500–550 grid points. At the footpoints the model loop is anchored to a dense chromosphere, the structure of which follows the treatment by Vernazza et al. (1981) and in which the energy balance is maintained throughout the simulation. We assume the loop to be symmetric with respect to its apex, so that the evolution is computed along one loop half and symmetry boundary conditions are imposed at the apex. The lower boundary is maintained at a fixed temperature at the chromospheric temperature minimum.

6.4.2 Explosion modeling

We specifically consider a simulation with $\tau_{dep} =$ 10 sec and a total deposited heat fluence $E_{tot} = 1.8 \cdot 10^{13}$ erg cm^{-2}, assumed to be deposited at a height of 2000 km above the photosphere. The results of our simulation are shown in Fig. 6.5, where we plot the run of density and temperature vs. loop length for the initial state and every 2 seconds into the flare evolution. The main effect of the transient heating is a rapid temperature increase of the "old" (i. e., pre-flare) corona and transition region of the loop and parts of the "old" chromosphere to temperatures of 20–40 MK. Because of the high-density of the latter, a high-pressure region, sandwiched between the low-pressure "old" corona and low-temperature unheated chromosphere/photosphere, is formed at the bottom of the "old" transition region. An expansion wave starts propagating upwards with speeds in excess of 1000 km/s to increase the density of the "old" corona ("loop filling"). This explosive filling of the loop occurs on a time scale of 10 seconds, comparable to the sound crossing time of the structure. Once the loop is rapidly filled, the material is more gently accumulated and compressionally heated, leading to a slower rise in emission measure and temperature. At the same time, the high-pressure "new" transition region moves inwards into the chromosphere with speeds of ~30 km/s; a narrow density spike separates inward moving outer regions from not yet accelerated inner regions. Once the heating stops, the temperature in the lower loop portions drops through conductive losses into the chromosphere, while the temperature at the loop top still increases through compressional heating. From the runs of temperature and density we compute the temperature-dependent emission measure and cooling in the energy range 0.5-8 keV, displayed in Fig. 6.5. Obviously during the first ≈10 seconds the main contribution to the X-ray flux comes from the bottom parts of the loop, while at later times the evaporated plasma dominates the overall coronal emission.

6.4.3 Comparison to observations and interpretation

The theoretical curves displayed in Fig. 6.5 can be readily compared to our *XMM-Newton* data. It is straightforward to compute the total X-ray flux assuming some loop cross sectional area and in Fig. 6.6 we juxtapose our model predictions (solid line) computed under the assumption of an emission area of $A_{fl} = 10^{19}$ cm^2 and the observed X-ray luminosities computed from the pile-up corrected PN lightcurve using a count-rate-to-flux conversion of $1.8 cdot 10^{-12}$ erg cm^{-2} count^{-1} and the known distance towards CN Leo. Although no best fit (in terms of the temporal model evolution) has been attempted we note the good agreement between theoretical expectations and observations. The X-ray peak coincides with the end of the heating phase and the spike in the light curve at t = 13 sec may represent another soft X-ray burst.

The above interpretation of the *XMM-Newton* light curve is supported by the observed run of the evolution of count rate and mean photon energy for

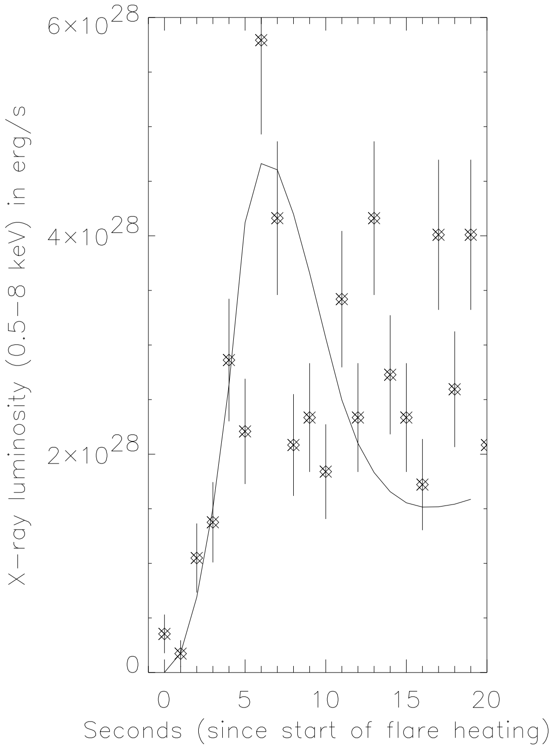

Figure 6.6: *XMM-Newton* X-ray light curve (in erg/s) overplotted over hydrodynamic model prediction; time is with respect to the modeled start of the energy input. Note the good agreement between data and model although no best fit was performed. Also note that the event at t = 13 sec might represent a further soft X-ray burst.

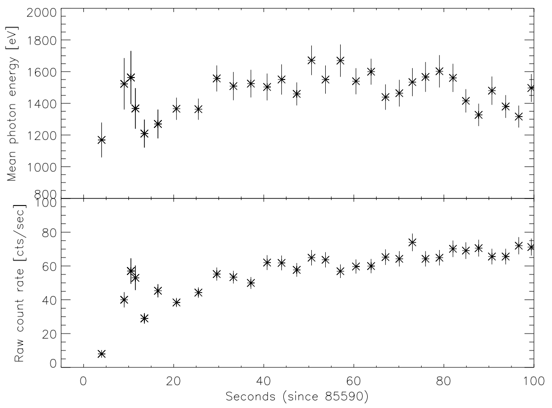

Figure 6.7: *XMM-Newton* EPIC light curve (bottom panel) and mean photon energy (top panel) vs. time for the first 100 seconds around flare onset; all times are relative to May, 19^{th}, 2006, 23:46:20. The mean photon energy has been derived from all photons with registered energies >500 eV; each data point represents the mean energy of 200 photons.

the first 100 seconds into the flare shown in Fig.6.7. As is clear, the mean photon energy and therefore the mean X-ray temperature are decreasing, implying that the X-ray emitting plasma is cooling. In the downward direction conductive cooling is the dominant cooling process; computing the cooling time scale at the heat pulse center through conduction via $\tau_{cond} = \frac{21nk}{2\kappa_0}\frac{L^2}{T^{5/2}}$ we find $\tau_{cond} \approx 1.7$ s using $n = 7{\cdot}10^{12}$ cm^{-3}, $L = 1{\cdot}10^8$ cm and $T = 3.4{\cdot}10^7$ K. The rapid cooling in the lower section of the loop leads to a pressure deficit accompanied by a density decrease and ensuing decrease in X-ray emission (cf., Fig.6.5), driven by the fast evaporation front moving ahead. The short lasting soft X-ray burst shown in Fig.6.1 is thus explained with a highly coherent plasma evolution, i.e., by flaring plasma confined in a single magnetic flux tube and by assuming that a major fraction or all of the observed energy release of $> 3.8\ 10^{31}$ erg occurred on a rather short time scale of 10 seconds or less. We therefore conclude that we are directly witnessing the process of evaporation as a result of the explosive heating of the lower chromosphere.

6.4.4 Thick target bremsstrahlung

As is clear from the above description the energy input in our modeling occurs in an *ad hoc* fashion by specifying an arbitrary spatially and temporally varying heating function. Since the precise nature of the heating physics is unknown, this approach seems justified. Of course, the physical picture we have in the back of our minds is that of energetic particles (electrons) penetrating deep into the chromosphere and upper photosphere, dissipating their energy there and heating up the adjacent atmosphere. Since the UVES light curves are well co-aligned with the initial X-ray light curve and since the former emission comes from relatively cool material far extending into the red wavelength band, we require fairly energetic electrons to energize these photospheric layers. Unfortunately, the precise properties of these electrons and, in particular, their energy spectra and spectral cutoffs are only poorly known for solar flares and essentially unknown in the case of stellar flares. At any rate, one expects thick-target bremsstrahlung from this non-thermal particle population, but at what level? To this end we follow the calculations by Syrovat-Skii & Shmeleva (1972) and Brown (1973), who considered the bremsstrahlung X-ray spectra for bremsstrahlung emitted by a population of electrons injected into the flare region with an energy distribution function of the form

$$F(E) = F_0(\frac{E_0}{E})^{\gamma}. \tag{6.1}$$

The approach taken by Brown (1973) is analytical, the most recent calculations of thick-target bremsstrahlung are those by Holman (2003), who computed microwave and X-ray spectra for such power law electron distributions using the appropriate relativistic cross sections and considering the effects of low and high energy cutoffs. As demonstrated by Brown (1973) and Syrovat-Skii & Shmeleva (1972), an electron power law distribution of the form given in eq.6.1 leads to a power law distribution of the observed photon flux density $I(\epsilon)$ of the form

$$I(\epsilon) = I_0(\frac{E_0}{\epsilon})^{\beta}, \tag{6.2}$$

i. e., again a power law distribution. The respective power law indices and normalizations are related through

$$\beta = \gamma - 1 F_0 E_0 = \frac{\beta(\beta-1)I_0}{AB(\beta-1,1/2)}; \tag{6.3}$$

$B(\beta-1,1/2)$ in eq. 6.3 denotes the Beta-function, and the constant A is given by

$$A = \frac{8}{3}\frac{r_o^2}{137}\frac{mc^2}{\pi e^4 Z^2 \Lambda}, \tag{6.4}$$

where the quantities c,r_o,m,e,Z and Λ denote speed of light, classical electron radius, electron mass, electron charge, ion charge number, and Coulomb logarithm respectively. Finally, the total energy content E_{tot} of the electron population in the energy range from E_0 to infinity can be computed from

$$E_{tot} = \frac{I_0 \beta E_0}{AB(\beta-1,1/2)} \tag{6.5}$$

Thus, as well known from solar physics, the power law index of the electron distribution as well as the normalization of the electron distribution and therefore its total energy content can be inferred from the observed photon power law index β and the observed photon fluence I_0, **if** the photons are indeed generated by the thick target bremsstrahlung mechanism. If we assume – for argument's sake – a thick target bremsstrahlung origin for the observed burst, we use the best-fit photon spectral index of $\beta \sim 2$ and the burst integrated photon fluence at 1 keV of $4.8 \cdot 10^{37}$ photons keV^{-1} to compute the total energy content E_{pl} of the power law electron population of $2.4 \cdot 10^{35}$ erg with a low energy cutoff of 1 keV; assuming a low energy cutoff of 0.1 keV, we instead find $E_{pl} = 2.4 \cdot 10^{36}$ erg. Regardless of the assumed low energy cutoff, the thus derived total energies are a few orders of magnitude above the observed soft X-ray energy output of $3.8 \cdot 10^{31}$ erg. In other words, under the assumption of non-thermal bremsstrahlung we would have to assume that unlike the solar case the bulk of the energy contained in the non-thermal electron population goes into other (unobservable) forms of energy. Applying Occam's razor we thus conclude that both observations and theory suggest that the observed soft X-ray emission is **not** due to thick-target bremsstrahlung. At the same time we have shown that thick-target bremsstrahlung, which is of course expected to be produced at some level, can be easily accommodated with in the existing observational framework, even if its low energy cutoff were to extend down to below 1 keV and therefore our theoretical modeling is fully consistent with the existing data.

6.4.5 Physical consistency of modeling

Does our theoretical modeling capture all of the important physics of the flare explosion? A basic assumption in our modeling is the 1-D character of the problem. Enormous pressure differences exist between "bottom" and "top" of the flaring plasma, while the magnetic field imposes a strong 1-dimensional directionality of the plasma along the field lines. Inspecting the maximally occurring gas pressures, we find values of up to 10 000 dyn cm^{-2}, requiring a magnetic field of >300 G for confinement. The mean photospheric field in CN Leo was simultaneously measured to exceed 2000 G (Reiners et al. 2007), thus plasma confinement is no problem and our 1-D modeling should be correct. The released energy is assumed to come from magnetic reconnection. An efficient energy conversion requires the incoming flow velocity to be less than 10% of the Alfven speed v_A and hence the time scale τ_{diss} for an efficient magnetic field dissipation on a spatial scale L becomes $\tau_{diss} \sim \frac{L}{0.1 v_A}$. Using $L \sim 2 \cdot 10^9$ cm and $\tau_{diss} \sim 5$ seconds, we find $v_A \sim 4 \cdot 10^9$ cm/s, which appears unrealistically large. However, since we expect coronal fields on the order of ≈300 G and particle densities of $\approx 5 \cdot 10^8$ cm^{-3}, we find Alfven velocities of $v_A \sim 3 \cdot 10^9$ cm/s, and therefore the assumption of Alfven speeds in excess to 10^9 cm/s is reasonable.

6.5 Discussion and conclusions

Heating by so-called "microflares" and "nanoflares" (Cargill & Klimchuk 2004; Klimchuk 2006) is a popular hypothesis to explain the heating of the corona of the Sun and that of other stars. Their nanoflare model assumes that any coronal loop is composed of many unresolved strands of magnetic flux and that these strands are "heated impulsively by a small burst of energy (which, for convenience, are called a nanoflare, although the range of energies is completely arbitrary". Further, the strands are thermally isolated from each other and can be viewed as elemental magnetic flux tubes with a small value for the plasma beta (Cargill & Klimchuk 2004). An individual heating event on such a strand leads to a dynamic evolution of the affected plasma located on this particular strand. In a typical observation of a star and even in a typical observation of the solar corona, a multitude of heating events occur more or less simultaneously on different strands located in the field of view or are integrated over during a typical exposure time. Therefore in this picture any solar or stellar coronal observation represents a mean of the heating and cooling history of possibly a very large number of individual energy releases. For a computation of the global properties of solar and stellar coronae in terms of the distributions of plasma densities, temperatures and flow velocities, a knowledge and modeling of the relevant heating and cooling processes is mandatory. Such models specifically assume an impulsive heating of the strands of magnetic flux, which can be recognized only in data with very high time resolution ($\sim$1 s), and then cool, first, by conduction and then by radiation (Cargill & Klimchuk 2004). This is precisely what appears to have happened on CN Leo: An energy release on a time scale of less than 10 sec in a single loop has to our knowledge never been observed in any star nor on the Sun. Therefore, with our high time-resolution soft X-ray and optical observations of the impulsive flare on CN Leo – by its energetics definitely not a nanoflare – we may have isolated the relevant physics for nanoflare heating of the corona of the Sun and that of the stars.

7 Multiwavelength observations of a giant flare on CN Leonis – The chromosphere as seen in the optical spectra

The detailed analysis of the giant flare is split into a series of three papers, dealing with the the chromospheric emission, the modeling of the optical spectra with the atmosphere code PHOENIX (Fuhrmeister et al. 2010), and with the study of the coronal flare plasma (Chapter 8). For the first part, I performed the data reduction of the red-arm optical spectra, the analysis of the optical and UV lightcurves, and the blackbody fitting of the optical spectra, as well as minor parts of the writing. It has been published by

B. Fuhrmeister, C. Liefke, J. H. M. M. Schmitt, and A. Reiners
A&A, **487**, 293-306 (2008)

Abstract

Flares on dM stars contain plasmas at very different temperatures and thus affect a wide wavelength range in the electromagnetic spectrum. While the coronal properties of flares are studied best in X-rays, the chromosphere of the star is observed best in the optical and ultraviolet ranges. Therefore, multiwavelength observations are essential to study flare properties throughout the atmosphere of a star. We analysed simultaneous observations with UVES/VLT and *XMM-Newton* of the active M5.5 dwarf CN Leo (Gl 406) exhibiting a major flare. The optical data cover the wavelength range from 3000 to 10 000 Å. From our optical data, we find an enormous wealth of chromospheric emission lines occurring throughout the spectrum. We identify a total of 1143 emission lines, out of which 154 are located in the red arm, increasing the number of observed emission lines in this red wavelength range by about a factor of 10. Here we present an emission line list and a spectral atlas. We also find line asymmetries for H I, He I, and Ca II lines. For the last, this is the first observation of asymmetries due to a stellar flare. During the flare onset, there is additional flux found in the blue wing, while in the decay phase, additional flux is found in the red wing. We interpret both features as caused by mass motions. In addition to the lines, the flare manifests itself in the enhancement of the continuum throughout the whole spectrum, inverting the normal slope for the net flare spectrum.

7.1 Introduction

Flaring is a commonly observed phenomenon on late-type stars. During a flare event, large amounts of energy are released probably from magnetic field reconfigurations and emitted over a wide range of the electromagnetic spectrum. Although white light flares are relatively rare for the Sun, they are quite common among M dwarf stars, because of their lower photospheric background emission in the optical. Chromospheric emission lines react sensitively to flares in amplitude, line width, line shape, and wavelength shifts. In addition, optical flares often have X-ray counterparts, although there is no one-to-one relationship between X-ray and optical flares. During large flares, dM stars can show an increase in X-ray luminosity by factors up to 100 (e. g. Güdel et al. 2002a, 2004), and even greater magnitude increases have occasionally been reported in the optical (e. g. Eason et al. 1992; Hawley & Pettersen 1991).

The thermal properties of the coronal flare plasma can be diagnosed from the emitted soft X-ray emission, while gyrosynchrotron radio and microwave emission typically traces nonthermal particles in the corona. Additionally, emission lines in the ultraviolet mainly diagnose the transition region. Different wavelength ranges thus provide complementary information, so that multiwavelength observations of flares allow to study the contemporaneous reaction of different layers of the stellar atmosphere. A prototypical multiwavelength campaign was carried out by de Jager et al. (1989) for UV Cet, which was simultaneously observed in X-ray, optical, and radio. As a more recent example, Mitra-Kraev et al. (2005) observed a correlation between ultraviolet and X-ray flux for stellar flares. Another recent multiwavelength campaign was aimed at the flare star EV Lac and provided data in the radio, the optical, the ultraviolet, and in X-rays (Osten et al. 2005, 2006). These data cover a huge radio flare and a number of optical and X-ray flares. Osten et al. (2005) note that, for a flare in one wavelength region, counterparts in other wavelength regions are often missing. An example of a giant flare on AD Leo observed in the ultraviolet and optical is described by Hawley & Pettersen (1991). AD Leo was again observed in multiwavelength by Hawley et al. (2003), where a number of medium-sized flares are covered and discussed. Smith et al. (2005) compare radio and X-ray flares on five active M dwarfs and provide possible mechanisms for uncorrelated flares. Multiwavelength observations also show that quiescent X-ray, optical, and radio emission strengths are no longer correlated for late M and early L dwarfs (Berger et al. 2005, 2008b,a).

Our target star CN Leo (Gliese 406) is a well-known nearby flare star with a spectral type of M5.5 (Reid et al. 1995) or M6.0 (Kirkpatrick et al. 1991). Reiners et al. (2007) find a mean magnetic field of $Bf \sim 2.2$ kG, exhibiting night-to-night and, with less certainty, intra-night flux variations. CN Leo has previously been the target of a multiwavelength campaign in December 2005, covering the optical (VLT/UVES) and X-ray regimes (*XMM-Newton*; Fuhrmeister et al. (2007)). During these observations, CN Leo once again proved to be quite active, showing two medium-sized and a number of smaller flares. Unfortunately, both larger flares occurred at the end of the optical observations and were therefore not properly covered. Now, CN Leo was again observed in the framework of a similar multiwavelength campaign, during which a spectacular flare occurred. This paper is the first in a series analysing the flare data, and it is structured as follows: In Sect. 2 we describe our observations obtained with UVES and *XMM-Newton.* In Sect. 3 we give an overview over the timing behaviour during the flare. The wide variety of chromospheric emission lines is reported in Sect. 4, while asymmetries found in the line shape of some emission lines are described in Sect. 5. A discussion and our conclusions are presented in Sect. 6.

7.2 Observations and data analysis

The multiwavelength observations reported in this paper were obtained simultaneously with *XMM-Newton* and ESO's Kueyen telescope equipped with the Ultraviolet-Visual Echelle Spectrograph (UVES) on three half nights in 2006: May, $19^{th}/20^{th}$ (first night), $21^{st}/22^{nd}$ (second night), and $23^{rd}/24^{th}$) (third night). We describe the optical data of the first night here in detail, whereas the X-ray data will be described in paper II of this series (Fuhrmeister et al. 2010).

UVES is a cross-dispersed echelle spectrograph that was operated using a dichroic beam splitter providing a blue arm spectrum (recorded with a single CCD) and a red arm spectrum (recorded with two CCDs).[1] For the blue arm, a standard setup with central wavelength at 3460 Å was used, while in the red arm a non-standard setup was used. The setup with central wavelength 8600 Å with blue end at 6600 Å was slightly blue-shifted to cover the Hα line. In our specific setup, used for the CN Leo observations presented here, the spectral coverage was between 3050 Å to 3860 Å in the blue arm and

---

[1] A detailed description of the UVES spectrograph is available under http://www.eso.org/instruments/uves/doc/

6400 Å to 10080 Å in the red arm with a small gap from 8190 Å to 8400 Å due to the CCD mosaic. We used a slit width of 1″, resulting in a resolution of $\sim 40\,000$. On May 19/20, the exposure times were 1000 s in the blue arm and 200 s in the red arm. In the three half-nights, our observations resulted in 68, 24, and 89 spectra in the red arm, and 16, 4, and 11 spectra in the blue arm.

The UVES spectra were reduced using the IDL-based `REDUCE` reduction package (Piskunov & Valenti 2002). The wavelength calibration was carried out using Thorium-Argon spectra and resulted in an accuracy of ~ 0.03 Å in the blue arm and ~ 0.05 Å in the red arm. Absolute flux calibration was carried out using the UVES master response curves and extinction files provided by ESO. For fitting individual line profiles, we made use of the CORA program (Ness & Wichmann 2002), that was originally designed for flux measurements of high-resolution X-ray emission lines.

In addition, photometry with a time resolution of ~ 1 sec was obtained with the UVES exposuremeters, i.e., two blue and red photometers located in the two arms of the spectrograph. However, the exposuremeters are mainly used for calibration and engineering rather than for science, so they are not flux-calibrated. We can nevertheless evaluate their spectral efficiency, taking into account the efficiency curves of all components in the optical path (i. e. dicroic and pre-slit filter) as provided by ESO[2], and assuming the quantum efficiency of a typical GaAS semiconductor device for the photometer itself. For our instrumental setup, the red exposuremeter should thus show a spectral efficiency similar to the Johnson R filter, covering the wavelength range from $\sim$ 5900–7100 Å, with its maximum at 6150 Å. The blue exposuremeter covers a broader wavelength range, from $\sim$ 3500–5800 Å, with a broad peak between 4600–5100 Å, and thus comprises a mixture of typical B and V filters.

The *XMM-Newton* satellite carries three co-aligned X-ray telescopes, each of which is equipped with one of the EPIC (European Photon Imaging Camera) MOS or PN instruments. These X-ray CCD detectors are photon-counting and thus provide timing information at the subsecond level and medium-resolution spectral resolution. Two of the X-ray telescopes are additionally equipped with Reflection Grating Spectrometers (RGS) that provide high-resolution X-ray spectroscopy. The X-ray instruments are accompanied by the Optical Monitor OM, an optical/UV telescope that can be used with different filters in imaging or fast readout mode; the latter mode provides photometry with a time resolution of ~ 1 sec. All instruments are normally operated simultaneously.[3]

Some of the X-ray data has already been published (Schmitt et al. 2008), and we will give a detailed analysis of the X-ray data in a subsequent paper (Liefke et al. 2010). In this paper we focus on the Optical Monitor, which was operated in fast mode with the U-band filter covering wavelengths between 3100–3900 Å, perfectly matching the spectral range of the blue arm UVES spectra. The observations are split into several exposures, each with an exposure time of 3200 s with gaps of about 300 s in between. We analysed the XMM-Newton data with the OM packages of the *XMM-Newton* Science Analysis System (SAS) software, version 7.0.

7.3 Time resolved spectral response of the flare

At the beginning of the first night of our observing campaign, a giant flare occurred; the onset properties of this flare have been described in detail by Schmitt et al. (2008). The corresponding red, blue and the U-band lightcurves as derived from the two UVES exposuremeters and the OM, are shown in Fig. 7.1, where we also show the start times of the blue and red spectra. Note that the spectra in the blue and red arms never start at the same time. Besides this large flare, several weaker flares occurred during the three half nights, which will be discussed in a separate publication. In this paper we concentrate on the emission observed from the giant flare.

The flare onset at UT 23:46:30 is seen as an enormous intensity increase in all wavelength bands, i. e. in X-rays, in the U band, as measured with the OM, and with the blue and red UVES exposuremeters. During the first few seconds of the flare, a sharp peak in the optical and in soft X-ray occurs. Schmitt et al. (2008) interpret this as the signature of a coronal explosion. After the first sharp peak, a broader peak is visible in the optical UVES exposuremeter data, followed by an even broader maximum in X-rays. The quasi-quiescent level after the flare is 8 percent higher than the pre-flare level in the blue arm and 6 percent in the red arm. Also, the chromospheric emission lines remain enhanced after the flare. A very similar time response of a large flare on UV Cet with a sharp first peak, a broad second peak, and the quiescent level after the flare higher than before was described by de Jager et al. (1989).

At the first flare peak, the flux increased by a

---

[2] http://www.eso.org/instruments/uves/tools/

[3] More details on the instruments onboard *XMM-Newton* can be found in the *XMM-Newton* Users' Handbook, available at http://xmm.vilspa.esa.es/external/xmm_user_support/documentation/uhb/index.html

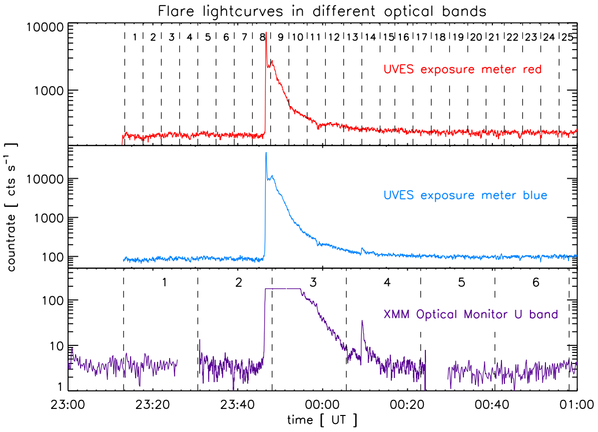

Figure 7.1: Optical lightcurves of the large flare on CN Leo. Top: UVES red arm exposuremeter. Middle: UVES blue arm exposuremeter. Bottom: *XMM* Optical Monitor (cut above count rates >200 cts s^{-1}). The vertical dashed lines in the red and U band plots mark the start times of the red and blue UVES spectra, respectively.

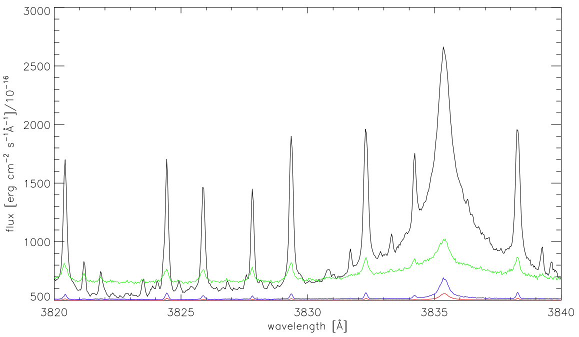

Figure 7.3: Spectral region around the Balmer line H9 in the blue arm. The evolution of the hydrogen and of several metal lines can be seen. The blue/lowest line denotes the pre-flare spectrum (no. 1). The green/light grey line denotes the spectrum covering flare onset (no. 2). The black line and the red/grey line denote the two following spectra (no. 3 and 4). The black spectrum (no. 3) was used for the line identification.

factor of about 550 in the blue UVES arm ,and by about 40 in the red arm compared to the pre-flare level. During the whole flare peak, the Optical Monitor entered saturation, i. e. the count rate in the U band exceeded the valid range for a reliable deadtime correction and flux conversion so that no reliable count rates can be derived. Additionally, the source extraction window suffers extremely from the so-called modulo-8 readout pattern, which disturbs the PSF of the OM. We thus do not consider the reconstructed shape of the lightcurve as trustworthy for count rates >200 cts s^{-1} and cut the lightcurve for count rate values exceeding this number.

The blue and red exposuremeter lightcurves are quite similar, and the decay after the broad second maximum is rather fast. In contrast, the decay time of the U-band lightcurve is much longer. Since the wavelength ranges covered by the exposuremeters contain far fewer chromospheric emission lines than the U-band, they mainly reflect the behaviour of the continuum, while the chromospheric emission lines dominate U-band lightcurve during the decay phase.

7.3.1 Blue part of the spectrum

In the blue arm, the large flare is covered by spectra no. 2, 3, and 4. They are shown, together with the quiescent spectrum no. 1, in Fig 7.2. The last ≈ 60 seconds of exposure no. 2, taken from UT 23:30:46 to 23:47:26, cover the impulsive phase of the flare; the contribution of quiescent emission in exposure no. 2 should be negligible. The spectrum is dominated by blackbody emission (see section 7.3.3). The Balmer lines have gained in amplitude and developed very broad wings. Many other chromospheric emission lines start to show up as well, but they are totally outshone by the blackbody radiation during the first ≈ 60 seconds of the flare. Therefore, the true wealth of emission lines becomes visible only in spectrum no. 3, covering the broader peak of the flare from 23:48:16 to 00:04:56. In spectrum no. 4, most of the emission lines show still increased emission, while in spectrum no. 5, a new quiescent level is reached. Simultaneously, the flux reaches the quiescent level around UT 00:30 as shown in the lightcurve in Fig. 7.1. A detailed example of the evolution of a typical part of the blue spectrum covering the H_9 line is shown in Fig. 7.3. An atlas of spectrum no. 3, which was used to create an emission line list, can be found in Figs. 7.4 and 7.5 published as online material.

7.3.2 Red part of the spectrum

In the red arm, the very first seconds of the flare are covered by spectrum no. 8, taken from UT 23:43:20 to UT 23:46:40. In this spectrum, a slightly higher level of continuum emission is already visible, especially in the bluer part of the spectrum around Hα. Some lines, e. g. the He I line at 6678 Å, are starting to go into emission, while others are not. This should partly be due to a lack of sensitivity since only a rather short time interval of the flare is covered, which prevents weak lines from showing up

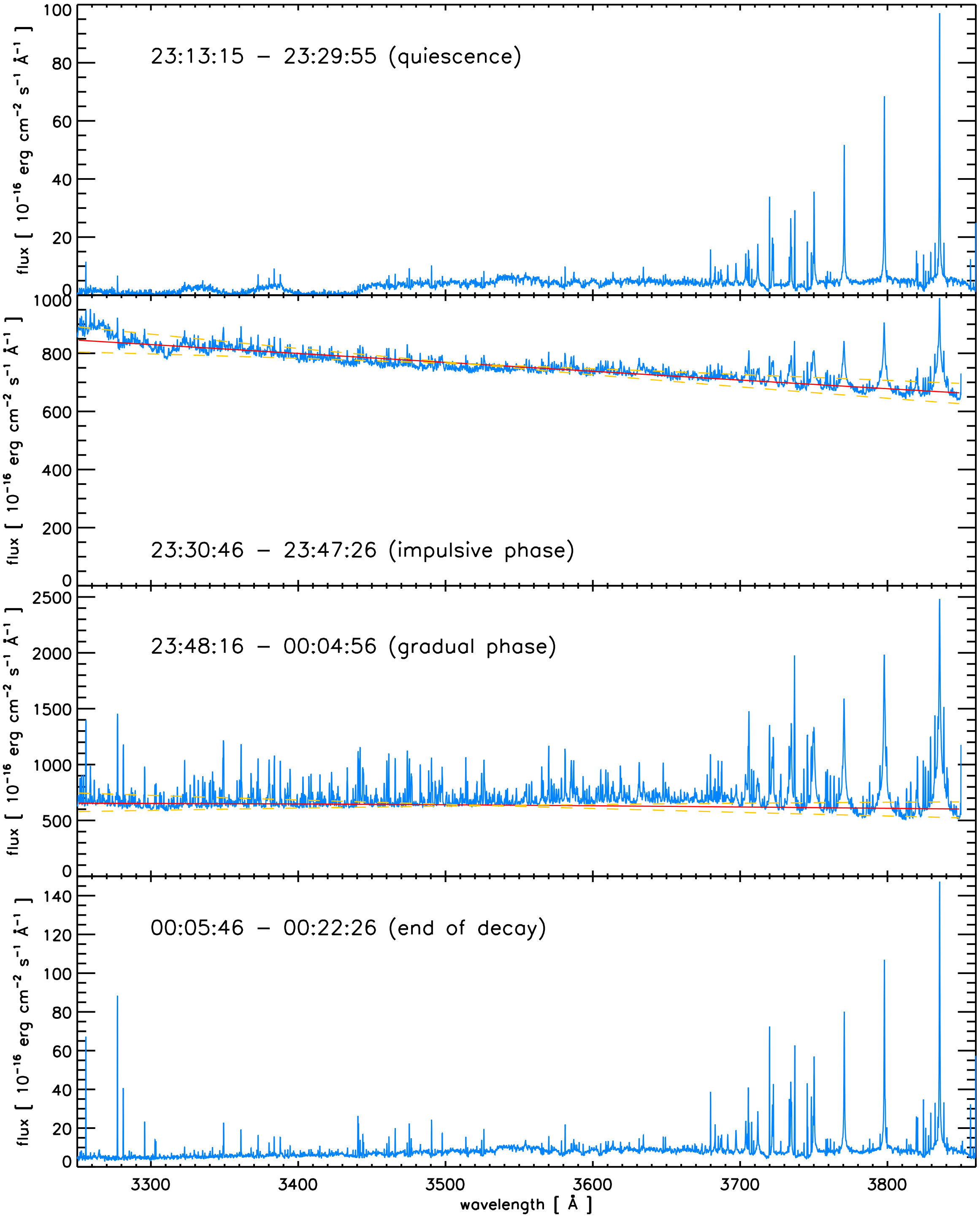

Figure 7.2: Sequence of blue UVES spectra no. 1 to 4 covering the flare (top to bottom). Note the different flux scales. Overlaid in red and orange are different blackbody fits.

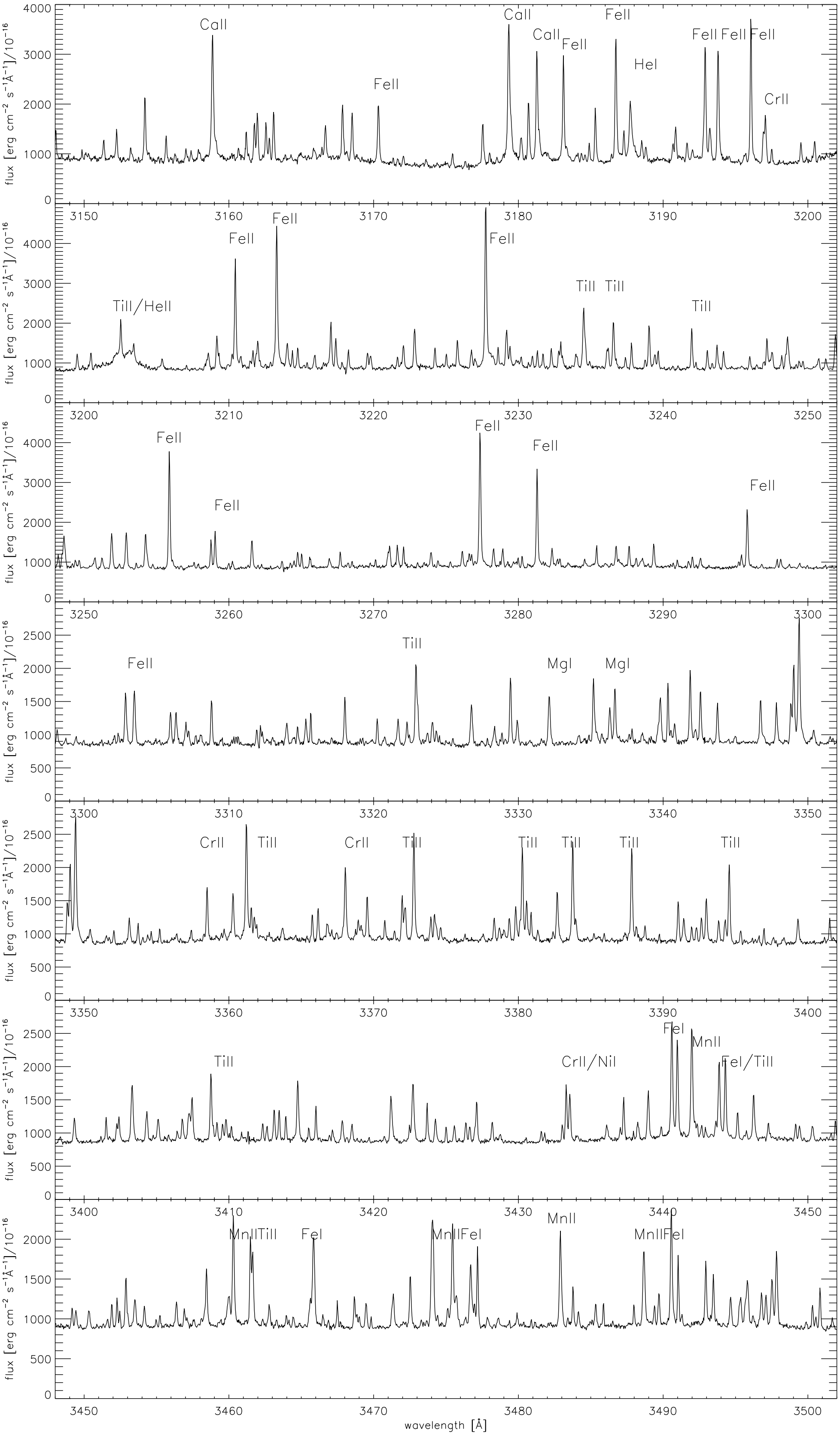

Figure 7.4: Spectral atlas of blue spectrum no. 3 from 3150 to 3500 Å. Some important emission lines are identified, for other identifications see the emission line list.

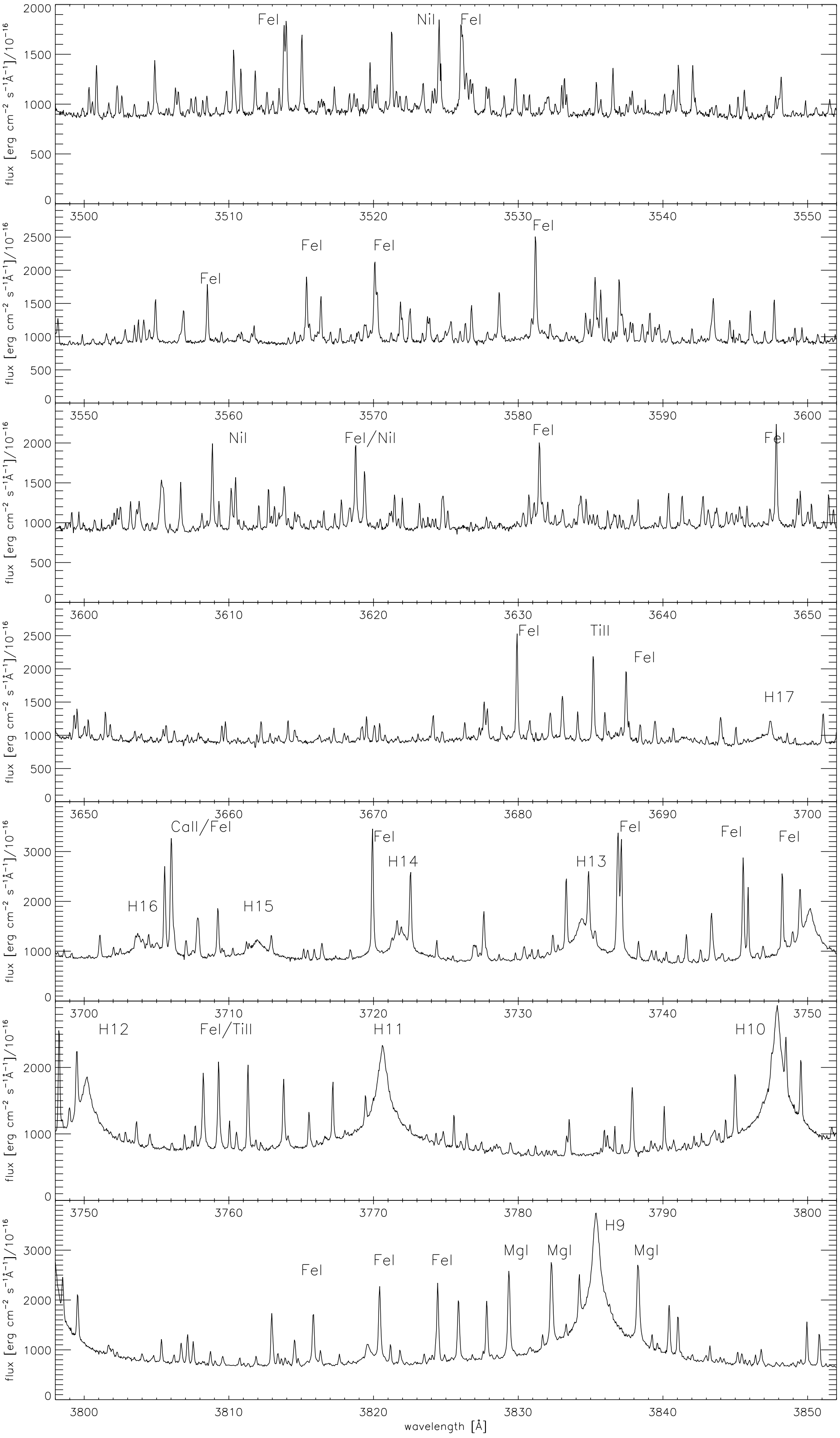

Figure 7.5: Same as Fig. 7.4 from 3500 to 3850 Å.

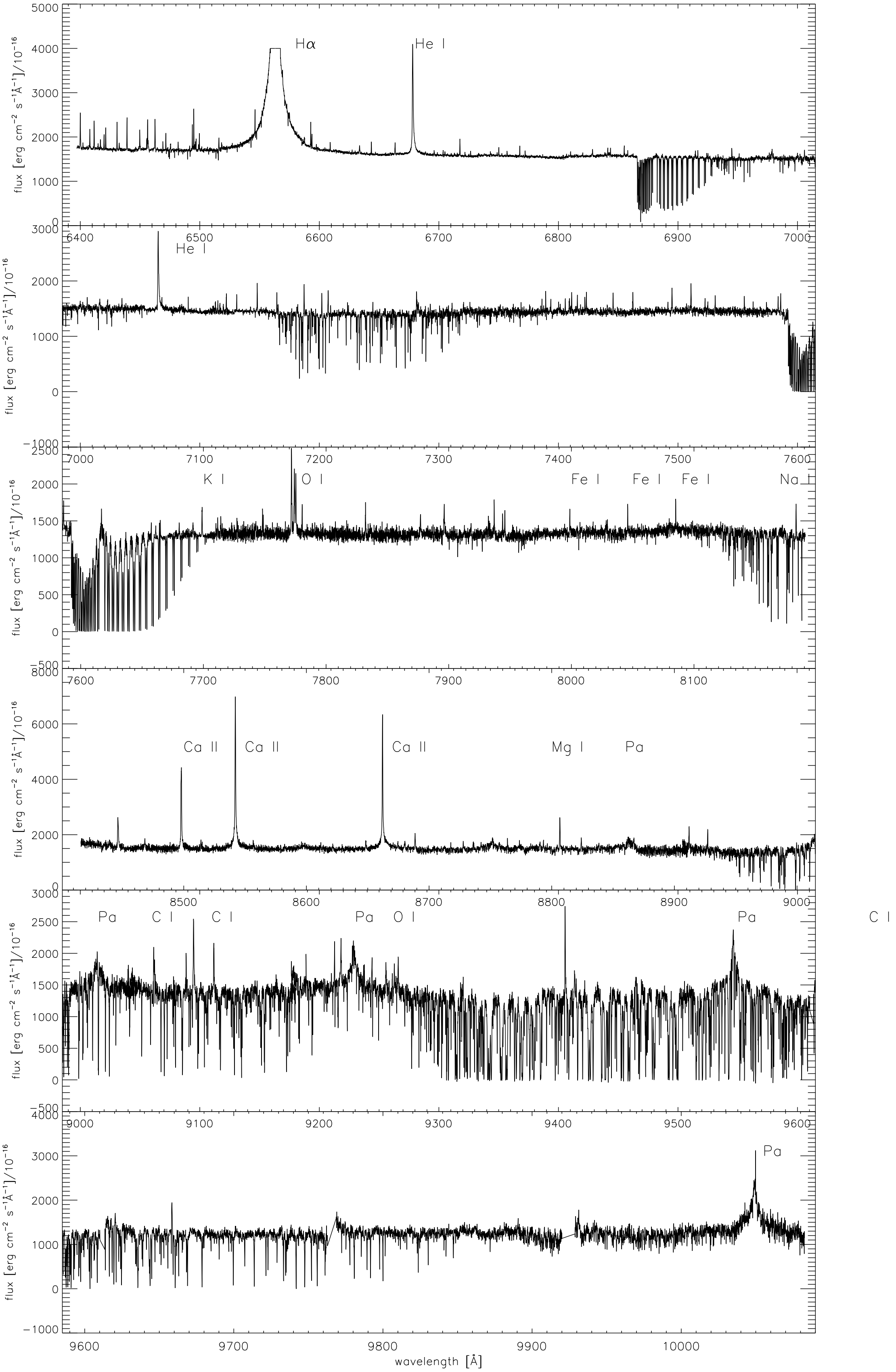

Figure 7.6: Difference (flare-only) spectrum of the red arm mosaic of spectrum no. 9 and 1 (same as in Fig. 7.7). A wide variety of emission lines can be noted, which is totally atypical for this wavelength range. Also the slope is inverted compared to the quiescent spectrum.

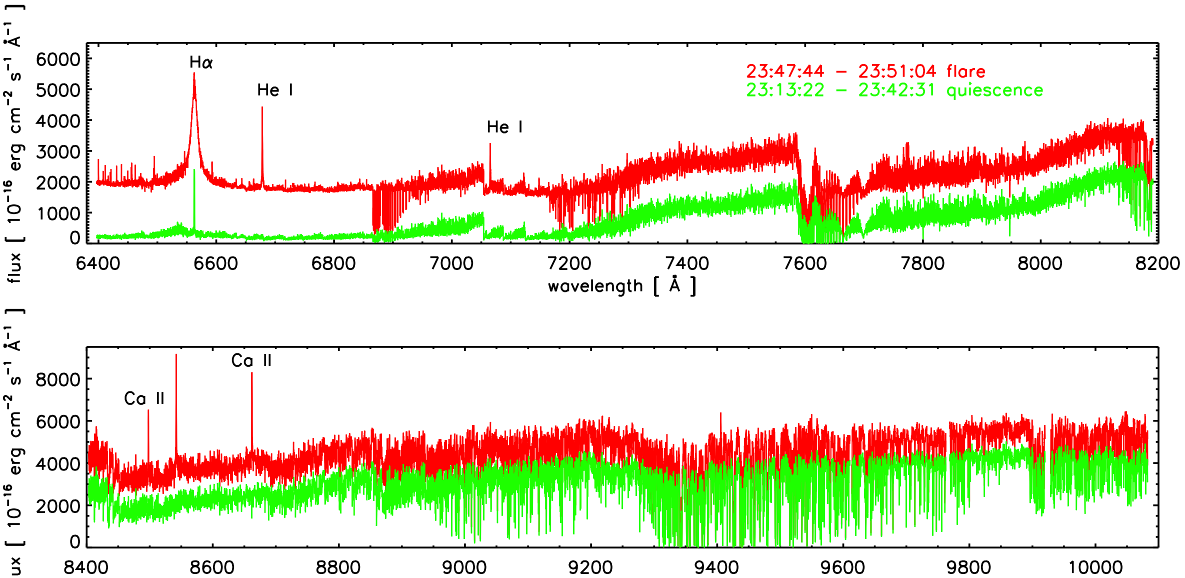

Figure 7.7: UVES red spectra in quiescence (spectrum no. 1 in green/grey) and in flare (spectrum no. 9 in red/black).

against the continuum. However, this may also be due to non-equilibrium conditions during the first few seconds of the flare, since lines formed at different atmospheric depths should react on different timescales.

The consecutive spectrum no. 9 starts at UT 23:47:37. Here, the continuum enhancement reaches a maximum and is clearly seen throughout the whole red spectrum. The net flare spectrum, i. e. with the quiescent flux subtracted, clearly shows an inverse slope with the flux increasing towards the blue end. This effect has already been described for a similar wavelength range for flares on 2MASS J0149090+295613 (M9.5, Liebert et al. 1999) and 2MASS J1028404-143843 (M7, Schmidt et al. 2007). Moreover, spectrum no. 9 shows a wide variety of emission lines never observed before in this spectral range. We show the flare spectrum no. 9 with spectrum no. 1 subtracted in Fig. 7.6, and the two spectra themselves in Fig. 7.7.

The emission lines decay on very different timescales. For example, emission of the Ca II triplet lines decays very slowly and can be noted until spectrum no. 16, while the emission core of K I is undetectable after spectrum no. 11. The same applies to the net flux of the three O I lines around 7772 Å, while the three O I lines around 9262 Å are only found in the flare spectrum no. 9. The timing behaviour of the line flux is shown in Fig. 7.8 for some important emission lines.

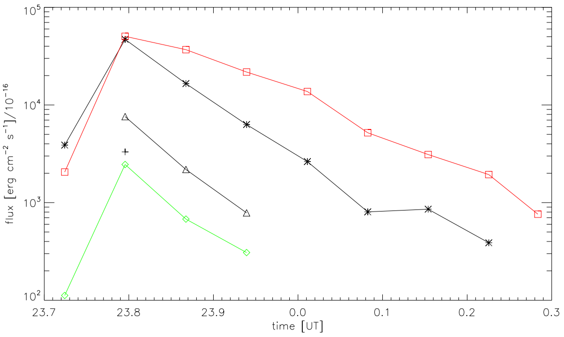

Figure 7.8: Timing behaviour of line fluxes with quiescent flux removed for some important emission lines. Red squares denote the Ca II line at 8542 Å (narrow and broad component; line core is saturated during flare peak),black asterisks denote the He I line at 6678 Å (narrow and broad component), black triangles denote the O I line at 7774 Å, green diamonds denote the emission core of the K I line at 7699 Å, and the black cross the line flux of the Na I line, which is elevated only during flare peak.

The continuum emission stays enhanced until about UT 00:15 (spectrum no. 15) in the blue part of the red arm, while the red part of the red arm is only elevated in spectra no. 8, 9, and 10.

7.3.3 Temperature evolution

The well-defined slope of the flare continuum in our spectra suggests a blackbody origin. We fitted temperature and emitting area to the smoothed blue spectra no. 2 and 3 after removing the emission lines. In both cases, the contribution of the quiescent atmosphere was neglected. The fit gives temperatures of $\sim$ 11 300 K for spectrum no. 2 (also discussed in Schmitt et al. 2008) and of $\sim$ 9100 K for spectrum no. 3; however these temperatures correspond to averaged values during the exposure (i. e. for the flare onset during the first minute of the flare in spectrum no. 2, and over the whole exposure time of 1000 s during the broader peak in spectrum no. 3), since the thermal continuum emission can be expected to undergo a rapid decrease in temperature and flux. Figure 7.2 shows the two best-fit blackbodies as straight (red) lines; blackbody fits with fixed temperatures of 10 000 K and 15 000 K in spectrum no. 2 and with 7000 K and 10 000 K in spectrum no. 3 are also shown for comparison as dashed (orange) lines. Thus the uncertainties of the temperature fit can be estimated not to exceed 1000 K. The resulting sizes of the emitting area are then $1–10 \cdot 10^{18}\,\mathrm{cm}^2$. In spectrum no. 4, the continuum level has nearly decreased to quiescent levels.

The same procedure can be applied to the red arm spectra no. 8, 9, and 10, with the quiescent flux subtracted. Since for temperatures around 10 000 K the wavelength range covered by the red arm spectra is located far in the Rayleigh-Jeans part of the blackbody spectrum, the derived temperatures have rather large errors, which we estimate to reach up to 5000 K. Additionally, the true continuum level at the position of the strong telluric absorption bands is difficult to assess. It is thus appropriate to restrict the analysis to the short-wavelength part of the spectrum. The red flare spectrum no. 8, covering the impulsive phase of the flare, can be fitted with a temperature of $\sim$ 27 700 K (and with $\sim$ 19 600 K considering both parts of the red arm). For the red spectrum no. 9 we determined a temperature of $\sim$ 5600 K. Spectrum no. 10 gives temperatures of 2600 to 3200 K, i. e. the flare plasma has cooled to CN Leo's quiescent photospheric temperature of $\approx$ 2900 K (Pavlenko et al. 2006; Fuhrmeister et al. 2005b). The values derived for the emitting area are consistent with those from the blue spectra alone.

Putting the derived temperatures in the right chronological order, one starts with red spectrum no. 8 (covering the first few second of the flare) with probably more than 20 000 K, then followed by the blue spectrum no. 2 (covering the first minute) with about 11 000 K. In the subsequent blue spectrum no. 3 and red spectrum no. 9, the measured temperature is rapidly dropping from 9100 K to 5600 K, reaching the quiescent photospheric temperature for red spectrum no. 10.

The optical flare continuum emission can most likely be attributed to photospheric plasma that is reprocessing UV and EUV line emission, which itself was induced by heating from nonthermal particles (as discussed by Hawley & Fisher 1992, where they confirm the blackbody hypothesis from photometric UV observations of flares on AD Leo). Several spectra covering flares on late M dwarfs can be found in the literature; however, they typically cover only the spectral range of Hα and longwards in wavelength, introducing large uncertainties into a possible blackbody fit. Our blue spectra allow us to assess the blackbody temperature from the slope of the spectra with reasonably small uncertainties. Together with the different temporal coverage of the flare in the red arm, we can conclude that the plasma is initially heated to temperatures probably greater than 20 000 K and cooling rapidly afterwards, reaching already the photospheric level when the chromospheric line emission is still seen near its maximum.

7.4 Identification of chromospheric emission lines

For the flare spectra, we point out the wealth of chromospheric emission lines. Because many of the lines, especially in the red part of the spectrum, were not observed in emission before, we provide an emission line list for the flare spectrum.

7.4.1 General information on the line catalogue

In the blue spectrum no. 3 and the red spectrum no. 9, we detected 1143 chromospheric emission lines altogether, with 989 out of them located in the blue arm and 154 in the red arm. Out of the 154 emission lines in the red arm spectrum, 110 were analysed in the flare-only spectrum. While the blue arm typically comprises pure emission lines, emission cores in absorption lines and filled in absorption lines are also found in the red arm. From our red spectra, we show the Paschen 7 line (pure emission) in the flare spectra (Fig. 7.9), the K I line (emission core) at 7699 Å (Fig. 7.10), and the Na I line (filled in absorption) at 8183Å (Fig. 7.11) as three representative examples of each type of enhanced flare emission.

To determine the line parameters we used an IDL routine that automatically fits background, central wavelength, FWHM, and line flux as free parameters using a Gaussian parameterisation for every manually indicated emission line in a certain wavelength range. We typically chose 10 Å as the wavelength range for one fitting process, since the background variations on such an short wavelength interval are acceptable. The applied program was

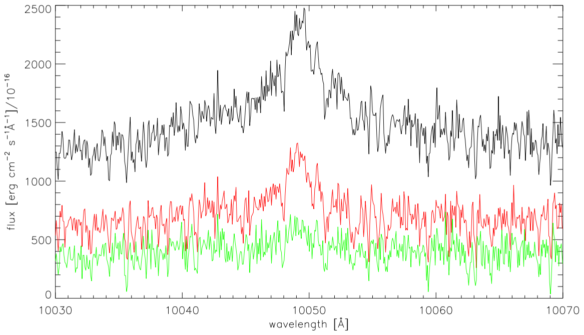

Figure 7.9: Paschen (P7) line at 10049 Å with a cosmic removed at 10049.972 Å. The black line corresponds to the red flare-only spectrum no. 9. Also shown are the two consecutive flare-only spectra, where the line quickly decays.

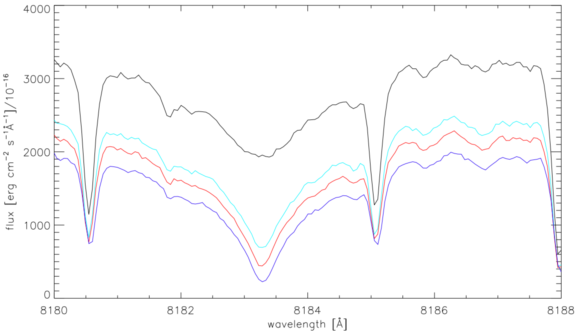

Figure 7.11: Na I line at 8183 Å. The quiescent spectrum no. 1 is shown in blue/lowest line. Colour coding as in Fig 7.10. In contrast to the K I line in Fig. 7.10, no emission core is seen, but the line fills in with chromospheric emission, resulting in an emission line in the flare-only spectra.

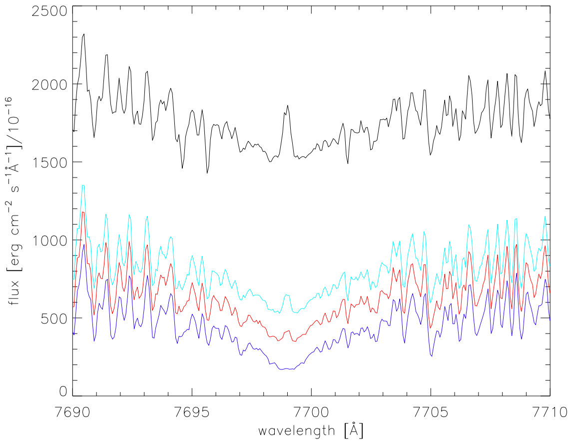

Figure 7.10: K I line at 7699 Å. The quiescent spectrum no. 1 is shown in blue (lowest line). The black line denotes the flare spectrum no. 9, the turquoise/light grey and red/grey lines denote the two following spectra. Note the emission core during the flare.

kindly provided to us by Dr. Jan-Uwe Ness. The line fit parameters including a (possible) identification can be found in Table 7.1.

In the line catalogue we provide the measured emission line fluxes. These may be affected by rather large errors mainly for two reasons. First, the description with a Gaussian may result in a poor fit if the lines have broad wings. The 18 affected lines belong to the ions H I, O I, Fe I, and He II and are flagged accordingly. Second, the background/quasi-continuum may be somewhat ill-defined. This is true for emission lines in a broader emission line wing (stated in the remarks), but also for emission cores of absorption lines and for varying background, with the latter found especially in the red arm due to molecules. Also, the Hα line and the Ca II triplet lines are saturated in the peak flare spectrum, which was used for the identification list. Moreover, 5 Balmer/Paschen lines could not be fitted at all due to their large width (but they are clearly present). Therefore, individual lines may have flux errors larger than a factor of 2, but normally the flux measurements should have errors below 30 percent.

We mainly used the Moore catalogue (Moore 1972) for identifying the lines, a few lines were identified using the NIST database [4]. For the identifications from the Moore catalogue, the multiplet is also given in the catalogue. The spectra were first shifted to the rest wavelength for the identification process. This enables us to find systematic lineshifts caused by the flare, which was not the case in general. The average displacement between measured central wavelength and laboratory wavelength is 0.01 Å in the blue arm and 0.05Å in the red arm.

We were not able to identify 7 emission lines. Another 167 (15 %) lines have only tentative identifications for one of the following reasons: (1) the line was not found in the Moore catalogue, (2) the wavelength shift to the possible laboratory wavelength is large, (3) the line is severely blended with other lines, and (4) (most often) the line is the only one out of the multiplet. However, there are few lines, which are single identifications out of a multiplet or are from a singlet, that are flagged as secure identifications. The catalogue includes a set of flags

---

[4] Available online under http://physics.nist.gov/PhysRefData/ASD/index.html

Table 7.1: First 5 rows of the line catalogue. The whole table is accessible electronically via http://cdsweb.u-strasbg.fr/cgi-bin/qcat?J/A+A/.

central wavelength [Å]	FWHM [Å]	flux [$\mathrm{erg\,s^{-1}\,cm^{-2}}$]	catalogued wavelength [Å]	ion	multiplet	id flag	comment
3057.45	0.057	4.43e-13	3057.446	Fe I	28	0	n
3059.09	0.057	4.27e-13	3059.086	Fe I	9	1	n
3062.26	0.045	2.08e-13	3062.234	Fe II	108	0	n
3064.62	0.042	9.17e-14	3064.623	Ni I	26	0	n
3065.32	0.042	1.34e-13	3065.315	Fe II	97	0	n

providing information on the identification status of the line. If there are other possible identifications for the line, these are normally given as remarks, even if the line is identified securely. The latter may be the case if the line belongs to a multiplet out of which a number of lines are already found, but there are other (plausible) identifications with identical or very near laboratory wavelength.

Since we excluded doubtful features from our line list, the list cannot be claimed to be complete, especially for the weak lines with fluxes below $5 \cdot 10^{-14}$ $\mathrm{erg\,s^{-1}\,cm^{-2}}$. Also, we partly used the flare-only spectrum in the red arm, as denoted by the identification flag for individual lines. To create this flare spectrum, we subtracted the first spectrum of the May 19/20 night, which shows CN Leo in quiescence.

The identified lines belong to 35 different ions in total, and the basic statistics of these flare lines can be found in Table 7.2. For the appearance of V II lines in emission, we are not aware of any description of V II chromospheric emission lines for flare stars in the literature.

Table 7.2: Chromospheric emission line identification

ion	no. lines[1]	ion	no. lines[1]
H I	15(15)	Mg I	13(11)
He I	7(5)	Mg II	5(3)
He II	1(1)	Na I	2(1)
Sc II	16(16)	Na II	0
Ti I	15(6)	K I	1(0)
Ti II	125(116)	Ca I	13(11)
V II	32(30)	Ca II	9(8)
Cr I	16(12)	C I	5(5)
Cr II	72(59)	N I	1(0)
Mn I	13(11)	O I	6(6)
Mn II	9(8)	Ne I	1(0)
Fe I	494(428)	S I	2(0)
Fe II	90(70)	Al I	4(2)
Co I	47(43)	Si I	10(3)
Co II	1(1)	Si II	1(0)
Ni I	98(87)	Y II	1(0)
Ni II	5(3)	Zr II	2(2)
Cu I	3(2)		
Ba II	1(1)	no id	7

[1] in parenthesis the number of secure identifications

7.4.2 Comparison to other work

Many of the emission lines in the flare-only spectrum (with the quiescent spectrum subtracted) have not been observed before. Flare stars are traditionally observed in the ultraviolet and X-ray regime, rather than at these red wavelengths. In addition, observations in this wavelength range often lack the resolution necessary for resolving the metal emission lines without wings. Nevertheless, most of the stronger emission lines like the Paschen lines, the He I, the Ca II lines, and others have been described in spectacular flares on very late-type M dwarfs. For example, 2MASS J0149090+295613 (spectral type M9.5 V) was observed by Liebert et al. (1999) during a flare showing 16 emission lines in the red part of the spectrum among them 5 Paschen lines and the Ca II triplet. Schmidt et al. (2007) also describes two flare events on LP 412-31 (M8) and 2MASS J1028404-143843 (M7), showing emission lines in the considered wavelength range. Both stars show the Ca II triplet and hydrogen Paschen emission up to P_{11}. During all these three flares, the Paschen lines are much more prominent than in our case. We ascribe this to the earlier spectral type of CN Leo, which has more continuum flux at these wavelengths.

As another example we compare our observations to flares on the old inactive M4 star Gliese 699 (Barnard's star) by Paulson et al. (2006). There, the wavelength coverage was from 3700 to 10 800 Å, with a spectral resolution of ∼ 60 000. Paulson et al. (2006) have also produced an emission line list. In the overlapping wavelength range with our blue arm (from 3730 to 3860 Å) they find 28 lines, where we find 135 emission lines. Among these, there is one line at 3772 Å where we located Ni I at 3772.530 Å, while Paulson et al. (2006) identified Fe I at 3772.23 Å. With the exception of this one line, we found all lines also identified by Paulson et al. (2006) in the blue wavelength range. In the red arm, we found 154 lines, while Paulson et al. (2006) detected 11 enhanced lines redward of 6400 Å. Again, we were able to locate all of their lines with one discrepancy at 6462 Å, where we found a line at 6462.566 Å tentatively identified as Ca I, while Paulson et al. (2006) found an enhanced line at 6462.73 Å identified as an Fe I line. It is not clear why we do not see these two Fe I lines identified for Barnard's star. Our resolution is sufficient to detect these two lines and not to confuse them with our additional detections.

He II emission from the transition region

Among the chromospheric emission lines, there is an He II line at 3203.104 Å originating from the transition region. This line, which is barely recognisable outside of flares, reacts to the flare as well, but not as strong and fast as the chromospheric lines. During the flare peak in spectrum no. 3, the He II line is not as strong as the two flanking chromospheric Ti II emission lines. In the following spectrum no. 4, the two Ti II lines have completely decayed, while the He II line is still present. As found by Fuhrmeister et al. (2007), the situation is quite different during the flare onset of 13 December 2005 as seen in spectrum no. 12. There, the He II line reacts much more strongly than the two Ti II lines, which may be interpreted as due to different energy deposition heights for the two flares. The strong flare discussed here had an energy deposition into very deep layers (as can also be seen from the strong blackbody/photospheric reaction and the enormous width of the Balmer series lines). Thus, the transition region seems to be heated more gently, but of course this is difficult to decide from only one line.

7.5 Line asymmetries

Line asymmetries during flares have been described at various times for different emission lines. Blue excess-line emission was described for example by Gunn et al. (1994) for a flare on AT Mic, while Crespo-Chacón et al. (2006) note red line asymmetries in the Balmer lines during various flares on AD Leo (M3V). The latter found the asymmetries stronger for larger flares and stronger for higher members of the Balmer series. They also analysed the Ca II H & K lines, but did not find any asymmetry. Also, Fuhrmeister et al. (2005a) found red wing asymmetries in the Balmer and He I lines for a long duration flare on LHS 2034 (M6V). The additional red wing flux decayed faster for the Balmer lines than the line flux. For the He I lines, the flux creating the asymmetry first increased relative to the line flux and then decayed; examples of papers describing line asymmetries are given by these authors.

Additional blue wing flux is normally interpreted as upmoving material, which is expected for stellar flares, while additional red wing flux has been ascribed mostly to downflows during the flares. For the Sun, similar mass flows (chromospheric downward condensations) are known (Canfield et al. 1990) to last for a few minutes. Since the asymmetries in M dwarfs often persist much longer, various flare kernels producing several downflows have been proposed (Doyle et al. 1988; Fuhrmeister et al. 2005a).

In the present data, line asymmetries have also been found. Besides asymmetries in the Balmer and He I lines, asymmetries for Ca II lines have been found for the first time. Asymmetries may be present in the Mg II lines, but they are all very weak, so that a red wing is hard to distinguish from the noise/molecular lines.

In the following we give a detailed presentation of the line asymmetries.

7.5.1 He I lines

Seven He I lines are observed in the flare peak spectra no. 9 (red arm) and 3 (blue arm). Five lines clearly show additional flux in the red wing, one is located in a wavelength region too crowded to recognise any asymmetry, and one line is very weak, but looks slightly asymmetric. An example of these asymmetries can be found in Fig. 7.12 for the double He I line at 7065 Å.

We also fitted the two strongest flare-only (quiescent spectrum removed) He I lines with CORA (Ness & Wichmann 2002). An example of the fit quality can also be found in Fig. 7.12. We fitted the double line at 7065 Å with two Gaussian components plus one broad Gaussian for the additional line flux in the asymmetry. For each Gaussian the free fit parameters are central wavelength, FWHM, and amplitude. The background was fitted manually, since the line is very broad and therefore contributes significantly to the background as fitted by CORA. The same fit procedure was applied to the line at 6678 Å, but with the background fitted automatically and only one main component. The fit results can be found in Table 7.3.

In the spectrum no. 8, covering the flare onset, the two strongest He I lines at 6678 and 7065 Å start to react to the flare. Both lines are blue-shifted and exhibit additional broad, blue-shifted components.

Table 7.3: Line-fit parameters of the He I line at 7065 and 6678 Å.

No.	flux narrow 1 [10^{-16} erg s^{-1} cm^{-2}]	flux narrow 2 [10^{-16} erg s^{-1} cm^{-2}]	flux broad [10^{-16} erg s^{-1} cm^{-2}]	FWHM broad [Å]	velocity km s^{-1}
He I at 7065 Å[1]					
8	1294 ±118	—	1212 ±192	0.85 ±0.09	-3.8±11.9
9	11143 ±206	4139 ±223	8844 ±442	1.11 ±0.03	38.6±19.5
10	5562 ±112	1386 ±101	2112 ±192	1.04 ±0.10	45.8±13.1
11	2389 ±78	437 ±62	908 ±154	1.13 ±0.01	28.0±19.5
He I at 6678 Å[2]					
8	1646 ± 145	—	2235 ± 217	0.66 ±0.03	-10.8±11.2
9	22360± 295	—	24583 ±467	1.02 ±0.01	24.7±0.5
10	10033± 150	—	6512 ±207	0.91 ±0.05	22.4±2.7
11	3993± 105	—	2310 ±140	0.68 ±0.07	10.8±14.8
12	2022± 75	—	610 ±110	0.84 ±0.08	9.0±25.1
13	628± 46	—	—	—	—

[1] The first narrow component of the line is stable at 7065.19 Å, the second is stable at 7065.73 Å. Only for spectrum no. 8, the line center is shifted to 7065.10± 0.12 Å. The FWHM of both narrow components is ∼0.23 Å. The background is fitted manually.

[2] The narrow component of the line is stable at 6678.15 Å besides for spectrum no. 8, where it is blue-shifted to 6678.03±0.10 Å.

For the line at 7065 Å, we did not find the second narrow component in the data, although this may be due to the low flux in the line. No blue asymmetries can be found in the blue arm of the spectrum, since the blue spectrum no 2 covering the flare onset is dominated by the continuum and the He I lines are too weak against this strong background.

7.5.2 Ca II lines

During the flare, we found 9 Ca II lines, out of which 5 are located in the blue arm. Seven lines show additional red wing flux, one is clearly blended with an Fe I line, and another one is so weak that no asymmetry – if present – can be recognised. The Ca II triplet is saturated in the line cores in spectrum no. 9, but the wings are not affected. All three lines show red asymmetries in the wings, although not as strong as the He I lines. We fitted the three lines in the flare-only spectra, again using a narrow and a broad Gaussian, bearing in mind that the narrow component flux is saturated. Nevertheless, the line shifts are unaffected by the saturation. Our line fit parameters are given in Table 7.4. After spectrum no. 11, the broad component vanishes. In spectrum no. 8, covering the flare onset, no broad component is present. However, all three lines are blue-shifted, although only within 1 to 2 σ (see Table 7.4).

Table 7.4: Line shift of the broad component of the Ca II triplet lines from the flare-only spectra.

No.	position [Å]	velocity [km s^{-1}]	FWHM [Å]
Ca II at 8498.018 Å[1]			
9	8498.32±0.02	11.6±0.7	0.89±0.04
10	8498.48±0.10	17.3±3.5	0.72±0.02
11	8498.34±0.43	12.3±15.2	0.72±0.02
Ca II at 8542.089 Å[2]			
9	8542.22±0.13	5.3± 4.6	1.00±0.01
10	8542.17±0.17	3.5± 6.0	0.78±0.02
11	8542.07±0.15	0.0±5.3	0.78±0.05
Ca II at 8662.140 Å[3]			
9	8662.33±0.01	7.3±0.3	0.91±0.02
10	8662.23±0.19	3.8±6.6	0.70
11	8662.22±0.22	3.4±7.6	0.70

[1] The narrow component is stable at 8497.99±0.02 Å, besides spectrum no.8 which is blue-shifted to 8497.80±0.11 Å (-6.7 ± 3.9 km s^{-1}).

[2] The narrow component is stable at 8542.07±0.03 Å, besides spectrum no. 8 which is blue-shifted to 8541.96±0.11 Å (-3.8 ± 3.8 km s^{-1}).

[3] The narrow component is stable at 8662.12±0.04 Å, besides spectrum no. 8 which is blue-shifted to 8662.02±0.07 Å (-3.8 ± 2.4 km s^{-1}).

7.5.3 H I lines

Asymmetries have also been found for the Hα line. During the flare onset in spectrum no. 9, the line has a footpoint width of about 70 Å and the inner wings are also saturated; therefore, we refrained from using this spectrum for the analysis. In the decay phase, the core is saturated for spectra no. 10 to 14, but the wings, where the asymmetries are found, are

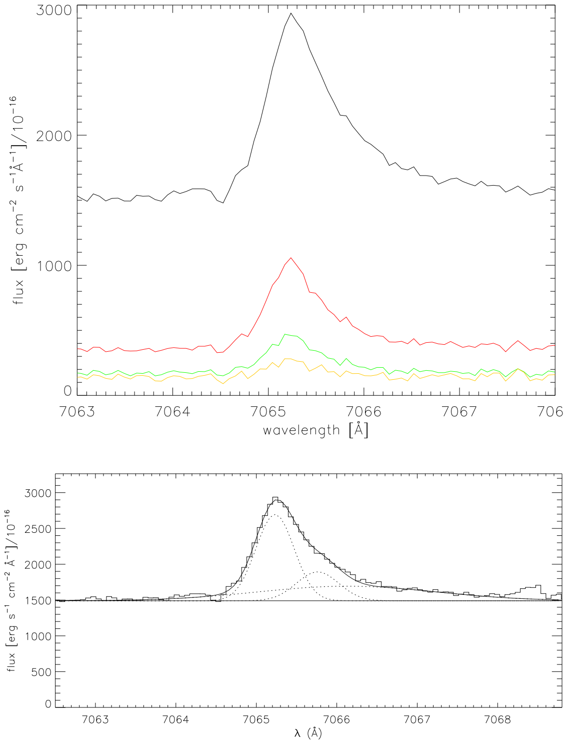

Figure 7.12: Red-wing asymmetry for the He I line at 7065.30/7065.93 Å. Left: Flare spectrum no. 9 of the line and the three consecutive spectra (with the quiescent spectrum subtracted for each spectrum). Right: Three-component Gaussian fit of the line with CORA. The asymmetry manifests itself in the broad Gaussian component. The background has been fitted manually.

not affected. We fitted the net-flare line (with the quiescent spectrum no. 1 subtracted) with CORA using two Gaussians, which gives a good empirical description of the line.

The Hα line starts to react to the flare in spectrum no. 8, where it develops broad wings. Moreover, the narrow component is slightly blue-shifted at 6562.71±0.06 Å, whereas the broad component is clearly blue-shifted leading to a blue asymmetry, as can be seen in Fig. 7.13. The line core (note, that spectrum no 8 is not saturated) exhibits a self-reversal due to non-LTE effects, which is typical for dMe stars and also reproduced in chromospheric modelling of M dwarfs; see e. g. Cram & Mullan (1979); Robinson et al. (1990), and Houdebine & Doyle (1994). The weak asymmetry of the red and the blue peaks also points to the complicated dynamical processes during flares and may be due to a wave propagating downwards. Examples of theoretical Hα profiles from radiative hydrodynamic flare models for M dwarfs also exhibiting peak asymmetries due to propagating waves can be found in Allred et al. (2006).

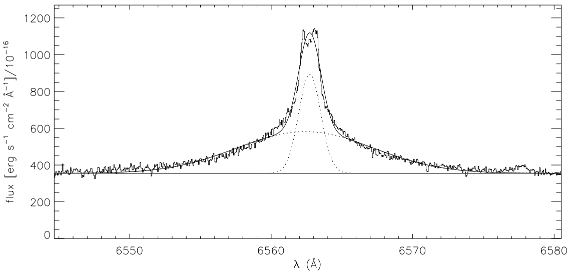

Figure 7.13: The Hα line from spectrum no. 8 with the quiescent spectrum subtracted. The line exhibits a clear blue asymmetry due to the blue-shifted broad component. The narrow component is also slightly blue-shifted.

Table 7.5: Line parameters for the broad component of the Hα line. Note, that there is no measurement for spectrum no. 9.

No.	position [Å]	velocity [km s^{-1}]	FWHM [Å]
8	6562.47± 0.10	-15.8± 4.6	4.82±0.02
10	6563.39± 0.01	26.2±0.5	4.10 ±0.01
11	6563.08± 0.01	12.0±0.5	2.90 ± 0.01
12	6563.21± 0.01	17.9±0.5	2.12 ± 0.02
13	6563.60± 0.06	35.8±2.7	1.50 ± 0.09
14	6562.88± 0.38	2.9 ±17.4	3.10 ± 0.11

The broad component is red-shifted in the spectra covering the flare decay phase. The derived wavelength shifts are listed in Table 7.5, assuming a rest wavelength of 6562.817 Å (Moore 1972). The broad component has vanished in spectrum no. 15.

Besides the Hα line, we also analysed the H$_9$ line in detail. For the even higher Balmer lines, we refrained from a detailed analysis, since the broad wings of these lines have to be deblended from metal lines, Due to decreasing flux this becomes more and more difficult for higher Balmer lines.

We performed a simultaneous fit with three metal lines for the H$_9$ line, i. e. a 5-component Gaussian fit with three Gaussians for the metal lines and one narrow and one broad Gaussian for the H$_9$ line itself. This procedure led to a very good description of the data, except for spectra no. 2 and 3. For these two spectra, we changed the narrow Gaussian profile to a Lorentzian profile again leading to acceptable fits. For spectrum no. 2, which covers the flare onset, a weak blue asymmetry could be detected with the broad component at 3835.34±0.03 Å. The Lorentzian describing the narrow component is only blue-shifted within the error bars: 3835.36±0.08 Å. The FWHM is 0.51 Å for the Lorentzian and 2.20 Å for the broad Gaussian. During the flare peak spectrum no. 3, the broad component is red-shifted at 3835.47±0.01 Å with a FWHM of 3.34 Å. The following spectra tend to have red-shifted broad components, but within the large errors. Nevertheless, no line shift in the consecutive spectra agrees with what we found for Hα, where the broad component vanishes after spectrum no. 14 (cf., Fig. 7.1).

In addition to the Balmer lines, we searched the Paschen lines for asymmetries, but none were found; however, since these lines are very broad and noisy, an asymmetry could easily be hidden in the data (see Fig. 7.9).

7.5.4 Discussion of the line asymmetries

We measured line asymmetries for He II, Ca II, and Balmer lines during the flare, but not for the Paschen lines and other metal lines (although the Mg II lines also may exhibit small asymmetries). While in the case of the Paschen lines this can be attributed to the enormous line widths hiding asymmetries, this argument is not valid for the metal lines. However, the lines of the above-mentioned ions tend to form at different chromospheric heights (and therefore at different temperatures) than the rest of the observed metal lines. While the line cores of the above-mentioned ions tend to form in the upper chromosphere or transition region onset, the line cores of the other metals tend to form in the lower to mid chromosphere (Vernazza et al. 1981; Fuhrmeister et al. 2005b). This gives a hint at least to the temperature of the moving material, which we ascribe the asymmetries to. The material must be rather hot (about 8000 to 10 000 K) compared to the rest of the chromosphere. We also ascribe the non-uniform reactions of the asymmetries of the different lines to different line formation conditions. Nevertheless, trends in the reaction of the lines can be noticed: In our spectra, we find asymmetries in the blue as well as in the red wings. Asymmetries on the blue side are found during flare onset, red wing asymmetries during decay phase. This makes the interpretation as moving material very straightforward. At the flare onset, the chromospheric evaporation is seen as a blue shift (although partly only within the errors) of the main/narrow components of the analysed strong lines. In addition, there seems to be a rising ‘cloud’ of material, but moving with a different velocity producing the broad component. The main/narrow line component does not indicate any moving material in the decay phase, but the ‘cloud’ is now moving downward, leading to the observed red asymmetries. For the Hα line, we detected not only a decay of the asymmetry, but also variations in the asymmetry from spectrum to spectrum, favouring a scenario of not one single uniform downflowing ’cloud’, but of a multitude of downflows. These are de-accelerated when hitting deeper and denser atmospheric layers, which is seen in the generally decreasing velocity of the broad component with evolution of the flare.

During the decay phase, downflow velocities range from $\sim$ 5 to 40 km s^{-1}, which is probably supersonic. The sound velocity in models of quiescent chromospheres is about 10 km s^{-1} (Jevremović et al. 2000). Similar downflow velocities have been measured for the flare on LHS 2034 (Fuhrmeister et al. 2005a), but downflow velocities of up to 60 km s^{-1} are normally observed for the Sun (Fisher 1989).

Interpretating the FWHM of the broad component is difficult because it may have different components. At least for the hydrogen lines, Stark broadening should contribute to the line width, and turbulent motions are also a possible interpretation. Since there may be different downflow kernels, the width of the line may be due to the different bulk motions of these kernels that are integrated in our spectra.

In conclusion, we tentatively interpret our observations in a scenario of a chromospheric prominence that is lifted during the flare onset and then raining down during the decay phase.

7.6 Discussion and conclusion

We presented the optical part of a multiwavelength campaign that caught CN Leo in a spectacular flare. There are only few observations of such giant flares, but even these few examples show very different timescales and lightcurve characteristics. While the CN Leo flare lasted about 50 minutes, a 5-magnitude flare in the U-Band on UV Cet lasted only 12 minutes (Eason et al. 1992), while the large flare on AD Leo from 1985 lasted more than 4 hours (Hawley & Pettersen 1991). Compared to somewhat smaller (but nevertheless very large) flares, these can be of the same duration or even longer than the CN Leo flare. For example, a 2.1 magnitude flare in the U-band was observed on AD Leo to last about 50 minutes (Houdebine et al. 1993), while a large flare on AT Mic lasted about 1.5 hours (García-Alvarez et al. 2002).

Most of the large flares show a double (or triple) peaked lightcurve in the U-band and also for Balmer emission lines like the CN Leo flare (Hawley & Pettersen 1991; Houdebine et al. 1993; García-Alvarez et al. 2002). The UV Cet flare had an even more complicated substructure with at least 4 peaks in the major outburst (Eason et al. 1992). This multiple-peak flare pattern is usually interpreted in terms of different reconnection events, which may trigger each other in succession. The CN Leo flare shows two major peaks that can be easily noticed in the exposuremeter data in Fig. 7.1, with a minor peak between the two. The time between the two major peaks is about 200 seconds. For the 2.1 mag flare on AD Leo, the two major peaks are separated by about 9 minutes (Houdebine et al. 1993). For all other mentioned flares (besides UV Cet), the separation is even longer.

The flux peaks of chromospheric lines are typically delayed with respect to the U-band flux peak, with the Ca II H and K lines even more delayed than the Balmer lines (e. g. García-Alvarez et al. 2002; Hawley & Pettersen 1991). The time resolution of our spectra is unfortunately too low to observe any delay in the peak, but as is apparent in Fig. 7.8, the flux of the Ca II triplet line decays more slowly than the other lines. This behaviour is compatible with what is normally observed for the Ca II H and K lines, which decay more gradually than Balmer and Helium lines (e. g. Houdebine et al. 1993), consistent with an interpretation of a faster evolution of high-temperature lines in the chromosphere (Houdebine 2003).

The optical spectral data allowed us to trace the chromospheric reaction to the flare (with one He II transition line covered). We found a wealth of chromospheric emission lines that has not been observed before, especially in the red part of the spectrum; also, V II and Sc II lines show up in the blue arm. Especially in the flare onset spectrum no. 2, the higher Balmer lines develop very broad damping wings that can only be fitted involving a Lorentzian profile. With respect to line shapes and profiles, we find asymmetries varying from blue excess flux during flare onset to red excess flux during the decay phase. In the red excess for Hα, not only a general decay is found, but also variations from spectrum to spectrum, providing strong evidence for a scenario involving multiple flare kernels, each triggering chromospheric downward condensations. We ascribe the blue excess flux during flare

The optical quasi-continuum is also quite massively affected by the flare. The blue spectrum is clearly blackbody-dominated during flare onset. The same is true for the red spectrum with the quiescent spectrum removed. The derived temperatures for the gas producing the blackbody radiation in the first few seconds of the flare onset exceed of 20 000 K and then rapidly cool.

This set of excellent optical data, which characterises the photosphere and chromosphere of CN Leo during a giant flare is suited well to classical semi-empirical chromospheric flare modelling with a stellar atmosphere code. Modelling using a multitude of emission lines will be presented in a forthcoming paper in this series.

8 Multiwavelength observations of a giant flare on CN Leonis – Temporal evolution of coronal properties

The concluding part of the analysis of the giant flare focusses on the analysis of the hot coronal flare plasma. I presented preliminary results of this study at the 15th Cool Star Workshop (Liefke et al. 2009) and at the X-ray Grating Spectroscopy Workshop. For the final publication, Birgit Fuhrmeister provided the analysis of the data of the optical Fe XIII line.

C. Liefke, B. Fuhrmeister, and J. H. M. M. Schmitt
A&A, **514**, A94 (2010)

Abstract
Stellar flares affect all atmospheric layers from the photosphere over chromosphere and transition region up into the corona. Simultaneous observations in different spectral bands allow to obtain a comprehensive picture of the environmental conditions and the physical processes going on during different phases of the flare. We investigate the properties of the coronal plasma during a giant flare on the active M dwarf CN Leo observed simultaneously with the UVES spectrograph at the VLT and *XMM-Newton*. From the X-ray data, we analyze the temporal evolution of the coronal temperature and emission measure, and investigate variations in electron density and coronal abundances during the flare. Optical Fe XIII line emission traces the cooler quiescent corona. Although of rather short duration (exponential decay time $\tau_{LC} < 5$ minutes), the X-ray flux at flare peak exceeds the quiescent level by a factor of ≈100. The electron density averaged over the whole flare is greater than $5 \cdot 10^{11}$ cm^{-3}. The flare plasma shows an enhancement of iron by a factor of ≈2 during the rise and peak phase of the flare. We derive a size of < 9000 km for the flaring structure from the evolution of the the emitting plasma during flare rise, peak, and decay.The characteristics of the flare plasma suggest that the flare originates from a compact arcade instead of a single loop. The combined results from X-ray and optical data further confine the plasma properties and the geometry of the flaring structure in different atmospheric layers.

8.1 Introduction

Flares are among the most prominent signs of stellar activity. They can be observed over the entire electromagnetic spectrum from X-ray to radio wavelengths, demonstrating that all layers of the stellar atmosphere are affected, with a wide range of plasma temperatures and densities involved. A flare is a highly dynamic event, revealing the complex behavior of the stellar atmosphere with rapidly changing physical conditions, i. e. its interplay with varying magnetic fields in time and its response to the sudden release of large amounts of energy. In the commonly accepted picture of a stellar flare (Haisch et al. 1991; Priest & Forbes 2002), a magnetic reconnection event in the corona drives the acceleration of particles that radiate in nonthermal hard X-rays and radio gyrosynchrotron emission as they spiral down along the magnetic field lines. Lower atmospheric layers are strongly heated by the impact of these particles and immediately start cooling by radiation in the optical and UV continuum as well as in chromospheric and transition region emission lines. Chromospheric evaporation then brings "fresh material", emitting soft thermal X-ray emission, into the corona. The strong X-ray and UV radiation field finally induces further chromospheric emission (Hawley & Fisher 1992).

Flares on the Sun and on stars show a wide variety of amplitudes, from the smallest micro/-nanoflares to giant flares with luminosity increases by orders of magnitude, and timescales ranging from a few seconds up to several days. Depending on energy budget, decay time and shape of the lightcurve, impulsive and gradual flares can be discerned. On the Sun, the former have been associated with compact emission regions, i. e., single loops, while the latter typically involve a series of eruptions in a whole arcade of loops (so-called two-ribbon flares, see Pallavicini et al. 1977). For stellar flares, the loop geometry can usually not be observed directly, but scaling laws based on the hydrostatic case, relating the loop temperature and pressure with the size of the loop, as derived and tested for the quiet Sun (Rosner et al. 1978) can be adapted to stellar flares to give an estimate of the dimensions of the involved coronal structures (Aschwanden et al. 2008). Additionally, hydrodynamic loop modeling approaches allow to assess the loop length from the analysis of the decay of the flare in X-rays and to estimate the amount of additional heating (Serio et al. 1991; Reale et al. 1997). This approach has recently been extended to an analysis of the rise phase of the flare (Reale 2007). Individual flare events can thus be characterized with respect to to the physical properties of the flaring structure from observational quantities also available for stellar events. The greater the spectral coverage and the better the spectral and temporal resolution, the more information can be gained and the better are the constraints on the physical properties of the flare plasma and the geometry of the flaring active region. Simultaneous observations in multiwavelength bands allow to study the flare throughout all atmospheric layers from the photosphere into the corona.

Strong flares dominate the overall flux level in all wavelength bands; the X-ray luminosity can increase by more than two orders of magnitude during the strongest events (e. g. Schmitt & Favata 1999; Favata & Schmitt 1999; Favata et al. 2000), which allows the strongest events even on relatively faint targets to be investigated in great detail. For outstanding flares like the long-lasting giant flare observed on Proxima Cen with *XMM-Newton*, the temporal evolution of plasma temperatures, densities and abundances during different flare phases could be observed directly (Güdel et al. 2002a, 2004); detailed and specific hydrodynamic loop modeling revealed a complex flare geometry with two loop populations and differing heating mechanisms (Reale et al. 2004).

Even for much smaller flares, low- and intermediate-resolution X-ray spectroscopy makes it possible to follow the evolution of plasma temperature and emission measure during flare rise and decay. The temperature of the flare plasma is typically observed to peak before the maximum emission measure is reached, verifying the overall framework of initial heating, evaporation, and conductive and radiative cooling as predicted by hydrodynamic loop models (e. g. Reale 2007). High-resolution spectroscopy is needed to directly measure coronal densities during flares and thus to obtain the weights of changes in plasma density or volume. In general, coronal densities deduced from the ratio of the forbidden and intercombination lines in He-like triplets, especially from O VII and Ne IX at formation temperatures of 2 MK and 3.5 MK, respectively, during smaller flares are consistent with the quiescent value within the errors but tend to be higher (see e. g. Mitra-Kraev & Ness 2006); unambiguously increased coronal densities have so far only been measured during the giant flare on Proxima Centauri (Güdel et al. 2002a).

Another aspect of the evaporation scenario is the observation of abundance changes during flares, leading directly to the question to what extent flares influence the overall coronal abundance pattern. Nordon & Behar (2007, 2008) systematically analyzed abundance trends in a sample of flares observed with *Chandra* and *XMM-Newton* and found that the most active stars with a pronounced inverse FIP effect during quiescence compared to solar photospheric values showing a shift to a FIP effect compared to the corresponding quiescent values, and vice versa for the less active stars showing the solar-like FIP effect during quiescence. This confirms the existence of the inverse FIP effect and of strong discontinuities in the abundance patterns of corona and chromosphere/photosphere also for stars where photospheric abundances are difficult to measure, however, the question what causes this bias is left unanswered .

We present the observation of a giant flare on the active M dwarf CN Leo with *XMM-Newton* and the UVES spectrograph at the VLT. An extremely short impulsive outburst at the beginning of the flare has already been discussed by Schmitt et al. (2008). This paper is the concluding third paper of a series analyzing the whole flare event in greater detail. Paper I (Fuhrmeister et al. 2008) reports the observational results on the chromospheric emission as diagnosed by the UVES spectra, while Paper II (Fuhrmeister et al. 2010) describe model chromospheres and synthetic spectra obtained with the atmospheric code *PHOENIX*. Here we focus on the temporal evolution of the coronal plasma temperature, emission measure and abundances determined by the X-ray data and their implications on the geometry of the flaring structure, on the physical conditions dominating the flare environment, and on the abundance patterns predominating in different atmospheric layers.

8.2 The active M dwarf CN Leo

CN Leo (GJ 406, Wolf 359) is, after the α Centauri system and Barnard's star, the fifth-nearest star to the Sun at a distance of 2.39 pc. Despite its proximity, it is a faint object with a V band magnitude of 13.54; recent spectral classification ranks it as an intermediate M dwarf of spectral type M5.5 (Reid et al. 1995) or M6.0 (Kirkpatrick et al. 1991). Fuhrmeister et al. (2005b) fitted $T_{\rm eff}$=2900 K and $\log g = 5.5$ based on a model grid with $\Delta T_{\rm eff} = 100$ K and $\Delta \log g = 0.5$, while Pavlenko et al. (2006) found $T_{\rm eff} = 2800 \pm 100$ K at a fixed $\log g$ of 5.0 and solar metallicity. From $M_{\rm bol} = 12.13 \pm 0.10$ the latter determined a mass of 0.07–0.1 $M_\odot$ and a rather young age of 0.1–0.35 Gyr, consistent the lower limit of 0.1 Gyr deduced from the absence of lithium signatures (Magazzu et al. 1993). However, based on its kinematics, Delfosse et al. (1998) and Mohanty & Basri (2003) classify CN Leo as intermediate young/old disk or old disk star.

Nevertheless, CN Leo is well-known to show several signs of activity. Lacy et al. (1976) and Gershberg & Shakhovskaia (1983) found high optical flare rates, however, at the lowest flare energies in their samples of UV Ceti stars. Robinson et al. (1995) analyzed UV flare events on CN Leo down to the microflare scale observed with the High Speed Photometer onboard *HST*. From 6 cm and 20 cm VLA observations, O'Dea & McKinnon (1987) could only specify a 3σ upper limit on its radio flux, thus CN Leo is underluminous in this wavelength regime compared to other active M dwarfs. Güdel et al. (1993) were able to detect CN Leo in the 3.5 cm and 6 cm bands during a flare in a simultaneous observing campaign with the VLA at radio wavelengths and with the *ROSAT* PSPC in X-rays. During quiescence, however, again only upper limits were found at radio wavelengths. Reale & Micela (1998) discussed the X-ray data of the flare and derived a loop half-length of $\approx 7 \cdot 10^9$ cm from the analysis of the flare decay. The first X-ray detections of CN Leo have already been reported from *Einstein* data (Vaiana et al. 1981; Golub 1983), and even during quiescence, it is a relatively strong X-ray source with $\log L_{\rm X} = 26.97$ and 27.01 in the *ROSAT* All-Sky survey and a second pointed PSPC observation, respectively (Schmitt & Liefke 2004). CN Leo is the only star where persistent but variable optical coronal Fe XIII emission has been confirmed (Schmitt & Wichmann 2001; Fuhrmeister et al. 2004). Fe XIII is an indicator for cool coronal plasma ($\approx$ 1.5 MK), while typical coronal emission measure distributions of earlier M dwarfs peak around 7–8 MK (e. g. Robrade & Schmitt 2005), i. e., temperatures where the ionization equilibrium is shifted towards Fe XVII. Fuhrmeister et al. (2007) found significant amounts of cooler plasma in the corona of CN Leo from X-ray spectra obtained with *XMM-Newton*, consistent with the Fe XIII line fluxes from simultaneous optical spectroscopy. In addition to its high X-ray luminosity, CN Leo shows strong Hα emission ($\log L_{\rm H\alpha}/L_{\rm bol} = -3.89$ or -3.39: Mohanty & Basri 2003; Reiners & Basri 2007) and a multitude of other chromospheric emission lines (Fuhrmeister et al. 2004). Reiners & Basri (2007) measured an integrated magnetic surface flux of 2.4 kG, that varies by $\approx$ 100 G on timescales ranging from hours to days (Reiners et al. 2007).

8.3 Observations and data analysis

The giant flare on CN Leo discussed in this series of papers has been observed during a multiwavelength campaign on this star in X-rays and in the optical. This campaign consisted of six half nights of optical high-resolution spectroscopy monitoring with UVES at the VLT, and simultaneous *XMM-Newton* observations. The first three observations have been performed on 19/20 May 2004, and 12 and 13 December 2005; they are discussed in detail by Fuhrmeister et al. (2007). The last set of observations has been performed on 19/20, 21/22, and 23/24 May 2006; here we focus on the giant flare that occurred in the first of these three nights.

XMM-Newton consists of three co-aligned X-ray telescopes, accompanied by the Optical Monitor OM, an optical/UV telescope that can be used with different filters in imaging or fast readout mode. The OM data of the flare, obtained in fast mode with the U band filter, has already been discussed by Fuhrmeister et al. (2008) in conjunction with the behavior of the optical chromospheric emission lines. *XMM*'s X-ray telescopes are equipped with EPIC (European Photon Imaging Camera) detectors, X-ray CCDs providing medium-resolution imaging spectroscopy with $E/\Delta E \approx 20$–50 and timing analysis with a time resolution at the subsecond level. There are two identical EPIC MOS detectors (MOS 1 and MOS 2), operating in the energy range of 0.2–12.0 keV, and one EPIC PN detector, which covers the energy range of 0.2–15.0 keV. The PN has a higher sensitivity, while the MOS detectors provide better angular and spectral resolution; several filters and operating modes are available for these instruments. The two X-ray telescopes with the MOS detectors are additionally equipped with reflective gratings and their corresponding CCD detectors. The Reflection Grating Spectrometers (RGS1 and RGS2) provide high-resolution spectroscopy in the energy range of 0.35–2.5 keV (5–38 Å) with $E/\Delta E$ ranging between 200 and 800 and a spectral resolution of ≈0.06 Å FWHM which allows to resolve individual emission lines. All instruments are usually operated simultaneously.[1]

In the *XMM-Newton* observation of 19/20 May 2006 (ObsID 0200530501), the EPIC detectors were operated in Full Frame (MOS) and Large Window mode (PN) with the medium filter. All X-ray data were reduced with the *XMM-Newton* Science Analysis System (SAS) software, version 7.0. Spectral analysis of the EPIC data was carried out with XSPEC V12.3 (Dorman & Arnaud 2001), making use of multi-temperature component models with coupled abundances for each component. The plasma models assume a collisionally-ionized, low-density optically-thin plasma as calculated with the APEC code (Smith et al. 2001a,b). Abundances are calculated relative to solar photospheric values from Anders & Grevesse (1989). Individual line fluxes in the RGS spectra have been measured with the CORA program (Ness & Wichmann 2002) using Lorentzian line profiles with a fixed line width of 0.06 Å.

UVES (Ultra-violet and Visible Echelle Spectrograph) is one of the high-dispersion spectrographs of the VLT, operating from 3000 to 11 000 Å with a maximum spectral resolution of 110 000[2]. It was used in a non-standard setup using dichroic beam splitter No. 2 (DIC2), with spectral coverage from 3050 Å to 3860 Å in the blue arm and from 6400 Å to 8190 Å and 8400 Å to 10080 Å in the red arm at a spectral resolution of ≈40 000. Exposure times were 1000 s in the blue arm and 200 s in the red arm. Here we discuss only the temporal behavior of the optical coronal Fe XIII line at 3388 Å during the flare, which is covered by the blue arm spectra. The UVES spectra were reduced using the IDL-based `REDUCE` package (Piskunov & Valenti 2002). The wavelength calibration was carried out using Thorium-Argon spectra and resulted in an accuracy of ≈0.03 Å in the blue arm and ≈0.05 Å in the red arm. Absolute flux calibration was carried out using the UVES master response curves and extinction files provided by ESO. The flux in the Fe XIII line has been measured with CORA.

8.4 The Flare

8.4.1 Timing analysis

The *XMM-Newton* observation of CN Leo from 19/20 May 2006 covers the giant flare discussed here, and two additional larger flares. The quasi-quiescent X-ray emission surrounding the three flares sums up to 20 ks, while the giant flare lasted ≈1.4 ks. The countrate increased from quiescent values of ≈0.7 cts/s in the PN and ≈0.14 cts/s in the two MOS detectors to ≈65 cts/s and ≈14 cts/s, respectively, at the flare peak. Due to the long frame times of the EPIC imaging modes used, not only the spectral response but also the shape of the lightcurve is heavily affected by pileup. From the ratio of countrates during flare and quiescence from circular and annular shaped extraction regions (the latter excluding the innermost part of the point spread function PSF), we determined that the amount of pileup reached values up to 30% for the PN at the time of maximum countrate. The effect on the two MOS detectors is even stronger. Figure 8.1 shows the EPIC PN lightcurve extracted from an annular extraction region with the innermost 150 pixels (corresponding to the innermost 7.5″ of the PSF) excluded. The lightcurve has been scaled by the ratio of the quiescent countrates in

---

[1] Further details on the instruments onboard *XMM-Newton* can be found in the *XMM-Newton* Users' Handbook, available at http://xmm.vilspa.esa.es/external/xmm_user_support/documentation/uhb/index.html

[2] A detailed description of the UVES spectrograph is available under http://www.eso.org/instruments/uves/doc/

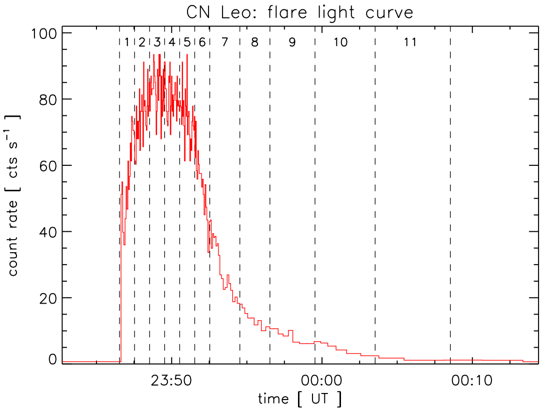

Figure 8.1: EPIC PN lightcurve of large flare, corrected for pileup as described in the text. Time bin sizes are chosen to contain 100 counts per bin before scaling the annular region to the total level. Time intervals used for spectroscopic analysis are marked.

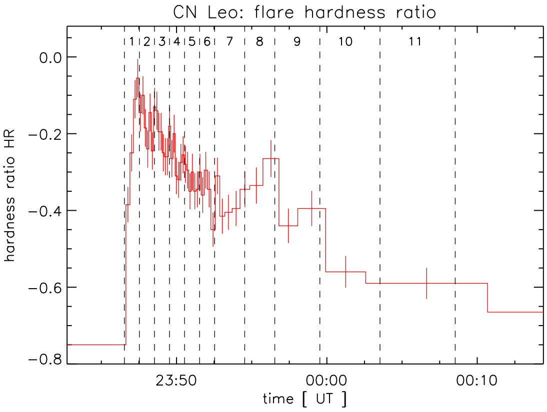

Figure 8.2: Temporal evolution of the hardness ratio. Time bin sizes are chosen to contain 400 counts per bin in the total = $H + S$ band.

circular and annular extraction regions in order to visualize the true countrates.

The initial rise of the few-second outburst at the beginning of the flare at 23:46:40 UT discussed by Schmitt et al. (2008) was very steep, after its short decay, the main flare continued to rise less steeply. However, still within less than two minutes, the maximum countrate was reached. Even with the effects of pileup eliminated, the flare peak is flattened, resulting in a kind of plateau of about 3 minutes duration. The subsequent decay phase can be fitted with an exponential decay time τ_{LC} of 257±13 seconds, however, it shows slight deviations from an exponential shape. Especially, during the first two minutes after the plateau phase, the decay seems to have been faster, and an additional bump peaked at 0:00 UT. Less than 25 minutes after the initial outburst, CN Leo has returned to the quiescent level before the flare event. Stellar X-ray flares of that amplitude typically last much longer, i. e. from several hours up to days (see e. g. Kürster & Schmitt 1996; Schmitt & Favata 1999; Favata et al. 2000; Güdel et al. 2004). Integrating the total energy flux in the 0.2–10.0 keV band, yields a radiative loss in the X-ray regime of $E_X \approx 4.4 \cdot 10^{31}$ erg, which can be considered to represent the major contribution of the total radiative loss. Though very energetic, the short dynamical time scales already suggest a very compact structure. The large flare is followed by a much smaller one at 0:10 UT (X-ray amplitude ≈2, duration ≈3 minutes), that is also visible in the optical (see Figure 1 in Paper I).

In Fig. 8.2 we show the temporal evolution of the spectral hardness during the flare. We define the hardness ratio HR as $HR = \frac{H-S}{H+S}$, with the hard and soft bands ranging from 1.0–15.0 keV and 0.15–1.0 keV, respectively. To avoid pileup effects, the annular extraction region has been used for both spectral bands. The shape of the HR lightcurve is fairly different from the normal lightcurve. Before the flare, the hardness ratio is ≈−0.75, well consistent with what Fuhrmeister et al. (2007) found for the low-activity state of CN Leo on 19 May 2004. With the flare rise, the hardness ratio steeply increases, peaking at a value of ≈−0.05 about one minute before the plateau phase of the lightcurve is reached. At the maximum of the HR lightcurve, the contribution from X-ray photons above the dividing line of 1 keV therefore almost equalled the amount of photons below, while during quiescence, the spectral energy distribution is by far dominated by lower energies. Güdel et al. (2004) found a very similar behavior for the large flare on Proxima Cen. The decay of the hardness ratio is interrupted by a new rise, peaking at 23:56 UT, approximately the time when the small bump in the lightcurve starts to emerge.

8.4.2 Plasma temperature and emission measure

The striking changes of the spectral energy distribution are clearly visible in the X-ray spectra. Figure 8.3 compares the EPIC PN spectra of the quiescent state before the flare, of the flare rise, plateau phase and decay. The quiescent spectrum is very soft, even somewhat softer than the spectrum from 19 May 2004. Fuhrmeister et al. (2007) found CN Leo to show three different quasi-quiescent X-ray flux levels in May 2004 and on 11 and 13 December 2006, and assumed that the two enhanced states in December 2006 reflect the decay phases of one or two long-duration flares. Our new obser-

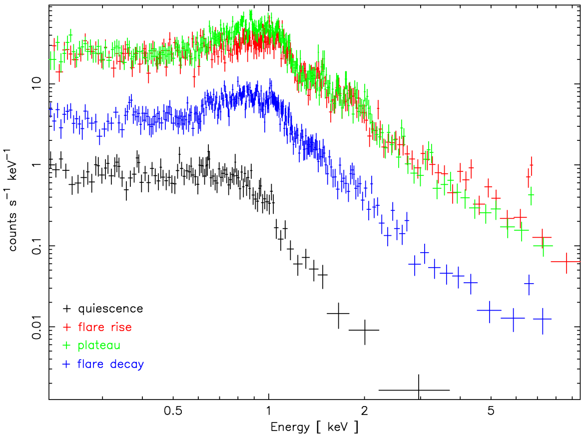

Figure 8.3: EPIC PN spectra of the quiescent state before the flare (black), of the rise phase (red, time intervals 1 and 2), of the flare peak (green, time intervals 3 and 4), and of the decay phase (blue, time intervals 5 to 11).

vations now confirm the low-level quiescent state, which is also consistent with the previous *ROSAT* and *Einstein* data.

We fitted the quiescent spectra before and after the flare with two-temperature component APEC models. While the temperatures and emission measures proved to be stable, rather large uncertainties for the individual elemental abundances occurred with the abundances treated as free parameters. We therefore chose to adopt the values of Fuhrmeister et al. (2007), i. e. C/H = 1.49, N/H = 1.28, O/H = 0.62, Ne/H = 1.20, Mg/H = 0.85, Si/H = 0.78, S/H = 1.41, and Fe/H = 0.59 relative to the solar photospheric values of Anders & Grevesse (1989). The properties of the two quiescent spectra are very similar, however, for the second quiescent phase the fit quality can be improved with a three-temperature component model. In Table 8.1 we summarize the properties of the two spectra and their associated fit parameters.

Schmitt et al. (2008) already showed that the flare plasma of the initial short-duration outburst is thermal and consistent with that of the following rise phase of the main flare. The large increase in temperature and emission measure during the flare rise compared to the quiescent state is obvious from Fig. 8.3; the iron K complex clearly emerges. Enhanced line emission between 0.6 and 1.1 keV sets in, when the plateau phase of the flare peak is reached, while during the decay both emission measure and temperatures slowly decrease.

We divided the flare into eleven time intervals, the first six lasting 60 s, followed by two intervals of 120 s, and three intervals of 180 s, 240 s, and 300 s each. The first two intervals cover the flare rise, the next two the flattened peak, and the following seven intervals the different phases of the decay until the small flare at 0:10 UT sets in. We created spectra for each time interval and fitted them with various combinations of APEC models, using different numbers of temperature components and sets of variable elemental abundances as described in the following. Our models always include the quiescent emission, i. e. the parameters of the first two temperature components are fixed to the plasma properties of the quiescent spectrum before the flare as listed in Table 8.1. With this approach, we account for the contribution of the quiescent corona to the overall X-ray emission and neglect only the quiescent emission of the active region (flaring loop or arcade), where the flare takes place. This affects primarily the analysis of the last phases of the decay where the plasma properties have almost returned to the quiescent state, while the contribution of the quiescent emission is negligible from the flare rise to the middle of the decay.

The eleven flare spectra have then been fitted with one, two, and three additional temperature components. The last spectrum however contains very few counts, considering the resulting few degrees of freedom, only a one-temperature component fit is appropriate. In order to compare the plasma properties of the different sets of models with n additional temperature components, we make use of the total the emission measure EM, i. e. the sum of the emission measures of each temperature component i

$$EM = \sum_{i=3}^{n+2} EM_i \tag{8.1}$$

and the flare temperature T,

$$T = \sum_{i=3}^{n+2} \frac{T_i \cdot EM_i}{EM} \tag{8.2}$$

defined as an emission measure weighted sum of the temperatures from each flare component.

In a first approach, we fixed the elemental abundances for the flare plasma at the values listed above. One additional temperature component turns out to fit the last two spectra at the end of the decay well, while rather large residuals remain until the middle of the decay. However, already two temperature components give a reasonable fit for these phases of the flare. Even for the well-exposed rise and peak spectra, the addition of a third component does not provide an improvement in terms of χ^2, and models with two and three temperature components provide consistent flare temperatures and total emission measures.

The flare temperature peaks sharply at ≈35 MK in the second spectrum, and immediately starts

Table 8.1: Fit parameters to the quiescent spectra before and after the flare

	before the flare	after the flare	
Exposure time [s]	3004	5046	
kT_1 [keV]	0.14±0.01	0.19±0.01	0.13±0.01
EM_1 [10^{50} cm^{-3}]	$0.16^{+0.03}_{-0.02}$	0.21±0.01	0.16±0.02
kT_2 [keV]	$0.40^{+0.09}_{-0.02}$	0.58±0.02	0.34±0.01
EM_2 [10^{50} cm^{-3}]	$0.21^{+0.02}_{-0.04}$	0.13±0.01	$0.22^{+0.01}_{-0.02}$
kT_3 [keV]	–	–	$1.11^{+0.19}_{-0.18}$
EM_3 [10^{50} cm^{-3}]	–	–	0.04±0.01
red. χ^2	1.05	1.40	1.05
d.o.f.	96	149	147
log L_X [0.2–5.0 keV]	26.78	26.77	26.80

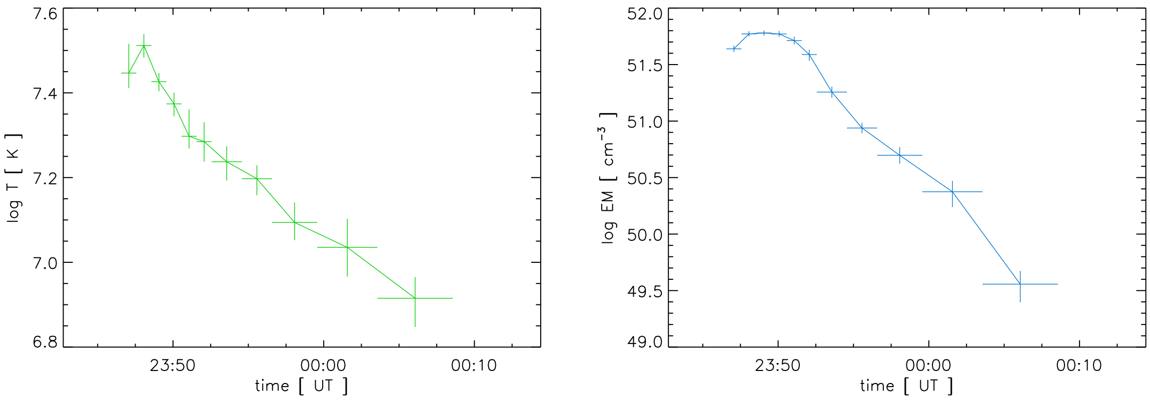

Figure 8.4: Temporal evolution of flare temperature (left) and total emission measure (right) of the flare plasma obtained from a two-temperature component fit with variable Fe abundance.

Table 8.2: Model parameters for the flare spectra with variable Fe abundance

Spect. No.	Exp. time [s]	kT_3 [keV]	EM_3 [10^{50} cm^{-3}]	kT_4 [keV]	EM_4 [10^{50} cm^{-3}]	Fe	log L_X [0.2–10.0 keV]	red. χ^2	d.o.f.
1	60	$0.74^{+0.04}_{-0.05}$	$4.81^{+1.18}_{-0.92}$	$2.62^{+0.46}_{-0.21}$	$38.76^{+1.76}_{-1.74}$	$1.03^{+0.32}_{-0.19}$	28.90	0.99	91
2	60	$0.84^{+0.09}_{-0.02}$	$6.99^{+1.26}_{-1.02}$	$3.06^{+0.19}_{-0.20}$	$52.11^{+1.98}_{-1.95}$	$1.38^{+0.21}_{-0.20}$	29.07	1.22	130
3	60	0.75±0.02	$9.57^{+1.32}_{-1.13}$	$2.59^{+0.13}_{-0.13}$	$50.60^{+2.01}_{-1.98}$	$1.33^{+0.17}_{-0.15}$	29.08	1.23	141
4	60	0.73±0.03	$10.97^{+1.60}_{-1.38}$	$2.34^{+0.15}_{-0.16}$	$48.06^{+2.04}_{-2.03}$	$1.07^{+0.14}_{-0.13}$	29.05	1.09	132
5	60	$0.75^{+0.02}_{-0.03}$	$14.46^{+2.15}_{-1.85}$	$2.08^{+0.37}_{-0.14}$	$37.13^{+2.06}_{-2.11}$	$0.89^{+0.09}_{-0.11}$	28.99	1.10	121
6	60	$0.71^{+0.03}_{-0.07}$	$10.67^{+2.19}_{-2.68}$	$2.02^{+0.24}_{-0.21}$	$28.15^{+1.89}_{-2.01}$	$0.72^{+0.14}_{-0.12}$	28.84	1.02	91
7	120	$0.71^{+0.03}_{-0.05}$	$6.32^{+1.16}_{-0.97}$	$1.91^{+0.18}_{-0.20}$	$11.75^{+0.95}_{-1.01}$	$0.75^{+0.13}_{-0.11}$	28.52	1.26	91
8	120	$0.61^{+0.06}_{-0.07}$	$1.64^{+0.39}_{-0.31}$	$1.53^{+0.11}_{-0.13}$	$7.05^{+0.58}_{-0.57}$	$0.85^{+0.18}_{-0.15}$	28.20	0.89	46
9	180	$0.58^{+0.07}_{-0.08}$	$1.64^{+0.49}_{-0.35}$	$1.31^{+0.15}_{-0.11}$	$3.33^{+0.41}_{-0.42}$	$0.59^{+0.14}_{-0.12}$	27.94	0.91	40
10	240	$0.55^{+0.06}_{-0.10}$	$1.24^{+0.35}_{-0.31}$	$1.35^{+0.27}_{-0.18}$	$1.13^{+0.24}_{-0.32}$	$0.52^{+0.24}_{-0.13}$	27.62	0.95	28
11	300	$0.71^{+0.09}_{-0.10}$	0.36±0.11	–	–	$0.49^{+0.36}_{-0.20}$	26.84	0.80	10

Table 8.3: T and EM calculated with Eqns. 8.1 and 8.2 and based on the values from Table 8.2.

Spect. No.	T [MK]	EM [10^{50} cm^{-3}]
1	$27.97^{+2.18}_{-4.82}$	$43.58^{+2.94}_{-2.66}$
2	$32.50^{+2.06}_{-2.07}$	$59.10^{+3.23}_{-2.97}$
3	$26.69^{+1.34}_{-1.29}$	$60.18^{+3.33}_{-3.12}$
4	$23.66^{+1.55}_{-1.49}$	$59.03^{+3.64}_{-3.40}$
5	$19.84^{+1.27}_{-3.13}$	$51.59^{+4.21}_{-3.97}$
6	$19.27^{+1.98}_{-2.13}$	$38.82^{+4.09}_{-4.69}$
7	$17.27^{+1.66}_{-1.52}$	$18.07^{+2.10}_{-1.98}$
8	$15.75^{+1.35}_{-1.19}$	$8.69^{+0.97}_{-0.87}$
9	$12.42^{+1.14}_{-1.43}$	$4.98^{+0.90}_{-0.77}$
10	$10.85^{+1.59}_{-1.81}$	$2.37^{+0.59}_{-0.64}$
11	$8.23^{+1.19}_{-1.00}$	0.36 ± 0.11

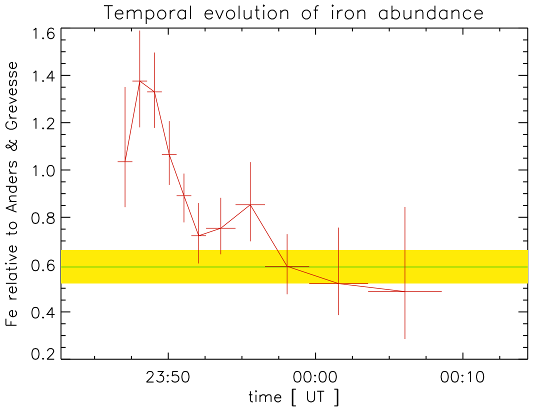

Figure 8.5: Temporal evolution of the iron abundance (relative to Anders & Grevesse (1989)). The quiescent value of 0.59±0.07 found by Fuhrmeister et al. (2007) is shown for comparison.

to decay. For the first six spectra, the flare-temperature lightcurve resembles the hardness-ratio lightcurve very well, which reflects the high-temperature continuum enhancement at higher energies. In the later phases of the flare, line emission becomes more important, disturbing the direct relationship between hardness ratio and temperature. The total emission measure shows the flat top already known from the lightcurve, and also the bump at 0:00 UT. Compared to the flare temperature, the decay is delayed by about two minutes.

When using two additional temperature components to fit the flare plasma, T_3 varies between 6 and 11 MK, while the hotter component T_4 covers a temperature range between 15 and 45 MK, with both temperature components decreasing starting with the second time interval. The ratio of the two corresponding emission measures EM_3/EM_4, however, continuously increases until and including the seventh time interval; the growing fraction of lower-temperature plasma shows the cooling of the flaring material. The smaller secondary peak in the hardness ratio lightcurve covered by the eighth spectrum makes EM_3/EM_4 temporarily decrease again.

8.4.3 Abundance variations

Even with two and three additional temperature components, residuals remain between 0.8–1.1 keV and and also at ≈2 keV, where many emission lines are located. This can be confirmed from the RGS spectra: Separating the RGS data into flare and quiescence, not only the continuum enhancement but also the flux increase in many emission lines in the wavelength range of 10–17 Å becomes clearly visible. Since many of the lines located at these wavelengths originate from highly-ionized iron, this may however also be a temperature effect. In order to improve the fit and to disentangle temperature and abundance variations, we introduced single elemental abundances as additional free parameters to the sequence of fits. Particularly, we tested iron, neon, silicon and oxygen.

With the iron abundance as a free parameter, the maximum flare temperature is reduced to 32 MK; a strong enhancement in iron during the flare compensates part of the flux of the iron K complex, which serves as a major temperature indicator. The total emission measure only slightly decreases. However, the general behavior of the one-, two-, and three-temperature component fits remains unchanged, so the shape of both the flare temperature and the total emission measure lightcurves is preserved, as shown in Fig 8.4. With the iron abundance as a free parameter, the fit quality clearly improves. Table 8.2 lists the fit parameters for the optimum combination of two flare components for the first ten spectra and one component for the last spectrum.

Figure 8.5 shows the corresponding time series of the iron abundance relative to Anders & Grevesse (1989) with the 1σ confidence range of the quiescent abundance found by Fuhrmeister et al. (2007) marked as a shaded area. The Fe abundance increases from a clearly subsolar level of 0.59±0.07 during quiescence by more than a factor of two to a maximum value of 1.38±0.20, when the flare peak is reached. It then decays even faster than the flare temperature; consistency with the quiescent value is reached again with the 6th spectrum. A re-increase at 23:55 UT in the eighth spectrum may not be significant, however, it coincides with the second rise of the hardness ratio lightcurve. By the end of the decay, the iron abundance has eventually dropped to the quiescent value again. A very similar behavior has been found by Favata & Schmitt (1999) for the overall metallicity during a long-duration giant flare on Algol observed with *BeppoSAX*.

Even with the Fe abundance as a free parameter, the second and the third spectrum cannot be fitted with a statistically acceptable value of χ^2_{red}. Residuals remain mainly around 1 keV in the second and between 0.7 and 1.2 keV as well as at 2 kev in the third time interval, respectively. There are quite a few emission lines at these energies, not only from iron but also from oxygen, neon and silicon. This indicates that further abundances may deviate from the quiescent values. When the neon abundance is set free, it seems to be generally enhanced compared to the value of 1.20±0.16 from Fuhrmeister et al. (2007), the Ne abundance does however not give a clear pattern like the iron abundance in Fig. 8.5 but shows a large scatter, and the uncertainties are rather large. Most values are on the 1σ level consistent with the old quiescent value. A free neon abundance therefore only marginally improves the fit, most of the residuals remain, with flare temperature and emission measure consistent stable at the initial values. Silicon shows a similar behavior, with its abundance values scattering around the quiescent value of 0.78±0.33. Again, temperature and emission measure stay at the values obtained from the fitting sequence with all abundances fixed. The same procedure with oxygen tends to result in unreasonable fits with either the oxygen abundance or at least one of the temperature components diverging or approaching zero. We also combined two or more free elemental abundances, i. e. Fe and Ne, Fe and Si, as well as Fe, Ne and Si, but none of these combinations provided further improvement in the quality of the fit compared to Fe set free only. These fits even start to diverge, especially for the less well-exposed last two spectra with few degrees of freedom. Additionally, the residuals in the fits of the second and the third spectrum cannot be reduced significantly.

Iron therefore seems to be the only element, where a clear variation of the elemental abundance during the flare and compared to the quiescent state can be observed. In the common picture of stellar flares, the evidence of changes in the iron abundance indicates that the flare plasma, i. e. fresh material evaporated from photosphere and chromosphere, shows a different composition with a higher iron abundance compared to the ordinary coronal plasma. Since CN Leo's quiescent corona shows the inverse FIP effect (Fuhrmeister et al. 2007), this confirms the finding of Nordon & Behar (2008) that IFIP-biased coronae tend to show a FIP bias during flares compared to their quiescent state. However, the Fe abundance seems to decrease much faster than temperature and emission measure of the flare plasma, and the iron abundance has returned to values consistent with the quiescent level when the X-ray emission of CN Leo is still by far dominated by the flare. The time-resolved evolution of the iron abundance in the flare plasma suggests either the existence of some kind of iron-depleting mechanism in the flare plasma, which would be rather difficult to explain, or the possibility that different parts of the lower atmosphere with different abundance levels were affected during the early and later stages of the evaporation process.

Finally we would like to address the possibility that systematic errors in our fit models actually mimic an enhanced iron abundance. At the very hot plasma temperatures as encountered during a flare, the iron abundance fit is affected by the flux of iron lines from lower ionization stages around 0.8–1.2 keV and – more importantly – by the flux of the emission complex at 6.7 keV, mainly originating from iron in ionization stages from Fe XXIII to Fe XXV. An incorrect temperature model would lead to an incorrect prediction of the emission both in the 0.8–1.2 keV energy range and in the 6.7 keV line complex, which would then have to be compensated by changing the iron abundance. Whether this is the case or not is hard to tell, yet a detailed study undertaken by (Favata & Schmitt 1999) suggests that this is unlikely to happen. Further, Fe Kα fluorescence at 6.4 keV, excited in the neutral photospheric material by intense high-energy radiation >7.1 keV from the flare plasma, may also contribute. Fe Kα fluorescence has been observed during strong stellar flares (e.g. Osten et al. 2007; Testa et al. 2008). The Kα excitation depends on the photospheric iron abundance and on the inclination angle and height of the X-ray emitting flare plasma above the photosphere (Testa et al. 2008; Ercolano et al. 2008; Drake et al. 2008). A compact loop structure as probably responsible for the short decay time of the flare on CN Leo is expected to produce rather strong fluorescence, yet no excess emission at 6.4 keV is visible, especially during the second and third time intervals, where the spectral fits yield the largest Fe abundance values. All eleven spectra are well consistent with models without any Fe Kα fluorescence emission at 6.4 keV. A possible explanation for this finding is an unfavorable viewing angle. At any rate, the expected Fe Kα line features are relatively weak, they can be spectrally separated from the 6.7 keV complex and should therefore not lead to incorrect Fe abundance estimates. Deviations from ionization equilibrium may also affect the strength of the 6.7 keV complex; Reale & Orlando (2008) have shown that the effect is significant for flares with heat pulse durations less than a minute. However, it is difficult to quantify this effect for the CN Leo flare, also such

Table 8.4: Measured line counts, f/i ratios and deduced coronal densities from the O VII triplet in the RGS spectra of quiescence and giant flare in Fig. 8.6.

Line	Wavelength [Å]	Quiescence	Flare
O VII r	21.60	30.2±6.8	25.4±5.9
O VII i	21.81	9.4±4.5	14.0±4.7
O VII f	22.10	27.1±6.3	1.2±2.0
f/i		2.88±1.53	$0.09^{+0.15}_{-0.09}$
log n_e		<10.77	>11.70

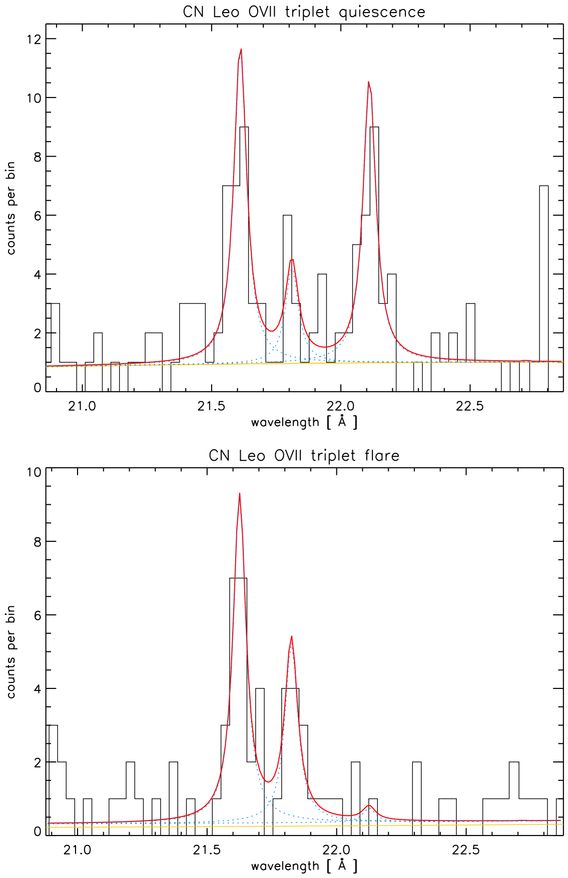

Figure 8.6: The O VII triplet in the RGS spectra of CN Leo during quiescent (top) and flaring (bottom) state. The flare spectrum covers the same time interval as the eleven EPIC spectra, the quiescent data include the time intervals before and after the giant flare, with two further flares excluded.

deviations from ionization equilibrium are strongest at flare onset, while ionization equilibrium is established rather quickly with time in a high density environment as encountered with the flaring plasma in CN Leo, so non-equilibrium effects appear to be an unlikely cause for the observed changes in iron abundance. Thus in summary, no clear systematic effects are known that would mimic an enhanced iron abundance during the flare evolution.

8.4.4 Densities

The RGS spectra allow to investigate the electron densities of the coronal plasma from the density-sensitive ratio of the forbidden and intercombination lines of helium-like triplets. With this method, Güdel et al. (2002a) found the density of the coronal plasma as traced by the O VII and Ne IX triplets to vary by more than an order of magnitude during a giant flare on Proxima Centauri, which is the only unambiguous measurement of increased coronal densities during a stellar flare. While the two flares were comparable in maximum countrate, the duration of the CN Leo flare was much shorter, so that, in contrast to the Proxima Centauri flare and to the CN Leo EPIC data, the CN Leo RGS data can only be separated into quiescent state and flare; the RGS signal is too low for further sub-division.

In Fig. 8.6 we show the RGS1 spectrum centered on the O VII triplet during the 20 ks of accumulated quiescence and during the flare together with the best fits to the three triplet lines r (resonance), i (intercombination), and f (forbidden) provided by the CORA program. The measured line counts, deduced f/i ratios and electron densities are listed in Table 8.4. In order to convert the measured f/i ratios to densities, we used Eq. 2.3 with values of $N_c = 3.1 \cdot 10^{10}$ cm^{-3} and $R_0 = 3.95$ from Pradhan & Shull (1981) for the critical density and the low-density limit, respectively. During quiescence, the f/i ratio is well consistent with the low-density limit, which is in good agreement with the values found for CN Leo in May 2004 by Fuhrmeister et al. (2007). In the flare spectrum, the forbidden line has almost vanished, while the intercombination line is stronger. The electron density therefore clearly deviates from the quiescent value of $n_e = 1.2^{+4.9}_{-1.2} \cdot 10^{10}$ cm^{-3} during the flare, and is definitely incompatible with the low-density limit. The average density during the flare has a nominal value of $n_e = 1.4 \cdot 10^{12}$ cm^{-3}. Taking into account the 1σ error on the line fluxes, a lower limit of $n_e > 4.9 \cdot 10^{11}$ cm^{-3}, i. e. at least an order of magnitude higher than the quiescent value, can be derived.

f/i ratio and electron density obtained from the RGS flare spectrum represent mean values for the whole flare. In order to give a rough estimate of the peak flare density, one can derive a modifying scaling factor of ≈1.2 based on the square root of the maximum and mean total emission measure values from the EPIC data and assuming a constant plasma volume during the flare. The flux in the forbidden and intercombination lines measured during the whole flare is therefore dominated by the high countrates at the flare peak, and with a lower limit of $n_\mathrm{e} > 5.9 \cdot 10^{11}$ cm^{-3} the maximum density is only slightly larger than the average value.

With a peak formation temperature of ≈2 MK, the O VII triplet traces only the cooler component of the coronal and flare plasma, and the density sensitivity of its f/i ratio is optimal between 10^{10} and 10^{11} cm^{-3}. As the O VII triplet suggests densities probably even higher than 10^{12} cm^{-3}, it would be desirable to probe higher densities and the higher-temperature plasma with the helium-like triplets of heavier ions. Unfortunately, the flux in the RGS2 spectrum in the Ne IX triplet, where the density-sensitive range has shifted to 10^{11}–10^{12} cm^{-3} and the peak formation temperature has increased to ≈4 MK, is too low and its contamination with highly-ionized iron during the flare is too strong to give any conclusive result. Mg XI and Si XIII cover even higher densities up to 10^{14} cm^{-3} and temperatures up to 10 MK, but in the two RGS spectra, the resonance lines of both triplets are only barely visible. A density survey of the flare at different plasma temperatures is therefore not possible.

8.4.5 The optical coronal Fe XIII line

With the RGS, the wavelength range ≈6–37 Å can be observed; including individual emission lines with peak formation temperatures from ≈1.5–2 MK in the low-temperature range (C VI, O VII) up to 15 MK (Si XIV). The optical coronal Fe XIII line at 3388 Å included in the blue-arm UVES spectra provides additional time-resolved information on the lowest coronal temperatures (peak formation temperature ≈1.5 MK).

Compared to the previous observations in December 2005, the Fe XIII line is rather weak in all three observations in May 2006. The measured line fluxes have large uncertainties, sometimes the line is not even clearly detected. The measured FWHM is also smaller than previously observed. Unfortunately, no Fe XIII line data is available for comparison from the observation in May 2004, where CN Leo's quiescent X-ray emission was at a lower level, similar to the quiescent phase outside the large flare. However , it is reasonable to assume that the overall reduction in emission measure, which affects the lower temperatures where Fe XIII is formed as well, is responsible for the lower line fluxes.

The most significant detections are obtained after the giant flare and after a second larger X-ray flare. A third larger X-ray flare is not covered by the optical observations anymore. The Fe XIII line is not visible in the pre-flare spectrum and in the two flare spectra; but during the flare, a chromospheric Co I line emerges at the same wavelength position.

Even during quiescence, the bulk of iron in the coronal plasma should exist in the form of neon-like Fe XVII, with only minor contributions of the cooler Fe XIII. With the onset of the flare, the temperature of the X-ray emitting plasma shifts to even higher values, and therefore the ionization balance should be dominated by far by higher ionization stages. Even with an increased iron abundance, Fe XIII can be expected to be depleted until the end of the decay, when the plasma has cooled down again. The excess emission measure then allows the detection of the Fe XIII, which is consistent with the observations.

8.5 Loop modeling

Direct imaging demonstrates the great complexity of flaring active regions on the Sun. In order to obtain a consistent model describing the physical properties and evolution of the involved structures, a stellar flare can be reduced to a sequence of processes taking place in a simplified geometry. Such a generalized description starts with an initial heat pulse in a single coronal loop and efficient conduction until the whole loop has reached the maximum temperature. Lower atmospheric layers are strongly heated and chromospheric evaporation fills the loop with denser material. Conductive cooling sets in while the filling of the loop may still go on. Radiative cooling dominates as soon as the maximum density is reached, and loop depletion is initiated. Cooling and loop depletion may be decelerated by potential residual heating. The transitions between these processes can be described in terms of equilibrium conditions, but their possible overlap and interplay complicate the modeling. However, over the last decades, model approaches for flares have evolved from scaling laws valid only for (quasi)static conditions or simple analytical estimates to complex hydrodynamic loop models taking into account various initial conditions. These models have been successfully applied to a wide variety of solar and stellar flares.

8.5.1 The decay phase

A basic finding for solar and stellar flares is that the decay time of a flare scales with the length of the flaring loop. In order to quantify this effect, Serio et al. (1991) developed an analytic approximation relating the thermodynamic decay time τ_{th}, the loop half length L and the loop top maximum temperature T_0 of a flaring loop, based on the underlying set of hydrodynamic equations and assuming semicircular loops with constant cross section cooling from equilibrium conditions and uniformly heated by an initial heat pulse without any further heating during the decay. This approach has been refined by Reale et al. (1993) to account for loops comparable or larger than the pressure scale height h at the loop top

$$h = \frac{k_B T_0}{\mu g} \tag{8.3}$$

where k_B is the Boltzmann constant, μ is the effective mass per particle and g the surface gravity of the star. The pressure scale height for the giant flare is greater than 100 000 km.

In their models, Reale et al. (1993) also consider the effect of a gradually decaying heating function, and finally, for loops smaller than the pressure scale height, Reale et al. (1997) derived and tested an empirical expression to determine the flaring loop length including the effect of sustained heating during the decay that uses the slope ζ of the flare decay in the density-temperature plane to evaluate the amount of sustained heating during the decay:

$$L = \frac{\tau_{LC}\sqrt{T_0}}{\alpha\, F(\zeta)} \qquad \text{or} \qquad L_9 = \frac{\tau_{LC}\sqrt{T_{0,7}}}{120\, F(\zeta)} \tag{8.4}$$

where $\alpha = 3.7 \cdot 10^{-4}$ cm^{-1} s K$^{1/2}$.

The term $F(\zeta)$ describes the ratio of observed and thermodynamic decay time τ_{LC}/τ_{th} as a function of the ratio of temperature and density decay ζ. The higher $F(\zeta)$, the larger is the amount of prolonged heating during the decay, while $F(\zeta) \approx 1$ would indicate the absence of additional heating. $F(\zeta)$ is monotonically decreasing and can be approximated with analytical functions; here we use the hyperbolic form

$$F(\zeta) = \frac{\tau_{LC}}{\tau_{th}} = \frac{c_a}{\zeta - \zeta_a} + q_a \tag{8.5}$$

The coefficients c_a, ζ_a, and q_a depend on the energy response of the instrument used. For XMM/EPIC, the values are $c_a = 0.51$, $\zeta_a = 0.35$, and $q_a = 1.36$ according to Reale (2007). Additionally, the observed maximum of the flare temperature $T_{0,\mathrm{obs}}$, which is an averaged value over the whole loop, must be corrected with

$$T_0 = \xi\, T_{0,\mathrm{obs}}^{\eta} \qquad \text{or} \qquad T_{0,7} = \xi \cdot 10^{-7} \cdot T_{0,\mathrm{obs}}^{\eta} \tag{8.6}$$

in order to obtain the true T_0 independently of the detector. The values of the coefficients are $\xi = 0.13$ and $\eta = 1.16$ for XMM/EPIC (Reale 2007). With the maximum flare temperature found in the second time interval, we determined $T_{0,7}$= 5.6±0.4.

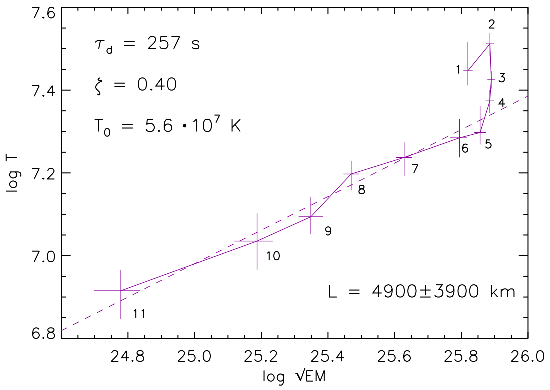

Figure 8.7: Flare evolution in the density-temperature plane.

Figure 8.7 shows the evolution of the giant flare in the density-temperature plane, where we use $\sqrt{EM}$ as a proxy for the density. We fitted the slope ζ of the decay, i. e. with the data from first three spectra excluded, to $\zeta = 0.40 \pm 0.05$. This value is rather small, and on a 1σ level consistent with the minimum value of 0.35, which means that the limit of validity for this method is reached. For very small ζ, the corrective term $F(\zeta)$ that accounts for the presence of heating during the decay becomes very high and also rather uncertain, as the hyperbola approaches infinity. For $\zeta = 0.40$, we obtain a formal value of $F(\zeta) = \tau_{LC}/\tau_{th} = 10.7$; the thermodynamic decay time would therefore lie in the range of ≈ 25 seconds, which is extremely short and hints to very effective cooling. The size of the involved loop structure is thus very small, the resulting loop half length is $L = 4900 \pm 3900$ km. The uncertainty in L is dominated by far by the uncertainty in ζ in this flat part of the hyperbola of $F(\zeta)$. Effectively, we can therefore only give an upper limit for L, which can be set to ≈ 9000 km using the 1σ error.

The original approach of Reale et al. (1997) is based on hydrostatic and energy equilibrium at the beginning of the decay. This would result in a simultaneous onset of the decay of temperature and density, which is apparently not the case for the giant flare on CN Leo. In order to account for this, the flare temperature at the time of maximum density T_{M} should be used instead of T_0 according to Reale (2007), otherwise the loop length will be overestimated. However, considering that the dependency of L on the square root of T_0 is comparably weak, we keep at the original value for the upper limit. Additionally, the exact point in time of maximum density is difficult to assess from flat top of the emission measure lightcurve, while the temperature already decreases significantly.

8.5.2 Flare rise and peak

Following the approach of Reale (2007), the duration of the flare rise and a possible delay between the decay of temperature and density can also be used to characterize the dimensions of a flaring loop. Both time scales can be traced back to equilibrium states of heat input and cooling. The occurrence of such a delay, as it is also observed for the giant flare on CN Leo, indicates an initial heat pulse too short to bring the flare plasma to equilibrium conditions, again pointing toward short time scales and a compact structure.

The maximum density is reached when conductive and radiative cooling equal. This gives

$$L_9 = 3\psi^2 \sqrt{T_{0,7}}\; t_{\mathrm{M},3} \tag{8.7}$$

as an estimate for the loop length from time t_{M} at which the maximum density occurs and the ratio ψ of the maximum temperature T_0 and the temperature at maximum density T_{M}:

$$\psi = \frac{T_0}{T_{\mathrm{M}}} \tag{8.8}$$

From the time $\Delta t_{0-\mathrm{M}} = t_{\mathrm{M}} - t_0$ between the start of the temperature decay and the density maximum, i. e. the start of the density decay, one obtains

$$L_9 = 2.5\frac{\psi^2}{\ln\psi}\sqrt{T_{0,7}}\;\Delta t_{0-\mathrm{M},3} \tag{8.9}$$

adopting the conductive cooling time.

These two independent approaches are particularly useful, if only the earlier phases of the flare are observed, i. e. Eq. 8.7 can be applied if the complete rise phase of the flare is available until the density maximum is reached, while bigger parts of the decay are not required. Eq. 8.9 can be used if additionally the quiescent phase before the flare and the flare onset itself are missing. When the flare is completely covered by the observations, the two methods yield independent estimates of the loop half length which can be cross-checked.

Both Eqns. 8.7 and 8.9 depend strongly on ψ and also on the two onset times of the temperature and density decay, which have to be determined as accurately as possible. Using the time intervals from Sect. 8.4.2, the temperature maximum occurs during the second spectrum, which would result in $t_{0,\mathrm{spec}} = 90 \pm 30$ s, i. e. a rather large uncertainty due to the length of the time interval compared with the rise time itself. It is, however, not reasonable to divide the sequence any further. The hardness ratio lightcurve from Fig. 8.2 provides a better time resolution, assuming that especially during the early phases of the flare, the hardness ratio represents a good temperature indicator. The hardness ratio lightcurve undergoes major changes during the first time interval; it peaks already at $t_{0,\mathrm{HR}} = 47 \pm 5$ s, earlier than the spectral fit sequence, that provides only the average temperature of each interval. We would therefore prefer to use the hardness ratio as a temperature tracer, but subsequently, the true maximum temperature T_0 will be larger than the 56 MK derived from the flare temperature of the second time interval, and it is difficult to give an accurate estimate. The difference between the two possibilities to choose for t_0 will at any rate strongly affect the results of the loop length estimate.

It is even more difficult to define the maximum of the density. The emission measure, which we have used as the density indicator in Sect. 8.5.1, peaks in the third time interval. However, due to the flattened shape of the emission measure lightcurve, the uncertainty in t_{M} is probably even larger than the corresponding value of 150 ± 30 s. Consistent results are obtained when using a smoothed version of the countrate lightcurve, which would nevertheless result in an underestimate of t_{M} according to Reale (2007). T_{M} is therefore determined from the flare temperature in the third time interval.

Using the numbers obtained from the analysis of the time intervals only, we obtain $L = 25\,000 \pm 18\,400$ km from Eq. 8.9. When sticking to T_0 from the second time interval but in combination with t_0 from the hardness ratio lightcurve, L increases to $43\,000 \pm 15\,300$ km, and a higher value for T_0 would even result in a further increase, with the corresponding value being unknown. Eq. 8.7 gives $L = 16\,700 \pm 4900$ km, closer to the value from the upper limit from the analysis of the decay. Considering the large error bars, the results from Eqns. 8.4, 8.9, and 8.7 are consistent at least on the 2σ level. The overall uncertainties are dominated by the uncertainties of the two time scales t_0 and t_{M}: For the results obtained from the flare rise from Eq. 8.7, the uncertainty in t_{M} makes up 53% of the uncertainty in L, while T_0 and T_{M} share 33% and 13% respectively. When the time intervals are used to determine t_0 in Eq. 8.9, $\Delta t_{0-\mathrm{M}}$ accounts even for 91% of the uncertainty in L. Using t_0 from the hardness ratio lightcurve, this reduces to 63%. As Eq. 8.9 yields indeterminate results, Eq. 8.7 should be preferred.

8.6 Discussion

8.6.1 Implications of the modeling

The giant flare on CN Leo has a very short exponential decay time of only a few minutes compared to other flares with similar amplitudes in X-rays, which typically last for hours. This holds even if one considers only flares on active M dwarfs (e. g. Favata et al. 2000; Güdel et al. 2002a). Such flares mostly originate from large loop structures with dimensions of at least a significant fraction of the size of the star itself. The short duration of the CN Leo flare on the other hand points at short cooling times and therefore a rather compact involved structure. Respective estimates assuming a single flaring loop have confirmed this picture, the resulting loop half length is of the order of about a tenth of the stellar radius or even smaller.

We can assess the emitting plasma volume V via

$$V = \frac{EM}{n_e^2} \tag{8.10}$$

and obtain the area A of the loop footpoint on the stellar surface

$$A = \frac{V}{2L} \tag{8.11}$$

approximating the loop with an unbent tube with a circular base area and constant cross-section over the loop length. In order to compute V and A, we can use the electron density derived from the helium-like O VII triplet of the flare spectrum in Sect. 8.4.4, and the total emission measure averaged over the eleven time intervals from Sect. 8.4.2, $EM = 1.8 \cdot 10^{51}$ cm^{-3}, and obtain $V < 7.4 \cdot 10^{27}$ cm^3 from the lower limit of the density, or $V = 9.1 \cdot 10^{26}$ cm^3 using the nominal value. This results in values of $1.3\text{–}80 \cdot 10^{17}$ cm^3 for A, depending on the value used for L. Larger loop lengths, as they are provided by the data from the flare rise and peak, give the smallest footpoint area. A good reference point is $A \approx 1 \cdot 10^{18}$ cm^2, which would correspond to a short loop with a length close to the nominal value derived from the decay (i. e. ≈4500 km) at the nominal electron density value of $n_\mathrm{e} = 1.4 \cdot 10^{12}$ cm^{-3}, or a longer loop with L ≈35 000 km at a lower density of $5 \cdot 10^{11}$ cm^{-3}.

Another possibility to estimate n_e independently from the emission measure is to make use of the scaling laws of Rosner et al. (1978)

$$T_0 = 1400 \sqrt[3]{pL} \tag{8.12}$$

which assume equilibrium conditions and the plasma equation of state $p = 2n_e k_B T$:

$$n_0 = 1.3 \cdot 10^6 \frac{T_0^2}{L} \qquad \text{or} \qquad n_{0,10} = 13 \frac{T_{0,7}^2}{L_9} \tag{8.13}$$

This results in density values between $n_\mathrm{e} = 3.9 \cdot 10^{11}$ cm^{-3} and $n_\mathrm{e} = 2.8 \cdot 10^{12}$ cm^{-3} for the largest and smallest possible loop lengths respectively, which matches the maximum density estimate from Sect. 8.4.4 quite well. The maximum density n_M should be somewhat higher than n_0. However, due to the large uncertainties in L, the derived densities cannot be fixed to an order of magnitude. Similarly, footpoint areas between $A = 7.7 \cdot 10^{17}$ cm^3 and $A = 3.2 \cdot 10^{18}$ cm^3 are obtained, but again with large uncertainties on individual values. In addition, it is unclear to which level this particular flare follows the established scaling laws at all, as the initial assumptions like equilibrium or constant flaring volume are not necessarily fulfilled.

In order to model the short initial burst, Schmitt et al. (2008) assumed a single loop with a half length of 20 000 km. Along the loop, they obtain densities of $1\text{–}10 \cdot 10^{11}$ cm^{-3} after it is filled with evaporated material. The temperature in the loop model reaches maximum values around $4 \cdot 10^7$ K, both numbers are well consistent with what we obtain also for the major flare event.

Aschwanden et al. (2008) compiled statistical correlations between peak temperature T_0, peak emission measure EM, X-ray luminosity L_X, total X-ray-radiated energy E_X, and flare duration τ_f for a large sample of observed stellar flares. They find the following relations as a function of the maximum temperature T_0,

$$EM(T_0) = 10^{50.8} \cdot T_{0,7}^{4.5 \pm 0.4} \tag{8.14}$$

$$\tau_f(T_0) = 10^{2.5} \cdot T_{0,7}^{1.8 \pm 0.2} \tag{8.15}$$

$$L_X(T_0) = 10^{27.8} \cdot T_{0,7}^{4.7 \pm 0.4} \tag{8.16}$$

$$E_X(T_0) = 10^{30.7} \cdot T_{0,7}^{6.1 \pm 0.5} \tag{8.17}$$

however, the correlation between τ_f and (T_0) in Eq. 8.15 is only marginally significant due to large scatter in the data. Our measurements from giant flare on CN Leo clearly deviate from the relation between peak temperature and emission measure, the observed maximum emission measure is more than an order of magnitude lower than the value provided by Eq. 8.14. While the densities we observe seem to be common for such a huge flare, the flaring structure is rather compact, i. e. the flaring volume is very small, which apparently causes the low emission measure. Eq. 8.15 predicts a flare duration of about 45 minutes, more than two times longer than observed. However, as the correlation between τ_f and T_0 is not that strong, this matches the data regime from the flare sample. As a consequence of the deviation of the emission measure, Eq. 8.16 overestimates the X-ray luminosity at the flare peak also by an order of magnitude. The total radiative loss in X-rays from Eq. 8.17 is too high even by two orders of magnitude as a result of both the overestimated emission measure and flare duration.

8.6.2 Single loop or arcade?

The Sun shows us that the model of an accumulation of isolated single loops oversimplifies a stellar corona. Instead, loops of different sizes often group to complex structures of arcades, especially in the active regions where flares originate. Such loop structures are non-static; individual loops resize, their footpoints move, and they realign in magnetic reconnection events. Unfortunately, we cannot even resolve individual active regions directly on stars other than the Sun. Doppler imaging is a common indirect method to reconstruct photospheric spots or prominences in the chromosphere of fast rotators spectroscopically in the optical (see e. g Strassmeier 2009b). Lightcurve-based eclipse mapping techniques provide an additional approach, as successfully demonstrated by Wolter et al. (2009). However, the solutions of such image reconstruction methods are usually not unique, becoming more and more ambiguous the better the targeted spatial resolution is. Additionally, such observations are very rare in the X-ray regime, cf. Güdel et al. (2001, 2003), and Schmitt et al. (2003).

There are however other clear indications for the substructuring of active regions in stellar coronae. Flare lightcurves often deviate from the simple scheme of rise and exponential decay, and instead show multiple peaks or variations in the decay time, like a double exponential decay (e. g. Wargelin et al. 2008). The lightcurve of the giant flare on CN Leo shows several irregularities like the initial outburst and the flat peak. Its decay deviates from an exponential shape, and there is the small bump in the lightcurve which is apparently related to a second peak in the hardness ratio lightcurve. This event obviously interrupts the otherwise continuous cooling of the flare plasma. Such features suggest that multiple components of the active region from which the whole flare event originates are successively involved, each of them with its own properties like shape and size, temperature and density, and hence cooling time.

Further evidence for flare substructure can be obtained from the spectral analysis of the flaring plasma. A strong correction $F(\zeta)$, i.e. when heating dominates the decay of the flare, points to an arcade of loops involved, as observed for two-ribbon flares on the Sun; this was first pointed out by Reale (2002). For the giant flare, $F(\zeta)$ is very high. We therefore interpret the whole event in terms of a flaring arcade. In this scenario, the flat top of the lightcurve can be explained by the superposition of several loops flaring consecutively. Later during the global decay, further loops not affected so far became involved and caused the small bump. This flare series was triggered by the short initial outburst, which could be localized in an almost isolated single loop (Schmitt et al. 2008). If we assume that the flat peak of the main flare is composed of a sequence of unresolved individual peaks with similar luminosity, the true values of t_{M} and in particular $\Delta t_{0-\mathrm{M}}$ would be lower while τ_{LC} will stay roughly the same, which would in turn reduce L from Eqns. 8.7 and 8.9, i.e. bring the results from the analysis of rise and peak closer to the upper limit obtained from the decay.

A theoretical model framework for solar two-ribbon flares has been developed by Kopp & Poletto (1984) and – with restrictions – successfully applied also to stellar flares, see e.g. Poletto et al. (1988) for the modeling of two long-duration flares on the active M dwarfs EQ Peg and Proxima Centauri observed with *Einstein* and *EXOSAT*. The single-loop model approach of Reale et al. (1997) can be extended to multi-loop structures if different phases of the flare are analyzed separately. Reale et al. (2004) investigated the evolution of the long-duration giant flare on Proxima Cen observed with *XMM-Newton*. In their best-fit model, the X-ray emission is dominated by a single loop for the first part of the flare, while later on during the decay an additional arcade of loops with approximately the same length as the initial single loop emerges. This picture is supported by the analysis of spatially resolved observations of strong solar two-ribbon flares (e.g. Aschwanden & Alexander 2001). For the giant flare on CN Leo, the primary single loop was causing the 2-second initial outburst. Due to its short duration it is impossible to analyze this very first part of the flare in more detail in order to obtain flare temperature and loop length. We can, however, conclude that even if the whole flare event is treated as originating from an arcade-like structure, it would be very compact, probably even smaller in terms of loop length than a single loop. Reale et al. (2004) found a loop length larger by 30% if the flare on Proxima Cen is interpreted with Eqns. 8.4–8.6 instead of with detailed hydrodynamic loop modeling. For a single loop, the flaring volume scales with L, while an arcade of loops implicates $V \propto L^3$. For solar flares, an empirical correlation $V \propto L^{2.4}$ is obtained (Aschwanden et al. 2008), reflecting the observation that arcades are not uniformly filled but consist of individual loops.

8.6.3 The multiwavelength context

Plasma temperature, density, and optical thickness of the stellar atmosphere change by orders of magnitude, when going from the photosphere via chromosphere and transition region up into the corona. According to its spectral type, i.e. the effective temperature, the major contribution to the photospheric spectrum of an M dwarf like CN Leo is emitted the infrared, with a much smaller proportion observed in the optical. The chromosphere adds line emission, mainly in the UV and in the optical. Line formation at these wavelengths is a complex process. Photospheric absorption lines may turn into emission in the chromosphere, and the strength and shape of chromospheric lines is extremely sensitive to the atmospheric conditions. A sophisticated modeling of M dwarf chromospheres is challenging, and current models are still far from providing a complete description (see e.g. Fuhrmeister et al. 2005b). Nevertheless, as for each line the formation takes place under specific physical conditions which basically translate into certain heights above the the "surface", different lines probe the structure of the stellar atmosphere. Transition region and corona emit mainly in X-rays and in the EUV. Complemented by non-thermal processes like e.g. radio gyrosynchrotron emission, the different atmospheric layers can therefore be studied over a broad wavelength range.

Solar and stellar flares can affect all parts of the atmosphere, with the strongest impact observed on chromosphere and corona. However, as on M dwarfs the quiescent photospheric continuum is low in the optical, photospheric flare continuum emission, that accompanies strong events like the giant flare on CN Leo discussed in our series of papers, is much more obvious compared to the Sun, where white light flares are rarely observed. When integrating over the full disk, they would go unnoticed in optical broad band measurements. In Paper I, we analyzed the observed optical continuum emission during the CN Leo flare. We found that the photospheric material was rapidly heated to temperatures probably exceeding 20 000 K at the onset of the flare and rapidly cooling afterwards. The size of the affected region in the photosphere agrees very well with the area derived in Sect. 8.6.1. Our chromospheric modeling in Paper II confirmed the strong heating of the lower atmospheric layers, during the flare the chromosphere is shifted towards higher column masses, i.e. deep into the photosphere. In Paper I we presented a detailed list of emission lines observed in the optical flare spectra; the included lines provide good indicators for the structure of chromosphere and transition region. However, as shown in Paper II, a self-consistent model of the flare and especially of its early phases would require to consider also non-equilibrium conditions. Additionally, the flare plasma is non-static, line shifts and asymmetries are tracers of mass motions, i.e. chromospheric evaporation into the corona and later on material that has cooled down and falls back towards the surface. Unfortunately, the limited spectral resolution of the X-ray data does not allow to verify this for the hot plasma in the corona.

Nevertheless, our multiwavelength study has revealed a very detailed picture of the flare. We were able to determine plasma temperatures, densities and abundances, apart from the latter not only in the corona but also in photosphere and chromosphere. We learned that the active region and its associated coronal loop structure where the flare originated were rather compact but probably also much more complex than a simple single loop with two footpoints. Multiwavelength observations can provide a comprehensive picture of stellar activity phenomena. Wolter et al. (2008) have complemented their X-ray observations of the fast rotator Speedy Mic with Doppler imaging information, which allowed to localize not only spots on the stellar surface but also prominences and a flare. As theoretical models become more and more complex, with both stellar atmosphere codes and hydrodynamic simulations approaching the non-static 3D domain, including magnetic fields or further physical conditions, only detailed observing data can provide complementary information. For stellar flares, this requires good spectral and temporal resolution over a wavelength range as broad as possible.

8.7 Summary and conclusion

We have analyzed simultaneous X-ray and optical data covering a giant flare on the active M dwarf CN Leo with regard to the plasma properties in the corona and the geometry of the flaring structure. As it could be expected from other events of similar strength observed in X-rays, temperature and density are enhanced by more than an order of magnitude compared to the quiescent corona at the flare peak. The flare plasma, which can be considered to consist mostly of material evaporated from chromosphere or photosphere, shows a different composition. Despite its high amplitude, the flare was only of short duration, indicating a rather compact flaring structure, which is also comfirmed by simple loop modeling. Sustained heating during the decay as well as substructure in the lightcurve and hardness ratio however suggest an arcade-like structure much more complex than a single flaring loop. Broad multiwavelength coverage allowed us to characterize this exceptional event in great detail.

9 Summary and outlook

9.1 Developed techniques and obtained results

In the course of this work, I have investigated the coronal properties of the low-activity star α Cen, the active M dwarf binary EQ Peg, and the mid M dwarf CN Leo. In particular, I have analyzed a giant flare on CN Leo in great detail. The most important aspects can be summarized as follows:

Analysis methods

- The differential emission measure of a stellar corona can be roughly approximated over a broad temperature range using single analytical functions like e. g. polynomials. However, the BEXST challenge showed that the uncertainties are large when it comes to verifying discontinuities or structures occurring on small scales. This kind of non-uniqueness is inherent in all DEM reconstruction methods. It is therefore appropriate to apply Occam's razor and keep the reconstructed differential emission measure as simple as possible.

- Emission measure-independent linear combinations of emission line fluxes are a simple and robust approach to determine coronal abundance ratios. While each specific ratio of linear combinations has different temperature-dependent residuals, it can be optimized to the (assumed) temperature structure of a given target.

- The cumulative distribution of X-ray spectra provides a valueable tool for comparing spectral energy distributions which is appropriate also for grating spectra with low signal-to-noise.

- Activity affects the whole stellar atmosphere. With the physical properties of photosphere, chromosphere, and corona differing by orders of magnitude, only multiwavelength observations with simultaneous coverage and high temporal and spectral resolution provide a comprehensive and detailed view of the ongoing processes and their interplay.

Coronal structures and abundances

- The low coronal Ne/O abundance ratio in the old, solar-like binary α Centauri revealed that the Sun as the prototype of a low-activity star is not as atypical as suspected, but instead that our view of stellar coronae is strongly biased towards high activity levels, i. e. like in young stars, active M dwarfs, or RS CVn binaries. However, with the Ne/O ratio indeed being low in the coronae of rather inactive stars, the crucial discrepancy between recent solar photospheric abundance determinations and models of the solar interior remains.

- The two components of the M dwarf binary EQ Peg show very similar coronal properties, with indications of higher activity levels in the M3.5 primary compared to the M4.5 secondary. Both of them are typical representatives of active M dwarfs.

- Persistent strong flaring as observed in early M dwarfs changes to low-level flickering interrupted by discrete flares in the M5.5 star CN Leo. Mid M dwarfs therefore appear as intermediate objects considering the low quiescent X-ray luminosities but rather strong flares of late M dwarfs.

- Lower X-ray luminosities (in terms of $L_\mathrm{X}/L_\mathrm{bol}$) and lower coronal temperatures as observed in less active stars like intermediate or late M dwarfs are accompanied with less pronounced abundance anomalies.

- The smooth decline of coronal activity indicators from early M dwarfs towards the low-mass end of the main sequence suggests that also the underlying transition from the solar-like $\alpha\Omega$-dynamo to a fully convective interior with turbulent or α^2-dynamo mechanisms at work must take place seamlessly.

The flare process

- A very short but strong thermal X-ray burst triggered a huge flare on CN Leo. Hydrodynamic modeling of this burst showed that stellar flare events can be restricted to structures as small as single magnetic flux tubes, while nanoflares, scaled down in terms of energy release by orders of magnitude compared to the burst but candidates for the source of coronal heating, remain unresolved as well on the Sun as on other stars.

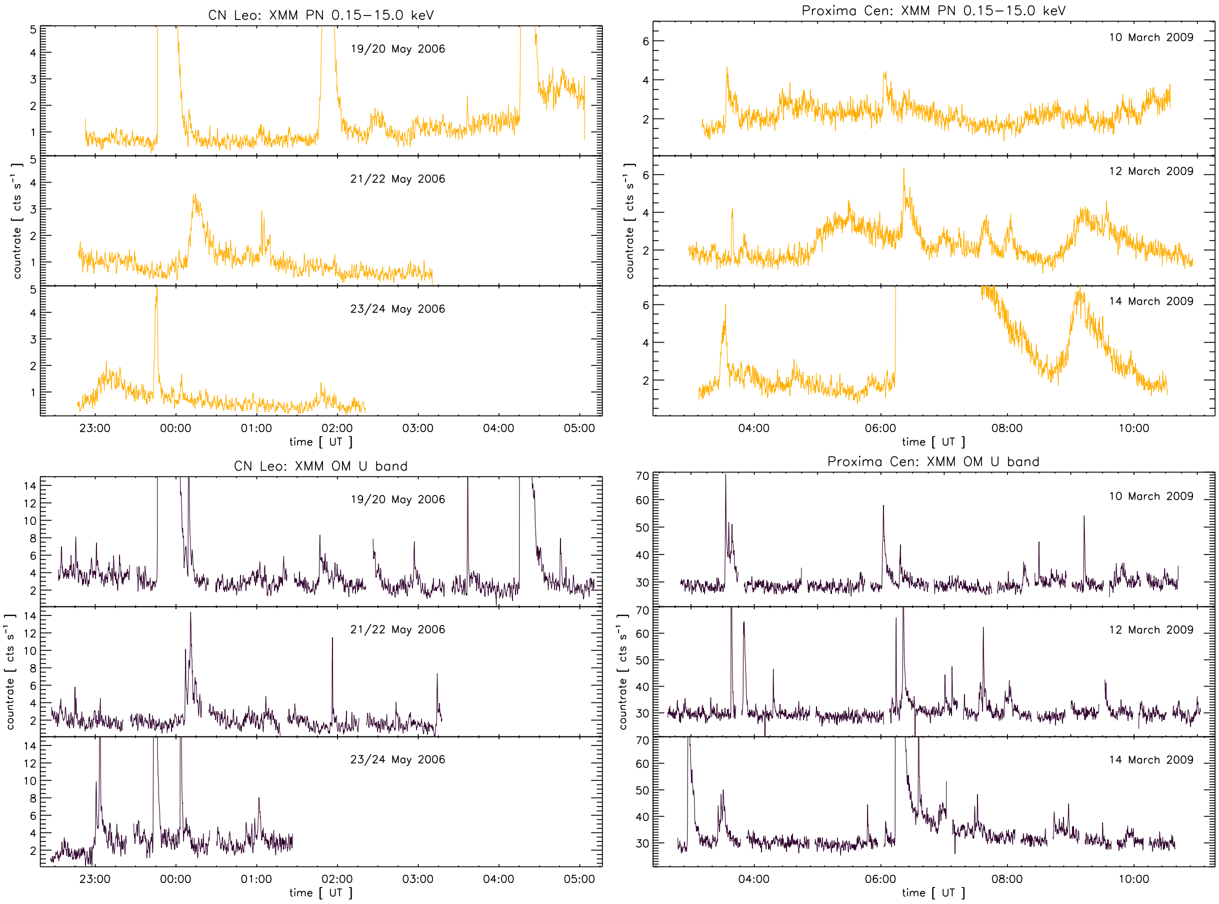

Figure 9.1: *XMM-Newton* X-ray (top) and U band (bottom) lightcurves of the two M dwarfs CN Leo (left) and Proxima Cen (right) from our two multiwavelength campaigns in May 2006 and March 2009.

- Although at first sight a simple impulsive event of short duration, time-resolved X-ray spectroscopy and fine structure in the X-ray lightcurve and hardness ratio revealed that the active region on CN Leo where the giant flare was located was a compact but complex arcade-like structure.

- Chromospheric evaporation significantly changed the chemical composition of the plasma in the flaring loop, demonstrating that the fractionation processes leading to divergent elemental abundances in different heights of the stellar atmosphere are not restricted to the Sun.

- The photosphere in the flare region was heavily affected during the early phases of the flare and heated to temperatures probably exceeding 20 000 K. Contemporaneously to the initial X-ray burst, rapid cooling set in; the continuum emission observed in the optical can be described well by blackbody radiation, a pronounced Balmer jump is not visible.

- A wealth of optical emission lines emerges, tracing the evolution of chromosphere and transition region. Line shifts and asymmetries are caused by mass motions, with evaporating material moving upwards during the early phases of the flare and plasma that has already cooled down falling back to the surface later.

9.2 Future perspectives and things to be done

Although the problems I addressed in the course of this study led to new insight into the physics of stellar coronae and especially into the processes going on in the stellar atmosphere during a flare, several open questions remain. However, the available data provide several opportunities for further investigation, which is particularly valuable considering the foreseeable end of the *Chandra* and *XMM-Newton* missions within the next few years, while the launch of their successor, now called *ATHENA*, is not planned before 2021.

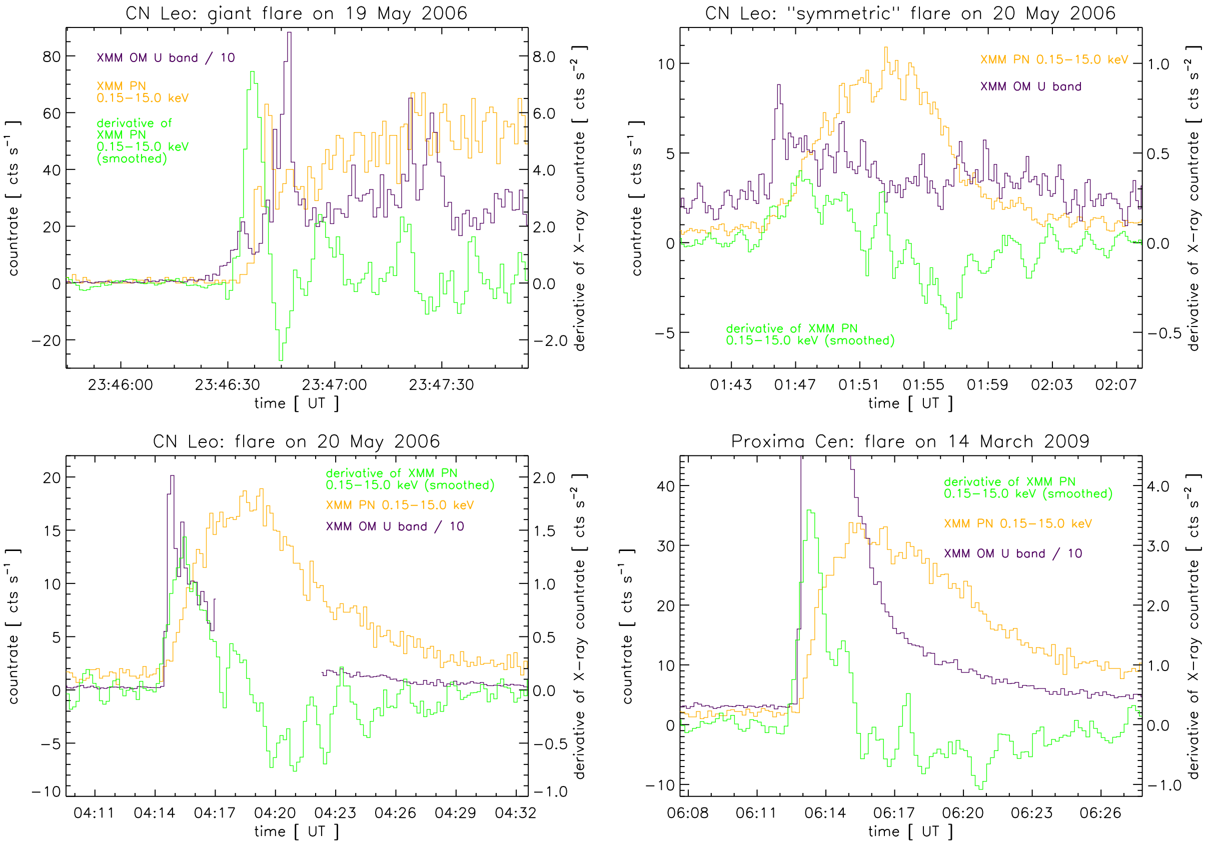

CN Leo: giant flare on 19 May 2006

CN Leo: "symmetric" flare on 20 May 2006

CN Leo: flare on 20 May 2006

Proxima Cen: flare on 14 March 2009

Figure 9.2: *XMM-Newton* X-ray and U band lightcurves for four larger flares on CN Leo and Proxima Cen. The Neupert effect scenario is valid for only two of them (bottom).

Further observations

While the giant flare observed on CN Leo on 19/20 May 2006 has been investigated in great detail, it covers only a small part of the multiwavelength campaign. As shown in Fig. 9.1, two further large X-ray flares worth a separate analysis occurred during the same night. Especially the first event at 1:45 UT is interesting, as despite its strength in X-rays, it had no obvious effect on the photospheric continuum and was also only barely visible in the chromospheric emission lines, which indicates that it did not penetrate deep into the lower layers of the stellar atmosphere. A preliminary analysis of the X-ray data of the two flares (Liefke et al. 2009) yields loop lengths similar to the values obtained for the giant flare, which is in line with the assumption that all three flares originated from the same active region. Several smaller flares are additionally visible in the X-ray and UV data.

In addition to the six observations targeting CN Leo with *XMM-Newton* in X-rays and with the UVES spectrograph at the VLT in the optical, another multiwavelength campaign with three observing runs on the M5.5 star Proxima Centauri has been performed in March 2009 with the same instruments and using a similar setup. Lightcurves of these data are also shown in Fig. 9.1. A huge flare, not as strong as the giant flare on CN Leo but of longer duration and therefore also allowing a detailed analysis, has been observed on 14 March 2009; and again, several smaller flares are covered. The analysis of the multiwavelength data of the flare has been performed by Fuhrmeister et al. (2011).

Flare statistics

The six *XMM-Newton* X-ray observations of CN Leo add up to 112 ks of data. Simultaneous optical photometry and spectroscopy is available for the most part of it, which allows to search for dependencies between flux increase and exponential decay time in different spectral bands for a large number of flares: A total number of 27 flares are covered by the data, with 19 of them observed in X-rays, 15 in the U band, and 10 in the optical blue band. Most of them were of short duration (<1 hour) in X-rays, and even shorter in the optical or in the UV. Average flare durations are 28 minutes in X-rays, 325 seconds in the U band, and 106 sec-

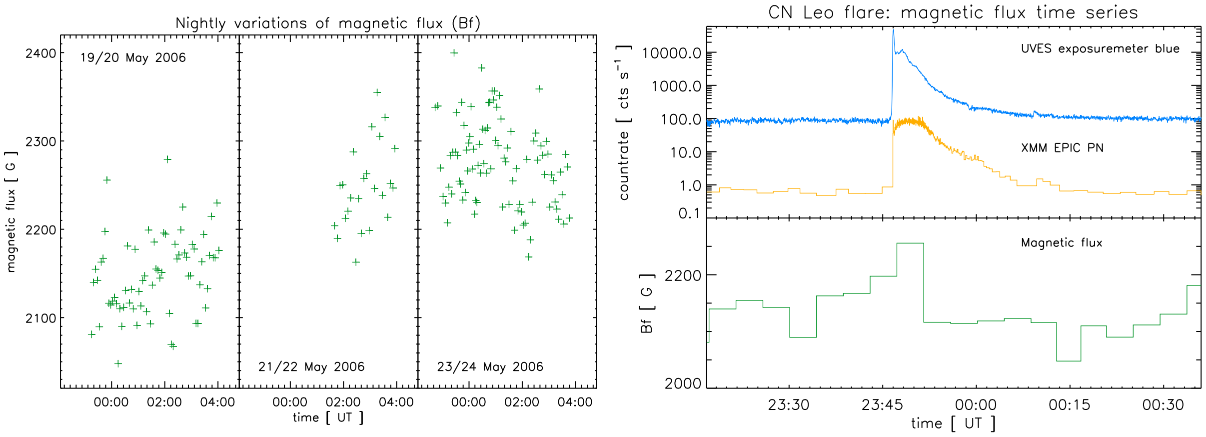

Figure 9.3: Variations in magnetic flux observed on CN Leo. Left: night-to-night variations and nightly scatter. Right: magnetic flux lightcurve of the giant flare.

onds in the optical. No tight correlations between the amplitudes and decay times can be confirmed, these quantities show a broad distribution (Liefke et al. 2009).

A similar analysis could be performed for the flares observed on Proxima Centauri, where almost complete simultaneous coverage with *XMM-Newton* and UVES is reached. The two flare samples may reveal either similarities or differences between the two stars. The statistical basis for such a comparison will nevertheless be rather poor. At any rate, the multiwavelength flare census provided by the two observing campaigns is unique.

The Neupert effect

In principle, when taking into account all environmental conditions in the stellar atmosphere, i. e. geometrical considerations like the question whether it originates from a single loop or an arcade and the size (loop lengths) of the active region, and physical parameters like geometry and strength of the magnetic field, duration and characteristics of the heating and its penetration depth into the atmosphere, flare emission in different energy bands should be correlated temporally and energetically. However, many observed phenomena, like e. g. the occurrence of time lags in the emission in different energy bands, still require a quantitative description.

Additionally, empirical relations like the Neupert effect, where the time integral of the hard X-ray flux is meant to be proportional to the soft X-ray flux, should hold, but various examples in the literature show that this is not necessarily the case. Fig. 9.2 demonstrates this for the four stronger flares observed during our observing campaigns on CN Leo and Proxima Cen. Hard X-rays are difficult to observe in stellar flares with currently available instrumentation, and thus there is no clear confirmation so far, see e. g. the discussion of the origin of the Fe Kα emission during the *Swift*-detected giant flare on the RS CN binary II Peg by Osten et al. (2007) and Ercolano et al. (2008). We therefore used the emission in the U band as a proxy for hard X-rays, since the flare continuum emission, which dominates at these wavelengths during the initial phases of a flare, is supposed to be excited instantaneously by the accelerated electrons that cause the nonthermal hard X-rays. The Neupert effect relation holds only for two of the four flare events, so the question remains why this is the case. Further studies covering the broadest multiwavelength range possible should provide insight to the issue where the energy deposited by the hard X-Rays goes instead.

Correlation of magnetic fields and activity phenomena

Using magnetically sensitive and insensitive lines in the FeH band around 1 μm, we determined the photospheric magnetic flux from the optical spectra of CN Leo in May 2006, focussing on variations in the differential measurements. Fig. 9.3 shows that the data from the first and from the second night deviate, with an average offset of 100 G. Second and third night show an additional shift of 25 G. During two of the three nights, additional trends are visible in the magnetic flux, which correlate with the chromospheric activity as traced by the Hα line flux (Reiners et al. 2007). Further investigation of the variability of stellar photospheric magnetic fields on timescales of hours or days and its relation to the behavior of other activity indicators is highly desirable.

Fig. 9.3 also shows the time series of magnetic flux measurements together with the X-ray and optical lightcurves of the giant flare. The shape of the magnetic flux lightcurve with its slight increase before the flare, indicating a compression of the field lines, and a sudden drop after the reconnection event suggests that short-term variations related to the flare have been detected (Liefke et al. 2007). However, although the flare plasma strongly enhances the flux even at these long wavelengths, it will be difficult to assess its contribution to the properties of the global photospheric magnetic field of CN Leo. Additionally, the magnetic flux time series shows other variations of similar amplitude but apparently unrelated to other flare events. Only further observations of stronger flares, probably in combination with a careful statistical analysis, can therefore prove or reject whether such putative signatures of magnetic reconnection hold true even in light of the uncertainties of the differential measurements.

Long-term behavior of stellar magnetic fields

With the newest data obtained in March 2009, optical spectra of CN Leo covering the FeH band are now available for a timespan of more than five years. This allows to investigate not only changes in stellar photospheric magnetic fields on shorter timescales, but also long-term variability. In particular, it may provide a new approach to track down magnetic activity cycles in M dwarfs, i. e. highly active stars, where any long-term cyclic behavior – if existent – so far is hidden behind strong short-term variations like flares. The observation of activity cycles in fully convective stars would pose a challenge to current turbulent dynamo models.

Chasing the strongest stellar flares

For the very strongest stellar flares observed so far, the enormous initial energy release at the shortest X-ray wavelengths is able to trigger the Burst Alert Telescope (BAT) of the *Swift* satellite. In 2005, II Peg was the first star to be caught by *Swift* in this way (Osten et al. 2007). The detected giant flare event corresponded to X4400000 in the classification scheme of solar X-ray flares, with the strongest solar flare observed so far ranked as X28. However, such outstanding events are very rare, only four further detections have been made so far. Two of them involved the eclipsing binary Algol, the other two could be ascribed to the active M dwarfs EV Lac (Osten et al. 2010) and CC Eri (Evans et al. 2008).

Since the Gamma-ray Burst Coordination Network (GCN) automatically distributes burst alert notices for each trigger immediately after detection, it is possible to clearly identify a giant stellar flare detected by *Swift* within less than 80 seconds after the initial outburst. For three subsequent ESO periods, I successfully proposed to make use of an automated procedure to react instantaneously on such a rare event by now and to use the Rapid Response Mode ESO offers to obtain optical spectra of these extreme stellar flares immediately, i. e. within a few minutes after detection in X-rays with the UVES or X-Shooter spectrographs at the VLT. A timeseries of optical spectra covering the evolution of a stellar flare event even stronger than the one observed on CN Leo would offer a unique opportunity to gain even better insight into the physical processes in the lower stellar atmosphere after deposition of vast amounts of energy originating from a magnetic reconnection event.

In detail, one would be able to address several issues that have not been fully clarified by the CN Leo data: Up to which temperatures are lower atmospheric layers heated by the most energetic flare events? Which processes cool down the photosphere and chromosphere and how is the flare energy redistributed? How does the flaring plasma evolve at different heights above the stellar surface? In which states of the flare can mass motions like evaporating material moving upward or plasma that cools down and falls back to the surface be observed, and what amount of material is involved in such processes?

Many interesting aspects in the field of stellar activity are waiting for further investigation, such as more detailed studies of flares both large and small, or the time-resolved interaction of all kinds of activity indicators as observed in multiwavelength data.

Bibliography

Acton, L. W., Catura, R. C., & Joki, E. G. 1975, ApJ, 195, L93

Allred, J. C., Hawley, S. L., Abbett, W. P., & Carlsson, M. 2006, ApJ, 644, 484

Anders, E. & Grevesse, N. 1989, Geochim. Cosmochim. Acta, 53, 197

Antia, H. M. & Basu, S. 2005, ApJ, 620, L129

Arnaud, K. A. 1996, in ASP Conf. Ser. 101: Astronomical Data Analysis Software and Systems V, ed. G. H. Jacoby & J. Barnes, 17–+

Aschwanden, M. J. 2004, Physics of the Solar Corona. An Introduction (Praxis Publishing Ltd)

Aschwanden, M. J. & Alexander, D. 2001, Sol. Phys., 204, 91

Aschwanden, M. J., Stern, R. A., & Güdel, M. 2008, ApJ, 672, 659

Asplund, M., Grevesse, N., & Sauval, A. J. 2005, in ASP Conf. Ser. 336: Cosmic Abundances as Records of Stellar Evolution and Nucleosynthesis, 25–38

Asplund, M., Grevesse, N., Sauval, A. J., & Scott, P. 2009, ARA&A, 47, 481

Audard, M., Güdel, M., Sres, A., Raassen, A. J. J., & Mewe, R. 2003a, A&A, 398, 1137

Audard, M., Güdel, M., & Skinner, S. L. 2003b, ApJ, 589, 983

Bahcall, J. N., Basu, S., Pinsonneault, M., & Serenelli, A. M. 2005a, ApJ, 618, 1049

Bahcall, J. N., Basu, S., & Serenelli, A. M. 2005b, ApJ, 631, 1281

Baliunas, S. L., Donahue, R. A., Soon, W. H., et al. 1995, ApJ, 438, 269

Benedict, G. F., McArthur, B., Nelan, E., et al. 1998, AJ, 116, 429

Benz, A. O. & Güdel, M. 2010, ARA&A, 48, 241

Berger, E., Basri, G., Gizis, J. E., et al. 2008a, ApJ, 676, 1307

Berger, E., Gizis, J. E., Giampapa, M. S., et al. 2008b, ApJ, 673, 1080

Berger, E., Rutledge, R. E., Reid, I. N., et al. 2005, ApJ, 627, 960

Betta, R., Peres, G., Reale, F., & Serio, S. 1997, A&AS, 122, 585

Brinkman, A. C., Behar, E., Güdel, M., et al. 2001, A&A, 365, L324

Brosius, J. W., Davila, J. M., Thomas, R. J., & Monsignori-Fossi, B. C. 1996, ApJS, 106, 143

Brown, J. C. 1973, Sol. Phys., 28, 151

Browning, M. K. 2008, ApJ, 676, 1262

Canfield, R. C., Penn, M. J., Wulser, J.-P., & Kiplinger, A. L. 1990, ApJ, 363, 318

Cargill, P. J. & Klimchuk, J. A. 2004, ApJ, 605, 911

Chabrier, G. & Baraffe, I. 1997, A&A, 327, 1039

Chabrier, G. & Küker, M. 2006, A&A, 446, 1027

Charbonneau, P. 2010, Living Reviews in Solar Physics, 7

Craig, I. J. D. 1977, A&A, 61, 575

Craig, I. J. D. & Brown, J. C. 1976, A&A, 49, 239

Cram, L. E. & Mullan, D. J. 1979, ApJ, 234, 579

Crespo-Chacón, I., Montes, D., García-Alvarez, D., et al. 2006, A&A, 452, 987

de Jager, C., Heise, J., van Genderen, A. M., et al. 1989, A&A, 211, 157

Delfosse, X., Forveille, T., Perrier, C., & Mayor, M. 1998, A&A, 331, 581

Dere, K. P., Landi, E., Mason, H. E., Monsignori Fossi, B. C., & Young, P. R. 1997, A&AS, 125, 149

Dobler, W., Stix, M., & Brandenburg, A. 2006, ApJ, 638, 336

Dorman, B. & Arnaud, K. A. 2001, in Astronomical Society of the Pacific Conference Series, Vol. 238, Astronomical Data Analysis Software and Systems X, ed. F. R. Harnden, Jr., F. A. Primini, & H. E. Payne, 415–419

Doyle, J. G., Butler, C. J., Bryne, P. B., & van den Oord, G. H. J. 1988, A&A, 193, 229

Drake, J. J., Ercolano, B., & Swartz, D. A. 2008, ApJ, 678, 385

Drake, J. J. & Testa, P. 2005, Nature, 436, 525

Durney, B. R., De Young, D. S., & Roxburgh, I. W. 1993, Sol. Phys., 145, 207

Eason, E. L. E., Giampapa, M. S., Radick, R. R., Worden, S. P., & Hege, E. K. 1992, AJ, 104, 1161

Ercolano, B., Drake, J. J., Reale, F., Testa, P., & Miller, J. M. 2008, ApJ, 688, 1315

Evans, P. A., Page, K. L., Beardmore, A. P., et al. 2008, The Astronomer's Telegram, 1787, 1

Favata, F., Micela, G., Sciortino, S., & Barbera, M. 1994, in Astrophysics and Space Science Library, Vol. 187, Frontiers of Space and Ground-Based Astronomy, ed. W. Wamsteker, M. S. Longair, & Y. Kondo, 589–+

Favata, F., Reale, F., Micela, G., et al. 2000, A&A, 353, 987

Favata, F. & Schmitt, J. H. M. M. 1999, A&A, 350, 900

Feldman, U. & Laming, J. M. 2000, Phys. Scr, 61, 222

Fisher, G. H. 1987, ApJ, 317, 502

Fisher, G. H. 1989, ApJ, 346, 1019

Fleming, T. A., Giampapa, M. S., Schmitt, J. H. M. M., & Bookbinder, J. A. 1993, ApJ, 410, 387

Fuhrmeister, B., Lalitha, S., Poppenhaeger, K., et al. 2011, A&A, 534, A133

Fuhrmeister, B., Liefke, C., & Schmitt, J. H. M. M. 2007, A&A, 468, 221

Fuhrmeister, B., Liefke, C., Schmitt, J. H. M. M., & Reiners, A. 2008, A&A, 487, 293

Fuhrmeister, B., Schmitt, J. H. M. M., & Hauschildt, P. H. 2005a, A&A, 436, 677

Fuhrmeister, B., Schmitt, J. H. M. M., & Hauschildt, P. H. 2005b, A&A, 439, 1137

Fuhrmeister, B., Schmitt, J. H. M. M., & Hauschildt, P. H. 2010, A&A, 511, A83

Fuhrmeister, B., Schmitt, J. H. M. M., & Wichmann, R. 2004, A&A, 417, 701

Güdel, M. 2004, A&A Rev., 12, 71

Güdel, M., Schmitt, J. H. M. M., Bookbinder, J. A., & Fleming, T. A. 1993, ApJ, 415, 236

Gabriel, A. H. & Jordan, C. 1969, MNRAS, 145, 241

García-Alvarez, D., Jevremović, D., Doyle, J. G., & Butler, C. J. 2002, A&A, 383, 548

Gershberg, R. E. & Shakhovskaia, N. I. 1983, Ap&SS, 95, 235

Golub, L. 1983, in Astrophysics and Space Science Library, Vol. 102, IAU Colloq. 71: Activity in Red-Dwarf Stars, ed. P. B. Byrne & M. Rodono, 83–106

Golub, L. & Pasachoff, J. M. 2009, The Solar Corona (Cambridge University Press, ISBN 9780521882019.)

Gray, D. F. 2005, The Observation and Analysis of Stellar Photospheres (Cambridge University Press)

Grevesse, N. & Sauval, A. J. 1998, Space Sci. Rev., 85, 161

Güdel, M., Arzner, K., Audard, M., & Mewe, R. 2003, A&A, 403, 155

Güdel, M., Audard, M., Magee, H., et al. 2001, A&A, 365, L344

Güdel, M., Audard, M., Reale, F., Skinner, S. L., & Linsky, J. L. 2004, A&A, 416, 713

Güdel, M., Audard, M., Skinner, S. L., & Horvath, M. I. 2002a, ApJ, 580, L73

Güdel, M., Audard, M., Sres, A., et al. 2002b, in ASP Conf. Ser. 277: Stellar Coronae in the Chandra and XMM-NEWTON Era, ed. F. Favata & J. J. Drake, 497–501

Güdel, M., Benz, A. O., Schmitt, J. H. M. M., & Skinner, S. L. 1996, ApJ, 471, 1002

Gunn, A. G., Doyle, J. G., Mathioudakis, M., Houdebine, E. R., & Avgoloupis, S. 1994, A&A, 285, 489

Günther, H. M., Liefke, C., Schmitt, J. H. M. M., Robrade, J., & Ness, J.-U. 2006, A&A, 459, L29

Habbal, S. R., Druckmüller, M., Morgan, H., et al. 2010, ApJ, 708, 1650

Haisch, B., Strong, K. T., & Rodono, M. 1991, ARA&A, 29, 275

Haisch, B. M., Butler, C. J., Doyle, J. G., & Rodono, M. 1987, A&A, 181, 96

Hawley, S. L., Allred, J. C., Johns-Krull, C. M., et al. 2003, ApJ, 597, 535

Hawley, S. L. & Fisher, G. H. 1992, ApJS, 78, 565

Hawley, S. L. & Pettersen, B. R. 1991, ApJ, 378, 725

Henry, T. J., Subasavage, J. P., Brown, M. A., et al. 2004, AJ, 128, 2460

Hirayama, T. 1974, Sol. Phys., 34, 323

Holman, G. D. 2003, ApJ, 586, 606

Houdebine, E. R. 2003, A&A, 397, 1019

Houdebine, E. R. & Doyle, J. G. 1994, A&A, 289, 169

Houdebine, E. R., Foing, B. H., Doyle, J. G., & Rodono, M. 1993, A&A, 274, 245

Hudson, H. S., Strong, K. T., Dennis, B. R., et al. 1994, ApJ, 422, L25

Jackson, P. D., Kundu, M. R., & White, S. M. 1989, A&A, 210, 284

Jevremović, D., Doyle, J. G., & Short, C. I. 2000, A&A, 358, 575

Jones, C. A., Thompson, M. J., & Tobias, S. M. 2010, Space Sci. Rev., 152, 591

Judge, P. 2002, in Astronomical Society of the Pacific Conference Series, Vol. 277, Stellar Coronae in the Chandra and XMM-NEWTON Era, ed. F. Favata & J. J. Drake, 45–56

Kahler, S. 1975, in IAU Symposium, Vol. 68, Solar Gamma-, X-, and EUV Radiation, ed. S. R. Kane, 211–231

Kashyap, V. & Drake, J. J. 1998, ApJ, 503, 450

Katsova, M. M., Livshits, M. A., & Schmitt, J. H. M. M. 2002, in Astronomical Society of the Pacific Conference Series, Vol. 277, Stellar Coronae in the Chandra and XMM-NEWTON Era, ed. F. Favata & J. J. Drake, 515–520

Kenyon, S. J. & Hartmann, L. 1995, ApJS, 101, 117

Kippenhahn, R. & Weigert, A. 1994, Stellar Structure and Evolution (Springer-Verlag Berlin Heidelberg New York)

Kirkpatrick, J. D., Henry, T. J., & McCarthy, Jr., D. W. 1991, ApJS, 77, 417

Klimchuk, J. A. 2002, in Astronomical Society of the Pacific Conference Series, Vol. 277, Stellar Coronae in the Chandra and XMM-NEWTON Era, ed. F. Favata & J. J. Drake, 321–331

Klimchuk, J. A. 2006, Sol. Phys., 234, 41

Kopp, R. A. & Poletto, G. 1984, Sol. Phys., 93, 351

Kostiuk, N. D. & Pikelner, S. B. 1975, Soviet Astronomy, 18, 590

Kron, G. E. 1952, ApJ, 115, 301

Kürster, M. & Schmitt, J. H. M. M. 1996, A&A, 311, 211

Lacy, C. H., Moffett, T. J., & Evans, D. S. 1976, ApJS, 30, 85

Laming, J. M. 2004, ApJ, 614, 1063

Landi, E., Del Zanna, G., Young, P. R., et al. 2006, ApJS, 162, 261

Landi, E. & Landini, M. 1998, A&A, 340, 265

Liebert, J., Kirkpatrick, J. D., Reid, I. N., & Fisher, M. D. 1999, ApJ, 519, 345

Liefke, C. 2005, Differential emission measures and abundances of stellar coronae (Diploma thesis, Universität Hamburg, October 2005)

Liefke, C., Fuhrmeister, B., & Schmitt, J. H. M. M. 2009, in American Institute of Physics Conference Series, Vol. 1094, Proceedings of the 15th Cambridge Workshop on Cool Stars, Stellar Systems and the Sun, ed. E. Stempels, 608–611

Liefke, C., Fuhrmeister, B., & Schmitt, J. H. M. M. 2010, A&A, 514, A94

Liefke, C., Reiners, A., & Schmitt, J. H. M. M. 2007, Memorie della Societa Astronomica Italiana, 78, 258

Liefke, C. & Schmitt, J. H. M. M. 2006, A&A, 458, L1

Liefke, C. & Schmitt, J. H. M. M. in preparation

Linsky, J. L., Ayres, T. R., Brown, A., & Osten, R. A. 2002, Astron. Nachr., 323, 321

Love, J. 1999, Astronomy and Geophysics, 40, 14

Magazzu, A., Martin, E. L., & Rebolo, R. 1993, ApJ, 404, L17

Magee, H. R. M., Güdel, M., Audard, M., & Mewe, R. 2003, Advances in Space Research, 32, 1149

Maggio, A. 2006, in High Resolution X-ray Spectroscopy: towards XEUS and Con-X

Maggio, A., Drake, J. J., Favata, F., & Güdel, M. 2005a, in ESA Special Publication, Vol. 560, 13th Cambridge Workshop on Cool Stars, Stellar Systems and the Sun, ed. F. Favata, G. A. J. Hussain, & B. Battrick, 129–138

Maggio, A., Drake, J. J., Favata, F., Güdel, M., & Jordan, C. 2005b, in American Institute of Physics Conference Series, Vol. 774, X-ray Diagnostics of Astrophysical Plasmas: Theory, Experiment, and Observation, ed. R. Smith, 401–404

Maggio, A., Drake, J. J., Kashyap, V., et al. 2004, ApJ, 613, 548

Maggio, A. & Ness, J.-U. 2005, ApJ, 622, L57

Mahmoud, F. M. 1993, Ap&SS, 209, 237

Mason, H. E. & Fossi, B. C. M. 1994, A&A Rev., 6, 123

Mazzotta, P., Mazzitelli, G., Colafrancesco, S., & Vittorio, N. 1998, A&AS, 133, 403

McIntosh, S. W., Charbonneau, P., & Brown, J. C. 2000, ApJ, 529, 1115

Mitra-Kraev, U., Harra, L. K., Güdel, M., et al. 2005, A&A, 431, 679

Mitra-Kraev, U. & Ness, J.-U. 2006, in High Resolution X-ray Spectroscopy: towards XEUS and Con-X

Moffatt, H. K. 1978, Magnetic field generation in electrically conducting fluids (Cambridge, England, Cambridge University Press, 1978. 353 p.)

Mohanty, S. & Basri, G. 2003, ApJ, 583, 451

Monsignori Fossi, B. C., Landini, M., Fruscione, A., & Dupuis, J. 1995, ApJ, 449, 376

Moore, C. E. 1972, Nat. Stand. Ref. Data Ser., 40

Mullan, D. J. & MacDonald, J. 2001, ApJ, 559, 353

Ness, J.-U., Audard, M., Schmitt, J. H. M. M., & Güdel, M. 2003a, Advances in Space Research, 32, 937

Ness, J.-U., Brickhouse, N. S., Drake, J. J., & Huenemoerder, D. P. 2003b, ApJ, 598, 1277

Ness, J.-U., Güdel, M., Schmitt, J. H. M. M., Audard, M., & Telleschi, A. 2004, A&A, 427, 667

Ness, J.-U. & Jordan, C. 2008, MNRAS, 385, 1691

Ness, J.-U., Schmitt, J. H. M. M., Audard, M., Güdel, M., & Mewe, R. 2003c, A&A, 407, 347

Ness, J.-U., Schmitt, J. H. M. M., Burwitz, V., Mewe, R., & Predehl, P. 2002a, A&A, 387, 1032

Ness, J.-U., Schmitt, J. H. M. M., Burwitz, V., et al. 2002b, A&A, 394, 911

Ness, J.-U. & Wichmann, R. 2002, Astron. Nachr., 323, 129

Neupert, W. M. 1968, ApJ, 153, L59

Nordon, R. & Behar, E. 2007, A&A, 464, 309

Nordon, R. & Behar, E. 2008, A&A, 482, 639

Norton, A. J., Wheatley, P. J., West, R. G., et al. 2007, A&A, 467, 785

O'Dea, C. P. & McKinnon, W. B. 1987, PASP, 99, 1039

Osten, R. A., Drake, S., Tueller, J., et al. 2007, ApJ, 654, 1052

Osten, R. A., Godet, O., Drake, S., et al. 2010, ApJ, 721, 785

Osten, R. A., Hawley, S. L., Allred, J., et al. 2006, ApJ, 647, 1349

Osten, R. A., Hawley, S. L., Allred, J. C., Johns-Krull, C. M., & Roark, C. 2005, ApJ, 621, 398

Pallavicini, R., Golub, L., Rosner, R., et al. 1981, ApJ, 248, 279

Pallavicini, R., Kundu, M. R., & Jackson, P. D. 1986, in Lecture Notes in Physics, Berlin Springer Verlag, Vol. 254, Cool Stars, Stellar Systems and the Sun, ed. M. Zeilik & D. M. Gibson, 225–228

Pallavicini, R., Serio, S., & Vaiana, G. S. 1977, ApJ, 216, 108

Pallavicini, R., Tagliaferri, G., & Stella, L. 1990, A&A, 228, 403

Parker, E. N. 1955, ApJ, 122, 293

Parker, E. N. 1988, ApJ, 330, 474

Parkinson, J. H. 1977, A&A, 57, 185

Parsamyan, E. S. 1995, Astrophysics, 38, 206

Paulson, D. B., Allred, J. C., Anderson, R. B., et al. 2006, PASP, 118, 227

Pavlenko, Y. V., Jones, H. R. A., Lyubchik, Y., Tennyson, J., & Pinfield, D. J. 2006, A&A, 447, 709

Peres, G. 2000, Sol. Phys., 193, 33

Peres, G., Serio, S., Vaiana, G. S., & Rosner, R. 1982, ApJ, 252, 791

Pettersen, B. R. 1976, Institute of Theoretical Astrophysics Blindern Oslo Reports, 46, 1

Pettersen, B. R., Olah, K., & Sandmann, W. H. 1992, A&AS, 96, 497

Piskunov, N. E. & Valenti, J. A. 2002, A&A, 385, 1095

Pizzolato, N., Maggio, A., Micela, G., Sciortino, S., & Ventura, P. 2003, A&A, 397, 147

Poletto, G., Pallavicini, R., & Kopp, R. A. 1988, A&A, 201, 93

Pottasch, S. R. 1963, ApJ, 137, 945

Pradhan, A. K. & Shull, J. M. 1981, ApJ, 249, 821

Priest, E. R. & Forbes, T. G. 2002, A&A Rev., 10, 313

Raassen, A. J. J., Mewe, R., Audard, M., et al. 2002, A&A, 389, 228

Raassen, A. J. J., Ness, J.-U., Mewe, R., et al. 2003, A&A, 400, 671

Reale, F. 2002, in Astronomical Society of the Pacific Conference Series, Vol. 277, Stellar Coronae in the Chandra and XMM-NEWTON Era, ed. F. Favata & J. J. Drake, 103–114

Reale, F. 2007, A&A, 471, 271

Reale, F., Betta, R., Peres, G., Serio, S., & McTiernan, J. 1997, A&A, 325, 782

Reale, F., Güdel, M., Peres, G., & Audard, M. 2004, A&A, 416, 733

Reale, F. & Micela, G. 1998, A&A, 334, 1028

Reale, F. & Orlando, S. 2008, ApJ, 684, 715

Reale, F., Serio, S., & Peres, G. 1993, A&A, 272, 486

Reid, I. N., Hawley, S. L., & Gizis, J. E. 1995, AJ, 110, 1838

Reiners, A. 2007, A&A, 467, 259

Reiners, A. & Basri, G. 2007, ApJ, 656, 1121

Reiners, A., Schmitt, J. H. M. M., & Liefke, C. 2007, A&A, 466, L13

Robinson, R. D., Carpenter, K. G., Percival, J. W., & Bookbinder, J. A. 1995, ApJ, 451, 795

Robinson, R. D., Cram, L. E., & Giampapa, M. S. 1990, ApJS, 74, 891

Robrade, J., Ness, J.-U., & Schmitt, J. H. M. M. 2004, A&A, 413, 317

Robrade, J. & Schmitt, J. H. M. M. 2005, A&A, 435, 1073

Robrade, J., Schmitt, J. H. M. M., & Favata, F. 2005, A&A, 442, 315

Robrade, J., Schmitt, J. H. M. M., & Favata, F. 2008, A&A, 486, 995

Rosner, R., Tucker, W. H., & Vaiana, G. S. 1978, ApJ, 220, 643

Rutledge, R. E., Basri, G., Martín, E. L., & Bildsten, L. 2000, ApJ, 538, L141

Sanz-Forcada, J., Favata, F., & Micela, G. 2004, A&A, 416, 281

Schmelz, J. T., Nasraoui, K., Roames, J. K., Lippner, L. A., & Garst, J. W. 2005, ApJ, 634, L197

Schmidt, S. J., Cruz, K. L., Bongiorno, B. J., Liebert, J., & Reid, I. N. 2007, AJ, 133, 2258

Schmitt, J. H. M. M. 1997, A&A, 318, 215

Schmitt, J. H. M. M. & Favata, F. 1999, Nature, 401, 44

Schmitt, J. H. M. M., Haisch, B., & Barwig, H. 1993, ApJ, 419, L81

Schmitt, J. H. M. M. & Liefke, C. 2002, A&A, 382, L9

Schmitt, J. H. M. M. & Liefke, C. 2004, A&A, 417, 651

Schmitt, J. H. M. M. & Ness, J.-U. 2002, A&A, 388, L13

Schmitt, J. H. M. M. & Ness, J.-U. 2004, A&A, 415, 1099

Schmitt, J. H. M. M., Ness, J.-U., & Franco, G. 2003, A&A, 412, 849

Schmitt, J. H. M. M., Reale, F., Liefke, C., et al. 2008, A&A, 481, 799

Schmitt, J. H. M. M. & Wichmann, R. 2001, Nature, 412, 508

Serio, S., Reale, F., Jakimiec, J., Sylwester, B., & Sylwester, J. 1991, A&A, 241, 197

Shibata, K., Masuda, S., Shimojo, M., et al. 1995, ApJ, 451, L83

Smith, K., Güdel, M., & Audard, M. 2005, A&A, 436, 241

Smith, R. K., Brickhouse, N. S., Liedahl, D. A., & Raymond, J. C. 2001a, ApJ, 556, L91

Smith, R. K., Brickhouse, N. S., Liedahl, D. A., & Raymond, J. C. 2001b, in Astronomical Society of the Pacific Conference Series, Vol. 247, Spectroscopic Challenges of Photoionized Plasmas, ed. G. Ferland & D. W. Savin, 161–166

Somov, B. V., Spektor, A. R., & Syrovatskii, S. I. 1981, Sol. Phys., 73, 145

Spiesman, W. J. & Hawley, S. L. 1986, AJ, 92, 664

Stelzer, B., Burwitz, V., Audard, M., et al. 2002, A&A, 392, 585

Stelzer, B., Schmitt, J. H. M. M., Micela, G., & Liefke, C. 2006, A&A, 460, L35

Strassmeier, K. G. 2009a, A&A Rev., 17, 251

Strassmeier, K. G. 2009b, A&A Rev., 17, 251

Syrovat-Skii, S. I. & Shmeleva, O. P. 1972, Soviet Astronomy, 16, 273

Tamres, D. H., Canfield, R. C., & McClymont, A. N. 1986, ApJ, 309, 409

Telleschi, A., Güdel, M., Briggs, K., et al. 2005, ApJ, 622, 653

Testa, P., Drake, J. J., Ercolano, B., et al. 2008, ApJ, 675, L97

Testa, P., Drake, J. J., & Peres, G. 2004, ApJ, 617, 508

Testa, P., Drake, J. J., Peres, G., & Huenemoerder, D. P. 2007, ApJ, 665, 1349

Torres, C. A. O., Ferraz Mello, S., & Quast, G. R. 1972, Astrophys. Lett., 11, 13

Torres, G. & Ribas, I. 2002, The Astrophysical Journal, 567, 1140

Vaiana, G. S., Cassinelli, J. P., Fabbiano, G., et al. 1981, ApJ, 245, 163

Vaiana, G. S., Maggio, A., Micela, G., & Sciortino, S. 1992, Memorie della Societa Astronomica Italiana, 63, 545

van den Besselaar, E. J. M., Raassen, A. J. J., Mewe, R., et al. 2003, A&A, 411, 587

Vernazza, J. E., Avrett, E. H., & Loeser, R. 1981, ApJS, 45, 635

Vilmer, N., Trottet, G., Barat, C., et al. 1994, Space Science Reviews, 68, 233

Wallerstein, G. & Tyagi, S. 2004, PASP, 116, 554

Walsh, R. W. & Ireland, J. 2003, A&A Rev., 12, 1

Wargelin, B. J., Kashyap, V. L., Drake, J. J., García-Alvarez, D., & Ratzlaff, P. W. 2008, ApJ, 676, 610

Wolter, U., Robrade, J., Schmitt, J. H. M. M., & Ness, J. U. 2008, A&A, 478, L11

Wolter, U., Schmitt, J. H. M. M., Huber, K. F., et al. 2009, A&A, 504, 561

Wood, B. E. & Linsky, J. L. 2006, ApJ, 643, 444

Wood, B. E. & Linsky, J. L. 2010, ApJ, 717, 1279

Yıldız, M. 2007, MNRAS, 374, 1264

Young, P. R. 2005, A&A, 444, L45

Zboril, M. & Byrne, P. B. 1998, MNRAS, 299, 753

Zuckerman, B., Song, I., Bessell, M. S., & Webb, R. A. 2001, ApJ, 562, L87

Many thanks to

— Jürgen H.M.M. Schmitt —

für Inspiration und Unterstützung, aber auch unendlich viel Geduld

— Birgit Fuhrmeister, Moritz Günther, Ansgar Reiners und Beate Stelzer—
— Antonio Maggio und Jan-Uwe Ness —

die als Ko-Autoren an meinen Veröffentlichungen beteiligt waren
oder mich bei ihren Publikationen mitwirken lassen haben

— Moritz Günther und Christopher Wawrzyn —

meine fleißigen Korrekturleser

— Jan Robrade, Christian Schneider und Sebastian Schröter —

immer hilfsbereite Zimmergenossen

— dem gesamten Team der Hamburger Sternwarte —

für diese unvergleichliche Arbeitsatmosphäre

— Markus Pössel, Cecilia Scorza, Olaf Fischer und Natalie Fischer —

die mir den Rücken freigehalten haben als es eng wurde

— Dominik Elsässer —

Leidensgenosse auf einem Weg, der viel länger wurde als er hätte sein sollen

— Henrika Liefke —

für alles

I acknowledge financial support by the DLR under 50OR0105.